Magnetic tracing of lost time in Cenozoic sediments: Investigating dynamic topography of the Yellowstone plume, USA

Dieke Gerritsen

München, 2025

Magnetic tracing of lost time in Cenozoic sediments: Investigating dynamic topography of the Yellowstone plume, USA

Dissertation zur Erlangung des Doktorgrades
an der Fakultät für Geowissenschaften
der Ludwig-Maximilians-Universität München

Vorgelegt von
Dieke Gerritsen

München, 24.07.2025

Erstgutachter: Prof. Dr. Stuart Gilder
Zweitgutachter: Prof. Dr. Wout Krijgsman

Tag der mündlichen Prüfung: 05.12.2025

Ich kann nich‘in die Zukunft schau‘n,
nur in die Vergangenheit

AnnenMayKantereit

Come as you are

Nirvana, Aberdeen

Keep the earth below my feet
For all my sweat, my blood runs weak
Let me learn from where I have been
Keep my eyes to serve, my hands to learn

Mumford & Sons

Summary

Dynamic topography—vertical surface deflection caused by density variations and convective flow in the mantle—can profoundly reshape Earth's surface. It generates long-wavelength uplift that can reactivate faults, reorganize drainage networks, and influence regional climate and the evolution of flora and fauna. Yet, the spatial and temporal development of dynamic topography remains difficult to constrain, and its effects on surface processes are still poorly understood.

This thesis investigates the imprint of dynamic topography on the geological record, using the Yellowstone mantle plume in North America as a case study. We targeted three key regions in Montana, Wyoming, and Washington, each at a different distance from the plume center and reflecting different stages and expressions of uplift. These regions were selected for their well-preserved sedimentary successions that span the period before and after the eruption of the Columbia River Basalt at ~17 Ma. We collected over 2,000 oriented samples, conducted extensive rock and paleomagnetic analyses, and integrated these with stratigraphic, geochronological, and provenance data to constrain the timing, extent, and surface effects of plume-related uplift.

In Montana, we identified the clearest evidence for dynamic topography. We precisely dated a regional unconformity at ~20 Ma using magnetostratigraphy in combination with published U-Pb ages. Across eight sedimentary sections covering ~40,000 km^2, we observed a sharp increase in magnetite concentration at this unconformity. In parallel, our compilation of detrital zircon data revealed a marked shift in provenance from predominantly Cretaceous to Miocene sources. Together, these observations suggest a westward migration of the North American drainage divide, interpreted as a surface response to dynamic uplift from the Yellowstone plume.

In Wyoming, we detected a more gradual response. Our rock magnetic data show a steady increase in magnetite concentration in the upper Eocene, coinciding with increased input of Archean zircons. We interpret this as post-Laramide uplift and unroofing of the nearby Wind River Range, potentially reactivated by dynamic topography linked to lithospheric rebound or the arrival of the Yellowstone plume.

In Washington, the results are more ambiguous. We observed a stepwise increase in magnetic mineral content in a section draining the Olympic Mountains. However, given the region's complex tectonic setting, we attribute this signal to erosion of magnetite-rich

basalts from the Siletzia terrane, rather than to dynamic topography. More detailed rock magnetic and sedimentological analyses are needed to test this interpretation.

Our work shows that unconformities and associated shifts in magnetic mineralogy can reveal the surface expression of deep mantle processes. By integrating paleomagnetic, stratigraphic, and geochronologic datasets, we provide constraints on the spatial and temporal evolution of dynamic topography associated with the Yellowstone plume. These results provide valuable input for geodynamic and surface process models. Ultimately, this thesis contributes to a deeper understanding of how mantle dynamics shape Earth's surface and, indirectly, the ecosystems and climates that respond to it.

Contents

1

Introduction

1.1 Dynamic topography

The concept of dynamic topography emerged to explain regional surface anomalies that could not be accounted for by surface tectonic forces alone. It refers to the long-wavelength vertical motions of Earth's surface, driven by viscous flow within the mantle (Hager et al., 1985). Unlike isostatic adjustments that result from crustal loading and unloading, dynamic topography is a consequence of mantle convection: the buoyant rise and gravitational sinking of material within Earth's mantle (Figure 1). This process exerts vertical stresses on the base of the lithosphere, deforming the overlying surface over timescales of approximately 10–20 Myr (Vilacís et al., 2024). Dynamic topography includes subsidence associated with subducting slabs and uplift related to mantle plumes. It plays a key role in shaping continental interiors, influencing sedimentation patterns, drainage evolution, and even climate through changes in elevation (Cox, 1989).

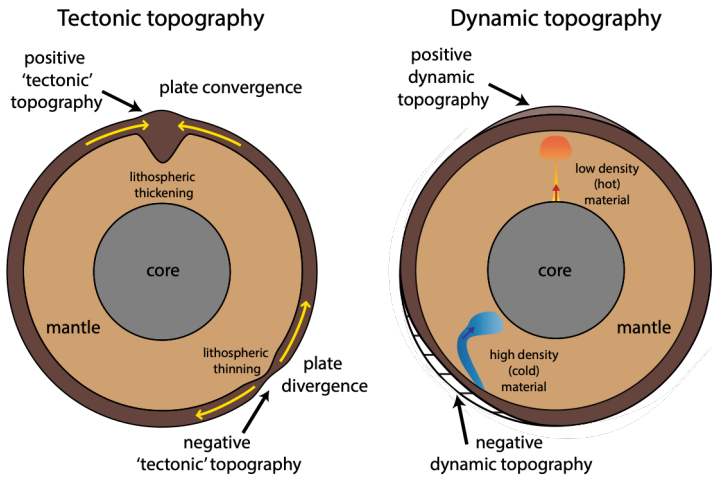

Figure 1. Simple sketch of isostatically compensated tectonic topography **(left)** and dynamic topography **(right)**. Modified from Braun (2010). Vertical deflections are strongly exaggerated; actual Earth topography is only a few kilometers high, which is negligible compared to Earth's 6700 km radius.

Present-day estimates of dynamic topography have been obtained using a variety of observational and modeling techniques. In the oceans, it is relatively straightforward to estimate dynamic topography, as oceanic depth increases with the square root of lithospheric age away from mid-ocean ridges (Fowler, 2004). So, by removing this isostatic component and accounting for crustal thickness anomalies from the current topography, present-day dynamic topography can be estimated; amplitudes of approximately ±1 km and wavelengths around 1000 km were found (Hoggard et al., 2016; 2017). On the continents, present-day dynamic topography has been estimated using a variety of seismologic datasets and laboratory-based velocity-density measurements (Holdt et al., 2022; Stephenson et al., 2024); estimates vary between ±1–2 km with wavelengths ranging from 1000–5000 km.

Isolating dynamic topography is challenging because its length scale overlaps with those of other signals, such as isostasy. However, because dynamic topography evolves over million-year timescales, the geological record provides a means to resolve its long-term behavior. One of the most iconic examples of dynamic subsidence is the Western Interior Seaway, where marine sediments were deposited on the cratonic interior of North America in response to dynamic subsidence attributed to the subducting Farallon slab (Burgess et al., 1997; Mitrovica et al., 1989; Sahagian, 1987). Dynamic uplift is more difficult to constrain, particularly in continental interiors where sea-level markers are absent. In such cases, subaerial erosion erases the geological record. Therefore, dynamic uplift is reflected in the geologic record by gaps (i.e., lost time), also called hiatuses, which can be recognized in the field by erosional surfaces (i.e., unconformities) (Friedrich, 2018; Friedrich et al., 2018).

The marginal region of a dynamically uplifted area is particularly interesting to study, as it records complex and transient patterns of vertical motion, erosion, and deformation (Friedrich, 2018; Friedrich et al., 2018; Rainbird and Ernst, 2001). Initially, the plume margin rises together with the plume center, followed by subsidence as the plume ascends further (Figure 2). During plume head flattening, renewed outward-migrating uplift leads to erosion, regional faulting, and drainage reorganization in the plume margin. This uplift phase is followed by large-scale magmatism in the plume center, manifesting as flood basalts (Campbell and Griffiths, 1990; Saunders et al., 2007).

To constrain the spatial and temporal expression of dynamic topography, hiatus surfaces have been mapped globally (Carena et al., 2019; Hayek et al., 2020; Vibe et al., 2018; Vilacís et al., 2022; 2024). However, quantifying the timing, magnitude, and extent of this dynamic signal at a finer resolution remains a significant challenge. One of the youngest mantle plumes on Earth is the Yellowstone plume, whose flood basalts (Columbia River Basalt Group) erupted in the early Miocene (<17.3 Ma, Cahoon et al., 2020). Moreover, the area is well mapped and easily accessible, making it particularly well-suited for the study of dynamic topography. This thesis integrates (magneto)stratigraphic, provenance, and geochronological data to improve constraints on the dynamic topography associated with the Yellowstone plume.

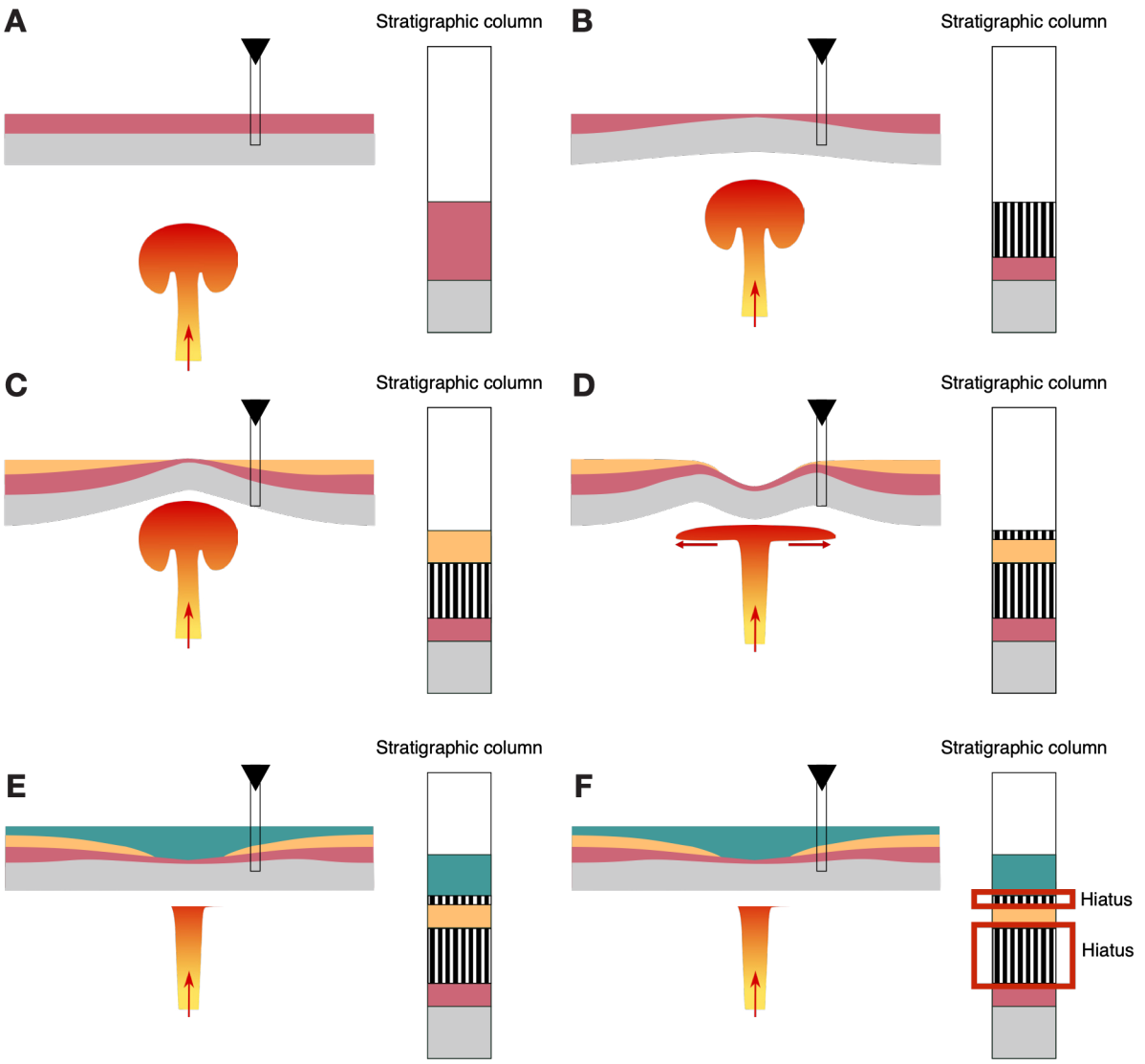

Figure 2. Simplified sketch showing the expression of dynamic topography in the geologic record during different stages for a column in the marginal region of a plume: **(A–C)** plume rise, **(D)** plume spreading, and **(E–F)** thermal relaxation. Stratigraphic column displayed illustrates the sedimentary record in the plume margin. Method from Friedrich et al. (2018); adapted from Vilacís (2025).

1.2 Rock magnetism and paleomagnetism

Earth's magnetic field is dominantly dipolar and, over geological timescales, can be approximated by a geocentric axial dipole (GAD) aligned with Earth's rotation axis. During sediment deposition, ferromagnetic minerals, mainly iron oxides like magnetite, can acquire a detrital remanent magnetization (DRM). The moments of these minerals statistically align with the ambient geomagnetic field during deposition, and their magnetic signal becomes locked in during diagenesis. The resulting remanent

magnetization can remain stable for hundreds of millions of years, preserving a record of the geomagnetic field at the time of deposition (e.g., Tauxe, 2010).

1.2.1 Sampling

To recover paleomagnetic directions, oriented samples are collected from a site or section. A site refers to a specific exposure, such as a sedimentary unit or an igneous cooling unit (i.e., a lava flow or dike), while a section represents a longer stratigraphic interval with a sampling level every few meters. Rock samples are collected using a water-cooled, electrically powered drill, whereas soft sediments are collected by hammering a corer into fresh outcrop faces. The orientation of each sample is measured using a magnetic and sun compass. Additionally, bedding attitude measurements (strike and dip) are measured to correct paleomagnetic directions for post-depositional tilting and obtaining the tilt-corrected orientation.

1.2.2 Paleomagnetism

Samples are subjected to stepwise alternating field (AF) or thermal demagnetization to isolate the characteristic remanent magnetization (ChRM) (Figure 3; Butler, 1992). The natural remanent magnetization (NRM) represents the initial magnetization before any demagnetization (step 0 in Figure 3). After each demagnetization step, samples are measured for their remanent magnetization, which yields a set of remanence vectors (Figure 3D). As demagnetization progresses, the magnitude of the remanent vector decreases as the magnetization is progressively unblocked due to increasing temperatures or peak AF amplitude (Néel, 1949). The temperature at which the remanent magnetization is lost due to thermal agitation is called the Curie temperature, which is characteristic for each magnetic mineral type. The ChRM direction is determined using principal component analysis (PCA) on the vector trajectory (Kirschvink, 1980), with linear segments trending to the origin interpreted as the primary remanence (e.g., steps 3-6 in Figure 3C).

As Earth's magnetic field has reversed its polarity numerous times throughout geologic history, sediments that lock in magnetic directions provide a record of these reversals. Magnetostratigraphy exploits the temporal pattern of geomagnetic polarity reversals by identifying polarity chrons from ChRM directions (Krijgsman and Turner, 2014). By matching the observed polarity sequence to the Geomagnetic Polarity Time Scale (GPTS), a chronological framework is established for the sedimentary section (Opdyke and Channell, 1996). Moreover, by comparing the mean for the reversed and normal polarity data, one can confirm the quality of the data through a reversal test (Tauxe, 2010). Other

tests include the fold test, comparing data clustering before and after tilt correction, and the SVEI test to check for inclination shallowing (Tauxe et al., 2024).

ChRM directions can be converted to Virtual Geomagnetic Poles (VGPs) using the dipole field assumption (e.g., Tauxe, 2003); their latitude and longitude reflect the position of the geomagnetic pole at the time of remanence acquisition. Averaging site-mean VGPs yields a paleopole, which is compared to a reference Apparent Polar Wander Path (APWP) from a fixed tectonic plate to test for tectonic rotations or displacements.

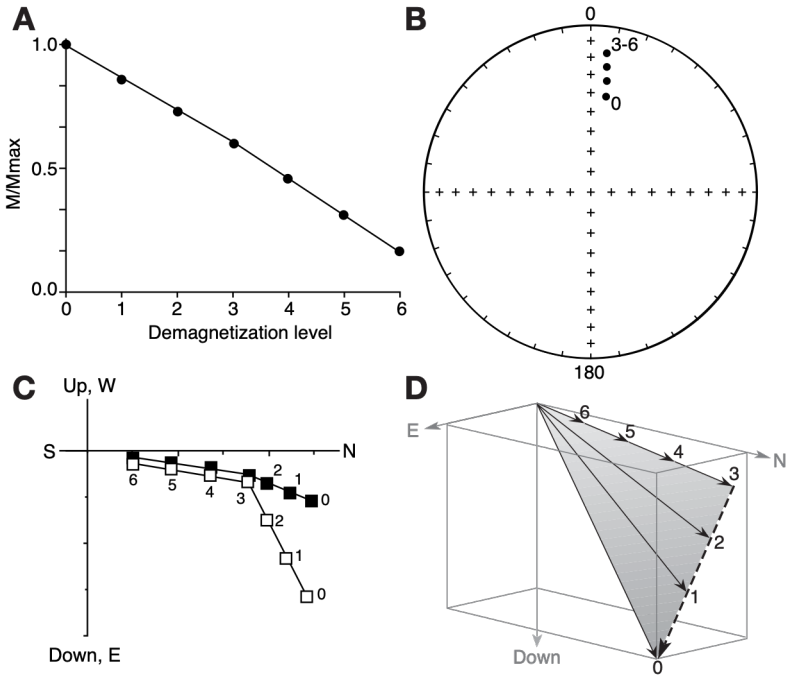

Figure 3. Stepwise demagnetization and vector analysis (modified from Butler, 1992). **(A)** The original remanent magnetization (Mmax) is progressively destroyed during demagnetization steps 0-6 (M/Mmax). The resulting sequence of vectors can be displayed on a stereographic projection **(B)** or a Zijderveld (1967) diagram **(C)** which projects the vectors onto two orthogonal planes **(D)**. It enables visual fitting of linear components; in this case, the characteristic remanent magnetization (ChRM) direction would be obtained by fitting a straight line through points 3-6.

1.2.3 Rock magnetism

Rock magnetic measurements are used to characterize the mineralogy of the magnetic mineral assemblage in rocks (e.g., Dunlop and Özdemir, 2007). Despite typically comprising <1% of the bulk sediment volume, they reflect provenance, environment, and climate, making rock magnetic parameters valuable proxies in paleoenvironmental studies (Evans and Heller, 2003). Rapid, non-destructive techniques such as magnetic susceptibility, hysteresis, and backfield measurements are used to characterize mineral type, grain size, and concentration.

Magnetic susceptibility (χ) quantifies the degree to which a material becomes magnetized in an external magnetic field. It is a bulk property sensitive to both concentration and type of magnetic minerals. Variations in susceptibility of sedimentary rocks can signal changes in provenance, depositional conditions, or post-depositional diagenesis.

Hysteresis loops are measured by subjecting samples to cycling magnetic fields (Figure 4; Butler, 1992). The key parameters extracted include:

- Saturation magnetization (Ms; Figure 4C): maximum magnetization.
- Remanent saturation magnetization (Mrs; Figure 4D): magnetization remaining when the field is removed after full saturation.
- Coercive force (Bc; Figure 4E): the field required to bring net magnetization to zero.
- Hysteresis shape parameter (σ_{hys}): shape of the hysteresis loop, indicative of superparamagnetic particles or mixtures of fractions with highly contrasting coercivities (Fabian, 2003).
- High-field susceptibility (χ_{HF}; Figure 4A): slope of the hysteresis loop after saturation; contribution of paramagnetic, diamagnetic and/or antiferromagnetic signals, separated from the ferromagnetic signal.

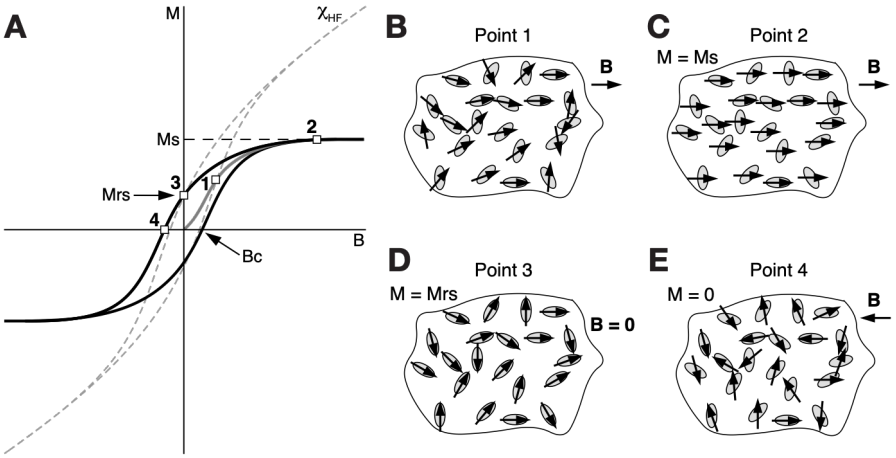

Figure 4. The simplified concept of a magnetization (M) versus applied field (B) curve, i.e., hysteresis loop (modified from Butler, 1992). Hysteresis loop displayed for a synthetic sample before (dashed) and after (bold) the high-field (paramagnetic) slope has been subtracted **(A)**. Heavy gray line displays initial behavior as applied field ramps up from zero field to a saturating field. Snapshots of net response of an assemblage of uniaxial single domain particles **(B–E)**. As the applied field is increasing **(B)**, the moment of each grain is rotated towards B. When all the moments are parallel to the applied field **(C)**, the magnetization is at saturation (Ms). Once the field is returned to zero **(D)**, the magnetization is a saturation remanence (Mrs); the moment of each grain has rotated back to the long axis closest to the previously applied field. When the field is applied in the opposite direction and the magnetization is reduced to zero **(E)**, the field is the bulk coercive field (Bc); the moment of every grain is slightly rotated toward B.

Backfield curves are measured by applying increasing reverse magnetic fields until the remanent magnetization is cancelled. They define the coercivity of remanence (Bcr), which is useful in conjunction with hysteresis parameters (Bcr/Bc and Mrs/Ms) for grain size (domain state) assessment (Day et al., 1977; Néel, 1955; Roberts et al., 2019).

The S-ratio is a measure of the relative abundance of low-coercivity (e.g., magnetite) versus high-coercivity (e.g., hematite) minerals. It is calculated by first applying a 1 T saturation isothermal remanent magnetization (SIRM) in the sample's +y axis, followed by a backfield IRM of −0.3 T in the -y axis: $S = \left[\left(-\frac{IRM_{-0.3T}}{SIRM}\right) + 1\right]/2$ (Bloemendal et al., 1992). Values near 1 suggest dominance of low-coercivity minerals, while a value of 0.5 indicates the dominance of high-coercivity phases.

Rock magnetic signatures are often non-unique and similar magnetic responses may arise from different mineral combinations or grain size distributions. Therefore, integrating rock magnetism with sedimentological and geochemical data is essential to resolve complex sedimentary histories.

1.3 Detrital zircon record

Zircons are robust, uranium-bearing accessory minerals commonly found in siliciclastic sediments. Owing to their exceptional resistance to weathering and metamorphism, they can persist through multiple sedimentary cycles while retaining the geochronological signature of their original magmatic or metamorphic source. U-Pb isotopic dating of individual grains allows precise determination of their crystallization ages.

In provenance analysis, detrital zircon age distributions from sedimentary deposits are compared to the known age signatures of potential source regions (Figure 5). Distinct age populations serve as diagnostic indicators of specific geological terranes, enabling the reconstruction of sediment source areas, paleodrainage systems, and temporal shifts in sediment routing.

1.4 Thesis outline and contributions

This thesis investigates traces of dynamic topography in the geological record, with a focus on the influence of the Yellowstone mantle plume in North America. The goal is to study how the development of dynamic topography created by the Yellowstone plume has reshaped the landscape of North America's landscape. Changes that, in turn, influenced regional climate and ecosystems.

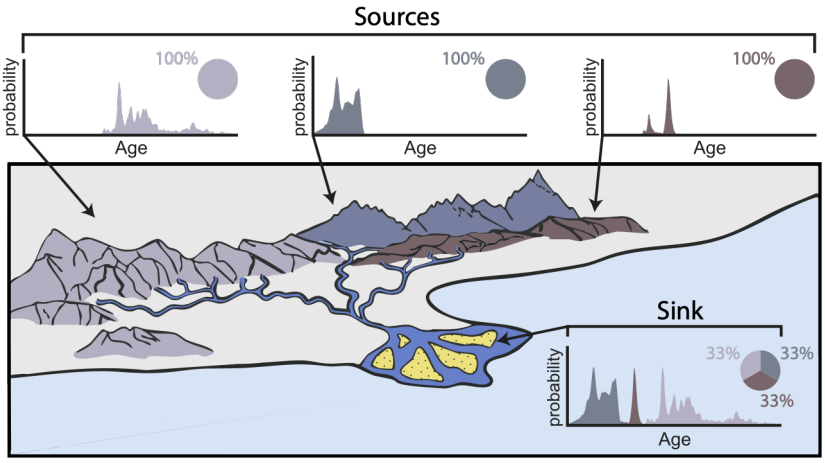

Figure 5. Source-to-sink model and resultant detrital zircon age spectra (modified from Dobbs et al., 2022).

During the rise of the Yellowstone plume in the Oligo-Miocene, a significant rain shadow developed along the west coast of North America, preventing winter precipitation from the Pacific Ocean from reaching the continental interior (Kukla et al., 2022). This climatic shift has been proposed as a mechanism for the open habitat transition, in which lowland forests were replaced by grass-dominated habitats (Strömberg, 2005; Strömberg, 2011), which in turn facilitated a diversification of mammalian species (Samuels and Hopkins, 2017). While the uplift of the Cascade Range has been proposed as the primary driver, the potential contribution of dynamic topography associated with the Yellowstone plume—active in the same region—has not been studied.

This study targets three regions at different distances from the Yellowstone plume center: Montana, Wyoming, and Washington (Figure 6). These areas were selected for their well-preserved sedimentary successions, including regional hiatus surfaces that predate flood basalt volcanism by less than 20 million years. More than 2,000 oriented samples were collected during three field seasons in 2022–2024. The samples were subjected to a range of rock and paleomagnetic experiments, and the results were integrated with published provenance and geochronologic data. The aim of this thesis is to constrain the spatial and temporal patterns of dynamic uplift and to improve our understanding of its surface expression through analyses of regional uplift signals and drainage network reorganization.

This thesis is structured in four main chapters. In each chapter, I contributed to all aspects of the work, including planning and organizing the field campaigns, executing and supervising laboratory work in rock and paleomagnetism, performing data processing and analysis, compiling published detrital zircon data, preparing figures, writing the initial drafts, and editing the manuscripts.

Chapter 2 introduces the first area in the northern Rocky Mountains of Montana, where the regional early Miocene unconformity (EMU) is precisely dated using magnetostratigraphy in combination with published U-Pb ages. Additionally, we show that the EMU is marked by an abrupt change in (magnetic) mineralogy, best explained by a reorganization of sediment source. This work was published in *Terra Nova* (Gerritsen et al., 2026).

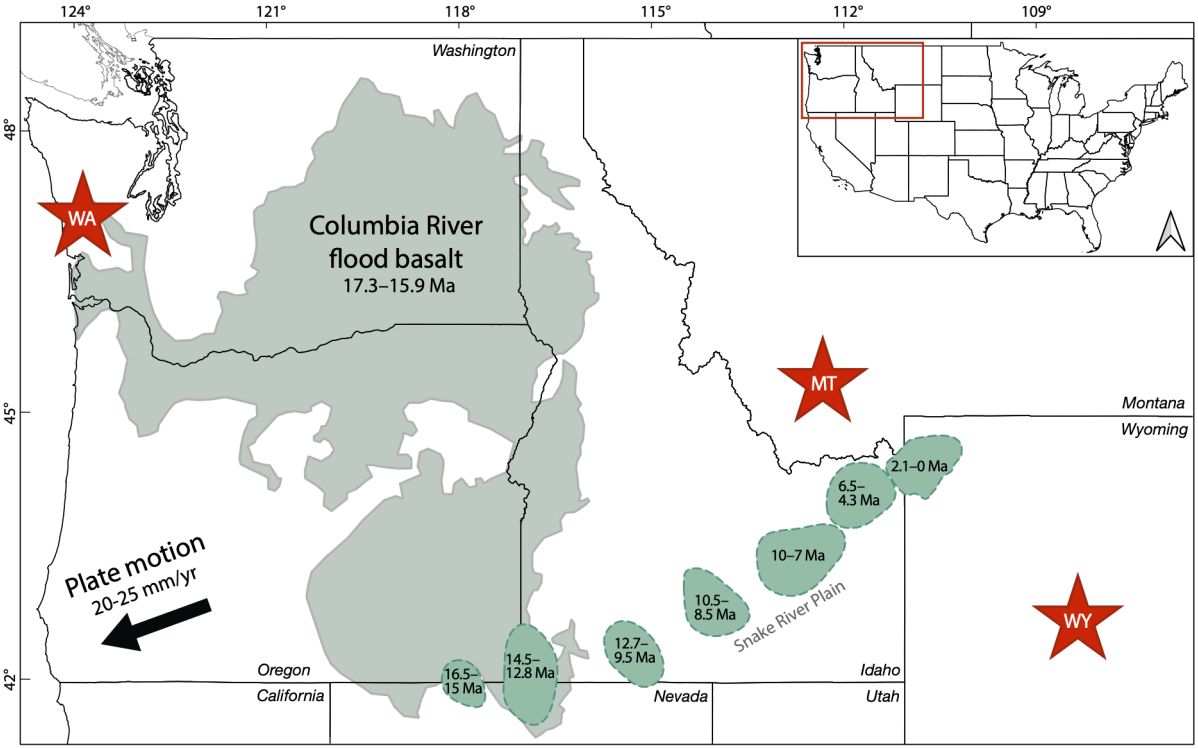

Figure 6. Extent of the Columbia River Basalt Group and the Yellowstone hotspot track (adapted from Coble and Mahood, 2012). Study locations of this thesis are indicated with the red stars.

Chapter 3 builds upon this idea by presenting an additional seven sections from Montana. Rock magnetic data reveal that the abrupt change in mineralogy observed in Chapter 2 occurs consistently around the EMU in all sections. These observations are integrated with published detrital zircon records and aeromagnetic maps to infer a major shift in the North American drainage divide during the early Miocene, which we interpret as an effect of dynamic topography generated by the Yellowstone plume. This paper has been published in *Science Advances* (Gerritsen et al., 2025).

Chapter 4 presents data from a section in the central Rocky Mountains of Wyoming, where a gradual increase in magnetite concentration is observed in the upper Eocene. This change coincides with high sedimentation rates and input from a source containing Archean zircons. The results suggest post-Laramide uplift and basement unroofing in the adjacent Wind River Range. We attribute this to dynamic topography, potentially linked

to lithospheric rebound or the earliest influence of the Yellowstone plume. This manuscript is currently under review in *GSA Bulletin*.

Chapter 5 presents preliminary findings from a study area in western Washington, on the opposite side of the plume center. Here, another increase in magnetite concentration was observed in a sedimentary section draining from the Olympic Mountains. This change is tentatively interpreted to reflect the exposure of oceanic basalts that were accreted to North America during the Oligocene.

2

Magnetostratigraphy and source characterization across the early Miocene unconformity, northern Rocky Mountains, USA

Dieke Gerritsen, Stuart A. Gilder, Alina L. Ludat, and Michael R. Wack

Published in 2026 in Terra Nova, Volume: 38, Issue: 1, Pages: 1-8
DOI: 10.1111/ter.12779

The early Miocene unconformity (EMU) formed during a transition in the tectonic regime of western North America that coincided with faunal diversification. The Railroad Canyon section in the northern Rocky Mountains provides a complete geologic record around this event. Our new magnetostratigraphic study in combination with published U-Pb ages from intercalated ash places the end of the EMU at ~20.1 Ma with a duration of up to 1.5 Myr. The EMU is marked by an abrupt change in rock color, an increase in magnetite concentration, and a decrease in calcite abundance. Average sedimentation rates are similar above and below the EMU, as are climate proxies; therefore, the changes in mineralogy likely reflect a reorganization in sediment source. Drainage network reorganization seemingly contributed to this, possibly related to a change in tectonic regime, such as the onset of Basin and Range extension and/or arrival of the Yellowstone plume.

2.1 Introduction

Unconformities represent gaps in the geologic record produced by a period of non-deposition or erosion. The early Miocene unconformity (EMU) in the northern Rocky Mountains occurred during a transitional period in the tectonic evolution of western North America from gravitational collapse of the Cordillera fold and thrust belt to Basin and Range extension (Constenius et al., 2003; Dickinson, 2002; Janecke, 2007; Vandenburg et al., 1998) and/or the arrival of the Yellowstone plume (Rasmussen, 2003; Sears et al., 2009). The transition coincided with a reorganization in biogeography and faunal diversification (Burbank and Barnosky, 1990; Finarelli and Badgley, 2010; Kohn and Fremd, 2008), such as the development of grass-dominated ecosystems (Strömberg, 2011). The EMU has been recognized throughout Montana (e.g., Fields et al., 1985; Vuke, 2020) and correlated to unconformities across the western United States (Constenius, 1996; Constenius et al., 2003; Hanneman and Wideman, 2006). Yet, the exact age and duration of the EMU are poorly constrained due to an absence of well-dated records. The Railroad Canyon section (RCS) provides the thickest and best exposed geologic record around this event in the northern Rocky Mountains. The section spans the EMU and thus provides crucial chronologic control on the proposed tectonic and biologic events during the late Oligocene to middle Miocene.

The age and duration of the EMU have been repeatedly revised (Barnosky et al., 2007; Harris et al., 2017; Retallack, 2009; Zheng, 1996). The most recent estimate, starting at 21.5 Ma and lasting 0.1 Myr, stems from U-Pb dating of zircons from three ash layers ranging from 22.65±0.37 to 15.76±0.22 Ma (2σ uncertainties) by Harris et al. (2017) and their correlation with the magnetostratigraphy of Zheng (1996, as reported in Barnosky et al., 2007). However, several details and documentation are lacking regarding the essentials of the paleomagnetic study; for example, no reversal test or rock magnetic data were included. Here, we report a new magnetostratigraphic study of the Railroad Canyon section (RCS) to revise the age and duration of the early Miocene unconformity (EMU). Using the improved age model in combination with a high-resolution rock magnetic investigation, we demonstrate a marked difference in mineralogy above and below the hiatus.

2.2 Geologic setting and methods

Topography of the northern Rocky Mountains is characterized by a series of north–trending uplifts separated by intermontane basins. The RCS lies along the Idaho – Montana border in one such basin, the Horse Prairie basin (Figure 1). The half-graben is bound by the Maiden Peak fault system on its east side (Janecke, 2007; Vandenburg et al.,

1998). It separates Cenozoic sedimentary and volcanic rocks on its hanging wall from Archean and Paleozoic rocks on its footwall (M'Gonigle, 1994). Cross-cutting relationships suggest fault activity from the middle Eocene to the middle Miocene. Cenozoic sediments in the basin are part of the Bozeman Group, which is split into Renova and Sixmile Creek formations. The Renova Formation consists of gray to white mud and siltstones with occasional gypsum and halite, deposited in an arid lacustrine environment (Barnosky et al., 2007; Fields et al., 1985). Arikareean North American land mammal age (NALMA) fossils are abundant and well documented in the RCS (Barnosky et al., 2007; Fields et al., 1985; Harris et al., 2017), indicating a late Oligocene to early Miocene age. The Sixmile Creek Formation consists of pink to tan silt- and sandstone with gravelly lenses deposited in a sediment-choked fluvial system (Barnosky et al., 2007; Fields et al., 1985; Rasmussen, 2003). NALMA fossils in this unit are Hemingfordian to Barstovian (Barnosky et al., 2007; Harris et al., 2017), indicating an early–middle Miocene age. The contact separating the two formations, the early Miocene unconformity (EMU), has been described in intermontane basins throughout southwestern Montana (Fields et al., 1985; Hanneman and Wideman, 1991; 2006; Rasmussen, 2003; Vuke, 2020 and references therein). The unconformity is regionally described as erosional and/or angular (Rasmussen, 2003; Vuke, 2020) or constitutes a correlative conformity (Hanneman and Wideman, 2010).

Here, we report a new magnetostratigraphic study of the RCS from field campaigns in 2022 and 2023 that netted 322 samples from 17 sections (Figures 1 and S2). We sampled each section at approximately 2-m intervals, taking two oriented cores per horizon (Figure S1). The stratigraphic position of each sample within a section was measured using a Jacob staff. We corrected magnetic compass readings with the average declination anomaly (13.3±3.7°) from 178 Sun compass readings, which agrees well with 12.2° predicted by the International Geomagnetic Reference Field. We observed fairly uniform bedding and calculated an average bedding attitude of dip direction = 44°N and dip = 6.4° (N=12, Table S1). We used this to project the measured GPS position and elevation of each sample into one stratigraphic column (Table S3). Correlation of the 17 sections resulted in a composite section of 675 m (Figure 2), which is ca. 300 m thicker than previous estimates (Barnosky et al., 2007; Harris et al., 2017; Retallack, 2009; Zheng, 1996). This discrepancy is in part because we extended the section ~190 m below and ~55 m above (our sections WH05, WH01, WH02, and RCS1 below and RCS5 above; Figures 1 and S2) with respect to Zheng (1996). The EMU was identified in the field at RCS4 as a very clear lithological color difference from white to gray below the EMU to pink to tan above the EMU, which is also visible on satellite images (Figure S1). Assuming the same bedding attitude, we projected the position of the EMU on the map (Figure 1), which agrees well with maps of Lonn et al. (2019); Lund (2018); and M'Gonigle (1994). We carried out

standard alternating field (AF) and thermal demagnetization procedures and a suite of rock magnetic measurements (for details, see Text S1).

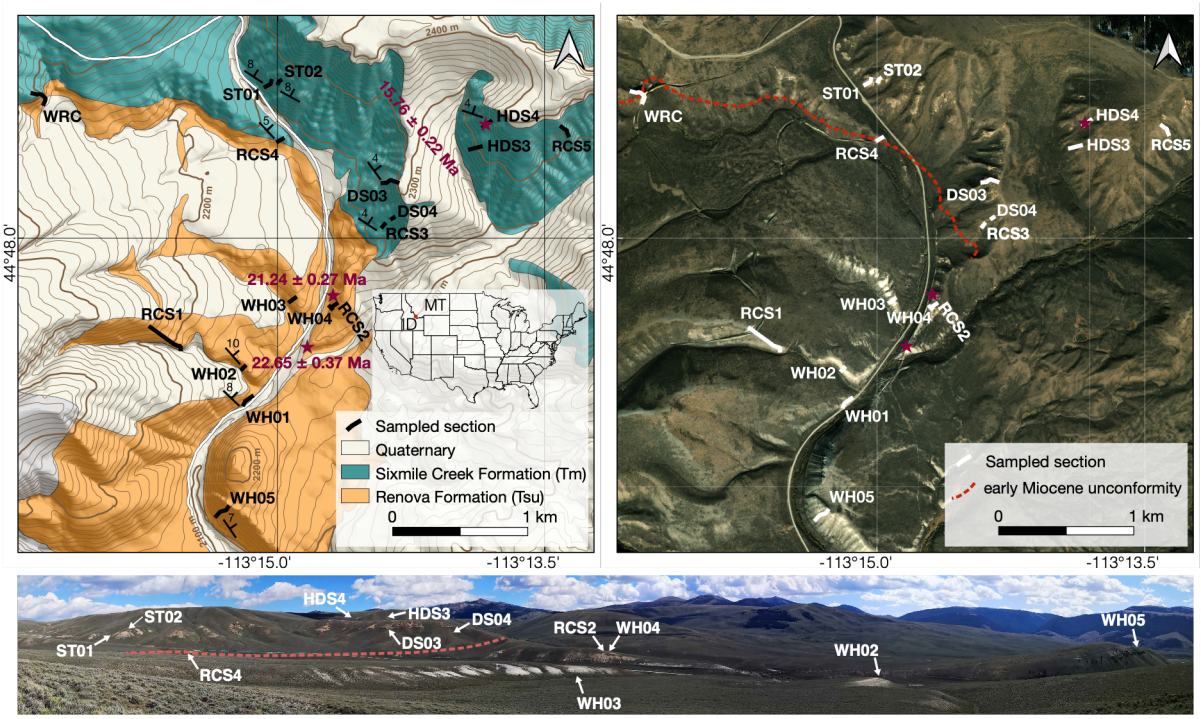

Figure 1. Geologic map of the Railroad Canyon section **(top left)**, satellite image **(top right)** (Environmental Systems Research Institute, 2009), and panoramic photo **(bottom)** taken from RCS1 looking east. The dashed red line shows the stratigraphic position of the early Miocene unconformity (EMU). Red stars indicate locations of zircon U-Pb ages derived from volcanic ash (2σ uncertainties, Harris et al., 2017). The geologic map is based on M'Gonigle (1994), Lund (2018), and Lonn et al. (2019), together with our field observations.

2.3 Results

Magnetic mineral concentration, reflected by mass-normalized bulk susceptibility (χ) and saturation magnetization (Ms), increases abruptly at the EMU by factors of 5 and 3.5, respectively (Figure 2). Simultaneously, calcite abundance decreases to nearly imperceptible values (Figures 2 and S7). High-field susceptibility (χ_{HF}) confirms the Renova Formation is characterized by a low magnetic mineral concentration and high (diamagnetic) calcite abundance, and vice versa for the Sixmile Creek Formation (Figure S3). This sharp transition coincides with the lithologic color change interpreted as the EMU. A mixing zone defined by rock magnetic parameters occurs within ca. 25 m around the EMU (opaque red zone in Figures 2 and S3). Magnetic grain size indicators, coercivity (Bc) and saturation remanent magnetization (Mrs) divided by Ms, remain constant throughout the section, as does the shape parameter (σ_{hys}) and the S-ratio. S-ratios reaching as low as 0.85 indicate the presence of a higher coercivity component like

titanohematite. First derivatives of the thermoremanence curves indicate Curie temperatures of 514-519°C (Figure S5); however, the moment reaches its minimum around 580°C, reflective of Ti-poor titanomagnetite. Altogether, the rock magnetic results suggest the section is dominated by (titano)magnetite with minor contributions of titanohematite, with a more uniform composition above the EMU (Figure S6).

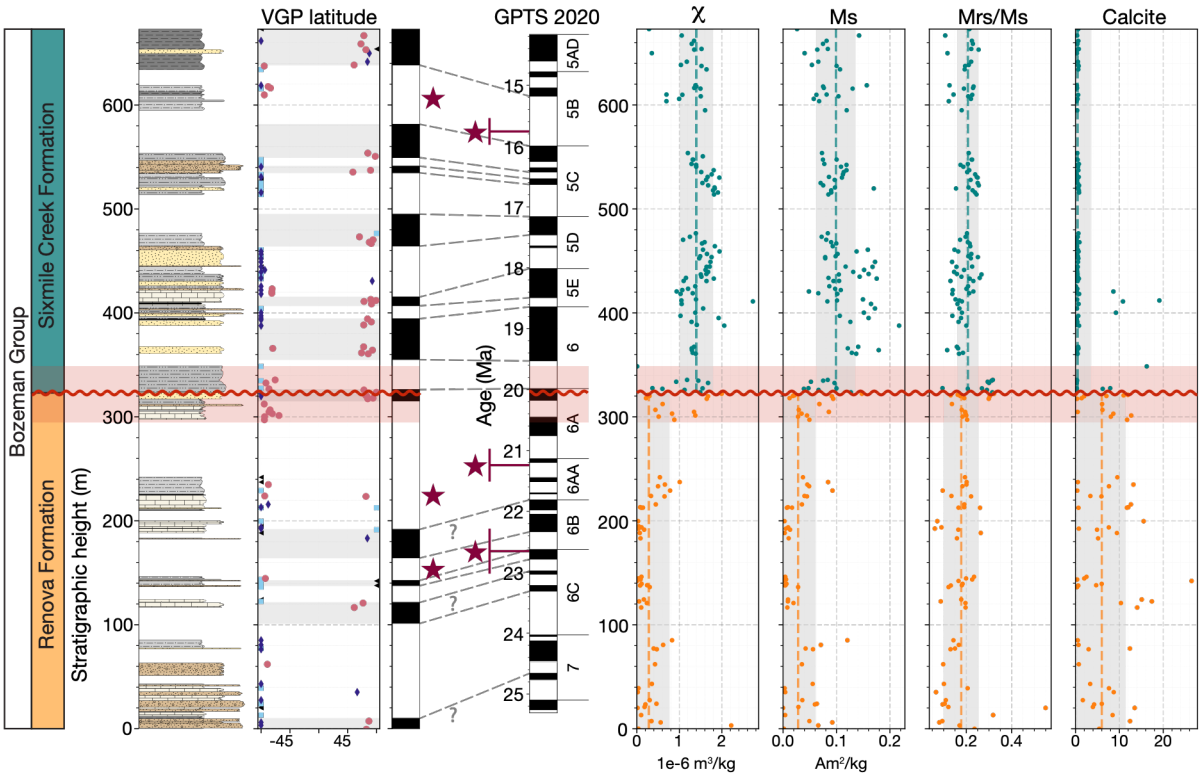

Figure 2. Simplified sedimentary log (legend in Figure S1), magnetostratigraphy and its correlation to the GPTS2020 (Ogg, 2020), and rock magnetic properties of the section. Class A, B, C, and D virtual geomagnetic pole (VGP) latitudes are indicated by pink circles, purple diamonds, blue squares, and black triangles, respectively. From left to right: magnetic susceptibility (χ), saturation magnetization (Ms), saturation remanent magnetization (Mrs) divided by Ms, and relative calcite abundance. Orange and teal points represent samples from the Renova Formation and Sixmile Creek Formation, respectively. Dashed orange and teal lines indicate median values (shaded regions 1σ uncertainty). Red stars are U-Pb zircon ages and their 2σ uncertainties (Harris et al., 2017). Curvy red line represents the early Miocene unconformity (EMU) and opaque red represents the zone of mixing.

The mean magnetization direction in tilt-corrected coordinates for Class A samples (N=56) is declination Ds=4.8°, inclination Is=60.0°, with a Fisher (1953) precision parameter k=48.6 and α_{95}=2.8° (Figures 3 and S4; Text S2; Table S2). The parametric reversal test is positive (Tauxe, 2010); however, the directional distribution was unamenable to the E/I correction. A comparable inclination of 63.9±3.0° and 62.7±1.9° at 20 Ma is predicted by the North American apparent polar wander paths of Gallo et al. (2023) and Torsvik et al. (2008), respectively.

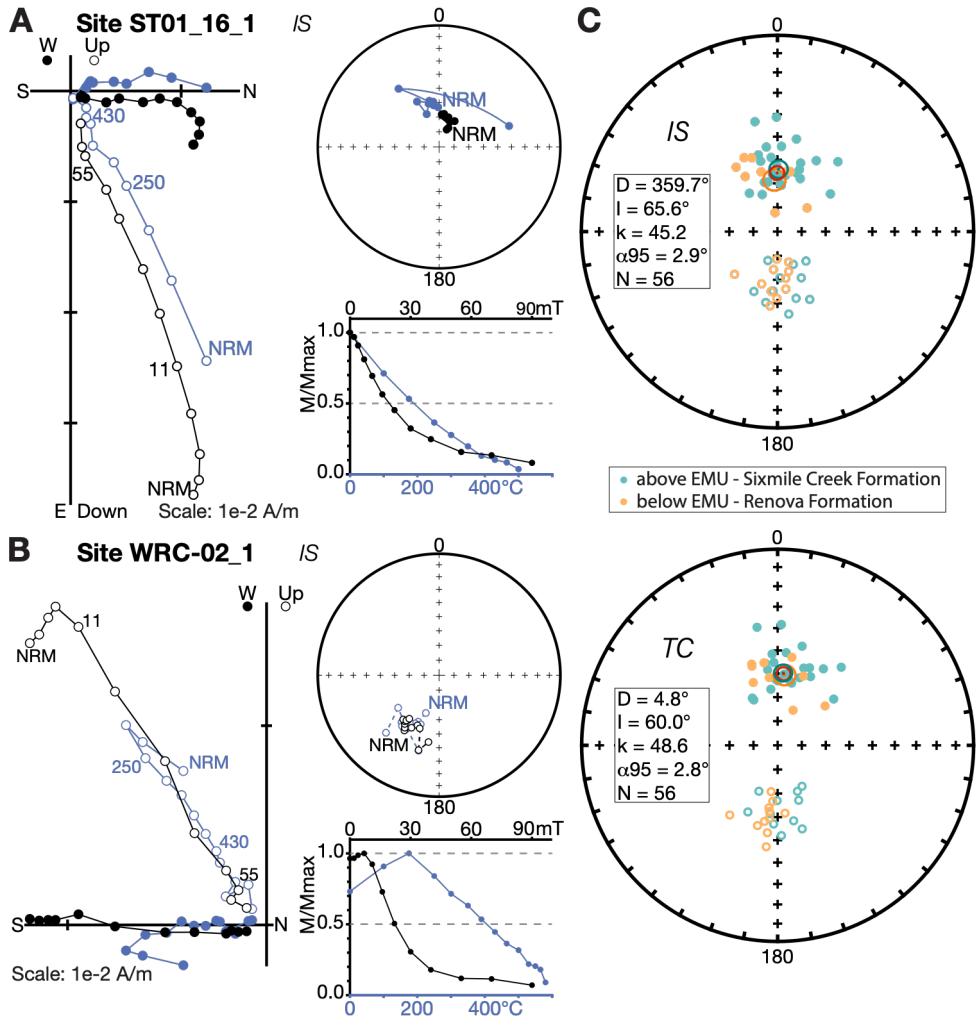

Figure 3. Summary of Class A paleomagnetic data. Stepwise alternating field (black) and thermal (blue) demagnetization data for a normal **(A)** and reversed **(B)** polarity sample pair from the same horizon. Thermal demagnetization of site ST01 was cut off at 500°C, above which the direction became unstable. (C) Stereographic projections of the best-fit line components in in-situ (IS) and tilt corrected (TC) coordinates. Fisher (1953) mean directions and their α_{95} confidence ellipsoids are for the complete section (red), Renova Formation (orange), and Sixmile Creek Formation (teal).

We constructed a magnetic polarity sequence by converting the magnetization directions into virtual geomagnetic poles (VGPs) and defined polarity intervals where at least two successive horizons have the same polarity (Figure 2). We placed the three radiometrically dated ash layers of Harris et al. (2017) into our magnetostratigraphy using their GPS locations and elevations (Figures 1 and 2). We then visually correlated our magnetostratigraphy with the GPTS2020 geomagnetic polarity time scale of Ogg (2020). Our interpretation indicates the section spans from ~24.8 Ma at the base to ~15.0 Ma at the top, with the end of the EMU occurring around 20.1 Ma (Figure 2). Following the algorithm of Lallier et al. (2013), we calculated the 100 most probable correlations

between 37.5 and 4.0 Ma, which matches well with our visual interpretation (Figure 4A). Due to a gap in age control between the 21.24±0.27 Ma radiometric date and the subsequent reversal at 19.98 Ma, the possible duration of the EMU spans up to 1.5 Myr (red rectangle in Figure 4B). We calculated the sedimentation rate separately for the bottom and top of the section by fitting a linear least-squares regression to the correlated reversal sequence and U-Pb dates (seven reversals and two U-Pb dates below the EMU; 12 reversals and one U-Pb date above the EMU). Interestingly, the sedimentation rate of 6.2±0.3 cm/kyr below the EMU is similar to that of 6.7±0.2 cm/kyr above; the instantaneous sedimentation rate fluctuates around these averages. Anisotropy of magnetic remanence data define a typical sedimentary fabric (Figure S8), with negligible differences below and above the EMU.

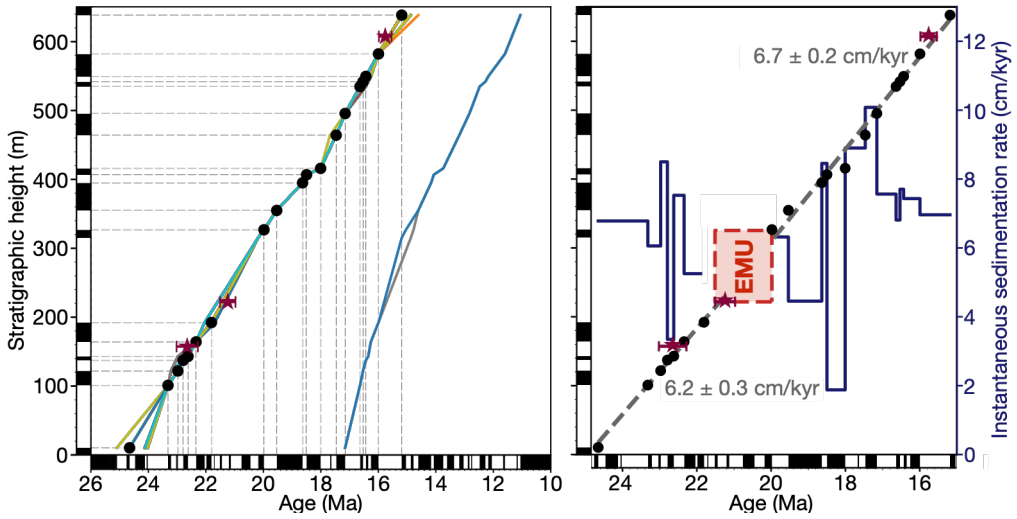

Figure 4. (A) Correlation of the magnetostratigraphy to the GPTS2020 (Ogg, 2020). Black points reflect reversals of magnetic polarity (left) and our correlation to the GPTS2020 (bottom). Dark red stars represent U-Pb dates with 2σ uncertainties of Harris et al. (2017). Colored lines are the 100 best matches according to the method of Lallier et al. (2013). **(B)** Sedimentation rate of the Railroad Canyon section (RCS). A linear least-squares regression (dashed gray line) and standard error were calculated separately below and above the EMU. Instantaneous sedimentation rate, calculated per polarity chron, is shown in blue. Red rectangle marks the possible extent of the early Miocene unconformity (EMU).

2.4 Discussion and conclusions

Our magnetostratigraphy of the 675-m thick Railroad Canyon section in combination with radiometrically dated ash layers (Harris et al., 2017), results in a fairly constant sedimentation rate of 6.2±0.3 cm/kyr below and 6.7±0.2 above the EMU (Figure 4B). This is significantly higher than the sedimentation rates of 3.2 cm/kyr below and 4.8 cm/kyr above the EMU constrained by Harris et al. (2017). Our correlation places the end of the EMU at ca. 20.1 Ma (Figure 2) with a duration of up to 1.5 Myr (Figure 4B). Previous

studies placed the end of the EMU at a slightly lower stratigraphic position (Barnosky et al., 2007; Harris et al., 2017; Zheng, 1996), resulting in an older age estimate of ca. 21.4 Ma with a duration of 0.1 Myr (Harris et al., 2017). Our magnetostratigraphic correlation above the EMU agrees well with previous authors, but the different stratigraphic position of the EMU leads to a revision of its age and duration.

The revised stratigraphic position of the EMU coincides with a distinct change in rock color, increase in magnetite concentration, and reduction in calcite abundance persisting for at least 5 Myr after the EMU (Figures 1, 2, and S3). Of particular interest is that climate proxies in the RCS remain constant before and after the EMU (Harris et al., 2020; Methner et al., 2021; Retallack, 2009). Moreover, Thompson et al. (1982) found smectite in both the Renova and Sixmile Creek formations, indicative of arid climate before and after the EMU. Kaolinite identified directly below the EMU was interpreted as evidence for high rainfall and consequent erosion during the EMU (Thompson et al., 1982).

As climate proxies are equivalent above and below the EMU, explaining the lithological differences should be independent of climate. Gradual increases in magnetite concentration are commonly found in central Asia, where the shift is interpreted as a change in source from sediment-dominated to crystalline basement-dominated, caused by uplift and erosion of the nearby mountain (Charreau et al., 2009; Gilder et al., 2001). A gradual change is not observed in the RCS. So, either such a change existed and then was eroded, or there was an abrupt change in the drainage network to a magnetite-rich catchment area. The former case implies a prolonged duration of the EMU. Conversely, as the RCS lies at the current drainage divide of North America, it is possible the source area of the basin abruptly shifted. A drainage reorganization could have been caused by dynamic uplift of the Yellowstone plume (Rasmussen, 2003; Sears et al., 2009), which extended up to 1000 km from the plume center prior to flood basalt eruptions (Friedrich et al., 2018). Paleocurrent analyses of the Renova (summarized by Vuke, 2020) and Sixmile Creek (e.g., Thomas and Sears, 2020) formations indicate a NE trending drainage system similar to today. Renova Formation provenance was dominantly local, but may include Idaho sources (Janecke et al., 2000; Schwartz et al., 2019b). Sixmile Creek provenance was generally local, but clasts with sources from Idaho, Nevada, or Utah have been suggested (Sears et al., 2009; Stroup et al., 2008). Taken together, the observed mineralogical changes are best explained by a reorganization in sediment source at the EMU.

The formation of the EMU is typically attributed to the onset of Basin and Range extension (Barnosky and Labar, 1989; Burbank and Barnosky, 1990; Constenius, 1996; Constenius et al., 2003). Basin and Range extension likely influenced the structural evolution of the RCS; dip directions we measured (Figure 1; Table S1) are parallel to the overall extension

direction of 45°N along the Idaho – Montana border (Stickney and Bartholomew, 1987) and the Maiden Peak fault system bounding the east side of the basin was active during the Oligo-Miocene (Janecke, 2007; Vandenburg et al., 1998). Consequences of the constant sedimentation rate in the RCS require careful consideration. First, the constant sedimentation rate and sedimentary bedding of the RCS suggest a constant offset on the fault system, creating accommodation space in the basin. Second, if one favors a longer hiatus estimate, a spike in sedimentation rate would be required for the uppermost part of the Renova Formation.

The observed combination of an abrupt change in mineralogy and constant sedimentation rate thus indicates constant Basin and Range fault activity as well as drainage network reorganization may have played a role during the late Oligocene – early Miocene in the northern Rocky Mountains. As the EMU is recognized regionally (Fields et al., 1985; Hanneman and Wideman, 1991; 2006; Rasmussen, 2003; Vuke, 2020 and references therein), investigating the EMU in other basins in SW Montana should provide further insight.

3

Yellowstone plume drives drainage reorganization in the early Miocene

Dieke Gerritsen, Stuart A. Gilder, Yi-Wei Chen, and Michael R. Wack

Published in 2025 in Science Advances, Volume 11, Issue 47
DOI: 10.1126/sciadv.adz4275

The rise of the Yellowstone plume coincided with a shift from orogenic collapse of the Cordillera to Basin and Range extension in the northern Rocky Mountains, yet its impact on regional uplift, sediment dispersal, and drainage patterns remains largely unexplored. Here, we present rock magnetic analyses from eight Oligo-Miocene sedimentary sections in southwestern Montana. Using two complementary datasets, we identify a sharp increase in magnetic mineral concentration immediately after the early Miocene unconformity [~20 million years ago (Ma)], concurrent with a shift in detrital zircon ages, indicating a major provenance shift. We identify bimodal volcanism of the Columbia River Basalt Group as the dominant Miocene source, requiring that the early Miocene Continental Divide lay ~400 kilometers west of its present position. This reorganization, driven by Yellowstone plume–induced uplift, persisted until at least 10 Ma. Our study provides geologically based, temporal, and spatial constraints on dynamic topography previously only estimated from modeling.

3.1 Introduction

The northern Rocky Mountains experienced a transition in tectonic regime during the Cenozoic (Constenius et al., 2003). Sevier-Laramide compression ceased in the early Eocene (DeCelles, 2004) and was superseded by orogenic collapse with low-angle detachment faulting and the formation of metamorphic core complexes during the late Eocene–early Miocene (Constenius, 1996), followed by the onset of high-angle normal faulting during Basin and Range extension (Dickinson, 2002; Janecke, 2007) and the rise of the Yellowstone plume in the early Miocene (Rasmussen, 2003; Sears et al., 2009). This transition not only transformed the landscape but also influenced faunal biogeography by facilitating species diversification through habitat fragmentation (Barnosky, 2001; Barnosky and Carrasco, 2002; Finarelli and Badgley, 2010; Kohn and Fremd, 2008). While Oligo-Miocene sedimentary exposures are relatively sparse in western North America, the northern Rocky Mountains preserve a moderately thick and relatively well-exposed record within a series of intermontane basins (Vuke, 2020). These basins captured the response of regional topography to tectonic and geodynamic processes, thereby providing insights into basin development, sediment dispersal patterns, and drainage evolution. As this region contains the modern North American Continental Divide, separating the watersheds draining into the Pacific Ocean from those draining into the Atlantic and Arctic oceans, it is particularly well suited for studying drainage migration and its relation to regional uplift.

Traditionally, drainage evolution has been inferred from provenance studies that analyze clast compositions and detrital zircon data (e.g., Schwartz and Schwartz, 2013). However, rock magnetic studies of sedimentary sections provide a time and cost effective, high-resolution alternative by capturing variations in rock magnetic mineralogy through time, which may signal changes in sediment source. Magnetic methods allowed Gerritsen et al. (2026) to identify an abrupt magneto-mineralogical change in a sedimentary section located at the Continental Divide near the Idaho-Montana border. This shift coincided with the formation of the regional early Miocene unconformity (EMU), which they precisely dated using magnetostratigraphy. Building on these initial findings, we present a comprehensive rock magnetic study of seven additional Oligo–Miocene stratigraphic sections in the northern Rocky Mountains. By integrating our high-resolution rock magnetic dataset with published detrital zircon records, we constrain the timing and spatial patterns of provenance changes associated with the EMU. This synthesis provides insights into regional uplift patterns, drainage divide migration, and shifts in sediment source in response to Cenozoic tectonics and mantle dynamics.

3.1.1 Geologic setting

The Rocky Mountains constitute the largest mountain range in North America, stretching from New Mexico (USA) to British Columbia (Canada). They formed during the Sevier-Laramide Orogeny in the Late Cretaceous–Paleocene (Chamberlain et al., 2012; Constenius, 1996). Near the Montana-Idaho segment of the Rocky Mountains (Fig. 1A), herein referred to as the northern Rocky Mountains, the main constituent of the orogenic belt is the Precambrian Belt Supergroup (Lonn et al., 2020), yet Paleozoic and Mesozoic sedimentary rocks (Barton et al., 2003) and Archean quartzofeldspathic gneiss (Harms and Baldwin, 2020) are also exposed. During the Late Cretaceous, the region was intruded by large magmatic bodies, such as the Pioneer, Boulder, and Idaho batholiths (Scarberry et al., 2020). Postorogenic extension began in the Eocene, forming the Bitterroot and Anaconda metamorphic core complexes and triggering volcanism, such as the Dillon, Challis, and Absaroka volcanic fields (Harlan, 2006). Volcanism in southwestern Montana was relatively subdued in the early Miocene, with only limited eruptions (e.g., the Dillon volcanics near Dillon in Fig. 1A) (Fritz et al., 2007; Mosolf, 2015,2021).

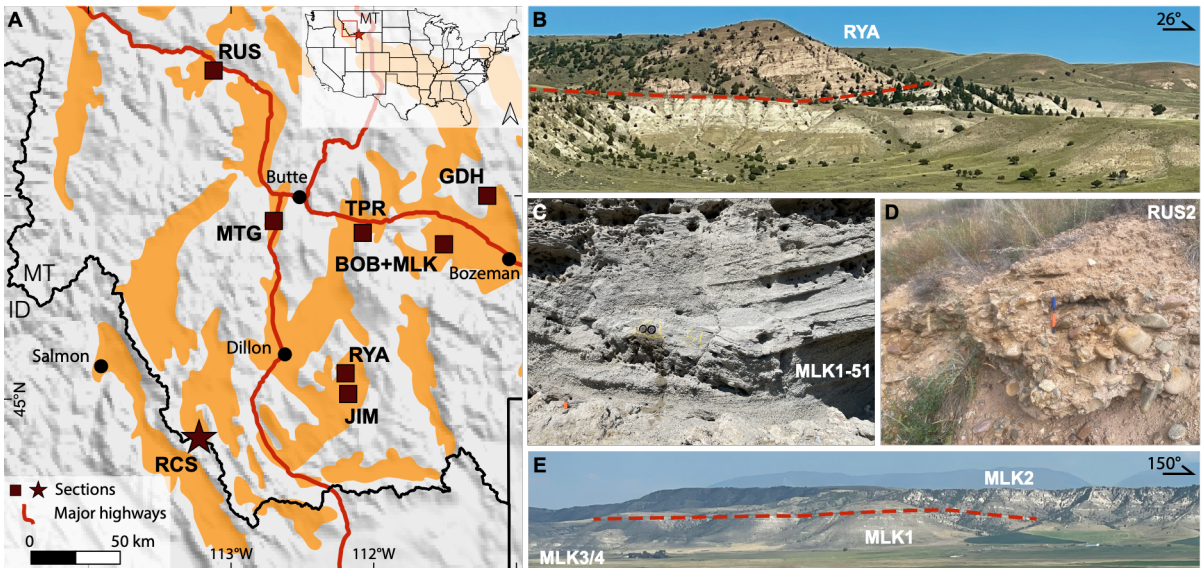

Figure 1. Map and field photographs of the study area in southwestern Montana (MT). (A) Map showing the basins containing Cenozoic sediments in orange (Vuke, 2020) and shaded relief topography (NOAA, 2022); brown squares indicate the locations of the seven sections sampled for this study and the brown star shows the Railroad Canyon section (RCS) along the Idaho (ID) border from Gerritsen et al. (2026). The red star in the inset denotes the present position of the Yellowstone hotspot. Field photographs of **(B)** the RYA section, **(C)** fluvial sedimentary structures in the Sixmile Creek Formation in the MLK section, **(D)** conglomerate capping the EMU (early Miocene unconformity) in the RUS section, and **(E)** the MLK section. Red dashed lines indicate the interpreted positions of the EMU.

Our study area in southwestern Montana is characterized by a series of north to south (N-S)–trending mountains separated by intermontane valleys (Fig. 1A). Details surrounding basin formation during the Eocene–early Miocene remain debated because of complications from subsequent Basin and Range extension. Hypotheses for basin development include: (i) formation of grabens and half-grabens through the reactivation of Sevier thrust faults (Constenius, 1996); (ii) generation of grabens and half-grabens within a N-S–oriented rift zone located within the Sevier thrust belt, accompanied by an alluvial plain on the eastern rift shoulder (Janecke, 1994); (iii) creation of a singular, expansive basin flanked by Eocene volcanic fields (Fritz et al., 2007); and (iv) establishment of a network of fluvially incised valleys during the final stages of Sevier-Laramide orogenesis (Schwartz and Schwartz, 2013). Subsequent Basin and Range extension continued to create accommodation space during the Neogene, creating a complex network of rectilinear basins (Janecke, 2007; Reynolds, 1979; Ruppel, 1982).

Cenozoic sediments in these basins constitute the Bozeman Group (Vuke, 2020). The Bozeman Group consists of two lithologically distinct depositional sequences, containing dissimilar fossil assemblages Kuenzi and Fields (1971). The lower sequence, the Renova Formation, is generally characterized by fine-grained fluvial and lacustrine strata incorporating a large volume of volcanic ash, with conglomerate as a relatively minor component (Fields et al., 1985; Kuenzi and Fields, 1971). In this study, we focus on the upper Renova Formation, of which fossils correspond to the Whitneyan-Arikareean stages of the North American land mammal age (NALMA) (Fig. 2 and references therein). The upper sequence, the Sixmile Creek Formation, predominantly consists of coarse-grained rocks, with increasing conglomerate layers toward the top (Fields et al., 1985; Kuenzi and Fields, 1971). It contains Hemingfordian-Hemphillian NALMA fossils (Fig. 2 and references therein). Specific lithologic features of the Renova Formation may help distinguish it from the Sixmile Creek Formation: mollusk and insect fossils, paper shale, diatomaceous and coal beds, etc. (Vuke, 2020), as well as rock color [e.g., Fig. 1B and Gerritsen et al. (2026)]. However, these features are often missing, and the lithology of both formations is variable across the study area, making it sometimes challenging to distinguish the two.

The two formations are separated by the EMU, which has been identified in intermontane basins across southwestern Montana (Fields et al., 1985; Hanneman and Wideman, 1991; 2006; Rasmussen, 2003; Vuke, 2020). Regionally, the EMU is categorized as an erosional and/or angular unconformity (Rasmussen, 2003; Vuke, 2020) or as a correlative conformity (Hanneman and Wideman, 2010). The age and duration of the EMU vary between basins (Fig. 2). At the Railroad Canyon section (RCS) near the Idaho-Montana border, Gerritsen et al. (2026) placed the end of the EMU at 20.1 million years ago (Ma)

with a duration up to 1.5 Myr based on magnetostratigraphy in combination with zircon U-Pb ages.

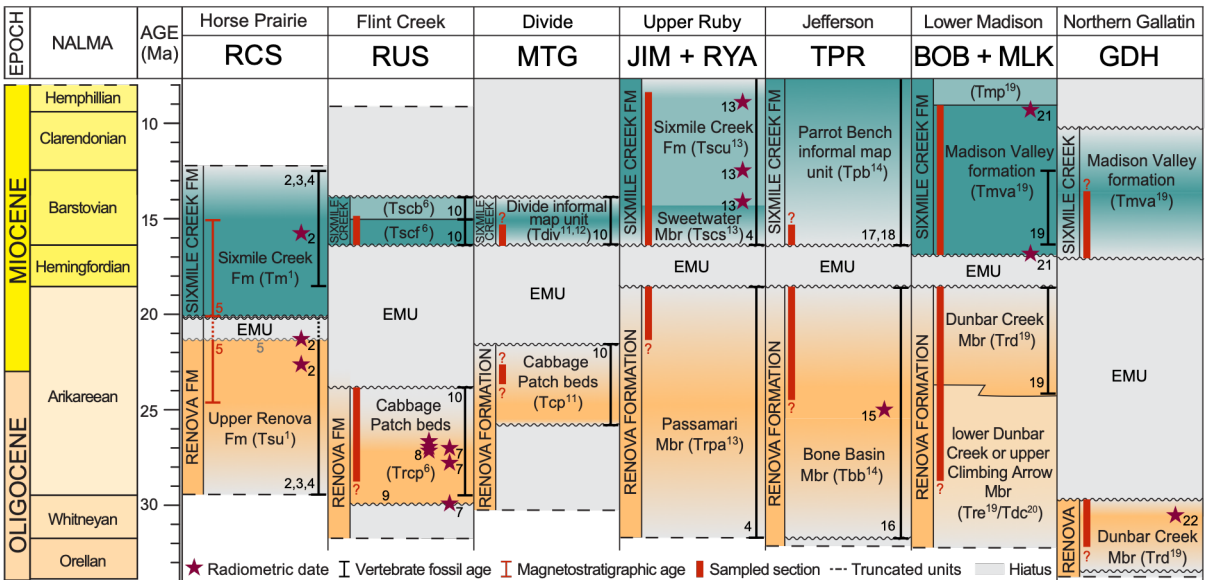

Figure 2. Correlation of the sections. Figure ordered from west to east [after figure 1 in Vuke (2020), reused with permission from S. Vuke and MBMG]. North American Land Mammal Ages (NALMA) from Barnosky et al. (2014). Numbers in superscript, adjacent to stars, next to vertebrate fossil ages, and above unconformities in the figure artwork refer to the following references: [1]M'Gonigle (1994) [2]Harris et al. (2017) [3]Barnosky et al. (2007) [4]Fields et al. (1985) [5]Gerritsen et al. (2026) [6]Portner and Hendrix (2005) [7]Calede (2020) [8]Portner et al. (2011) [9]Mosolf and Vuke (2017) [10]Calede and Rasmussen (2015) [11]Elliott and McDonald (2009) [12]Vuke (2004) [13]Brennan et al. (2024) [14]Vuke et al. (2004) [15]Link et al. (2008) [16]Axelrod (1984) [17]Kuenzi and Fields (1971) [18]Wang et al. (2004) [19]Vuke (2003) [20]Vuke (2006) [21]Montejo (pers. comm., 2024) [22]Hughes (1980). Dotted lines in the RCS represent the possible extent of the EMU (≤1.5 Myr). Color gradients and question marks indicate age uncertainties.

We collected samples at the boundary between the Missouri and Columbia River drainage systems at the present-day Continental Divide. Paleocurrent analyses of the Renova [summarized by Vuke (2020)] and Sixmile Creek (e.g., Thomas and Sears, 2020) formations indicate northeast (NE)-flowing drainage systems similar to today. Clast compositions suggest that Renova Formation provenance was locally derived but may include Idaho sources (Janecke et al., 2000; Schwartz and Schwartz, 2013). Sixmile Creek provenance was generally locally derived (e.g., Mosolf, 2015; Mosolf, 2021; Portner et al., 2011), but some clasts have affinity with sources from Idaho, Nevada, or Utah (Janecke et al., 2005; Sears et al., 2009; Stroup et al., 2008). A regional synthesis of late Miocene–Pliocene provenance data indicates a marked drainage reorganization linked to thermally induced topography of the Yellowstone plume tail (Staisch et al., 2022). However, the effect of dynamic topography generated during the Oligo-Miocene rise of the Yellowstone plume head on drainage evolution remains unexplored. Using rock magnetic analyses in

combination with published provenance data, our study provides a detailed analysis of the transition from the Oligocene Renova Formation to the early Miocene Sixmile Creek Formation in southwestern Montana.

3.2 Results

The stratigraphic position of the EMU coincides with a distinct change in rock magnetic properties between the Renova and Sixmile Creek formations (Fig. 3, figs. S1 to S8, and data S2). The magnetic mineral concentration, indicated by magnetic susceptibility (χ) and Ms (saturation magnetization), sharply increases immediately above the EMU in all sections (figs. S1 and S3 to S7) except in the MTG section (fig. S2), where the Renova Formation displays anomalously high magnetic mineral concentrations (Fig. 3). The median χ and Ms are $1.46 \pm 4.64\times10^{-7}$ m^3/kg and $1.07 \pm 4.17\times10^{-2}$ Am^2/kg below the unconformity and $1.03 \pm 0.62\times10^{-6}$ m^3/kg and $7.49 \pm 5.86\times10^{-2}$ Am^2/kg above, respectively. Magnetic grain size indicators, saturation remanent magnetization (Mrs) divided by Ms (Mrs/Ms; Fig. 3) and coercive force (Bc; fig. S8), have slightly lower medians in the Sixmile Creek Formation (0.19 ± 0.05 and 10.30 ± 3.13 mT) but still fall within the uncertainty of those for the Renova Formation (0.20 ± 0.08 and 13.60 ± 6.25 mT). The median hysteresis shape parameter (σ_{hys}) is positive in the Renova Formation (0.17 ± 0.29), which reflects the presence of wasp-waisted loops, indicative of a mixture of magnetic minerals with contrasting coercivities (fig. S8). Moreover, the Renova Formation has lower S-ratios on average (0.93 ± 0.10) compared to the Sixmile Creek Formation (0.97 ± 0.03), indicating a greater abundance of high coercivity minerals such as (titano)hematite (fig. S8; see Materials and Methods). Overall, rock magnetic properties are more uniform in the Sixmile Creek Formation, dominated by low-Ti titanomagnetite (fig. S9), whereas the Renova Formation displays more heterogeneity, with lower magnetic mineral concentrations that are still dominated by low-Ti titanomagnetite but slightly mixed with (titano)hematite.

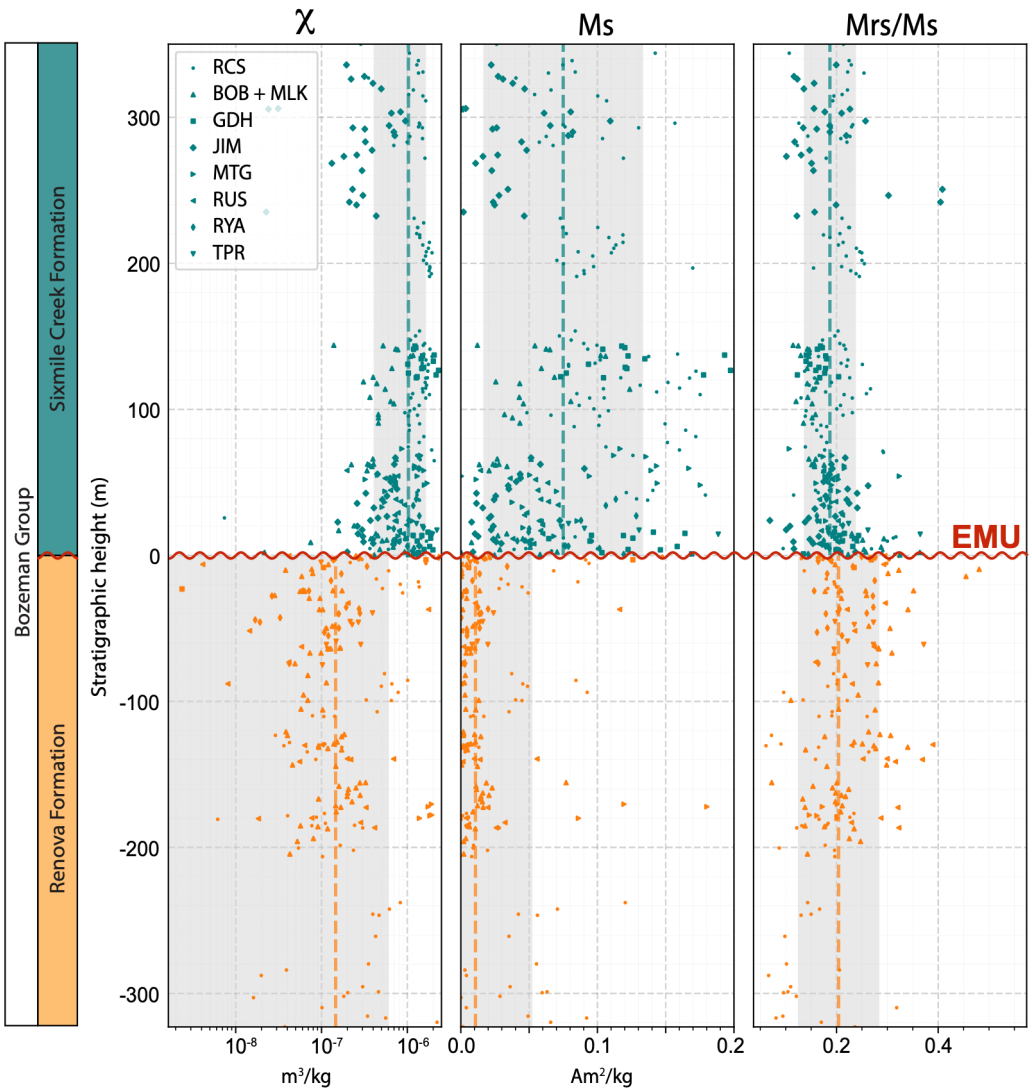

Figure 3. Rock magnetic properties of the eight sections. Sections aligned at the EMU (curvy red line) positioned at 0 m. From left to right: magnetic susceptibility (χ), Ms (saturation magnetization), and Mrs (saturation remanent magnetization) divided by Ms. Orange and teal points represent samples taken from the Renova Formation (N = 123) and Sixmile Creek Formation (N = 175), respectively. Dashed orange and teal lines indicate median values; shaded regions, 1σ uncertainty.

The measured bedding planes define similar northwest (NW)-oriented tilt axes, with extension directions oriented 75.2° ± 16.3° for the Sixmile Creek Formation and 67.9° ± 8.9° for the Renova Formation (Fig. 4A and data S2). The median dip of both formations is low: 7.0° ± 6.2° (N = 37) and 8.0° ± 7.1° (N = 35) for the Sixmile Creek and Renova formations, respectively. At first glance, the bedding planes suggest a continuous tectonic regime above and below the EMU; however, most bedding planes dip west for the Renova Formation, while those for the Sixmile Creek Formation dip east. For example, in the Ruby Basin, the Renova Formation at RYA dips west (Fig. 4B and fig. S4), while the lower Sixmile Creek Formation at JIM dips east (Fig. 4B and fig. S3). Although our dataset is

limited, this contrast might indicate differences in fault activation between the two formations, with NE-dipping listric or normal faults more active in the Oligocene and SW-dipping faults active in the Miocene. Further work should be carried out to resolve this.

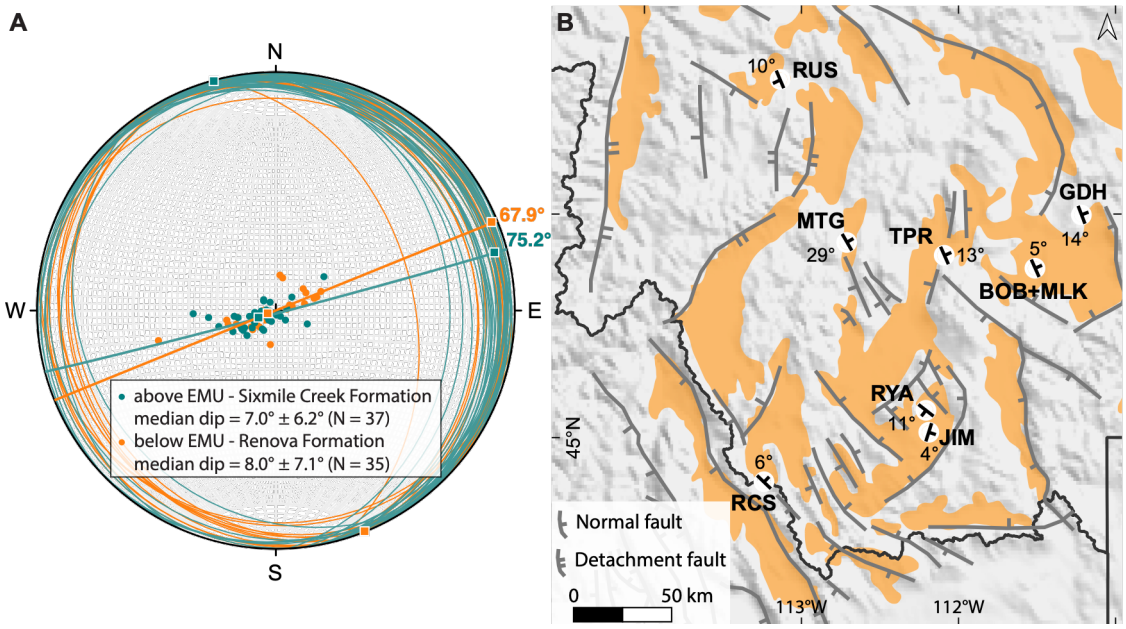

Figure 4. Summary of measured bedding planes. (A) Lower hemisphere stereographic projection of the measured bedding planes and poles to bedding. Renova Formation in orange and Sixmile Creek Formation in teal; maximum extension directions are 67.9° ± 8.9° and 75.2° ± 16.3°, respectively. **(B)** Map showing the average measured bedding planes at each section. Basins containing Cenozoic sediments are in orange (Vuke, 2020); major extensional faults are in gray [after figure 1 in Janecke (2007)]. N, north; W, west; S, south; E, east.

3.3 Discussion

Our rock magnetic study reveals an abrupt increase in magnetic mineral concentration (χ and Ms) immediately after the EMU across southwestern Montana (Fig. 3). Given the U-Pb ages in the sections and the precise age constraints of the EMU in the RCS (Gerritsen et al., 2026), we find that the enrichment in magnetic minerals persisted from 20.1 Ma until at least 10 Ma (Fig. 2). As stated earlier, identifying the EMU is routine in some sections (e.g., a lithologic color change; Fig. 1B and figs. S4 and S7); whereas it is challenging in others (fig. S5) (Vuke, 2020). However, the transition is clearly detectable with magnetic data, which are inexpensive and time efficient to obtain.

The MTG section is the sole exception to this trend (fig. S2), where the Renova Formation exhibits anomalously high magnetic mineral concentrations (Fig. 3). Given that the formations are difficult to distinguish at this location (Elliott and McDonald, 2009), it is possible that the lower part of the MTG section belongs to the Sixmile Creek Formation rather than the Renova Formation. In addition, the presence of faults crosscutting the

section complicates the stratigraphy. Moreover, a limited number of samples were taken from the Renova Formation (five samples from 10 m of section). We regard this section as an outlier and interpret an increase in magnetite concentration directly above the EMU as valid over the entire study area.

3.3.1 Climatic and pedogenic influences

The Renova Formation appears to contain more (titano)hematite compared to the overlying Sixmile Creek Formation (fig. S9), which could indicate that climate was different below and above the EMU. Oxidation of magnetite to the much less magnetic hematite could explain lower χ and Ms values, lower S-ratios, and positive σ_{hys} in the Renova Formation (Fig. 3 and fig. S8). However, if this were the case, we would expect different paleomagnetic polarities between the magnetite and hematite unblocking spectra (~500° to 580°C and ~600° to 680°C, respectively). In 123 thermally demagnetized samples from the RCS, including 41 from the Renova Formation, none displayed polarity or directional differences with distinct magnetization components segregated by unblocking temperature (Gerritsen et al., 2026). Furthermore, magnetic minerology remains relatively constant for ~10 Myr in both the Renova and Sixmile Creek formations (Figs. 2 and 3 and fig. S8), so the differences are not transitory signals. Climatic proxies reveal no clear shift at the EMU (Chamberlain et al., 2012; Harris et al., 2020; Methner et al., 2021; Retallack, 2009), meaning that the oxidation state of the magnetic minerals is unlikely to be attributed to long-term weather conditions (temperature, humidity, etc.) or pedogenic processes.

3.3.2 Compilation of detrital zircon data

Having ruled out the influence of climatic or pedogenic processes, the most plausible explanation for the shift in magnetic mineralogy is a change in sediment source following the EMU. The provenance must have changed from a magnetite-poor (e.g., sedimentary rocks) to a magnetite-rich source (e.g., crystalline basement or volcanic rocks). A common method to determine provenance is to study detrital zircon age spectra, which provide information on the age of the source rocks of the sediments. By combining our detailed rock magnetic study with detrital zircon data, we attempted to identify possible source areas. We note that the changes in magnetic and detrital zircon signals are not necessarily coupled; basaltic volcanism is rich in magnetite but poor in zircon, whereas silicic volcanism is poor in magnetite but richer in zircon. This decoupling means that an influx of basaltic material could enhance magnetite concentration independent of the zircon age spectrum.

We compiled detrital zircon age data that characterize the Renova (N/n = 35/2768; N = number of samples, n = number of zircon ages) and Sixmile Creek (N/n = 23/1570) formations from south-western Montana (Fig. 5 and data S3). By creating composite age spectra for the two formations, we spatially and temporally average the data, thereby highlighting the common source contributors while reducing local variants. During both Renova and Sixmile Creek times, fluvial interconnection between different basins allowed common sources to be transported across basins (Lielke, 2012; Sears et al., 2009; Vuke, 2020), while nearby topographic highs contributed proximal sources (Schwartz and Schwartz, 2013; Schwartz et al., 2019b). The use of composite detrital zircon data for each formation aligns with the distinctly different magnetic properties between the two formations yet relative consistency within each formation.

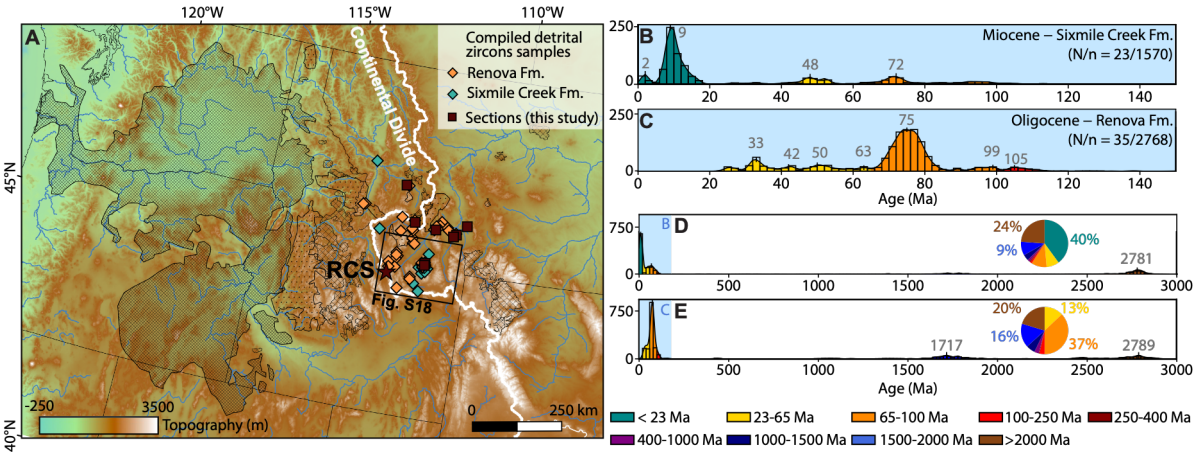

Figure 5. Detrital zircon data compilation. (A) Topographic map of the northwestern United States (NOAA, 2022), showing the present-day Continental Divide (white line), our sections, and the locations sampled for detrital zircon analysis. Legend for shaded regions in Fig. 6. **(B to E)** Composite detrital zircon age histograms for the Renova and Sixmile Creek formations with the <150 Ma spectrum in (B) and (C) and full spectrum in (D) and (E) (Link et al., 2008; Mosolf et al., 2023; Roe, 2010; Rothfuss et al., 2012; Schwartz et al., 2019b; Staisch et al., 2022; Stroup et al., 2008); N/n = number of samples/number of zircon ages.

The composite age spectrum of the Renova Formation is dominated by a Late Cretaceous signal (mostly 85 to 65 Ma), constituting 37% of all ages (Fig. 5, C and E). The nearby Late Cretaceous Boulder and Pioneer batholiths, and potentially the Idaho Batholith, likely sourced these zircons (Rothfuss et al., 2012; Schwartz et al., 2019b). A pre-1500 Ma signal comprises 36% of all zircons (Fig. 5E); peaks occurring at ~1.7 and ~2.8 billion years ago (Ga) are consistent with nearby Mesoproterozoic Belt Supergroup (Schwartz et al., 2019b) and Archean crystalline basement (Harms and Baldwin, 2020), respectively. Paleogene zircons (13%; 23 to 65 Ma; Fig. 5, C and E) most likely originate from the nearby Dillon, Absaroka, and Challis volcanic fields (42 to 55 Ma; Link et al., 2005) and ash sourced from the Cascade Arc (≤43.2 Ma; Priest, 1990). The youngest zircon ages

within the Renova Formation reach up to 22.7 Ma (data S3), which agrees with its depositional age (Fig. 2). Minor contributions consist of zircons with ages of 100 to 250 Ma (4%), 250 to 400 Ma (1%), 400 to 1000 Ma (3%), and 1000 to 1500 Ma (6%).

The composite age spectrum of the Sixmile Creek Formation is considerably different from that of the Renova Formation, with a dominant Miocene signal (<23 Ma, peak at 9 Ma) that encompasses 40% of all zircon ages (Fig. 5, B and D). This component replaces the Late Cretaceous dominance of the Renova Formation, which comprises only 11% in the Sixmile Creek Formation. The contribution of Paleogene zircons remains similar at 9% (Fig. 5D), but the younger 33 Ma peak is absent, further indicating that this was likely supplied by ash from the Cascade Arc to the Renova Formation. Meanwhile, the pre-1500 Ma contribution remains high in the Sixmile Creek Formation, comprising 33% and containing a peak at 2.8 Ga (Fig. 5D). Smaller contributions of zircons with ages of 100 to 250 Ma (1%), 250 to 400 Ma (1%), 400 to 1000 Ma (2%), and 1000 to 1500 Ma (4%) are present.

3.3.3 Sediment source identification

Pre–150 Ma detrital zircons found in both formations could be recycled from older sediments (Schwartz et al., 2019b). However, the presence of zircons with Precambrian ages is consistent with clast count analyses, which indicate that basement rocks were already exposed during Renova deposition (Schwartz and Schwartz, 2013). Some mafic dikes within the basement (Harms and Baldwin, 2020) could potentially be a magnetite-rich source, as seen on the aeromagnetic map (Fig. 6A); however, they should have contributed to both formations equally. Furthermore, the exposure of basement rocks would not explain a simultaneous provenance shift in all basins. Therefore, it appears unlikely that the basement rocks are the source of magnetite above the EMU.

If the magnetic and detrital zircon signals are coupled, i.e., if they come from the same rock unit, it becomes difficult to find suitable candidates of Miocene age near our sections. The Dillon volcanic field is the closest volcanic center that has a Miocene eruption phase (Fritz et al., 2007; Mosolf, 2015,2021), making it a potential candidate. Today, it has a very limited extent, but it was possibly more widespread than we can infer from its current exposure. However, the Dillon volcanics erupted mostly during the Eocene (Fritz et al., 2007; Mosolf, 2015), so they should have contributed to the Renova Formation as well. Moreover, when taking the paleo-drainage into account (Lielke, 2012), the Dillon volcanic rocks lay downstream of some of our sections (e.g., the RCS; fig. S10); hence, we think that Dillon volcanism cannot represent a substantial source of magnetite in the Sixmile Creek Formation.

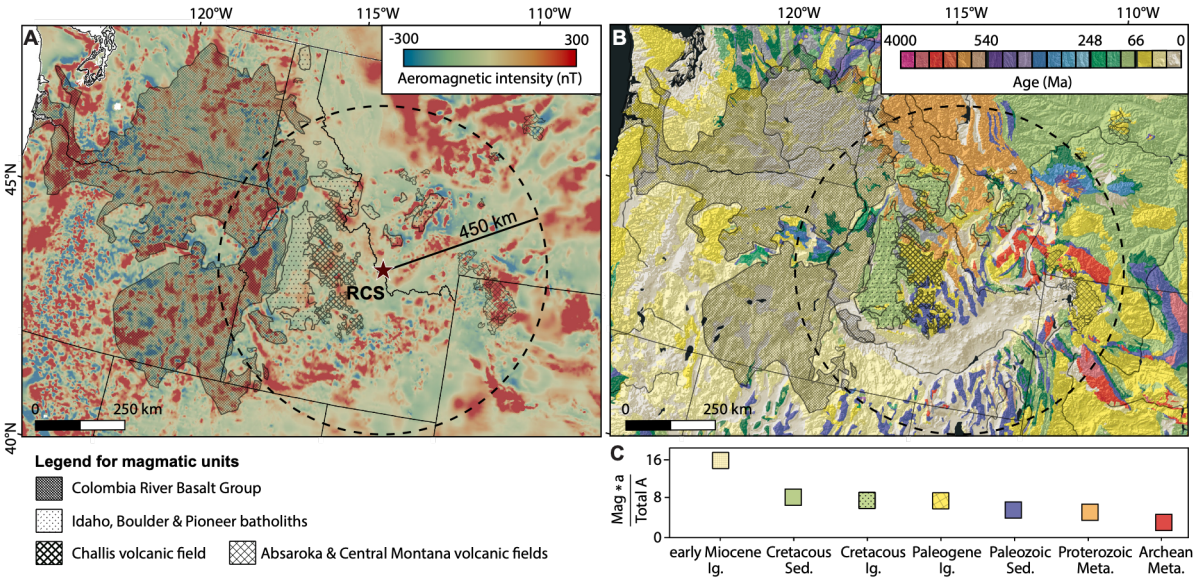

Figure 6. Magnetic contribution of major geologic units. (A) Aeromagnetic (McCafferty et al., 2023) and **(B)** geologic (Barton et al., 2003) map of the northwestern United States. The 450-km radius, dashed black circle centered on the RCS, defines the area considered for the magnetite source for the Sixmile Creek Formation. **(C)** The estimated magnetic contribution of each major geologic unit (see text for details). Shaded regions indicate the surface exposure of large magmatic units.

Although local volcanism during the Oligo-Miocene was limited, distal volcanism in the Cascade Arc was abundant during this time and could have supplied large volumes of ash, and thus magnetite, to southwestern Montana (Fig. 7A). Cascade products contributed to the Renova Formation during the Oligocene, as evidenced by its high ash content (e.g., Fields et al., 1985), as corroborated by regional volcanic records (fig. S11) (du Bray and John, 2011). However, deposition of the Sixmile Creek Formation coincided with a pronounced decline in volcanic productivity during the early Miocene, with silicic output dropping more than an order of magnitude (Priest, 1990; Sherrod and Smith, 2000; Smith, 1993), whereas we observe a marked increase in magnetite concentration (fig. S11). Volcanism during this time was dominated by the Yellowstone plume that emplaced the voluminous basaltic lavas of the Columbia River Basalt Group (CRBG) but little explosive ash (Fig. 7A). Cascade-derived air fall deposits within the CRBG are thin and locally restricted (Sherrod and Smith, 2000; Smith, 1993); the limited Yellowstone-related explosive volcanism that did occur was relatively iron poor, especially after 15 Ma (fig. S11) (Nash et al., 2006; Perkins and Nash, 2002). Although fluvially reworked tephra beds in the Sixmile Creek Formation can locally exceed 30 m, individual ash fall deposits interbedded within alluvial fans were likely no thicker than ~10 cm in our study area (Nielsen and Thomas, 2004). Inherited zircons within sampled tuffs reinforce this picture of ash reworking (Mosolf et al., 2023). The fluvial dominance of the Sixmile Creek Formation is further reflected in the lithology, where air fall tuff facies are described only

as minor constituents (Fields et al., 1985; Fritz and Sears, 1993; Portner et al., 2011; Thomas and Sears, 2020), consistent with our field observations of cross-bedding, channels, and gravel lenses (Fig. 1C and fig. S7). Collectively, these lines of evidence suggest that ash fall alone is insufficient to account for the observed magnetite enrichment, which must have been supplied primarily through fluvial transport.

We used aeromagnetic anomaly and geologic maps within a radius of 450 km around the RCS to evaluate the fluvial delivery of magnetite (Fig. 6). The factors that guided our choice of potential candidates were the intensity of the aeromagnetic anomalies (Fig. 6A) and the exposed surface area of each geologic unit older than 16 Ma (Fig. 6B). For a source to provide input to the large area of the Sixmile Creek Formation for a prolonged time (>10 Ma), there must be a relatively large exposed surface area. Figure 6C presents the total magnetic contribution of each major geologic unit by taking its average aeromagnetic intensity (Mag) and exposed surface area (a) normalized by the total explored area (total A). This analysis clearly shows that early Miocene igneous rocks of the CRBG are the greatest magnetic source, with more than twice the total magnetic contribution compared to other units. Cretaceous igneous rocks of the Idaho, Boulder, and Pioneer batholiths have relatively low magnetic contributions. These batholiths are primarily composed of two-mica granites, granodiorites, or quartz monzonites (Byerly et al., 2016; Foster et al., 2012), which lack magnetite. Being a main source for the Renova Formation (37%; Fig. 5E), this explains the weak magnetic signal in this formation. Although some of the sedimentary rocks have relatively high magnetic intensities (e.g., Cretaceous Sed. in Fig. 6C), the sources likely come from underlying units (Vuke et al., 2007).

The Yellowstone plume head eruption produced >98% of the CRBG volume between 16.7 and 15.9 Ma (Camp and Wolff, 2025). These basalt flows are rich in low-Ti titanomagnetite (Mankinen et al., 1985), identical to what we observe in the Sixmile Creek Formation. Synchronous rhyolitic centers could have provided airborne ash (Fig. 7A) (Coble and Mahood, 2012) or fluvially transported zircons to our study area. We note, however, that this ash is low in iron, particularly after 15 Ma (Nash et al., 2006; Perkins and Nash, 2002), while magnetite concentrations in our sections are consistently high between 20 and 10 Ma (fig. S11). In other words, the bimodal volcanism of the CRBG could explain the signals in the Sixmile Creek Formation by providing Miocene zircons from the rhyolitic rocks together with magnetite from the basaltic rocks. The location of the CRGB is also consistent with paleocurrent data that suggest a source area to the southwest (fig. S10). Adding the CRBG as a source, however, requires the Continental Divide to have been located ~400 km west of its present-day position (Fig. 5A), as discussed in the next section.

If the CRGB alone contributed the magnetite, a problem arises to explain why magnetite concentration increased already by ~20 Ma (the age of the EMU in the RCS; Fig. 2), about 3 Myr before the oldest known age for the CRGB (17.3 Ma, Cahoon et al., 2020). Perhaps older CRGB flows do exist but are covered by younger ones or the older units that did exist were subsequently eroded. The presence of a 20.8 ± 0.6 Ma zircon from the Sixmile Creek Formation might hint at the existence of older flows (Mosolf et al., 2023). Alternatively, some magnetite could have been shed from Paleogene basalts of the Challis volcanic field, which are located upstream of our study area (Fig. 7A). In this scenario, contribution from the Challis basalts again requires a westward shift of the drainage divide commensurate with the EMU. Other far-field sources to the southeast of our study area, such as the Absaroka volcanic field, are unlikely since they are located downstream (Fig. 7A) (Lielke, 2012; Sears et al., 2009).

In short, the early Miocene CRBG provides the most straightforward explanation for the source of the magnetite and the Miocene detrital zircon age peak in the Sixmile Creek Formation, perhaps with some contribution of magnetite from the Challis basalts. This requires the Continental Divide to have shifted westward simultaneously with the formation of the EMU.

3.3.4 Early Miocene shift of the Continental Divide

Our studied sections are distributed across the present-day Continental Divide (Fig. 7D). For example, the RUS section lies within the Columbia River watershed, the RCS and MTG sections lie on the Continental Divide, and the other sections are situated within the Missouri River watershed. Therefore, the current Continental Divide separates the RUS section from our other sections. Given the similar magnetic characteristics observed in all the sections (Fig. 3 and figs. S8 and S9), an interconnected fluviolacustrine system must have existed, linking them into a single, coherent drainage system during the Renova and Sixmile Creek periods. This suggests that the present-day Continental Divide was established after 10 Ma, the uppermost limit of our dataset.

In general, paleocurrent measurements from the Renova Formation [Fig. 7B; compiled by Vuke (2020)] and the Sixmile Creek Formation [Fig. 7C; compiled by Schwartz and Schwartz (2013)] indicate NE-directed flow, similar to the present-day Missouri River (Fig. 7D). The Renova provenance is dominated by weakly magnetic material with peak detrital zircon ages at 75 Ma. While we cannot rule out far-field sources like the Idaho Batholith, a closer source from the Boulder and Pioneer batholiths in combination with recycled zircons can sufficiently explain our observations (Schwartz and Schwartz, 2013; Schwartz et al., 2019b). An Eocene river has been proposed to exist in the western part of our study area (Fig. 7B). This river is thought to have flowed from Idaho, through

Montana, and into Wyoming, based on similarities in lead isotopes between the Challis volcanic rocks and coeval sediments in Wyoming (Chetel et al., 2011; Janecke et al., 2000). Given this regional paleogeographic context, a local source from the Boulder and Pioneer batholiths would be more compatible with regional paleogeographic reconstructions. The Eocene-Oligocene paleogeography in southwestern Montana thus appears to have been similar to the present-day landscape (Schwartz and Schwartz, 2013).

We propose that the early Miocene drainage system of southwestern Montana included the CRBG, which lies ~400 km west of the Continental Divide (Fig. 7C). Given that the present-day Continental Divide is broadly distributed over a wide area (cross section in Fig. 7D), slight adjustments (hundreds of meters) in local relief can highly affect the position of the divide. Sears and Ryan (2003) previously suggested a far-field source for the Sixmile Creek Formation, identifying exotic chert clasts in the Ruby Basin (our JIM section) and linking them to the Milligan chert in Idaho. They proposed that the Miocene paleo-Missouri River headwaters extended ~200 km west of the present-day divide. Our findings indicate that the headwaters extended even farther west, incorporating the CRBG into the source area. A drainage connection between Idaho and southwestern Montana has also been speculated on the basis of the NE-oriented tributaries and the sharp 90° turn of the Salmon River (Fig. 7A). Anderson (1947) proposed that the Salmon River once flowed along what is now the inverted course of the Carmen Creek, draining toward the present-day Missouri River (Fig. 7C). Anderson (1947) further observed NE-oriented wind gaps—dry valleys or passes that once carried rivers—indicating paleo-drainage pathways from Idaho to southwestern Montana. Paleocurrent measurements obtained from imbrication in the conglomerate capping the EMU in the Flint Creek basin (Portner and Hendrix, 2005), within our RUS section (Fig. 1D), also indicate an opposite flow direction during the early Miocene (Fig. 7C).

All in all, while local sources undoubtedly contributed to our source region—such as alluvial fans sourced from adjacent mountains (Schwartz and Schwartz, 2013)—our findings demonstrate that a through-going drainage system with far-field sources during the early Miocene is essential to account for both the magnetic and detrital zircon signals. This challenges previous interpretations invoking predominantly local sources for the western Montana basins (Schwartz and Schwartz, 2013; Schwartz et al., 2019a). Our data strongly support that notable changes occurred in the drainage network during the late Oligocene-Miocene.

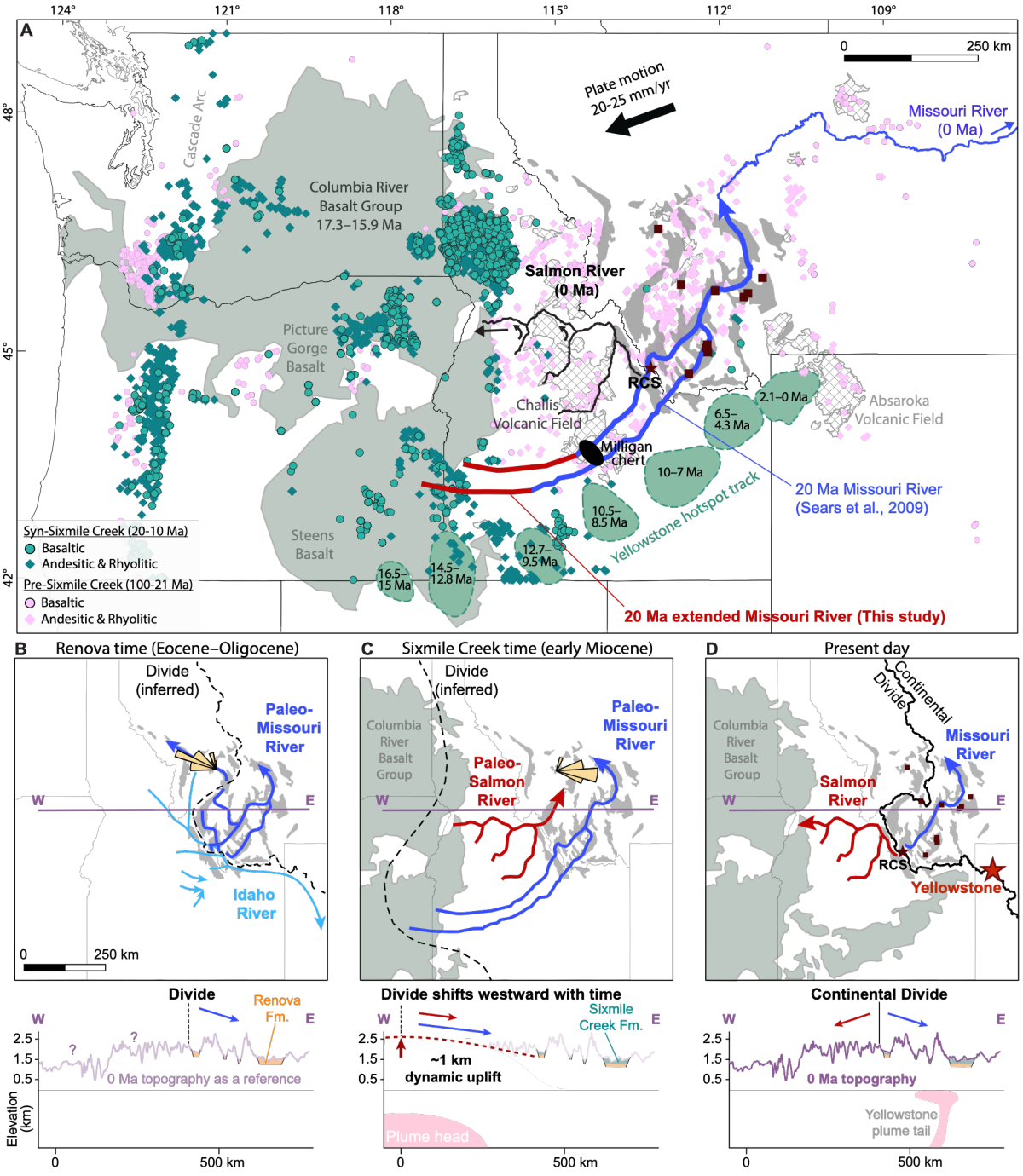

Figure 7. Drainage evolution of the northwestern United States. (A) Location of 100 to 10 Ma magmatism in the northwestern US compiled from the North American Volcanic and Intrusive Rock Database (NAVDAT) dataset (Walker et al., 2006) and Schwartz et al. (2019b). Bold red lines indicate the proposed extended Miocene Paleo-Missouri River. **(B to D)** Detailed evolution of the paleodrainage. (B) Eocene Idaho River in light blue (Chetel et al., 2011; Janecke et al., 2000), Eocene-Oligocene Paleo-Missouri River in dark blue [compiled by Vuke (2020)]; rose diagram (*N* = 21) from Portner and Hendrix (2005). (C) Miocene Paleo-Missouri River in dark blue (Sears et al., 2009), Paleo-Salmon River in red (Anderson, 1947); rose diagram (*N* = 13) from Portner and Hendrix (2005). (D) Present-day drainage situation with the projected position of the Yellowstone plume tail. Brown squares indicate sampling localities (Fig. 1); star indicates the RCS.

3.3.5 Controls on drainage reorganization

A shift in the tectonic regime, such as the onset of Basin and Range extension and/or dynamic uplift from the Yellowstone plume, can cause drainage reorganization. The influence of Basin and Range deformation is evident from our observations, with gently NE or SW dipping bedding planes (Fig. 4) aligned roughly parallel to the extension direction of 45°N measured by focal plane solutions (Schmeelk et al., 2017; Stickney and Bartholomew, 1987), perpendicular to the major extensional faults in the region (Fig. 4B). These low dip angles are likely caused by high-angle normal faulting, as is common during Basin and Range extension (Janecke, 2007; Vandenburg et al., 1998). Our limited dataset shows that bedding planes of the Sixmile Creek Formation predominantly dip NE, suggesting that SW-dipping listric or normal faults were more active in the Miocene, while the opposite pattern prevailed in the Oligocene. Although Basin and Range deformation clearly influenced the region, the drainage evolution we propose, in which the present-day drainage configuration reverts to its Eocene-Oligocene state (Fig. 7, B to D), necessitates a long-wavelength and transient topographic pulse.

For the drainage divide to shift and incorporate the CRBG into the source area, the CRBG needed to be ~1 km higher than its present elevation (Fig. 7D). The horizontal and vertical scaling is consistent with current estimates of dynamic topography: elevation changes caused by lateral density variations and convective flow in the mantle. Dynamic topography from the Yellowstone plume head extended up to 1000 km horizontally from the plume center (Friedrich et al., 2018). A maximum vertical amplitude of ~1000 m is suggested for dynamic topography on the continents (Hoggard et al., 2021), which has been proposed as a driver of large-scale drainage reorganization (Rasmussen, 2003; Sears et al., 2009). Moreover, analog modeling indicates that dynamic uplift precedes flood basalt eruptions by at least 3 Myr (Griffiths and Campbell, 1991), in line with our findings that drainage shifts occurred around 20 Ma. After the plume head erupted as the CRBG, uplift was no longer dynamically supported and waned, causing the drainage divide to eventually return to its preuplift position. Our results indicate that the CRBG continued to supply sediments to southwestern Montana until at least 10 Ma (Figs. 2 and 3), implying that dynamic topography persisted for at least 10 Myr. Our results thus support a whole-mantle Yellowstone plume scenario, as suggested by the geodynamic model of (Steinberger et al., 2019). An alternative origin of the CRGB—driven by asthenosphere flow from the Pacific through slab tear (Liu and Stegman, 2012)—is not preferred, since it would require dynamic uplift to be induced only after slab breakoff at 17 Ma, which is inconsistent with our observations. Our study therefore provides temporal and spatial constraints on dynamic topography previously only estimated from modeling.

In summary, our study reveals a pronounced increase in magnetic mineral concentration directly above the EMU across southwestern Montana, signaling a major shift in sediment provenance that is unrelated to climate change. Low magnetic concentrations combined with a predominance of 85 to 65 Ma zircon ages in the Renova Formation reflect sediment input primarily from Cretaceous batholiths, while the high magnetite content in the Sixmile Creek Formation points to the introduction of a new source during the early Miocene. The CRBG stands out as the primary candidate for this new source, as its bimodal volcanism provides both the magnetite and the Miocene-aged zircons observed in the sediments. This shift in provenance requires a substantial westward migration of the Continental Divide during the latest Oligocene to early Miocene, driven by dynamic uplift from the Yellowstone plume.

Our rock magnetic observations provide robust constraints on geodynamic model predictions, underscoring the importance of interdisciplinary approaches to linking mantle flow and surface processes. If the Renova drainage pattern was similar to the present-day, then the sediment source must have returned to a magnetite-poor lithology after 10 Ma. Future research should investigate late Neogene sedimentary sections to confirm such a shift by tracking declines in magnetic mineral concentration. In addition, further paleocurrent and provenance studies are needed to refine the timing and extent of the early Miocene drainage reorganization. Such studies will deepen our understanding of the complex interactions between mantle dynamics and surface processes in North America, revealing critical insights into how mantle processes shape continental-scale drainage systems.

3.4 Materials and methods

We conducted a rock magnetic study above and below the EMU in the northern Rocky Mountains (Fig. 1). Samples were collected during a field campaign in 2023 that netted 561 samples from seven composite sections (figs. S1 to S7). Data from the RCS were described by Gerritsen et al. (2026). Paleomagnetic cores were obtained using a battery-powered, water-cooled drill; poorly lithified strata were sampled with a handheld corer. We collected samples at roughly 2-m intervals throughout each section, obtaining two oriented cores per horizon (data S1), focusing on fine-grained materials, including silt and fine sandstones.

The average bedding attitude for each section (data S2) was used to project the Global Positioning System (GPS) position of each sample into a composite stratigraphic column per section (data S1). We could not determine the stratigraphic position of the BOB section with respect to the MLK section due to the large distance between them.

According to Vuke (2003), the lowest map unit of the MLK section correlates with the map unit we sampled in the BOB section (Vuke, 2006); therefore, we placed the base of the BOB section 60 m below the MLK section.

The stratigraphic position of the EMU was determined differently for each section. The EMU was usually accompanied by lithologic changes, such as a change in color (RYA section; Fig. 1B and fig. S4), the presence of a conglomerate layer directly above the EMU (RUS section; Fig. 1D and fig. S1), or a distinct resistant unit of stacked calcic paleosols (MLK section; Fig. 1E and fig. S6). Satellite images helped identify the location of the EMU in the GDH section (fig. S7), where we projected the observed position of the EMU on a map taking the average bedding attitude of the section (dip direction = 62°N, dip = 14°). Our position of the EMU lies west of the EMU according to the geologic map Vuke (2003) but is in good agreement with Hughes (1980). For the MTG, JIM, and TPR sections, we relied on geologic maps to situate the stratigraphic position of the EMU (figs. S2, S3, and S5).

We measured the rock magnetic properties of bulk samples to assess variations in magnetic mineral composition and grain size. A Bartington MS2 meter characterized the low-field (465 Hz) χ. Backfield curves (which define the coercivity of remanence, Bcr) and hysteresis loops were determined with a LakeShore MicroMag 3900 vibrating sample magnetometer. HystLab software (78) helped interpret the hysteresis loops to obtain the Bc, Ms, Mrs, and σ_{hys} (Fabian, 2003). S-ratios were obtained by first applying a 1 T saturation isothermal remanent magnetization (SIRM) in the sample's +y axis, followed by a backfield IRM of −0.3 T in the −y axis: $S = \left[\left(-\frac{IRM_{-0.3T}}{SIRM}\right) + 1\right]/2$ (Bloemendal et al., 1992). The S-ratio is a proxy for the relative hematite to magnetite concentration, with a value of 1.0 indicative of magnetite and 0.5 for samples rich in high coercivity minerals (>300 mT) like hematite.

4

Post-Laramide uplift of the Wind River Range, central Rocky Mountains

Dieke Gerritsen, Stuart A. Gilder, Yi-Wei Chen, Alina L. Ludat, and Michael R. Wack

Submitted to GSA Bulletin

The timing and mechanisms responsible for building the high topography (>3000 m) elevation of the central Rocky Mountains remain uncertain. Although the Laramide orogeny is recognized as the primary driver of initial uplift, emerging evidence indicates substantial post-Laramide topographic rejuvenation. We present rock and paleomagnetic data from an Eocene–Miocene sedimentary succession in the Wind River Basin, Wyoming. Lower to middle Eocene strata exhibit low concentrations of magnetic minerals, whereas upper Eocene deposits show a gradual increase, concomitant with the appearance of detrital zircons of Archean provenance. The sedimentation rate of the White River Formation (ca. 37–34 Ma) is more than five times greater than that of the underlying Wagon Bed Formation (ca. 50–40 Ma). This combination of high magnetic mineral concentrations, presence of Archean-aged detrital zircons, and increased sedimentation rates suggests renewed uplift and basement unroofing in the adjacent Wind River Range during the latest Eocene. These findings support a two-phase uplift history: an early Eocene phase associated with Laramide tectonics and a late Eocene phase of renewed uplift and basement exposure. This late Eocene phase is not explained by known tectonic events and may record lithospheric rebound or early Yellowstone plume influence, leading to reactivation of the Wind River thrust.

4.1 Introduction

The central Rocky Mountains, an extensive region of high mountains and intermontane basins along the eastern edge of the North American Cordillera, gained much of their current elevation during the Late Cretaceous–early Eocene Laramide orogeny. This orogenic event, driven by the shallow subduction of the Farallon plate beneath North America (e.g., Dickinson and Snyder, 1978), significantly reshaped the region's topography. Among the prominent features of the central Rocky Mountains, the Wind River Range in Wyoming stands out as a striking topographic feature, with peaks reaching over 4 km in elevation with relief exceeding 2 km above adjacent basins (Figure 1).

While Laramide deformation has been extensively studied, the processes governing post-Laramide uplift remain less well known. The Wind River Range has undergone significant post-Laramide uplift, yet the precise timing, mechanism, and extent of this uplift are subjects of ongoing debate. Previous studies have primarily focused on Late Cretaceous to lower Paleogene strata within the Laramide basins to assess resource potential, tectonic processes, and paleoenvironmental conditions (e.g., Dickinson et al., 1988). In contrast, the discontinuous and sparse post-Laramide deposits of the upper Paleogene and Neogene have been comparatively understudied.

By the end of the Laramide orogeny in the early Eocene, mountain ranges reached elevations of 3–4 km, while basin floors were at ~500 m (Fan and Dettman, 2009; Fan et al., 2011). Evidence for subsequent post-Laramide uplift in the Wind River Range includes: (1) Widespread hiatus surfaces, formed in the Eocene between ~42–36 Ma and during the entire Oligocene (Cather et al., 2012; Dickinson et al., 1988; Epis and Chapin, 1975); (2) Preservation of late Paleogene–Neogene strata on top of mountains built during the Laramide orogeny (McKenna and Love, 1972; McMillan et al., 2006); (3) Paleoaltimetry analyses, including stable and clumped-isotope studies, suggesting substantial elevation gain during the late Eocene (Fan et al., 2011; 2014a; 2014b); and (4) Apatite fission track (AFT) thermochronology. For the latter, some studies found evidence for rapid cooling at ~65–50 Ma, followed by slow cooling until 5 Ma whereafter the cooling rate increased (Cerveny and Steidtmann, 1993; Peyton et al., 2012; Stevens et al., 2016) while others found rapid cooling at ~75–50, subsequent reheating, and then more rapid cooling after 10 Ma (Caylor et al., 2023).

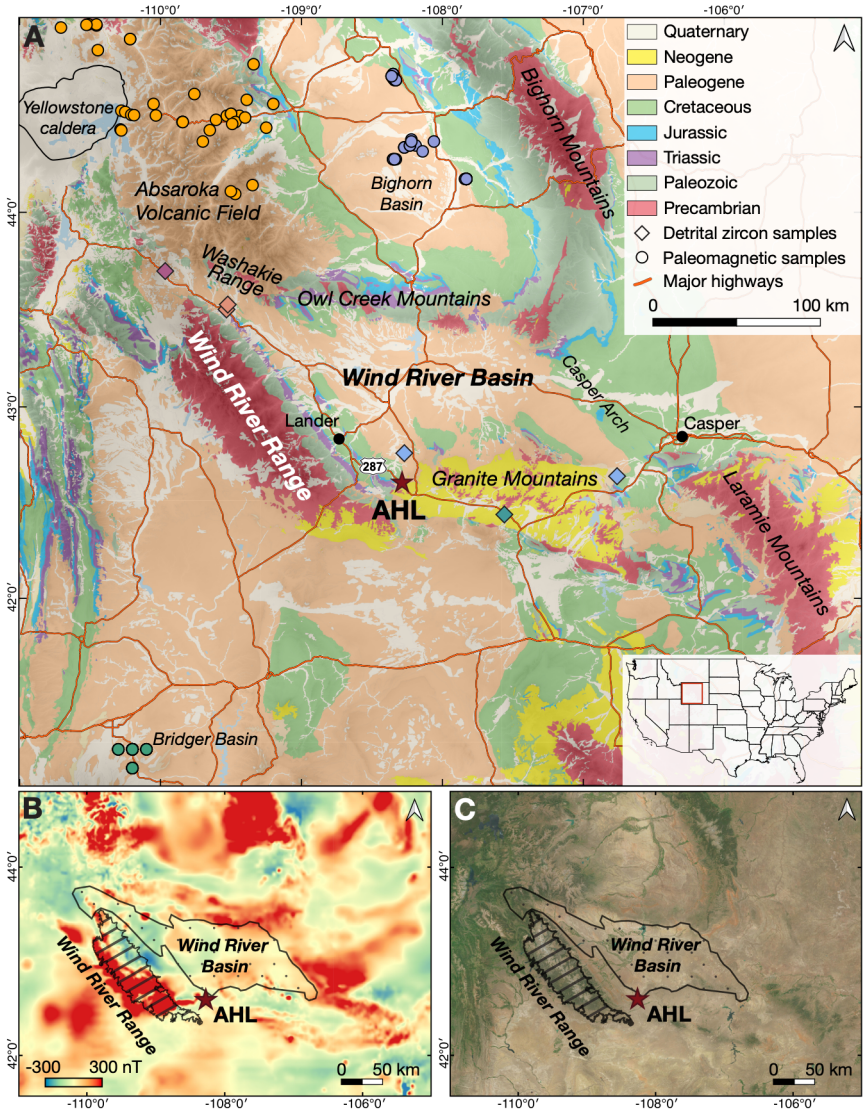

Figure 1. (A) Geologic map of the Wind River Basin area (Barton et al., 2003) (red rectangle in the inset). The Abandoned Highway Lander (AHL) section near U.S. Highway 287 in the Beaver Rim area is indicated by the brown star. Detrital zircon sample locations are shown as diamonds (Fan et al., 2011; Malone et al., 2017; Rowley and Fan, 2016); colors refer to formations where the samples were collected: teal = Split Rock Formation, blue = White River Formation, purple = Wagon Bed Formation, and salmon = Wind River Formation. Paleomagnetic sample locations are shown as circles; colors refer to different Eocene datasets: light purple = Bighorn Basin (Clyde et al., 2007), green = Bridger Basin (Tsukui et al., 2025), and orange = Absaroka Volcanic Field (Harlan and Morgan, 2010). Shaded relief map from NOAA (2022). Outline of Yellowstone caldera from Christiansen (2001). **(B)** Aeromagnetic map (McCafferty et al., 2023). **(C)** Satellite image (Environmental Systems Research Institute, 2009).

The mechanism driving post-Laramide uplift remains debatable. It is commonly attributed to thermal uplift induced by asthenospheric upwelling following the removal of the subducted Farallon slab or thickened mantle lithosphere (e.g., Dickinson and Snyder, 1978), or to thermal upwelling associated with the initiation of the Rio Grande

Rift (e.g., McMillan et al., 2006). Additionally, the rise of the Yellowstone plume during the latest Eocene to early Miocene has been proposed as a significant geodynamic driver in North America, potentially generating up to a kilometer of dynamic topography extending as far as 1000 km from the plume head (Friedrich et al., 2018). While this process is expected to have influenced surface topography and drainage patterns, definitive geological evidence for its impact remains sparse (Gerritsen et al., 2025).

This study reports rock and paleomagnetic analyses of a sedimentary section in the Beaver Rim area on the southern margin of the Wind River Basin. The section includes three unconformity-bound sequences spanning from the Eocene to the early Miocene, capturing the final phase of Laramide deformation and the subsequent post-Laramide phase. We calculated sedimentation rates and integrated our magnetic data with published detrital zircon ages to establish sediment provenance and estimate paleorelief. This integrated approach aims to improve understanding of the timing and process of post-Laramide uplift and consequent source exposure and erosion during a period of significant geodynamic transition in the central Rocky Mountains.

4.2 Geologic setting

The Wind River Basin in the central Rocky Mountains is a typical Laramide-style, elongate structural basin, surrounded by reverse fault-bounded uplifts: the Wind River Range to the west, the Washakie Range and Owl Creek Mountains to the north, the Casper Arch to the east, and the Granite Mountains (Sweetwater Uplift) to the south (Figure 1A). These uplifts developed during the Laramide orogeny in the Late Cretaceous to early Eocene (Dickinson and Snyder, 1978). The Wind River Range is bound by the Wind River thrust to the southwest and is composed primarily of granite, granitic gneiss, and migmatite of the Archean Wyoming Province (Frost et al., 1998). Northwest of the basin lies the Absaroka Volcanic Field (Smedes and Prostka, 1972), a large middle Eocene volcanic field that was active between ~55–44 Ma and reached peak activity between 50.5 and 47.5 Ma (Harlan and Morgan, 2010).

The Wind River Basin contains a sequence of sedimentary rocks up to 8.5 km thick, with the Paleocene Fort Union Formation forming the base of the Cenozoic (Keefer, 1970). This formation is absent in the Beaver Rim area, where up to 600 m of Cenozoic deposits are divided into four formations (Figure 2), as described in detail by Van Houten (1964).

An unconformity marks the base of the Wind River Formation, which is composed of yellow to varicolored mudstone with lenticular beds of sandstone and pebble conglomerate (Figure 2D). The upper part of the formation is locally tuffaceous, likely reflecting ash fall or volcaniclastic detritus from the nearby Absaroka Volcanic Field (Van

Houten, 1964). The Wind River Formation was deposited on low piedmonts and valley flats in a warm, humid climate (Van Houten, 1964), when braided river systems flowed mainly eastward (Fan et al., 2011). North American land mammal age (NALMA) fossils are middle and late Wasatchian (Van Houten, 1964). Evernden et al. (1964) performed K–Ar dating on a tuff, yielding an age of 49.2 Ma. Although late Wasatchian fossils were found near the dated horizon, the radiometric age falls within the Bridgerian; however, a high percentage of atmospheric argon in the dated sample leads to a high uncertainty on the age, so we excluded it.

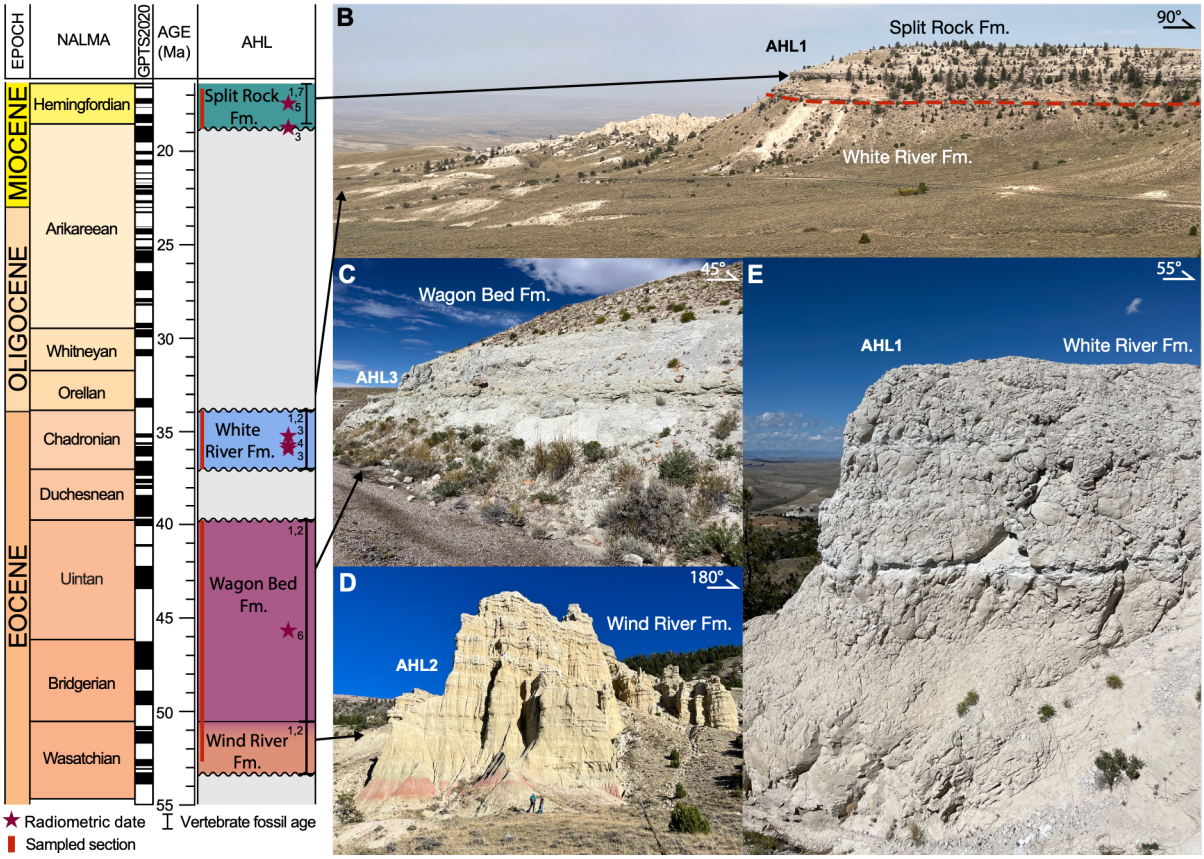

Figure 2. Chronostratigraphic chart of the Abandoned Highway Lander (AHL) section. North American Land Mammal Ages (NALMA) from Barnosky et al. (2014). References: [1]Van Houten (1964) [2]Emry (1975) [3]Rowley and Fan (2016) [4]Swisher and Prothero (1990) [5]Izett and Obradovich (2001) [6]Evernden et al. (1964) [7]Tedford et al. (2004). Geomagnetic Polarity Time Scale (GPTS2020) from Ogg (2020). Field photographs: **(B)** Split Rock Formation on top of White River Formation, with the dashed red line indicating the contact; **(C)** Wagon Bed Formation along the road; **(D)** Wind River Formation; and **(E)** close-up of the White River Formation.

The overlying Wagon Bed Formation marks a shift to deposition in poorly drained lowlands, broad flood plains, and lakes (Van Houten, 1964). It is composed of laterally persistent beds of well-sorted sandstone, siltstone, and mudstone (Figure 2C). The Wagon Bed Formation commonly contains bentonitic clay and volcanic debris, likely derived from the nearby Absaroka Volcanic Field, which was near its peak activity at that

time (Harlan and Morgan, 2010). Then, the Idaho River fluvial system flowed southward from north-central Idaho to northwestern Wyoming (Carroll et al., 2008; Chetel et al., 2011; Lillegraven and Ostresh, 1988). Bridgerian to Uintan NALMA fossils were identified in the formation (Emry, 1975; Van Houten, 1964). Evernden et al. (1964) obtained a 45.4 Ma K–Ar age from a tuff in this formation, which we corrected to 45.7 Ma using the updated radiogenic decay constants of Steiger and Jäger (1977) (Figure 2).

An unconformity separates the Wagon Bed Formation from the overlying White River Formation (Figure 2). This late Uintan–Duchesnean interval was marked by widespread erosion in the Rocky Mountains and incised deep canyons in several Laramide ranges (Evanoff, 1990; Steidtmann et al., 1989; Steidtmann and Middleton, 1991). The hiatus is documented across large parts of Wyoming and Colorado, and extends to adjacent areas of Montana, Utah, and beyond (Cather et al., 2012; Dickinson et al., 1988; Lillegraven, 1993). It was linked to lithospheric rebound following the cessation of the Laramide orogeny, causing uplift of the central Rocky Mountains with respect to the adjacent Great Plains (Cather et al., 2012; Fan et al., 2014a; 2014b).

The White River Formation consists of white to gray silty sandstone, siltstone, and claystone, which is calcareous and tuffaceous (Emry, 1975) (Figure 2E). It was deposited on broad floodplains, where recurrent volcanic ash falls periodically blanketed the landscape under subhumid and warm-temperate climatic conditions (van Houten, 1964). Paleocurrent measurements indicate that the drainage system predominantly flowed eastward (Fan et al., 2015; Lillegraven and Ostresh, 1988). NALMA fossil assemblages within the formation are exclusively Chadronian (Emry, 1975), a correlation supported by a $^{40}Ar/^{39}Ar$ age of 35.81±0.09 Ma obtained from an interbedded ash layer (Swisher and Prothero, 1990). The maximum depositional ages from detrital zircon U-Pb dating are 35.3±1.0 Ma and 36.0±0.3 Ma (Rowley and Fan, 2016). Although the White River Formation was often referred to as Oligocene in older literature because the Chadronian NALMA was historically assigned to that epoch, it is now recognized as latest Eocene following a revised NALMA chronology (Barnosky et al., 2014) (Figure 2). Prothero and Sanchez (2004) conducted a magnetostratigraphic study on the formation in the Beaver Rim area but interpreted two normal chrons based on only two single normal polarity sites and therefore relied primarily on biostratigraphy to make their correlation.

A hiatus follows the White River Formation in which the entire Oligocene is missing (Figure 2). Early Oligocene sediments are also absent on the southern end of the range (e.g., Steidtmann and Middleton, 1991). Deep erosion occurred over a broad region during the late Oligocene–early Miocene (Cather et al., 2012). Multiple hypotheses have been proposed to explain the emergence of this erosional interval. The hiatus has been linked to post-Laramide fault reactivation driven by lithospheric rebound and stress

changes along inherited basement structures (Hall and Chase, 1989; Steidtmann et al., 1989) or dynamic topography and widespread Oligocene volcanism associated with a buoyancy source in the mantle (Cather et al., 2012). These mechanisms likely acted in combination, as emphasized by Cather et al. (2012), who argued that only the combined effects of uplift, fault reactivation, and aridification can account for the extent and timing of erosion.

The youngest formation in the Beaver Rim area is the Split Rock Formation (Figure 2), which consists of massive, well-sorted sandstone and persistent beds of coarse conglomerate that contain arkosic and volcanic detritus (Figure 2B). It was deposited in a high-plains environment under more arid conditions than during deposition of the White River Formation (Van Houten, 1964). This aridification, also noted by Fan et al. (2014a), likely contributed to widespread eolian sedimentation in the central Rocky Mountains (Rowley and Fan, 2016). The formation's NALMA fossils are Hemingfordian (Tedford et al., 2004; Van Houten, 1964), which is in fairly good agreement with a detrital U-Pb age of 18.8±0.7 Ma (Rowley and Fan, 2016) and a $^{40}Ar/^{39}Ar$ age of 17.4±0.08 Ma from volcanic ash (Izett and Obradovich, 2001). Liter et al. (2008) performed a magnetostratigraphic study of the Split Rock Formation but only found two reversals; they thus used biostratigraphy and the 17.4±0.08 Ma $^{40}Ar/^{39}Ar$ age to correlate them to chrons C5Br–C5Cr, without providing additional age constraints. No Neogene rocks younger than the Split Rock Formation are present in the Beaver Rim area; to the southeast, the formation is overlain by an erosional unconformity and then by the late Barstovian–early Hemphillian Moonstone Formation (Cassiliano, 2008; Love, 1961).

4.3 Methods

We conducted a paleomagnetic and rock magnetic study of the Abandoned Highway Lander (AHL) section in the Wind River Basin, Wyoming (Figure 1). Samples were collected during a field campaign in 2022 that netted 181 samples from six profiles located near a now-abandoned stretch of U.S. Route 287 (Figure S1). We collected samples at roughly 2 m intervals at each profile, taking two oriented cores per horizon. A battery-powered drill was used to collect oriented inch-core rock samples and a hand sampler to collect oriented soft sediments. Our focus was on fine-grained materials, including silt- and fine sandstones. We corrected our magnetic compass readings with the average declination anomaly (10.1±2.2°) from 103 Sun compass readings, which agrees well with 9.8° predicted by the International Geomagnetic Reference Field. We observed a uniform, almost horizontal bedding of dip = 2° and dip direction = 50.1°. A Jacob staff was used to determine the stratigraphic position of each sample within a section (Table S2). We corrected our Jacob staff measurements by scaling them to the

handheld GPS elevation measurements (Table S1) and used lithological markers to place the six sections into one composite section of 315 meters (Figure S1).

We performed stepwise alternating field (AF) demagnetization with 11 steps up to 90 mT, anhysteretic remanent magnetization (ARM) acquisition experiments, and magnetic moment measurements using an automated system (SushiBar) integrated with a 2G Enterprises three-axis superconducting magnetometer (Wack and Gilder, 2012). In total, 88 specimens were subjected to AF demagnetization and 62 to thermal demagnetization; the specimens from sections AHL5, AHL6, and the bottom of AHL2 were collected in plastic cups using the soft sediment sampler, which precluded thermal treatment. We used an ASC Scientific TD-48 oven with 14 progressive heating steps up to 580°C for the AHL1 section or 18 progressive heating steps up to 680°C for the AHL2, AHL3, and AHL4 sections. Remanent magnetization directions were analyzed by principal component analysis (Kirschvink, 1980) using PaleoMac software (Cogné, 2003) and Fisher (1953) statistics, including the precision parameter (k) and the radius within which the mean direction lies with 95% confidence (α_{95}). For anisotropy, we measured ARM acquisition by applying a switching field window from 90 to 10 mT with a DC bias field of 0.1 mT in 12 independent directions (Wack and Gilder, 2012).

Rock magnetic properties of bulk samples were measured to assess variations in magnetic mineral composition and their relative grain sizes across the sections. Low frequency (465 Hz) magnetic susceptibility (χ) was measured with a Bartington MS2 meter. Hysteresis loops and backfield curves, which define the coercivity of remanence (Bcr), were measured with a LakeShore MicroMag 3900 vibrating sample magnetometer (VSM). HystLab software (Paterson et al., 2018) was used to interpret the hysteresis loops by computing the coercive force (Bc), saturation magnetization (Ms), saturation remanent magnetization (Mrs), the hysteresis shape parameter (σ_{hys}), and the high-field susceptibility (χ_{HF}). σ_{hys} is positive for wasp-waisted hysteresis loops and negative for potbellied loops, both indicating a mixture of coercivities and/or grain sizes (Fabian, 2003). S-ratios were obtained by first applying a 1 T saturation isothermal remanent magnetization (SIRM), followed by a backfield IRM of −0.3 T: $[(-IRM_{-0.3T}/SIRM) + 1]/2$ (Bloemendal et al., 1992). The S-ratio is a proxy for the relative hematite to magnetite concentration, with a value of 1.0 indicating magnetite and 0.5 for minerals with high coercivities (>300 mT) like hematite.

4.4 Results

4.4.1 Magnetic mineralogy

The sum of the rock magnetic experiments shows extremely variable properties between formations (Figure 3). Samples from the Wind River Formation generally demagnetize 75–95% by 390–580°C, indicative of low-Ti titanomagnetite, after which the moment starts to increase due to alteration (Figures 3E–F). The presence of hematite is signaled by incomplete AF demagnetization by 90 mT and wasp-waisted hysteresis loops (Figure 3D). Wagon Bed Formation samples exhibit similar behavior to the Wind River Formation (Figure 3C). Overall, the Wagon Bed and Wind River formations have nonuniform compositions (Figures 3G–H) and contain mixtures of high coercivity minerals (hematite and/or goethite) and low-Ti titanomagnetite.

Samples from the White River Formation lose ~70–90% of their moment by 175°C during thermal demagnetization (Figure 3B), which could be indicative of limonite or goethite; however, AF demagnetization readily removes the remanence, which argues against the presence of high coercive magnetic minerals, as corroborated by closed hysteresis loops. Albeit rare, some samples slowly demagnetize up to 580°C, reflecting the presence of pure magnetite (Figure 3B). Collectively, the rock magnetic properties reveal that the White River Formation is dominated by low-Ti titanomagnetite of fairly uniform composition (Figure 3H).

All Split Rock Formation samples display steady and complete thermal demagnetization up to 580°C and a steep drop off at low coercivities during AF demagnetization (Figure 3A), indicating low-Ti titanomagnetite as a carrier (Figures 3G–H).

4.4.2 Stratigraphic variation in magnetic properties

Despite the high variability throughout the section, it can be split into three parts based on similar rock magnetic parameters (Figures 3G–H and 4). The Wind River and Wagon Bed formations toward the base of the section are characterized by low magnetic mineral concentrations: χ is $6.88\pm2.43\times10^{-8}$ m^3/kg and $8.40\pm5.23\times10^{-7}$ m^3/kg while Ms is $1.18\pm2.14\times10^{-3}$ Am^2/kg and $2.60\pm3.50\times10^{-3}$ Am^2/kg, respectively (Figures 4 and S2B). The other rock magnetic parameters indicate mixtures of magnetic minerals and grain sizes. For example, the presence of a high coercivity mineral, such as hematite or goethite, is reflected by samples with higher Bc values and S-ratios distinctly less than 1.0 (Figures 4 and S2A). This is further confirmed by the presence of wasp-waisted hysteresis loops (positive σ_{hys}).

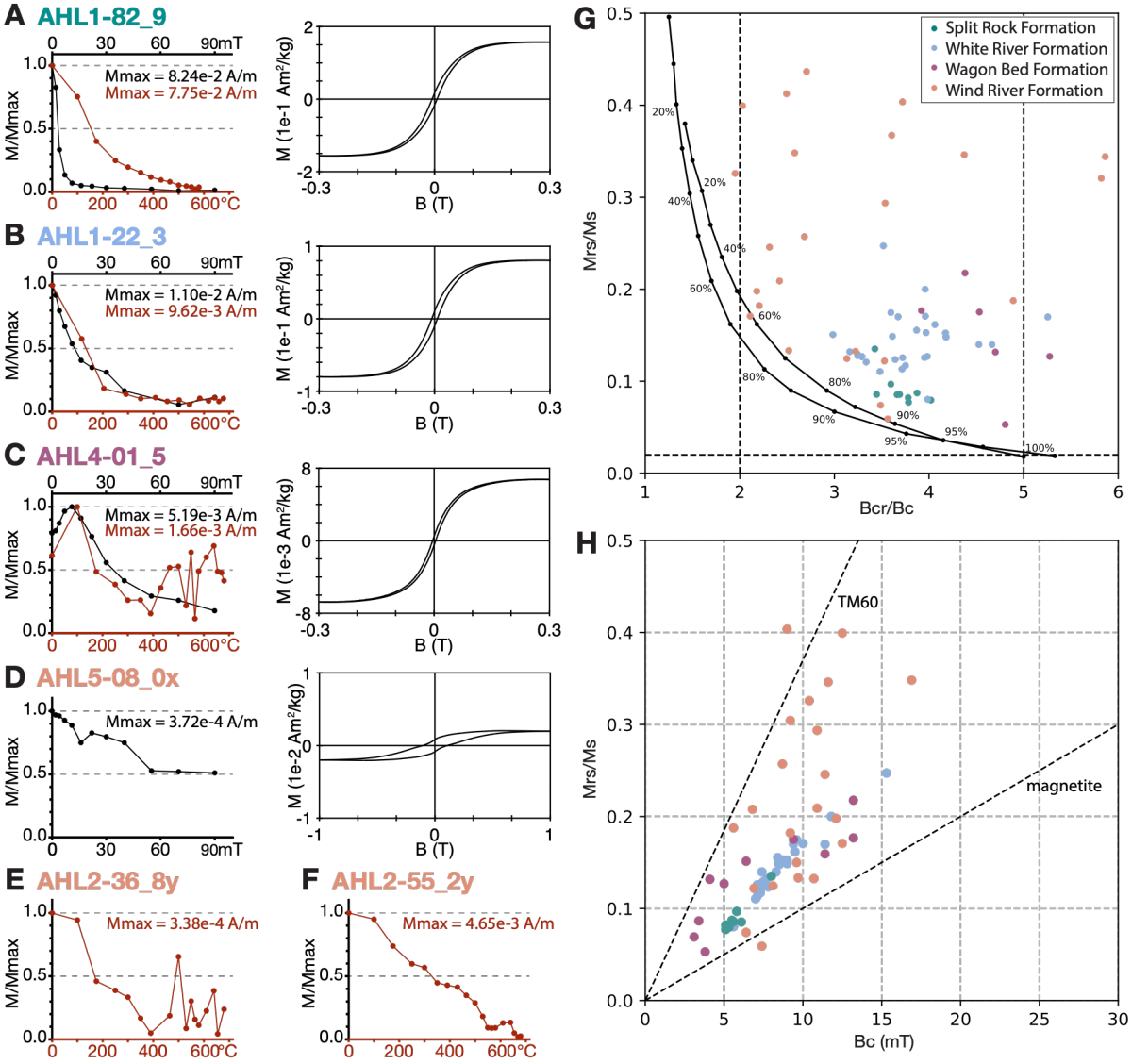

Figure 3. Examples of and moment decay diagrams of alternating field (black) and thermal (red) demagnetization and hysteresis loops from the **(A)** Split Rock Formation, **(B)** White River Formation, **(C)** Wagon Bed Formation, and **(D–F)** Wind River Formation. **(G)** Day diagram (Day et al., 1977) with the SD + MD mixing curves of Dunlop (2002). **(H)** Néel diagram (Néel, 1955) with the trend lines for magnetite and titanomagnetite with x = 0.6 (TM60) from Wang and van der Voo (2004).

The White River Formation contains a striking increase in magnetic mineral concentration, in which χ and Ms increase by factors of 4.4 and 6.6, respectively (Figure 4). Simultaneously, χ_{HF} decreases by a factor of 3.8, reflecting a decrease in the relative proportion of paramagnetic to ferrimagnetic minerals. The other parameters vary much less with stratigraphic height: σ_{hys}, Bc, and the S-ratio are 0.0135±0.0957, 8.05±1.81 mT, and 0.969±0.016, respectively, indicating the dominance of low coercivity minerals with large (multidomain) relative grain sizes (Mrs/Ms = 0.140±0.030) typical of magnetite.

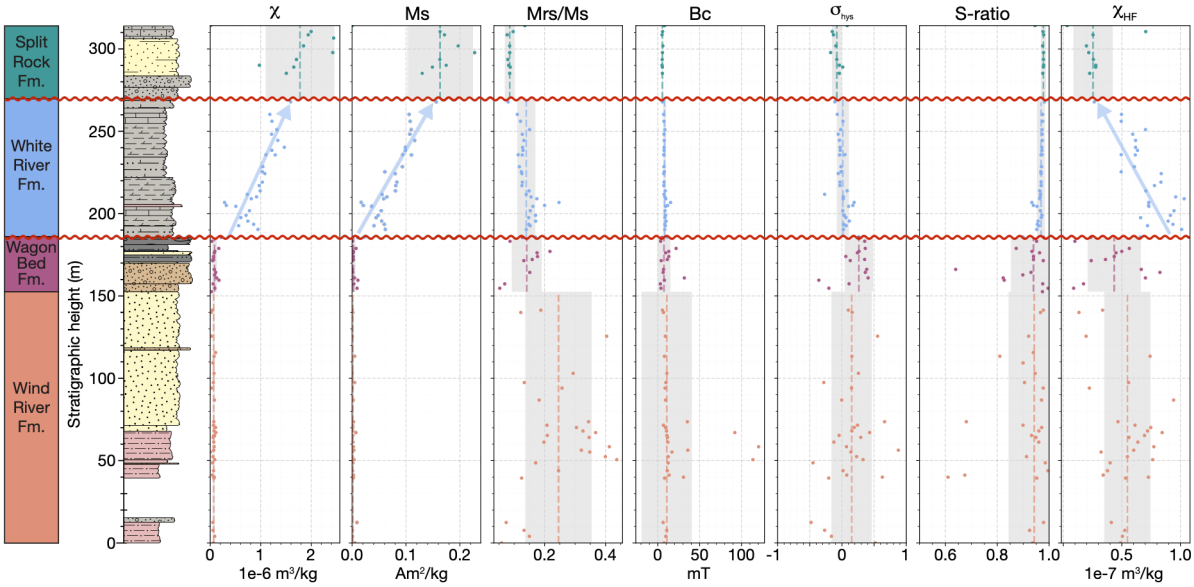

Figure 4. Composite sedimentary log and rock magnetic properties of the Abandoned Highway Lander (AHL) section. From left to right: magnetic susceptibility (χ), saturation magnetization (Ms), saturation remanent magnetization (Mrs) divided by Ms, coercive force (Bc), hysteresis shape parameter (σ_{hys}), hematite to magnetite concentration (S-ratio), and high-field susceptibility (χ_{HF}). Dashed lines indicate median values and shaded regions 1σ uncertainty. Figure S1 provides the legend to the sedimentary log; gray shading in the log represents carbonate-rich rocks.

The Split Rock Formation at the top of the section contains high magnetic mineral concentrations: χ = 1.78±0.65×10^{-6} m^3/kg and Ms = 1.63±0.60×10^{-1} Am^2/kg (Figure 4). It is dominated by ferrimagnetic minerals with low coercivity (Bc and S-ratio; 5.50±0.84 mT and 0.978±0.010, respectively) and larger grain sizes (Mrs/Ms = 0.086±0.017), likely multidomain titanomagnetite. No mixture of grain sizes or coercivities is apparent (σ_{hys} = -0.0800±0.0774).

Overall, the AHL section can be divided into three unconformity-bounded intervals. The early–middle Eocene Wind River and Wagon Bed formations have a heterogeneous magnetic mineralogy, characterized by low concentrations of hematite/goethite and low-Ti titanomagnetite. The concentration of low-Ti titanomagnetite progressively increases in the late Eocene White River Formation and remains high in the Miocene Split Rock Formation at the top of the section.

4.4.3 Paleomagnetic directions

Stepwise demagnetization produced variable results, revealing both normal (Figure S3) and reversed (Figure 5) polarity directions. Four horizons were excluded because their natural remanent magnetization (NRM) intensities/χ were >10^5 A/m, more than an order of magnitude greater than the median (9.43±0.13 × 10^3 A/m), indicative of lightning

strikes (gray in Figure S1). All excluded samples are from the Split Rock Formation (Figures S3A–B), likely due to their high elevation near the top of the plateau (Figure 2B).

Interpreting the paleomagnetic data proved challenging. First, the expected Eocene to Miocene directions lie close to the recent field direction, making it hard to distinguish between a primary remanence and a viscous, present-day field overprint for magnetization components with normal polarity. Second, the constant and shallow 2° bedding attitude limited the structural correction required for a fold test and hindered the ability to distinguish whether the normal polarity directions reflect present-day field overprints or a more ancient field. Third, the data themselves are scattered, further complicating interpretation.

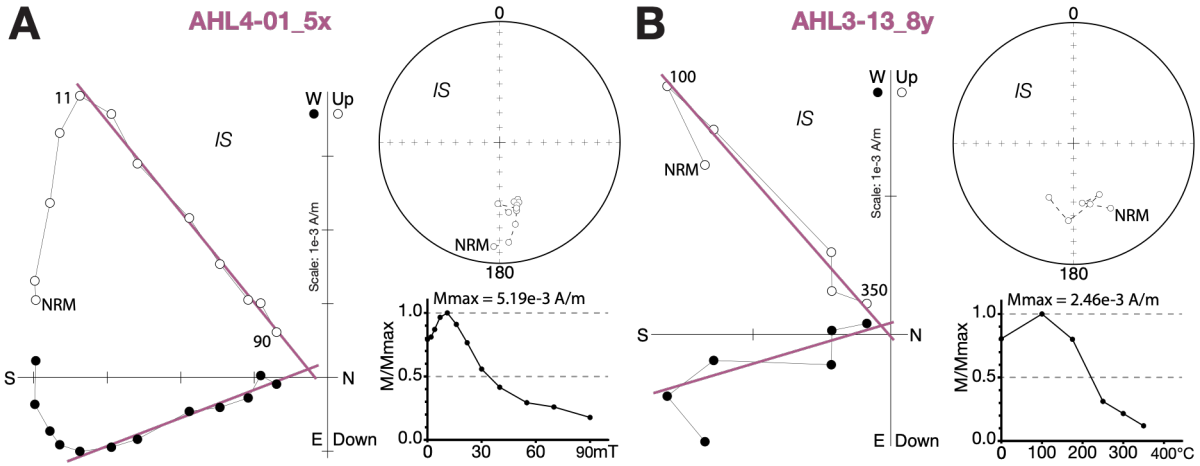

Figure 5. Zijderveld diagram, stereographic projection, and moment decay diagram of **(A)** alternating field and **(B)** thermally demagnetized samples from the Wagon Bed Formation. Thermal demagnetization was cut off at the lowest moment, whereafter the magnetization became unstable.

Thermal demagnetization yielded mostly noisy data. Best-fit lines (not forced to the origin) applied to the first few temperature steps on samples that lost 50–90% of their NRM by 175°C (Figure 3A–B) define normal polarity directions. The average declination (D) is 358.7° and inclination (I) is 65.7° (α_{95} = 4.3°, n = 33), closely aligning with the present-day field (D = 9.8°, I = 67.8°) and geocentric axial dipole (D = 0°, I = 61.5°) directions. Next, we selected directions from a single, 11 mT AF demagnetization step from all samples (Figure 6A). These data form two antipodal clusters, which pass the parametric bootstrap reversal test at the 95% confidence level (Tauxe, 2010), yielding a mean direction of Ds = 5.7°, Is = 65.4° (α_{95} = 5.9°, n = 84), where *s* indicates stratigraphic coordinates. Systematically applying best-fit line segments to the 4–11 mT steps (not forced to the origin and with maximum angular deviations less then 10°) yields a more tightly clustered mean direction (n = 40, Ds = 5.5°, Is = 60.2°, α_{95} = 4.5°; Figure S4A); however, these data fail the reversal test (Tauxe, 2010).

The distribution of the 11 mT directions from the Wind River Basin (Figure 6A) closely resembles those from Eocene sediments in the nearby Bighorn (~60–53 Ma; Figure 6B) and Bridger (~50–46 Ma; Figure 6C) basins (Figure 1A). Data from the Bighorn Basin (Clyde et al., 2007) fail the reversal test (Tauxe, 2010), which the authors attributed to an unremoved present-day field overprint. These data pass a fold test and their distribution is consistent with the THG24 field model (Tauxe et al., 2024). However, 15 of 17 reversed and 22 of 42 normal site directions have $\alpha_{95} > 20°$. After removing these directions, the reversal test cannot be applied; however, the mean direction based on n = 22 (Ds = 165.4°, Is = -63.5°, α_{95} = 5.9°) mimics that based on n = 59 (Ds = 167.7°, Is = -62.9°, α_{95} = 4.4°; Figure 6B). Site mean directions based on Class I data from the Bridger Basin (Tsukui et al., 2025) often have very large uncertainties (up to $\alpha_{95} > 50°$), so we filtered the data for $\alpha_{95} \leq 20°$ (Figure 6C). These filtered data pass the reversal test (Tauxe, 2010) and conform to the THG24 field model (Tauxe et al., 2024). Once again, the normal polarity directions cluster around the present-day field direction. In summary, Eocene sedimentary records from nearby basins are generally of low quality, but the averaged directions appear consistent from basin to basin.

A discrepancy arises when we examine magnetization directions from the Wind River Basin as a function of stratigraphy. Here, polarities divide almost exclusively by formation: the White River Formation contains only normal polarity, while samples from the Wagon Bed Formation are solely reversed (Figure 6A). Although the Wind River Formation has both polarities, 6 of 7 samples with reversed polarity lie far from the mean direction, and only one sample was retained when applying best-fit line segments from 4–11 mT (Figure S4A). This pattern runs counter to expectations from the Geomagnetic Polarity Time Scale (GPTS, Figure 2), which predicts both polarities in all formations.

4.4.4 Primary reversed directions

We now examine the magnetization components isolated at higher coercivity or temperature, which should reflect the more stable single-domain fraction. In this category, only samples from the Wagon Bed Formation have stable magnetization components that sometimes decay univectorially to the origin (Figure 5). White River Formation samples exhibit stable demagnetization behavior at higher demagnetization levels, especially during AF demagnetization, but rarely decay to the origin (Figures S3C–D). Wind River Formation samples tend to be weakly magnetic and often lack a stable component altogether (Figures S3E–F). Because the normal polarity directions cannot be distinguished from the present-day field, we focused specifically on the reversed polarity directions from the Wagon Bed Formation.

High coercivity or high temperature components from the Wagon Bed Formation display exclusively reversed polarities or great circle trajectories trending toward reversed polarity directions. AF demagnetization yields the most consistent results, typically showing linear decay from 11–90 mT (Figure 5A). We forced these steps to the origin when applying the best-fit procedure. Nine samples have stable thermal demagnetization trajectories, mostly between 100–350°C, above which the magnetization becomes unstable (Figure 5B). We calculated a mixed mean direction (McFadden and McElhinny, 1988) from the best-fit and great circle data (n = 25, Ds = 162.3°, Is = -56.7°, k = 46.0°, α_{95} = 4.3°; Figure 6D). This mean is indistinguishable from the Fisher (1953) mean of the best-fit data alone (n = 18, Ds = 163.1°, Is = -56.3°, k = 41.2°, α_{95} = 5.4°) (McFadden and Lowes, 1981), whose distribution is consistent with the THG24 field model and does not show evidence for inclination shallowing (Figure S5; Tauxe et al., 2024).

A tuff within the Wagon Bed Formation yielded a K–Ar age of 45.7 Ma (Evernden et al., 1964), which corresponds to reversed chron C20r (46.235–43.45 Ma) from the GPTS2020 of Ogg (2020) (Figure 2). The samples from the Wagon Bed Formation were collected in a stratigraphic interval of ~30 m. Given a sedimentation rate of 5 cm/kyr, this corresponds to approximately 0.6 Myr, which is fully consistent with the observed reversed polarity, as chron C20r spans nearly 3 Myr.

In conclusion, the reversed directions from the Wagon Bed Formation likely represent primary magnetizations. By contrast, the White and Wind River formations yield only normal polarity directions that cluster around the present-day field (Figures 6A and S3) and are inconsistent with correlation to the GPTS, making a primary origin unlikely. This also casts doubt on the data from the Bighorn and Bridger basins. How can we be confident that the normal polarity directions from those studies are primary and not recent field overprints? If we consider only reversed directions from all studies, the mean direction of the Wagon Bed Formation (~46–43 Ma) from the Wind River Basin is indistinguishable (within 95% confidence limits; McFadden and Lowes, 1981) from the mean reversed directions from the Bighorn and Bridger basins (Figure S4B).

Because the mean reversed directions from the three basins are indistinguishable, we combined them into a single Eocene sedimentary dataset (n = 76, Ds = 159.2°, Is = -52.9°, k = 17.2, α_{95} = 4.0°). The declination of the V2 direction ($V2_{dec}$) of this dataset is inconsistent with the THG24 field model, indicating that the sediments might have suffered from inclination shallowing (Figure S6; Tauxe et al., 2024). Progressive unflattening of the dataset yielded an optimal unflattening factor of f = 0.75°±0.2 (Figure S7). We applied this unflattening factor to the inclinations of the dataset, assuming a King (1955) relationship: $\tan(I_O) = f \tan(I_F)$, thereby yielding an inclination-corrected Eocene sedimentary mean direction of Ds = 158.9°, Is = -59.7° (n = 76, k = 20.8, α_{95} = 4.5°).

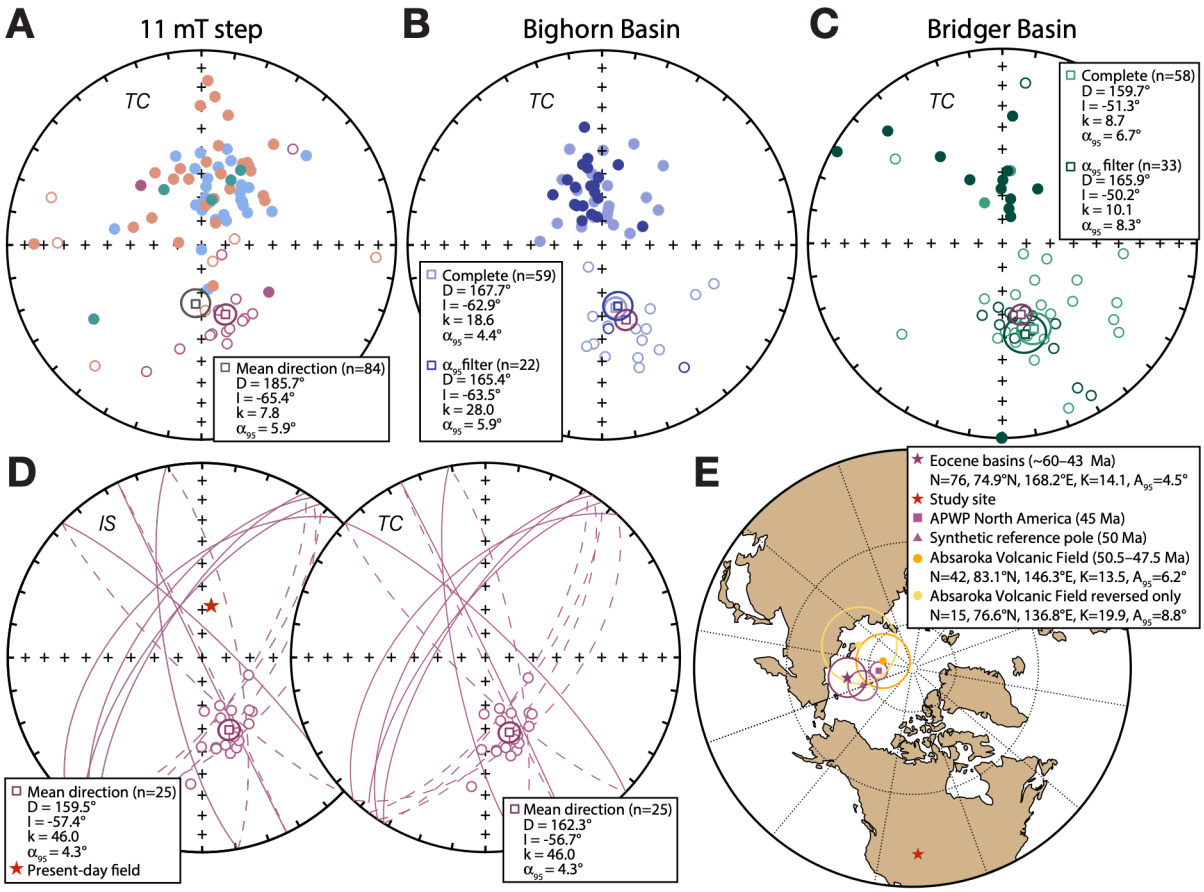

Figure 6. Stereographic projections in tilt-corrected (TC) coordinates of **(A)** directions from the 11 mT demagnetization step from the Wind River Basin (this study, excluding lightning struck samples); colors correspond to the four formations as shown in Figure 4. **(B)** Eocene directions from the Bighorn Basin (Clyde et al., 2007) without filters (light blue) and with a filter of site directions with $\alpha_{95} \leq 20°$ (dark blue), and **(C)** Class I Eocene directions from the Bridger Basin (Tsukui et al., 2025) without filters (light green) and with filter (dark green). The number of directions (n), declination (D), inclination (I), the Fisher (1953) precision parameter (k), and radius of 95% confidence (α_{95}) are provided. **(D)** Stereographic projections of best-fit and great circle directions from the Wagon Bed Formation in in-situ (IS) and TC coordinates. The mean direction is also plotted in purple in Figures 6A–C for comparison. **(E)** Orthographic projection of the paleomagnetic pole of the Wind River Basin (this study), the 45 Ma pole from the North American Apparent Polar Wander Path (APWP) (Gallo et al., 2023), the 50 Ma synthetic reference pole of North America (Besse and Courtillot, 2002), and two poles from the Eocene Absaroka Volcanic Field: one based on all 42 sites and one based on the 15 sites with reversed polarities (Harlan and Morgan, 2010).

4.4.5 Eocene paleomagnetic poles

We converted the directions to virtual geomagnetic poles (VGPs) and calculated an average Eocene (ca. 46.2–43.4 Ma) sedimentary paleomagnetic pole (N = 76, 74.9°N, 168.2°E, K = 14.1, A_{95} = 4.5°; Figure 6E). The nearest Eocene volcanic paleopole is from

the Absaroka Volcanic Field (50.5–47.5 Ma; Harlan and Morgan, 2010) (Figure 1A). These data pass the parametric bootstrap reversal test (Tauxe, 2010) and the SVEI test using the THG24 field model (Tauxe et al., 2024). The paleopole from the three sedimentary basins is rotated 11.5°±8.1° counterclockwise with respect to the Absaroka paleopole (Figure 6E) with insignificant latitudinal displacement (-0.3°±6.0°). However, when comparing only the reversed data, the Absaroka mean direction is indistinguishable (within 95% confidence limits; McFadden and Lowes, 1981) from the reversed mean directions of the Bighorn, Bridger, and Wind River basins (Figure S4B). Using only the reversed Absaroka sites (N = 15; Figure 6E), the sedimentary paleopole is neither significantly rotated (5.0°±9.9°) nor displaced (-4.7°±7.7°). This indicates that the discrepancy between the volcanic and sedimentary datasets arises from the normal-polarity Absaroka data, likely biased by an unremoved present-day field component.

We also compared our Eocene sedimentary paleopole with published reference poles (Figure 6E). Relative to the 50 Ma synthetic reference pole for North America (Besse and Courtillot, 2002), our pole shows insignificant rotation (4.1°±6.1°) and displacement (-2.7°±4.4°). Our pole is rotated 10.1°±5.2° counterclockwise relative to the 45 Ma pole from the North American Apparent Polar Wander Path (APWP) of Gallo et al. (2023) with insignificant displacement (0.0°±3.8°). This raises the possibility that the North American APWP may itself be affected by present-day field overprints, producing an apparent rotation. This is a plausible scenario given that the APWP of Gallo et al. (2023) incorporates the data from the Bighorn Basin (Clyde et al., 2007) and the Absaroka Volcanic Field (Harlan and Morgan, 2010).

4.5 Discussion

4.5.1 Origin of rock magnetic variations

The rock magnetic profile of the AHL section depicts low magnetic mineral concentrations (χ and Ms) during the Eocene, a continuous increase during the latest Eocene, and sustained high values into the Miocene (Figures 2 and 4). The low values in the Wagon Bed Formation align with findings from age-equivalent sediments along the southeastern Wind River Range, displaying similarly low χ values ($\sim 10^{-5}$ emu/g $\approx 10^{-7}$ m^3/kg; Clyde et al., 2001). These low values may result from pedogenic processes that dissolved magnetite (Grimley and Arruda, 2007).

Since pedogenesis is influenced by climate, we considered whether climate-driven alteration could explain the magnetic trends. Chamberlain et al. (2012) measured stable isotope records from calcite cement in Cenozoic sediments in the Wind River Basin. They

provided ages for the sediments without explaining how the ages were determined; in some cases, the ascribed formation is inconsistent with the geologic map. Despite this, Chamberlain et al. (2012) found insignificant differences in local climate proxies throughout the Eocene (Figure S8). Global deep-sea oxygen isotope records likewise indicate climate stability during the latest Eocene (Zachos et al., 2001). Regional studies suggest aridification started during the Oligocene or early Miocene (Fan et al., 2014a; Rowley and Fan, 2016). These observations indicate that climate-driven processes were not responsible for the observed increase in magnetic concentration during the late Eocene; instead, a shift in sediment provenance is a more likely cause.

4.5.2 Detrital zircon records

A common method to trace sediment provenance is to analyze detrital zircon age spectra, which helps determine the age of the source rocks. Therefore, we compiled available detrital zircon data from the Wind River Basin (Fan et al., 2011; Malone et al., 2017; Rowley and Fan, 2016), grouped into the three unconformity-bound parts of our section (Figure 7). Despite the limited number of dates (n= 501), several notable patterns emerge.

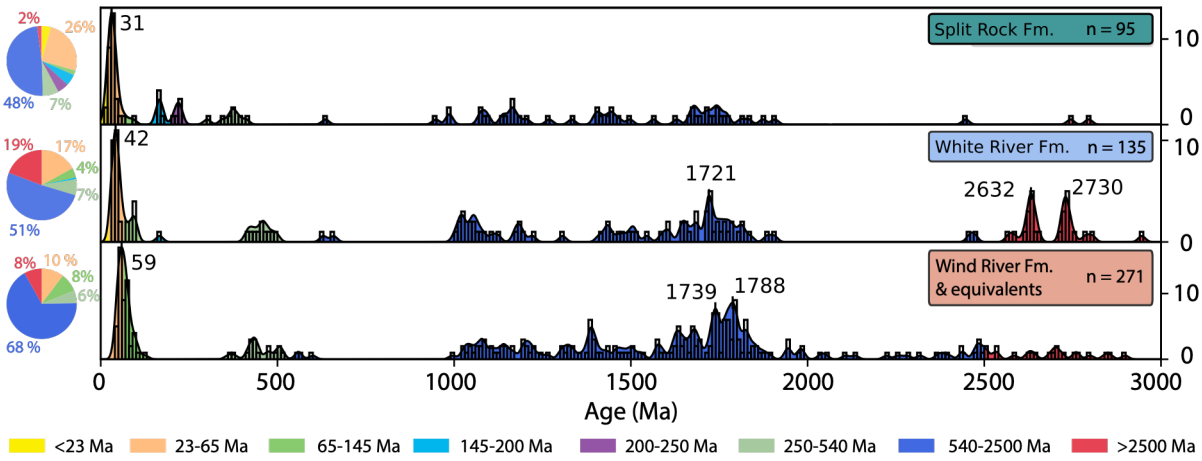

Figure 7. Composite detrital zircon age histograms of samples from the Wind River Basin (Fan et al., 2011; Malone et al., 2017; Rowley and Fan, 2016). Locations of samples shown in Figure 1.

All samples contain a large portion (18–32%) of Cretaceous–Cenozoic zircons (Figure 7). Their peak ages shift upward through the section, from 59 Ma to 31 Ma, likely reflecting input from the Absaroka Volcanic Field and from the ignimbrite flare-up in the Great Basin and the Cascade Arc. The Absaroka Volcanic Field consists largely of calc-alkalic andesite and dacite, lesser amounts of potassic alkalic mafic lava, and minimal rhyodacitic ash-flow tuff associated with the mafic lava (Smedes and Prostka, 1972). The volcanic field is of late Wasatchian, early Bridgerian, and possibly Uintan age (Smedes and Prostka, 1972), with the main eruptions occurring at 51–49 Ma (Harlan, 2006); equivalent in age

to the Wind River and Wagon Bed formations (Figure 2). Vast amounts of dominantly rhyolitic ash-flow tuff erupted from numerous calderas during the ignimbrite flareup in the Great Basin, mainly between 37–22 Ma (Henry and John, 2013). These ages match the young detrital zircon ages in the White River and Split Rock formations (Figure 7). Another contribution of ash to these younger formations likely comes from the distal Cascade Arc, which stretches from northernmost California to Washington and was active by ~45 Ma (du Bray and John, 2011). As the contribution of ash is relatively high in all formations, this cannot explain the observed increase in magnetic mineral concentration. Moreover, both magmatic centers were dominated by rhyolitic eruptions, which are rich in zircon but relatively poor in magnetite.

The youngest zircon grains in each formation closely match their depositional ages: 44.6 Ma for the Wind River Formation, 33.8 Ma for the White River Formation, and 17.3 Ma for the Split Rock Formation (Figure 7 and Table S3), lending confidence to the stratigraphic assignments in Figure 2. In all formations, the dominant zircon population comprises grains aged 2–1 Ga (48–68%), commonly interpreted as recycled material from the Grenville (1.3–1.0 Ga) and Yavapai-Mazatzal (1.8–1.6 Ga) terranes (Fan et al., 2011). Importantly, the White River Formation stands out with significant peaks at ~2.7 and ~2.6 Ga, accounting for 19% of the population. These ages correspond to Archean granitic plutons in the Wind River Range (2.67–2.55 Ga; Frost et al., 2000) and Washakie Range (3.1–2.7 Ga; Fan et al., 2011), respectively. Interestingly, modern river sands near the AHL section have a similar age spectra, where Archean basement contributes ~20% of the total zircon assemblage (Fan et al., 2011), reinforcing the presence of a local Archean source.

4.5.3 Changes in source region

The steady increase in magnetic mineral concentration throughout the White River Formation (Figure 4) may reflect the progressive unroofing of magnetite-rich basement rocks. Similar increases in magnetic mineral content have been documented in Asia and attributed to uplift and consequent basement exposure in the nearby mountains (Gilder et al., 2001).

To identify the source of the magnetic material in the White River Formation, we used a geologic map (Figure 1A) in combination with an aeromagnetic map (Figure 1B). High-intensity magnetic anomalies correspond to Laramide uplifts: the Wind River Range, Owl Creek Mountains, Bighorn Mountains, and Laramie Mountains, and to a lesser extent, the Washakie Range and Granite Mountains. Other, long-wavelength features can most likely be attributed to basement rocks lying below Paleogene–Neogene sediments. The nearest, high-intensity magnetic source is the Archean core of the Wind River Range. Combined

with the influx of ~2.7–2.6 Ga detrital zircons, we think the Wind River Range is the primary source of magnetic minerals in the White River Formation. This implies that significant exposure of magnetite-rich basement began in the late Eocene.

4.5.4 Two-stage uplift of the Wind River Range

Understanding the patterns of uplift and erosion in the Wind River Range and consequent sedimentation in the Wind River Basin is key to understanding our observations. Sedimentation rate calculations based on our measured thicknesses (Figure 4) and the minimum and maximum age constraints (Figure 2) provide a framework for our interpretation (Figure 8).

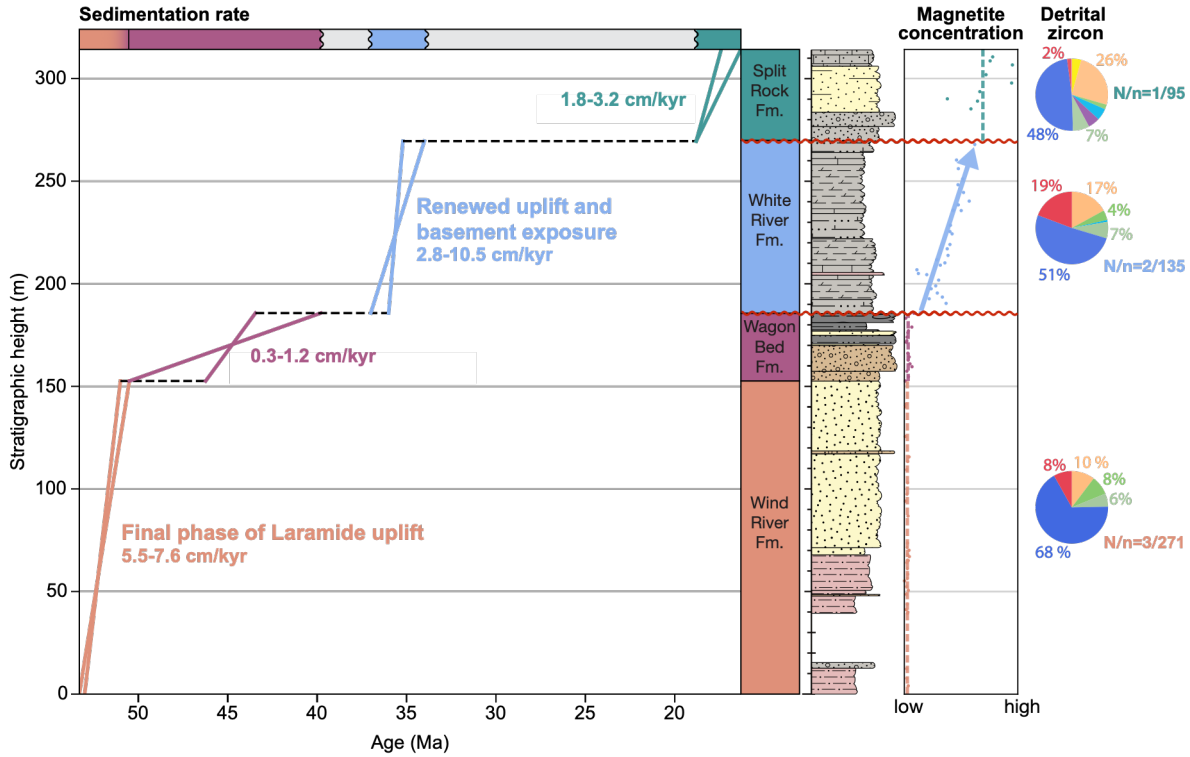

Figure 8. Proposed evolution of the Wind River Range. Minimum and maximum sedimentation rates for the four formations in the Abandoned Highway Lander (AHL) section, calculated by dividing our measured stratigraphic thickness by the minimum and maximum age constraints for each formation from Figure 2. On the right side, magnetite concentration and detrital zircon trends are displayed; legend to the pie chart in Figure 7, and N/n = number of samples/number of zircon ages.

The early Eocene Wind River Formation had a sedimentation rate of 5.5-7.6 cm/kyr (Figure 8). Stable isotope data from paleosol and fluvial cement carbonates suggest that the local relief between the Wind River Range and the basin floor was 2.3±0.8 km during that time (Fan et al., 2011). This is consistent with enhanced erosion and voluminous sediment delivery into the basin (Lillegraven and Ostresh, 1988), supported by

thermochronological evidence for uplift continuing until ~50 Ma (Caylor et al., 2023; Cerveny and Steidtmann, 1993; Peyton et al., 2012; Stevens et al., 2016). Though granite clasts in the formation suggest some basement exposure (Carroll et al., 2006; Fan et al., 2011), the scarcity of >2.5 Ga zircons and low magnetite content imply a limited contribution of basement materials.

In contrast, the middle Eocene Wagon Bed Formation accumulated at a much slower rate (0.3-1.2 cm/kyr; Figure 8). It was deposited on poorly drained lowlands, broad flood plains, and in lakes (Carroll et al., 2006; Lillegraven and Ostresh, 1988; Van Houten, 1964). Volcanic clasts from the Absaroka Volcanic Field found in the age-equivalent Bridger Formation south of the Wind River Range further support that the range was not a prominent topographic high in the middle Eocene (Steidtmann and Middleton, 1986). This matches the regional pattern, where the middle Eocene was recognized as an extended period of tectonic quiescence at the end of the Laramide era (Galloway et al., 2011).

A pronounced erosional surface separates the Wagon Bed and White River formations (Figure 8). This unconformity is regionally extensive, marking a major hiatus during the late Uintan–Duchesnian across the central and southern Rocky Mountains (Cather et al., 2012; Dickinson et al., 1988; Epis and Chapin, 1975; Lillegraven, 1993). Lithospheric rebound following the end of Laramide deformation has been proposed as a driver of this erosional event (Cather et al., 2012; Fan et al., 2014a; 2014b).

Renewed uplift and accelerated sedimentation resumed in the latest Eocene, as recorded in the White River Formation (2.8-10.5 cm/kyr; Figure 8). Although thermochronological data do not clearly resolve a new uplift pulse, the magnetic mineral concentration, sedimentation rate, and zircon age spectra together indicate significant uplift and consequent basement exposure of the Wind River Range at ~37–34 Ma. Paleobotanical paleoaltimetry studies and stable isotope data from mammal teeth confirm that kilometer-scale relief was present during this time (Barton and Fricke, 2006; Cather et al., 2012). Moreover, stable and clumped-isotope paleoaltimetry indicate that the central Rocky Mountains gained much of their present elevation during the late Eocene (Fan et al., 2011; 2014a; 2014b). Sedimentary onlap of the White River Formation onto mountain flanks (Love, 1978) and its deposition in large valleys reaching into the Precambrian cores of the mountain ranges (Evanoff, 1990) further illustrate substantial relief. Fault reactivation in nearby ranges such as the Bighorn Mountains around 37–34 Ma (Beaudoin et al., 2018) adds support for continued activity, coinciding with broader patterns of thermally driven uplift and consequent erosional exhumation of old mountain belts across the continent (Galloway et al., 2011).

An extended hiatus from the Oligocene–early Miocene follows (Figure 8), matching regional unconformities and paleosurfaces across the central Rocky Mountains (Cather et al., 2012). Its onset coincides with the transition from global greenhouse to icehouse climate around the Eocene–Oligocene boundary (Zachos et al., 2001), and the onset of a gradual drying period in the central Rocky Mountains based on hydrogen isotope data from volcanic glass (35–5 Ma, Fan et al., 2014a). The combined effect of global cooling and renewed uplift of the central Rocky Mountains during the late Eocene—creating a rain shadow effect—may have caused regional drying (Rowley and Fan, 2016) and an influx of eolian material that covered all but the highest peaks of the Laramide ranges (Fan et al., 2015; Rowley and Fan, 2016), potentially resetting AFT systems (Caylor et al., 2023).

Deposition resumed in the early Miocene with the Split Rock Formation, characterized by high magnetic mineral concentrations and low sedimentation rates (1.8-3.2 cm/kyr; Figure 8), suggesting continued erosion of basement rocks in the Wind River Range. The composition of the age-equivalent South Pass Formation on the southern edge of the range confirms erosion of Precambrian rocks (Steidtmann and Middleton, 1986; Sutherland and Hausel, 2006), which contradicts hypotheses that the Laramide ranges were almost completely covered by eolian deposits (Caylor et al., 2023; Rowley and Fan, 2016). Limited zircon data (Figure 7) do not clarify whether the Split Rock Formation represents a remnant of this hypothesized eolian cover. Nonetheless, the persistence of magnetic material suggests that the core of the Wind River Range remained at least partially exposed during the Miocene.

Overall, the AHL section in the Wind River Basin records the final stage of Laramide uplift of the Wind River Range in the early Eocene, a period of low relief in the middle Eocene, renewed uplift and basement exposure around ~37–34 Ma, and continued erosion of the range in the early Miocene.

4.5.5 Post-Laramide uplift mechanism

No known tectonic event adequately explains renewed uplift in the latest Eocene. The absence of folding of the Cenozoic sediments in the Wind River Basin (Figure S1) and the lack of rotation between the Wind River, Bridger, and Bighorn basins (Figure S4B) argue against horizontal tectonics, which often has a shear component, as a driving mechanism for late Eocene uplift. It is possible that this phase was driven by dynamic topography, which lacks significant horizontal shear, potentially from lithospheric rebound after the Laramide orogeny (Cather et al., 2012; Fan et al., 2014a; 2014b; Hall and Chase, 1989; Steidtmann et al., 1989) or the early influence of the Yellowstone mantle plume. The Wind River Basin, situated ~800 km from the plume's eruption center in central Oregon, lies at

the outer edge of the plume's dynamic influence (Friedrich et al., 2018). Dynamic uplift related to a deep mantle plume typically precedes surface volcanism by ~20 Myr (Vilacís et al., 2024) and affects regions on the order of ~1000 km in diameter (Friedrich et al., 2018). The uplifted region decreases in diameter as the plume rises through the mantle, therefore only potentially affecting the Wind River Basin early on. This mechanism is broadly consistent with the spatial and temporal scales of the short-lived renewed uplift phase inferred from our data and may have modified the regional stress field, thereby facilitating the reactivation of the Wind River thrust and promoting basement exposure in the Wind River Range.

4.6 Conclusions

A gradual increase in magnetic mineral concentration coupled with increased sedimentation rates in the Wind River Basin during the latest Eocene suggests intensified erosion and basement exposure of the neighboring Wind River Range. Published detrital zircon records support this interpretation, showing a shift toward an Archean source, particularly from the ~2.6 and ~2.7 Ga basement cores of the nearby Wind River Range. Together, these findings suggest a renewed uplift and unroofing of the range around ~37–34 Ma.

As this phase of uplift does not coincide with known tectonic events, we tentatively suggest it may be caused by lithospheric rebound following Laramide deformation or the rise of the Yellowstone mantle plume. This may have led to changes in the vertical regional stress field, causing reactivation of the Wind River thrust and a renewed phase of uplift in the Wind River Range. This provides a new perspective on post-Laramide landscape evolution in the central Rocky Mountains.

5

The emergence of the Olympic Mountains in western Washington

Dieke Gerritsen, Stuart A. Gilder, and Michael R. Wack

In progress

The Cenozoic strata of the Grays Harbor Basin in western Washington preserve a complex depositional and tectonic history related to the accretion and uplift of the Siletzia terrane. We collected 668 samples from Oligocene to middle Miocene sediments across four main locations, including an extended section along the Canyon River (ABY). In this chapter, we present preliminary rock magnetic and paleomagnetic data to investigate changes in sediment provenance and tectonic rotations. Rock magnetic data from the ABY section reflect a progressive increase in magnetic mineral concentration up-section, accompanied by an increase in grain size. This trend possibly reflects a provenance shift associated with the uplift and subaerial exposure of the magnetite-rich basalts of the Olympic Mountains, part of the Siletzia terrane, during the early Miocene. Regional comparisons suggest differing uplift histories across the region, with the Willapa Hills potentially rising earlier. Paleomagnetic results are dominated by present-day field overprints. Future experiments using refined demagnetization protocols offer potential for recovering the primary remanence and for constraining regional tectonic rotations and the timing of Siletzia terrane exhumation.

5.1 Introduction

The Pacific Northwest has experienced a complex tectonic history shaped by terrane accretion, magmatism, and mountain building throughout the Cenozoic. One of the most significant events in this evolution was the accretion of the Siletzia terrane, an oceanic plateau composed of thick accumulations of tholeiitic and alkalic basalt. Although Siletzia was accreted to the North American continent around 50 Ma (Wells et al., 2014), subaerial exposure of the terrane occurred much later. Constraining the timing and consequences of this exhumation is key to understanding the geologic development of coastal Washington.

Siletzia formed offshore and is proposed to be a large igneous province associated with early activity of the Yellowstone plume (Duncan, 1982; Murphy et al., 2003). It erupted rapidly between ~56–49 Ma, producing voluminous basalts with isotopic signatures similar to the early Columbia River Basalt Group (CRBG) (Pyle et al., 2009). The total volume of erupted material is estimated to be 8–12 times greater than that of the CRBG (Wells et al., 2014). The Yellowstone hotspot then entered into a new Farallon trench that formed west of Siletzia ~48–45 Ma, thus transitioning from the oceanic plate to the North American plate (Camp and Wolff, 2025). Hotspot-derived subaerial volcanism was subsequently established on the accreted terrane between 42–34 Ma (Wells et al., 2014). The plume material was consequently trapped beneath the subducting Farallon slab from ~35–20 Ma, where a secondary plume head was produced by continued flux from the plume. This much smaller volume then began around 17 Ma as the CRBG (Cahoon et al., 2020).

The Olympic Mountains in northwestern Washington, largely composed of Siletzian basalt, represent a key region in which to investigate the subaerial exposure of the Siletzia terrane. Thermochronology, particularly zircon and apatite fission-track dating, suggests that subaerial exposure began around 18 Ma (Batt et al., 2001; Brandon et al., 1998). The rise of the Olympic Mountains likely influenced regional drainage patterns and sediment pathways, but the extent and timing of this reorganization remain poorly understood. Tracking this provenance change is essential for reconstructing the Cenozoic paleogeography and tectonic history of western Washington.

A promising way to address this question is through analysis of rock magnetic and paleomagnetic signatures preserved in the Cenozoic sedimentary record. Changes in magnetic mineral concentration, grain size, and mineralogy can signal shifts in source lithology and erosional regimes, while paleomagnetic data may provide constraints on tectonic block rotations.

In this chapter, we present preliminary rock magnetic and paleomagnetic results from samples collected from Oligocene to middle Miocene sediments in the Grays Harbor Basin in western Washington, including an extended section along the Canyon River. Our aim was to investigate how sediment sources and magnetic mineralogy evolved in response to the uplift of the Olympic Mountains, and to assess the potential for paleomagnetic constraints on regional tectonic rotations.

5.2 Geologic setting

The studied area is located near the coast of Washington, west of the Cascade Range (Figure 1A). The area forms a structural and topographic low between the Olympic Mountains to the north, Black Hills and Doty Hills to the east, and Willapa Hills to the south (Figure 1B), which is referred to as the Grays Harbor Basin. The Cenozoic stratigraphy of the Grays Harbor Basin is separated into five depositional sequences, separated by regionally significant unconformities (Figure 2). The first and second sequence consist of the late Paleocene to middle Eocene Crescent Formation and the middle-late Eocene Cowlitz Formation, respectively (Armentrout, 1987). The latter is separated from the Lincoln Creek Formation by the early late Eocene regional unconformity (Figure 2).

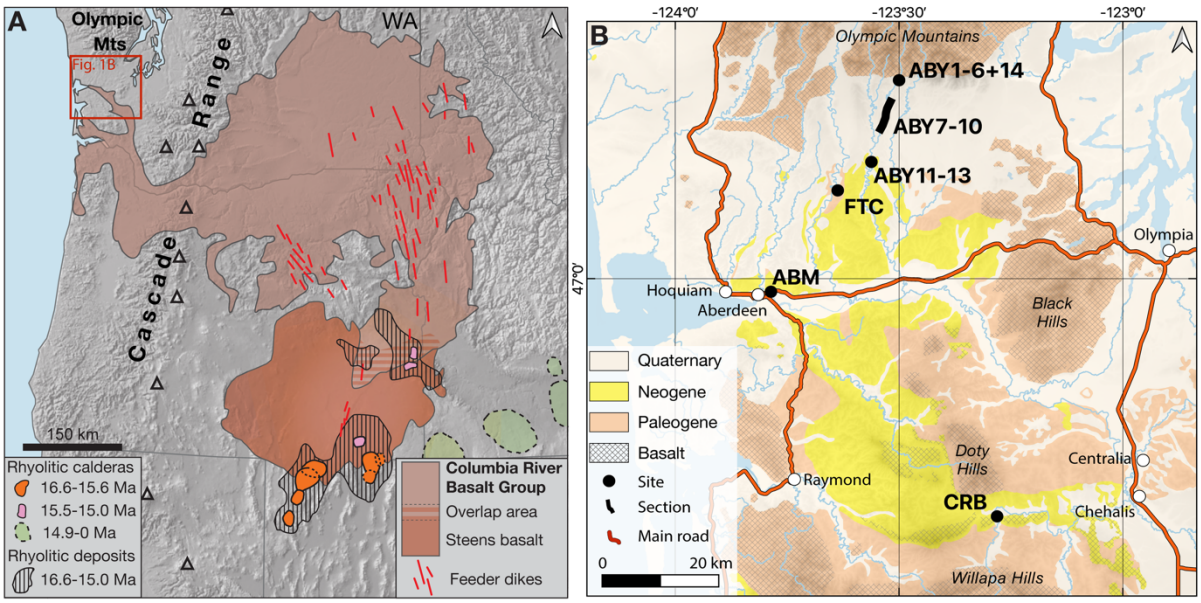

Figure 1. (A) Large scale map of the Columbia River Basalt Group, modified from Coble and Mahood (2012). **(B)** Geologic map of the Grays Harbor Basin in western Washington (Barton et al., 2003).

The Lincoln Creek Formation consists of marine glauconitic basaltic sandstone which grades upward to fine-grained tuffaceous sandstone and siltstone (Armentrout, 1987). It contains molluscan fauna from the Lincoln and Blakely stages of Weaver (1944) and

foraminifera of the Refugian stage of Schenck and Kleinpell (1936) and Zemorrian stage of Kleinpell (1938) (Rau, 1966,1967), making it roughly Oligocene in age (Figure 2). The Lincoln Creek Formation and the Astoria (?) Formation together make up the third sequence. The question mark after Astoria denotes probable correlation with the type Astoria Formation south of the Columbia River in Oregon (Niem and Niem, 1985). From here onwards, we omit the question mark for readability. The Lincoln Creek and Astoria formations are separated by an unconformity in the Centralia-Chehalis area, but the contact is conformable in other areas (Armentrout, 1987). The Astoria Formation consists of dark- to medium-gray micaceous and carbonaceous fine-grained sandstone (Armentrout, 1987). Molluscan fauna referred to Newportian or Pillarian Stages of (Addicott, 1976). Foraminifera from the formation relate well with those of the Saucesian stage of Kleinpell (1938) (Rau, 1966), also including the Relizian and possibly Luisian stages in for example the Wynoochee Valley (Rau, 1967), resulting in an early Miocene age (Figure 2). Overall, the third sequence contains a transgressive-regressive cycle in which nearshore and nonmarine basin-margin facies along the eastern side of Washington grade westward into deep shelf-margin basin facies (Figure 2). The third sequence is separated from the fourth sequence by the middle Miocene regional unconformity.

The base of the fourth sequence contains a tholeiitic basalt correlated with the Grande Ronde Basalt of the CRBG (Figure 1). It erupted in eastern and central Washington and flowed westward. A single flow extended northward from the Columbia River into the Centralia area and then westward, where it became interbedded with marine units along the coastline (Armentrout, 1987). This flow entered the sea and formed pillows and breccias near the Doty Hills (Pease and Hoover, 1957). It has been correlated to the Sentinel Bluffs member (Reidel, 2005), which was deposited in the normal chron N2 of the Grande Ronde Basalt sequence (Reidel and Tolan, 2013). This member has an $^{40}Ar/^{39}Ar$ plateau age of 15.48±0.22 Ma (Barry et al., 2010). The basalt is in unconformable contact with the overlying Montesano Formation (Figure 2), which consists of interbedded fluvial, lacustrine, brackish-water, and shallow-marine deposits (Armentrout, 1987). Montesano foraminifers are not entirely definitive, but considered within the Mohnian and Delmontian stages of Kleinpell (1938) (Rau, 1967). The lower Montesano Formation is characterized by a deepening and marine transgression, followed by rapid progradation of fluvial sediments having an eastern source (Fowler, 1965). The topmost sequence of the Cenozoic stratigraphy of western Washington consists of Pleistocene alluvium.

The Cenozoic sediments of the Grays Harbor Basin have been previously studied using biostratigraphy in conjunction with magnetostratigraphy. Notable studies include a 130

m section (n = 23) and a 60 m section (n = 8) of the Astoria Formation (Prothero et al., 2001); a combined 250 m section (n = 8) of the Lincoln Creek Formation and 100 m (n = 4) of the Astoria Formation (Prothero et al., 2008); and a 610 m section (n = 20) of the Montesano Formation (Prothero and Lau, 2001). The most extensive magnetostratigraphic record comes from a 2900 m section (n = 92) of the Lincoln Creek and Astoria formations along the Canyon River (Prothero and Armentrout, 1985); however, neither demagnetization data nor rock magnetic data from this study have been published.

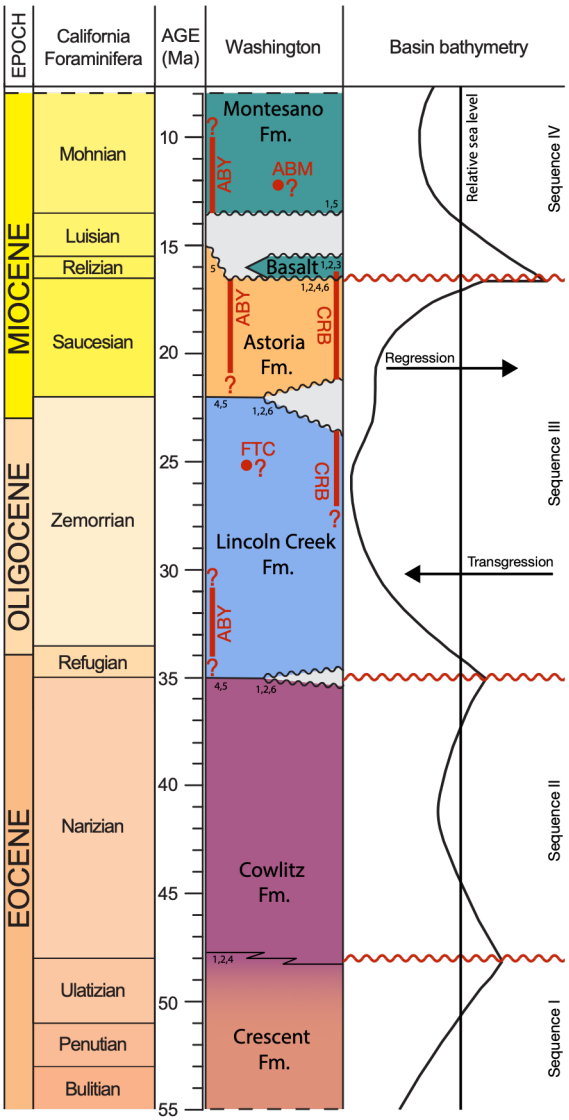

Figure 2. Generalized chronostratigraphic chart of western Washington with the span of the sampled sections indicated in red. California foraminifera stages from Rohde (2005) and basin bathymetry based on lithofacies analysis and molluscan faunas from Armentrout (1987). References: [1]Armentrout et al. (1983) [2]Armentrout (1987) [3]Pease and Hoover (1957) [4]Rau (1966) [5]Rau (1967) [6]Wells and Sawlan (2014).

5.3 Methods

We collected samples from four locations in western Washington during a field campaign in 2024 (Figure 1B). The Aberdeen (ABY) section netted 516 samples along five subsections and six sites along the Canyon River, and three sites in the West Fork of the Satsop River (Figure 3). This section partly overlaps with the Canyon River section of Prothero and Armentrout (1985). The bedding in most of the ABY section is dipping towards the south, so we combined the five subsections (ABY7–ABY10 and ABY14) and the six sites (ABY1–ABY6) of this part into one composite section of ~2760 meters (Figures S1 and 3 and Table S1). The distance between samples within each subsection was manually measured. GPS measurements in combination with bedding attitudes were used to calculate the stratigraphic distance between subsections. The other three sites (ABY11–ABY13) were regarded as separate sites, because of their northeastward dipping bedding and large distance to the rest of the section.

The Chehalis River Basalt (CRB) section contains 100 samples, distributed over four subsections and three sites along the Chehalis River (Figure S2). The Fallen Tree Creek (FTC) location has 35 samples distributed over four sites in Carter Creek, which flows into the Wynoochee River (Figure S3). The Aberdeen Montesano (ABM) location is next to the U.S. highway 12 in Aberdeen and consists of three sites with a total of 17 samples (Figure S4).

For sections, we collected samples at roughly 2 m intervals, obtaining two oriented cores per horizon. For sites, we collected around eight samples from different horizons. We used an electric powered drill to collect oriented, one inch-diameter core rock samples and a hand sampler to collect oriented soft sediments. Our focus was on fine-grained materials, including silt- and fine sandstones. We corrected all magnetic compass readings with the average declination anomaly (16.2±1.6°) from 44 Sun compass readings, which agrees well with 15.3° predicted by the International Geomagnetic Reference Field (2024).

We analyzed the rock magnetic properties of bulk samples to assess variations in magnetic mineral composition and grain size across the sections. Low-field frequency (465 Hz) magnetic susceptibility (χ) was determined using a Bartington MS2 meter. To measure backfield curves, which define the coercivity of remanence (Bcr), and hysteresis loops, we used a LakeShore MicroMag 3900 vibrating sample magnetometer (VSM). HystLab software (Paterson et al., 2018) was used to interpret the hysteresis loops, enabling the calculation of coercive force (Bc), saturation magnetization (Ms), saturation remanent magnetization (Mrs), the hysteresis shape parameter (σ_{hys}) (Fabian, 2003), and high-field susceptibility (χ_{HF}).

A large set of samples was analyzed to construct a preliminary dataset. Susceptibility was measured for 11 out of 17 samples from ABM, 414/516 from ABY, 88/100 from CRB, and 46/35 (including sister samples) from FTC. VSM measurements were conducted on 13/17 ABM samples, 143/516 ABY samples, 23/100 CRB samples, and 3/35 FTC samples. The remaining samples are available for future analysis.

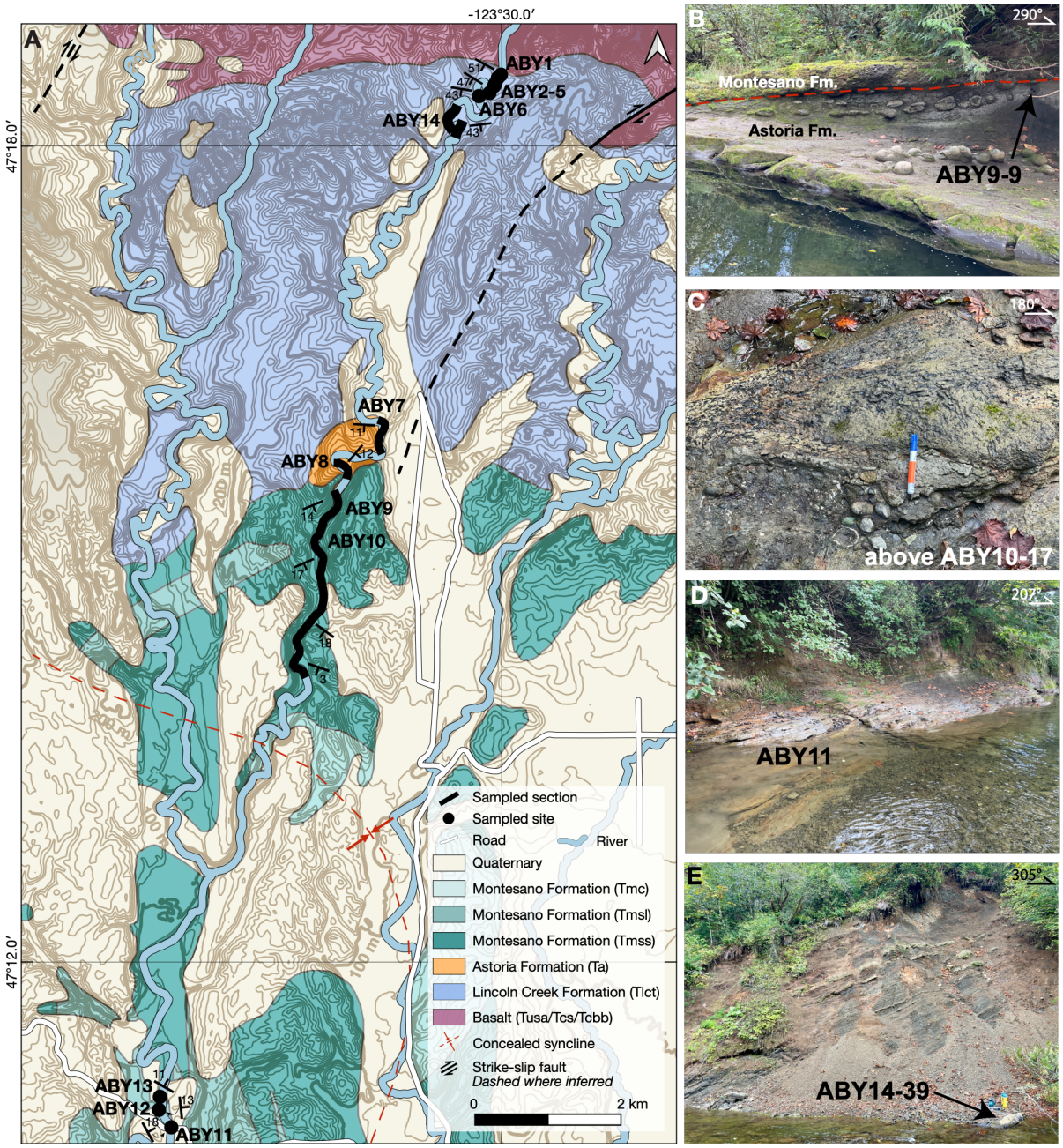

Figure 3. (A) Geologic map of the ABY section along the West Fork and Canyon River tributaries of the Satsop River (Rau, 1966; Tabor and Cady, 1978). Shaded relief map from NOAA (2022). Examples of field photographs: **(B)** Contact between Astoria Formation and Montesano Formation in ABY9. **(C)** Storm bed with shells, pebbles, and fossilized wood in ABY10. **(D)** Overview photo of site ABY11. **(E)** Photo of the ABY14 subsection.

We performed alternating field (AF) demagnetization with 11 steps up to 90 mT and magnetic moment measurements using an automated system (SushiBar) integrated with a 2G Enterprises three-axis superconducting magnetometer (Wack and Gilder, 2012). A total of 292 specimens underwent stepwise AF demagnetization. Thermal demagnetization was carried out on 268 specimens using an ASC Scientific TD-48 oven with 18 progressive heating steps up to 680°C. The remanent magnetization directions were analyzed through principal component analysis (Kirschvink, 1980) using PaleoMac software (Cogné, 2003).

5.4 Results

5.4.1 Rock magnetic results

The ABY section can be subdivided into three unconformity-bound formations based on their rock magnetic parameters (Figure 4). The most pronounced difference between the formations lies in the magnetic mineral concentration, where both χ and Ms increase significantly up-section: χ increases from $1.08\pm0.29\times10^{-7}$ m^3/kg to $1.58\pm9.93\times10^{-7}$ m^3/kg and then to $1.69\pm1.15\times10^{-6}$ m^3/kg and Ms increases from $1.92\pm2.42\times10^{-3}$ Am^2/kg to $0.14\pm1.35\times10^{-1}$ Am^2/kg and finally to $1.72\pm1.93\times10^{-1}$ Am^2/kg. Magnetite concentration thus increases up-section: χ increases with a factor 16 and Ms with a factor 89.

Magnetic grain size generally increases up-section, though it remains within the uncertainty bounds, as reflected by a decrease in Mrs/Ms from 0.24±0.08 to 0.19±0.08 and then to 0.12±0.02. The median Bc also decreases up-section from 12.60±1.71 mT to 11.25±7.48 mT to 7.45±1.54 mT, which may reflect the decrease in magnetic grain size. The σ_{hys} goes from slightly positive in the Lincoln Creek Formation (0.16±0.16), to around zero in the Astoria (-0.03±0.30), and to negative in the Montesano Formation (-0.36±0.17). This reveals the presence of potbellied loops in the Montesano Formation, indicative of larger grain sizes, consistent with the lower values of Mrs/Ms and Bc in this part of the section. The χ_{HF} is variable with $8.20\pm1.31\times10^{-8}$ m^3/kg in the Lincoln Creek Formation, slightly higher values of $1.45\pm1.06\times10^{-7}$ m^3/kg in the Astoria Formation, suggesting more paramagnetic material, and a return to $8.06\pm9.27\times10^{-8}$ m^3/kg in the Montesano Formation.

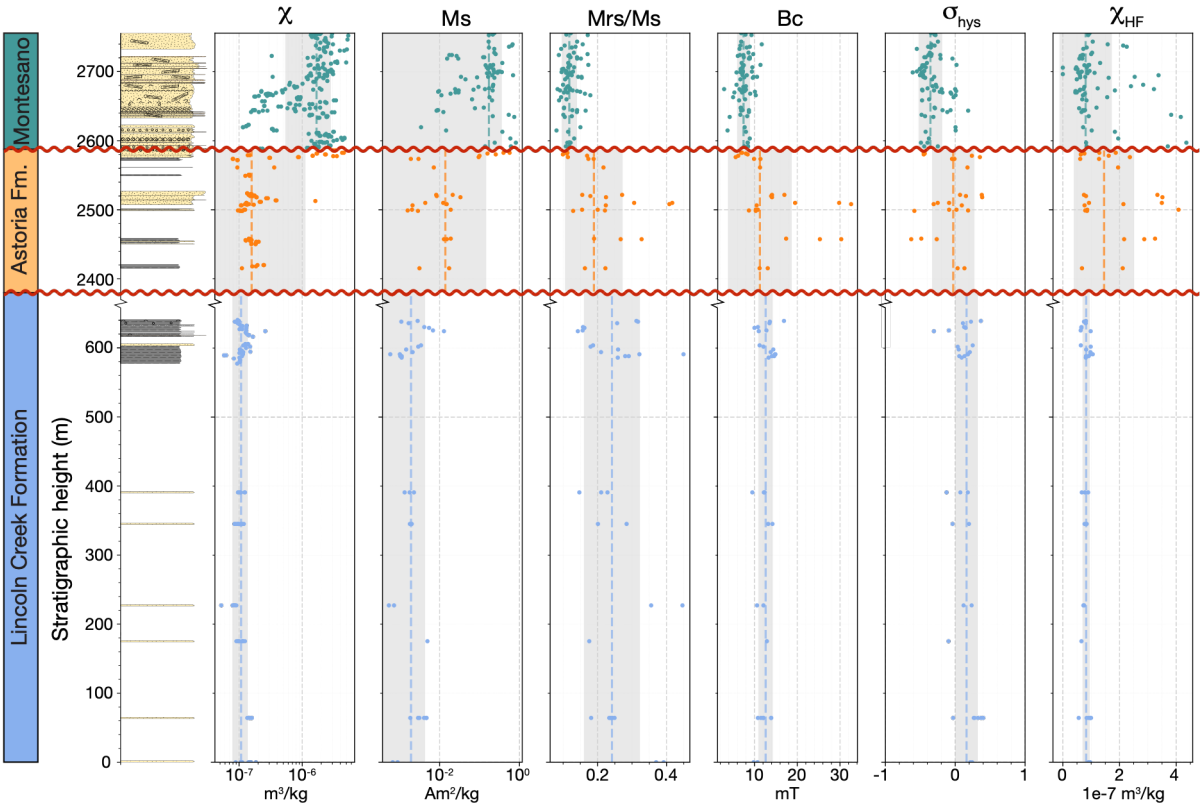

Figure 4. Rock magnetic properties of the ABY section. From left to right: magnetic susceptibility (χ), saturation magnetization (Ms), saturation remanent magnetization (Mrs) divided by Ms, coercive force (Bc), hysteresis shape parameter (σ_{hys}), and high-field susceptibility (χ_{HF}). Dashed lines indicate median values and shaded regions 1σ uncertainty. Vertical axis was cut out between 650 and 2380 m.

When integrating rock magnetic data across all localities, it becomes clear that differences occur between formations from the different locations (Figure 5 and Table S2). For example, the Lincoln Creek and Astoria formations in the CRB section contain considerably higher magnetic mineral concentrations than the same formations in the ABY section (Figure 5A). This suggests that the formations are not compositionally uniform across the study area.

The magnetic minerals span a wide range of grain sizes and mixtures of those (Figure 5C). Only a few samples lie directly on the mixing line, such as the one in Figure 5D, containing approximately 70% multidomain grains (Figure 5C). Samples of both ends of the spectrum are present, with samples displaying wide hysteresis loops reflecting single domain grains (Figure 5E) or very narrow hysteresis loops indicating multidomain grains (Figure 5F). Mixtures of coercivities or grain sizes are evidenced by the presence of wasp-waisted hysteresis loops (Figure 5G). In general, low-Ti titanomagnetite seems to be the dominant magnetic mineral in the samples.

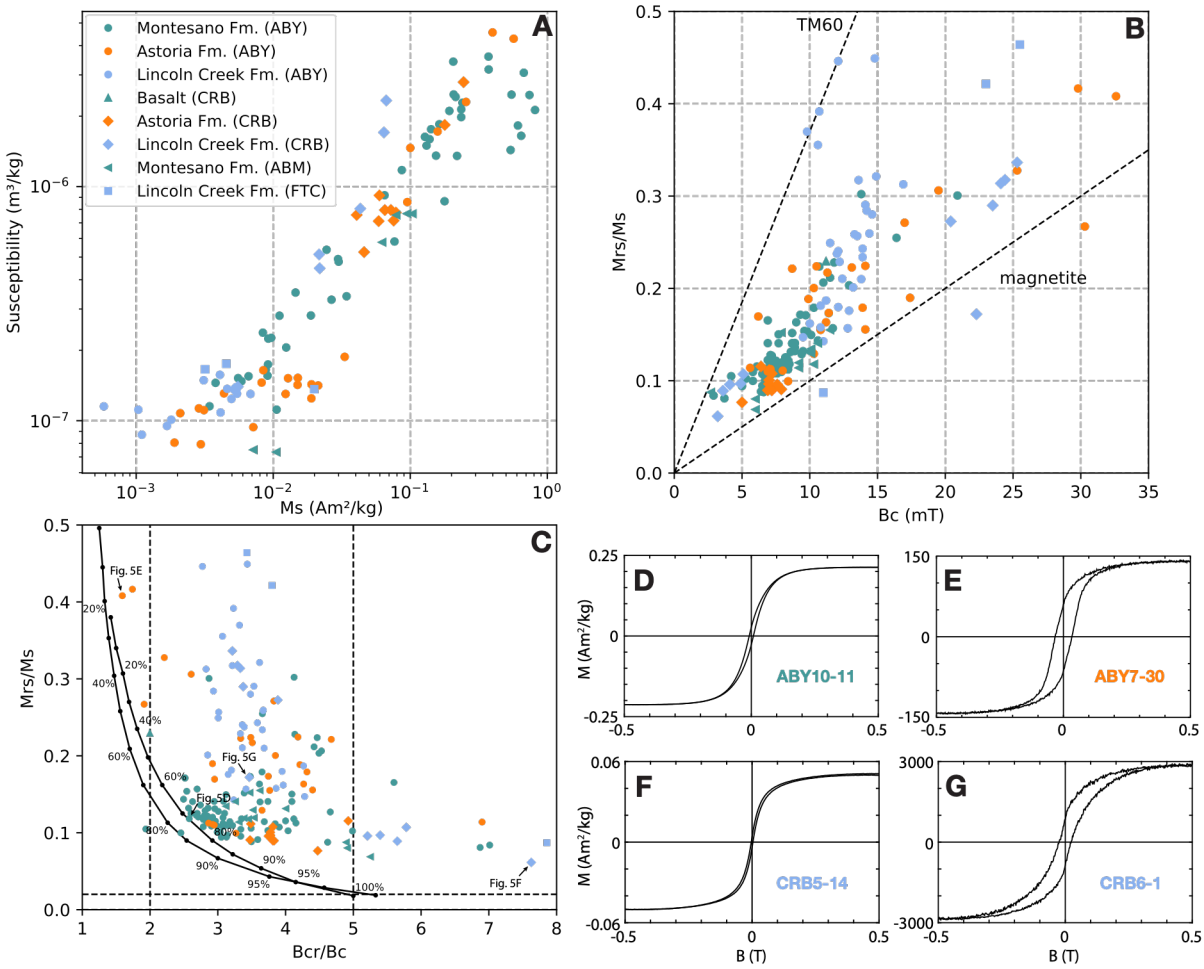

Figure 5. Rock magnetic data of all analyzed samples. **(A)** Susceptibility versus Ms. **(B)** Néel diagram (Néel, 1955) with the trend lines for magnetite and titanomagnetite with x = 0.6 (TM60) of Wang and Van der Voo (2004). **(C)** Day diagram (Day et al., 1977) with the SD + MD mixing curves of Dunlop (2002). **(D–G)** Examples of hysteresis loops.

5.4.2 Paleomagnetic results

The paleomagnetic results of this study are complex. Several samples acquired a gyroremanent magnetization (GRM) during AF demagnetization—as indicated by a strong increase in magnetization above ~40 mT (e.g., Figure 6B)—overprinting the primary remanence: 10 out of 27 samples from ABY7, 3/9 from ABY8, 8/9 from ABY11-13, and 2/35 from ABY14. GRM effects have typically been observed in sediments containing greigite (Hu et al., 2002). Most samples from the ABY section display stable thermal demagnetization up to ~400°C (e.g., Figure 6A and 6B). In combination with the relatively low Bc values (Figure 4), this behavior is consistent with the presence of medium-Ti titanomagnetite. Many samples begin to alter above 400°C (removed from Figure 6), which is often a sign of greigite, possibly removing the primary signal held by minerals with a Curie temperature. In some samples, stable demagnetization continues up to 600°C, pointing to the presence of pure magnetite.

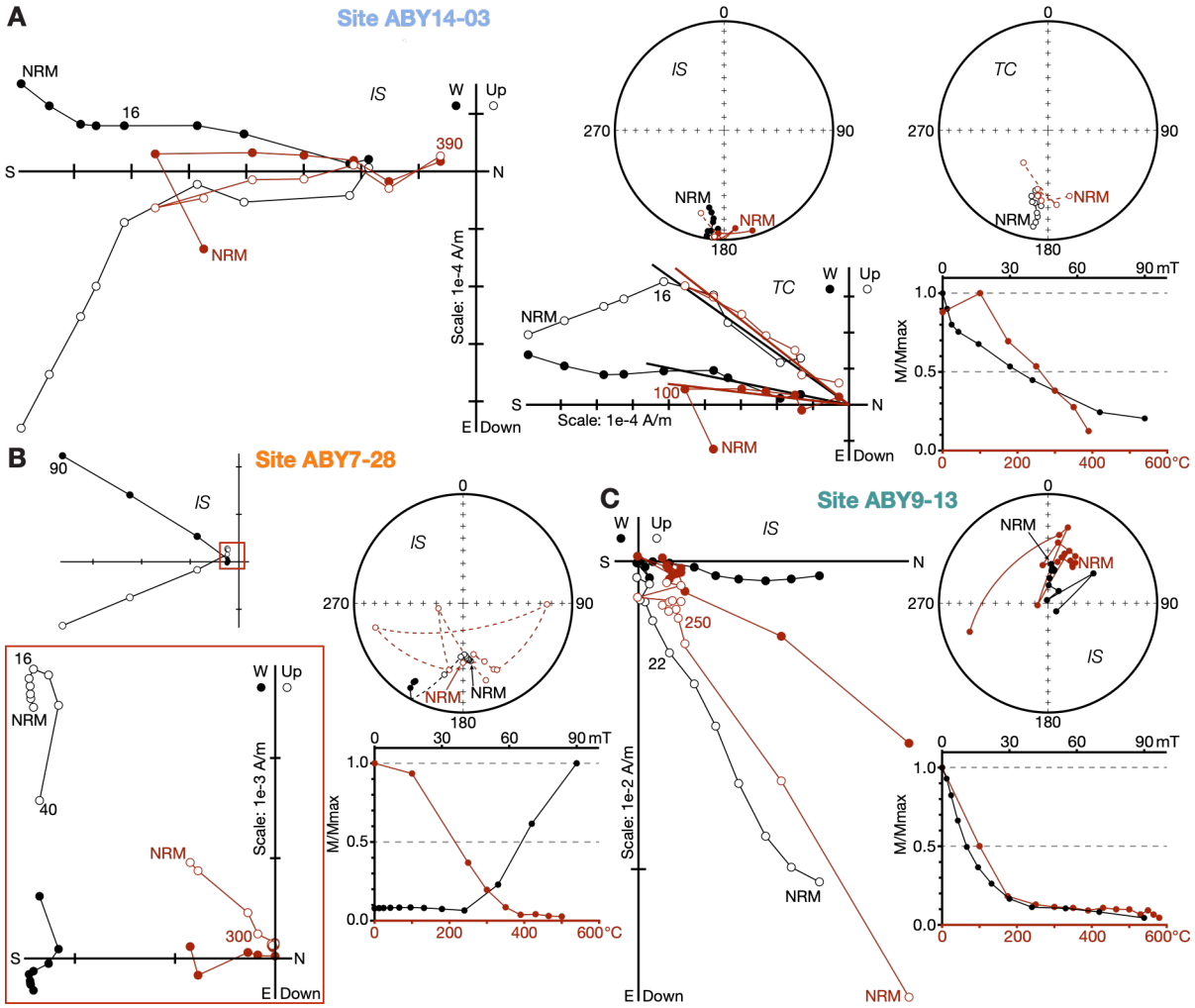

Figure 6. Zijderveld diagrams, stereographic projections, and moment decay diagrams of stepwise AF (black) and thermal (red) demagnetization trajectories for sample pairs from the same horizon in in-situ (IS) and tilt-corrected (TC) coordinates. Examples of **(A)** interpretable data, **(B)** data exhibiting a gyroremanent magnetization (GRM) acquisition after 40 mT, with a zoom-in showing the behavior prior to GRM acquisition, and **(C)** data with a present-day field overprint. Thermal demagnetization data were cut off at the minimum intensity. Colors refer to samples from the different formations: teal = Montesano Formation, orange = Astoria Formation, blue = Lincoln Creek Formation.

Interpreting the paleomagnetic signal is further complicated by the similarity between the Eocene–Miocene and present-day magnetic field directions. This, combined with a generally shallow bedding attitude and a lack of reversed polarity samples, makes it difficult to distinguish the primary signal from a present-day field overprint. For example, the CRB section contains no reversed polarity samples but includes samples that follow great-circle trajectories toward reversed directions (Figure S5). The mean direction (n = 32), however, is indistinguishable from the present-day field direction in in-situ (IS) coordinates. Moreover, the Fisher (1953) precision parameter (k) of the mean direction slightly decreases (k = 27.3 to k = 21.3), and confidence ellipse (α_{95}) slightly increases

(α_{95} = 5.0° to α_{95} = 5.6°) when tilt-corrected (TC). Therefore, these directions cannot be considered primary.

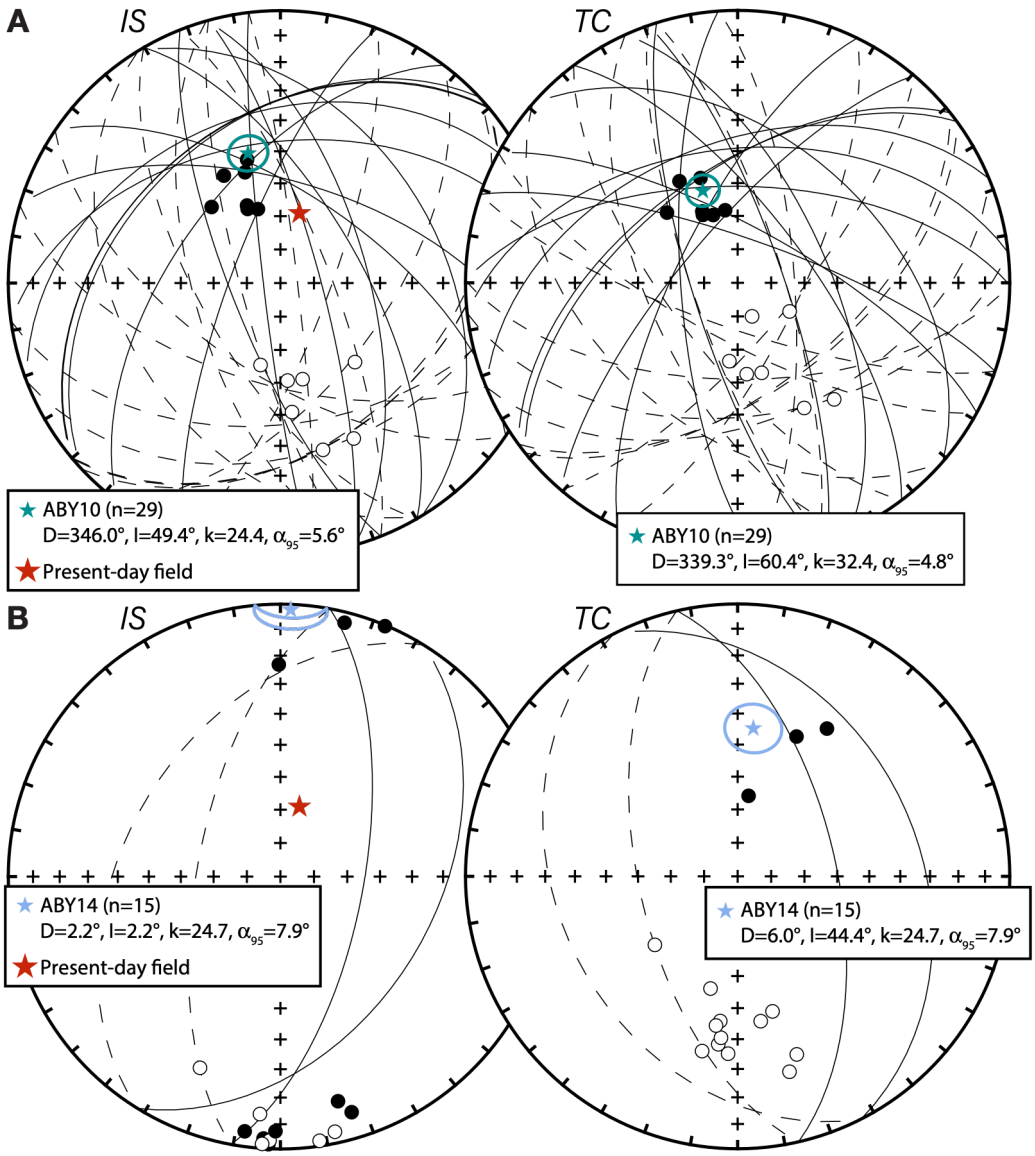

Figure 7. Stereographic projection of the best-fit (points) and great circle (lines) paleomagnetic directions of the **(A)** ABY10 and **(B)** ABY14 subsections in in-situ (IS) and tilt-corrected (TC) coordinates. Closed (open) symbols indicate lower (upper) hemisphere. The mixed mean direction for ABY10 (McFadden and McElhinny, 1988) and the ABY14 Fisher (1953) mean and their Fisher (1953) statistic parameters are displayed.

Indeed, most paleomagnetic results appear to reflect a present-day field overprint (e.g., Figure 6C). For instance, the FTC location (n = 11) shows a textbook overprint signature (Figure S5B): results cluster tightly around the present-day field in IS coordinates (k = 89.4 and α_{95} = 4.9°) and they split between the two limbs of the fold (Figure S3) in TC coordinates (k = 3.9 and α_{95} = 26.6°). The bootstrap fold test (Tauxe and Watson, 1994) on best-fit data (n = 9) confirms this interpretation, with the tightest grouping of vectors

occurring between -4% and -10% of unfolding (95% confidence bounds; Figure S6). These results clearly reflect a post-folding magnetization and therefore cannot be considered primary.

Only two sections contain samples with a clear reversed polarity (e.g., Figure 6A): ABY10 and ABY14 (Figure 7 and Table S2). Best-fit data from ABY10 (n = 14) and ABY14 (n = 15) pass the parametric bootstrap reversal test (Tauxe, 2010) at the 95% confidence level (Figures S7B and S8A). For ABY10, the bootstrap fold test (Tauxe and Watson, 1994) indicates a wide range between 27% and 90% of folding at the 95% confidence bounds (Figure S7A), likely due to the limited variation in bedding attitude within the section. Data cluster slightly better in TC coordinates (k = 20.2 and α_{95} = 5.5°) than in IS coordinates (k = 17.7 and α_{95} = 5.9°). Notably, the present-day field direction lies outside of the 95% confidence ellipse of the mean direction in IS coordinates. The data of ABY14 are not suitable for a fold test, as all samples have the same bedding attitude. Nevertheless, the results indicate a pre-folding magnetization: the shallow inclination in IS coordinates is not expected for Cenozoic North America (Figure 7B). Taken together, these observations provide evidence that the directions of ABY10 and ABY14 are likely primary. The data distributions from both ABY10 (Figure S7C) and ABY14 (Figure S8B) are consistent with the THG24 field model and do not show evidence for inclination shallowing (Tauxe et al., 2024).

When converted to paleomagnetic poles, these directions appear highly unrealistic. The ~12 Ma (ABY10) paleopole (N = 29, 74.1°N, 132.3°E, dp = 5.5°, dm = 7.3°) is rotated 26.8° ± 11.5° counterclockwise and displaced 15.3 ± 9.8° southward with respect to the ~32 Ma (ABY14) paleopole (N = 15, 68.3°N, 41.7°E, dp = 6.2°, dm = 9.9°). The ~12 Ma paleopole is rotated 14.9° ± 10.3° counterclockwise and displaced 6.5° ± 6.1° northward with respect to the 10 Ma Apparent Polar Wander Path (APWP) of North America (Gallo et al., 2023). The ~32Ma paleopole is rotated 18.6° ± 11.5° clockwise and displaced 22.6° ± 8.1° northward with respect to the 35Ma APWP (Gallo et al., 2023). These differences result in unrealistically large displacements of ~1500 km in 20 Myr. Therefore, these results should be reconsidered.

5.5 Discussion and conclusions

5.5.1 Tracking provenance shifts through rock magnetism

The ABY section in the Canyon River is characterized by three unconformity-bounded formations, between which χ and Ms increase, while Bc and the Mrs/Ms ratio decrease (Figure 4). These trends suggest a progressive increase in the concentration of magnetic

minerals with larger grain sizes. The dominant magnetic mineral is likely low- to medium-Ti titanomagnetite, as inferred from the stability of thermal demagnetization up to ~400°C (Figure 6A–B) and supported by hysteresis measurements (Figure 5B). However, the magnetic mineralogy remains only partially constrained. Measuring temperature curves of magnetic extracts would help to refine the mineralogical changes throughout the section.

Despite the magnetic carrier being poorly defined, the progressive up-section increase in magnetic mineral concentration is evident. This trend likely reflects a change in sediment provenance over time. At present, the Canyon River is sourced from the Olympic Mountains to the north, which consist largely of Eocene basalts (Figures 1B and 8A). These basalts, part of the Crescent Formation, are composed of massive flows, pillows, and breccias with a composition characteristic for oceanic basalts, typical of ridge, seamount, or intra-arc basin tholeiite (Tabor and Cady, 1978). These rock types are notably rich in magnetic minerals.

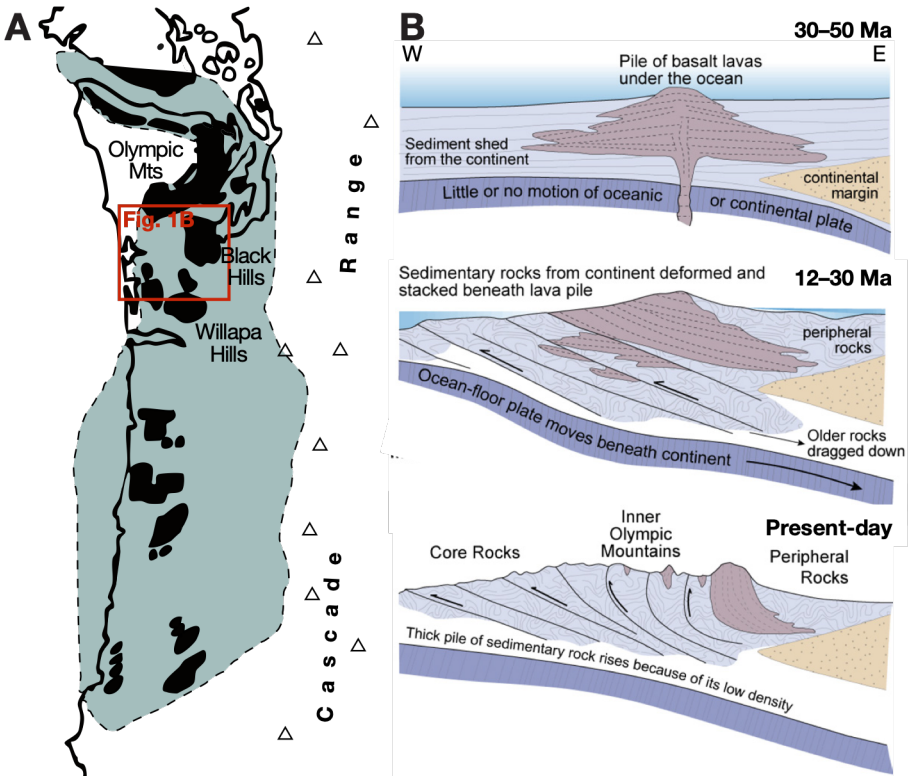

Figure 8. (A) Simplified map showing 63–46 Ma Crescent Formation volcanics and equivalents in black along the Oregon and Washington coast (modified from Armentrout, 1987). Siletzia terrane outlined in green. **(B)** Sketch illustrating the development of the Olympic Mountains (modified from Tabor, 1987 by Washington State Department of Natural Resources).

In the lower part of the section (early Oligocene), magnetic mineral concentrations are relatively low. At that time, sedimentation occurred in a deep marine shelf-margin basin (Armentrout, 1987). The source of these sediments was likely located on the continent,

and the Eocene basalts were still buried beneath sediment (Figure 8B). A major regression during deposition of the Astoria Formation (early Miocene) led to a transition to the more fluvial, lacustrine, and brackish environments of the Montesano Formation during the middle Miocene (Armentrout, 1987). This coincided with the subaerial exposure of the Olympic Mountains at ~18 Ma (Batt et al., 2001; Brandon et al., 1998), containing accreted oceanic basalts of the Siletzia terrane (Figure 8B). The development of the modern Canyon River drainage likely dates to this period, allowing the influx of magnetic material from the Olympic Mountains. This interpretation is supported by petrographic evidence showing that the Montesano Formation in the northern Grays Harbor Basin is dominated by sediment derived from the Crescent Formation in the Olympic Mountains (Bigelow, 1987). Moreover, the main magnetic carrier in the Crescent Formation is low-Ti titanomagnetite (Warnock, 1992; Wells and Coe, 1985), similar to what we identify in our samples. Together, these observations explain the observed up-section increase in magnetic mineral concentration.

Interestingly, the rock magnetic parameters of the upper Astoria Formation in the ABY section resemble those of the overlying Montesano Formation more closely than those of the lower Astoria Formation (Figure 4). This may indicate a misplacement of the unconformity, an earlier shift in sediment source, or the presence of a mixing zone around the unconformity. Similar zones of stratigraphic mixing around unconformities have been documented elsewhere, for example, in terrestrial Miocene sediments from Montana (Gerritsen et al., 2026). Additional rock magnetic data from remaining samples, along with a closer examination of sedimentary structures, are needed to refine the stratigraphic position of the unconformity and better constrain the timing of Olympic Mountain uplift and exposure.

Comparison of rock magnetic parameters across the study region reveals spatial variation within formations. For example, the Lincoln Creek and Astoria formations have a higher magnetic mineral concentration (χ and Ms) in the CRB section than in the ABY section (Figure 5B). The CRB section is located in the Chehalis River, which drains from the Willapa Hills, rather than the Canyon River. This may suggest that the Willapa Hills uplifted earlier than the Olympic Mountains, possibly during the late Oligocene (Figure 2). In the same section, we collected samples from the basalt capping the Astoria Formation (Figure S2A). By determining its magnetic polarity, it may be possible to correlate this flow with a specific member of the Grande Ronde Basalt, allowing for a more precise age constraint on the upper part of the CRB section.

In summary, the rock magnetic record of the ABY section documents a progressive increase in magnetic mineral concentration from the Oligocene to the middle Miocene. This may reflect the exposure of oceanic basalts in the Olympic Mountains as part of the

Siletzia terrane. Additional rock magnetic and sedimentary data are needed to constrain the timing of this event, as well as potential differences between the timing of exposure of basalts of the Olympic Mountains and, for example, the Willapa Hills.

5.5.2 Preliminary paleomagnetic results

The preliminary paleomagnetic results from this study are complex and, at present, inconclusive. Further rock magnetic analyses and more refined demagnetization experiments are necessary to resolve the primary remanent magnetization. Our ABY section overlaps with the Canyon River section of Prothero and Armentrout (1985), who identified a magnetostratigraphy including three reversals within the Astoria Formation. However, we cannot replicate these results; our samples from ABY7–8 within the Astoria Formation show no clear reversed directions and appear to be overprinted. Moreover, Prothero and Armentrout (1985) did not publish demagnetization diagrams or details of their protocols, making their findings impossible to verify or reproduce.

Much of their interpreted magnetostratigraphy pertains to the Lincoln Creek Formation. In our study, samples from the lower Lincoln Creek (ABY11–13) acquired a GRM during AF demagnetization. In contrast, samples from the ABY14 section—also in the lower Lincoln Creek Formation—yielded a reliable signal, including several reversed directions. It is possible that similarly well-preserved remanence exists higher in the Lincoln Creek Formation, but we have not yet sampled those intervals.

In a more recent and detailed study, Prothero et al. (2001), analyzed the Lincoln Creek Formation on the southwestern flank of the Black Hills (Figure 1B). Their demagnetization protocol involved initial AF demagnetization up to 10 mT to remove viscous overprints, followed by thermal demagnetization from 300–600°C, with a stable remanent signal typically isolated between 300–500°C. They also conducted IRM acquisition, Lowrie-Fuller tests, and thin section analysis, concluding that single-domain or pseudo-single-domain magnetite was the dominant magnetic carrier. These methods could offer a useful guideline for designing our future experiments.

However, compositional heterogeneity across the region (Figure 5) means that the magnetic properties observed by Prothero et al. (2001) may not be representative of the ABY section. In our samples, thermal demagnetization was commonly stable up to ~400°C (Figure 6A–B), but heating beyond this point caused significant alteration. To improve isolation of the primary magnetization, we recommend a combined AF and thermal demagnetization protocol: AF up to 10 mT followed by closely spaced thermal steps between 150–400°C. Additionally, to avoid GRM acquisition in critical intervals (ABY7–8 and ABY11–13), future AF demagnetization experiments should use permutated field axes.

Although the paleomagnetic results are currently inconclusive, they point to the need for improved experimental protocols. A combined AF and thermal demagnetization approach and AF demagnetization with permutated field axes to minimize GRM acquisition, shows promise for isolating primary remanence. Once more robust paleomagnetic data are obtained, they can be used to evaluate regional tectonic rotations and better constrain the timing of Siletzia terrane accretion and subsequent uplift in the Olympic Mountains.

6

Conclusions and outlook

The aim of this thesis was to find evidence for dynamic topography in the geologic record and thereby constrain its spatial and temporal dimensions. We used the Yellowstone plume in North America as a case study (Figure 1). The Yellowstone plume erupted with the Columbia River Basalt Group (CRBG) around 17 Ma, so we targeted sediments deposited before and after this event (Figure 1B). We targeted three key regions where these sediments are exposed: Montana, Wyoming, and Washington. Each is located at a different distance from the plume center and reflects a different expression of dynamic topography (Figure 1A).

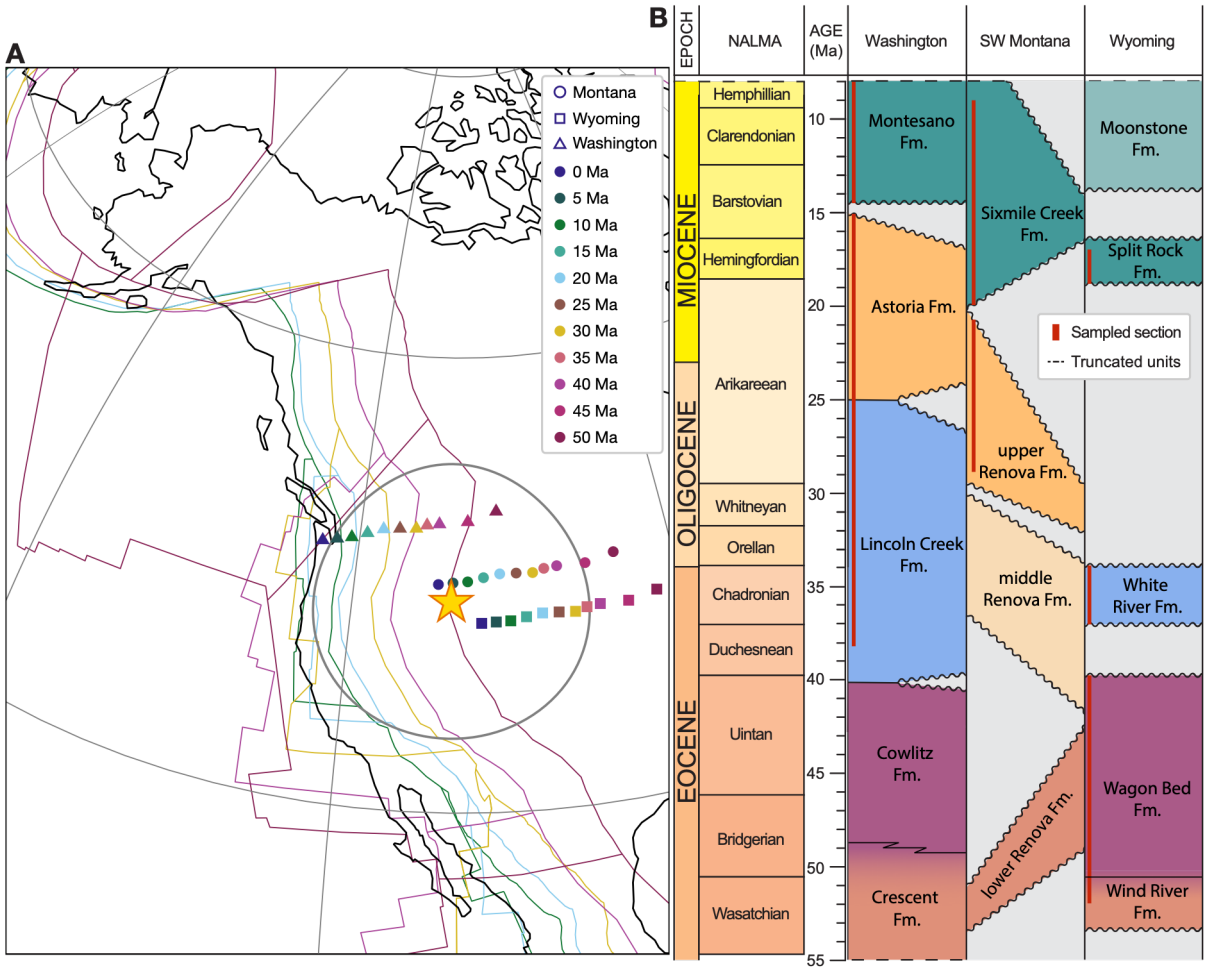

Figure 1. (A) Study locations reconstructed from 0 to 50 Ma using a global Mesozoic–Cenozoic plate motion model (Müller et al., 2016) with an Indo-Atlantic hotspot reference frame (O'Neill et al., 2005). Star indicates Yellowstone plume location (Courtillot et al., 2003) and the circle with a 1000 km radius indicates the region in which at least 100 m of dynamic topography is expected for a medium-sized plume with a diameter of 500 km. Contours show the reconstructed plate positions at 10 Myr intervals with the colors corresponding to the legend; black shows the present-day coastline. Credit to Berta Vilacís. **(B)** Simplified correlation chart of the formations in the three study areas. North American Land Mammal Ages (NALMA) from Barnosky et al. (2014).

6.1 Montana: A clear signal of dynamic topography

Montana, the region closest to the Yellowstone plume center and moving toward it over time, provides the clearest evidence for dynamic topography (Figure 1A). Here, a regional unconformity formed shortly before the CRBG eruptions (Figure 1B). We dated this unconformity with high precision in the Railroad Canyon Section (RCS) using magnetostratigraphy combined with published U-Pb ages, finding that it ended around 20.1 Ma and lasted between 0.1 and 1.5 Myr (Chapter 2). In other basins, however, the age and duration of this unconformity are less well constrained and may vary by >10 Myr. Obtaining additional absolute age constraints would allow for more precise timing of the associated source change and could clarify the proposed time-transgressive nature of the unconformity.

Across eight sedimentary sections in the region, we observed a pronounced increase in magnetite concentration at this unconformity, occurring in a region of ~40,000 km^2 (Chapter 3). Our comprehensive compilation of detrital zircon data further revealed a notable shift from predominantly Cretaceous to Miocene zircons. Together, these findings indicate a large change in provenance, which we link to the inclusion of the CRBG into the drainage area. We interpret this shift as the result of dynamic topography created by the Yellowstone plume, driving a ~400 km westward migration of the North American drainage divide.

A 3 Myr time lag occurs between the observed magnetic increase in the RCS (~20 Ma) and the earliest CRBG eruptions (~17 Ma). This lag may reflect the presence of older CRBG flows that were later buried or eroded, or alternatively, input from different sources such as Challis volcanism or local basement rocks. Given the RCS's key position on the present-day drainage divide, additional data from this section are essential to refine source attribution, particularly detrital zircon geochronology and paleo-flow indicators. To determine the origin of the increased magnetic input between 20–17 Ma, detailed geochemical analyses of detrital zircon and magnetite are needed, along with comparable data from potential source rocks, including CRBG rhyolitic and basaltic units, Challis volcanic rocks, and exposed basement lithologies. When integrated with our precise magnetostratigraphy, these data can strongly constrain both the timing and nature of drainage reorganization.

Our results also show that the high magnetite input from the CRBG persisted from ~20 Ma until at least 10 Ma. At 20 Ma, the region was located approximately 400 km from the plume center and continued to move closer over time (Figure 1A). However, following the CRBG eruptions around 17 Ma, the dynamically supported uplift began to dissipate. This led to an eastward migration of the drainage divide, toward its current position. As

a result, we expect a decline in magnetite input in Montana, as the CRBG source was progressively cut off. By analyzing post-10 Ma sediments, we can pinpoint when this decline occurred and thereby place tighter constraints on the timing of the dissipation of dynamic topography. These constraints can, in turn, be used in geodynamic and landscape evolution models, to study the influence of dynamic topography on surface processes.

The region may also have recorded earlier phases of dynamic topography. Numerical modeling suggests that a medium-sized plume with a radius of ~500 km would influence a region with a 1000 km radius, generating uplift of at least 100 meters (Figure 1A). Montana entered this predicted influence zone between ~40 and 45 Ma. Correspondingly, two older regional unconformities, estimated to ~30 Ma and ~40 Ma, have been identified in the sedimentary record of Montana (Figure 1B). These events may represent earlier responses to plume-related uplift. The relatively large number of sedimentary sections containing these unconformities provides an excellent basis for further study.

A central assumption of this work is that sedimentary basins (the sink) accurately reflect the lithologic and geochronologic characteristics of their upstream source regions, specifically in terms of magnetite concentration and detrital zircon ages. However, this assumption has not yet been rigorously tested. To evaluate its validity, modern analogues should be studied by sampling both sediments in active river systems and the rocks from their upstream sources. By comparing their magnetic properties and detrital zircon age distributions, we can assess how reliably the sink reflects the source, and whether this assumption holds true for reconstructing past drainage and provenance shifts.

6.2 Wyoming: Indirect evidence for dynamic topography

In Wyoming, we likely identified an indirect signal of dynamic topography (Chapter 4). The region lies within the plume margin area and moved progressively closer to the Yellowstone plume center over time (Figure 1A). It is characterized by prominent Laramide structures, which formed during the Late Cretaceous to early Eocene. By analyzing rock magnetic parameters throughout the studied section, we observed a gradual increase in magnetite concentration occurring after the Laramide orogeny, in the latest Eocene. We interpret this signal as evidence for a phase of post-Laramide uplift and associated unroofing of the nearby Wind River Range. In the absence of known tectonic activity during this period, we propose that this uplift phase resulted from the reactivation of Laramide structures due to dynamic topography, potentially triggered by

lithospheric rebound following Farallon slab breakoff or by the earliest influence of the Yellowstone plume.

Around 35 Ma, the region entered the predicted sphere of influence of the Yellowstone plume (Figure 1A), which aligns well with the timing of the observed uplift signal. Although our study area continued to migrate toward the plume center, the area affected by dynamic topography decreased in diameter and increased in amplitude as the plume rose through the mantle. The rate at which the plume ascended through the mantle, and thus the timing and contraction of its influence sphere, remains uncertain. Moreover, an erosional event in the early Miocene removed much of the Oligocene stratigraphic record. Consequently, we are unable to determine whether our region continued to experience effects of dynamic topography during this time.

Detrital zircon data from this area are extremely limited, and none are currently available for the specific section we studied. Expanding zircon sampling in this area is necessary to develop a more comprehensive understanding of sediment provenance. As in Montana, geochemical analysis of both detrital zircons and magnetite in the sediments, alongside geochemical data from potential source rocks in the Wind River Range, would help clarify the link between source and sink. In addition, a more detailed investigation of the depositional environment, drainage patterns, and paleoclimate is needed to better constrain source regions and evaluate the proposed increase in eolian deposition.

The paleomagnetic directions obtained from this section are notably complex; the directions of the magnetite-poor Wagon Bed Formation are relatively stable, whereas those from the magnetite-rich White River Formation appear to be consistently overprinted. To more accurately identify the magnetic carriers, additional rock magnetic experiments, such as Lowrie tests, are needed.

6.3 Washington: A subtle and complex record

Our preliminary results from Washington do not reveal a clear signal of dynamic topography (Chapter 5). Unlike the other study regions, Washington has been moving away from the plume center over time (Figure 1A). If dynamic topography had an early surface expression, this region might preserve its earliest signature. Previous studies in the area have reported significant sea-level fluctuations based on lithofacies analyses and molluscan fauna assemblages, which turned out to be independent of global sea-level trends. However, since the region remained submerged until approximately 17 Ma, estimating the effects of dynamic topography beyond changes in water depth is particularly challenging.

The tectonic complexity of the Washington region further complicates the interpretation of any dynamic topography signal. The interaction between the Yellowstone plume and the subducting Farallon slab, combined with the presence of accreted terranes, makes it difficult to isolate mantle-driven surface uplift. Nevertheless, our rock magnetic measurements in our primary section (ABY) revealed a stepwise increase in magnetic mineral concentration. We tentatively attribute this signal to the exhumation of oceanic basalts from the Siletzia terrane, which subsequently served as the source region for a river system transporting magnetite-rich sediments. To test this interpretation and explore alternative explanations, higher-resolution rock magnetic studies are needed. In parallel, more detailed sedimentological and biostratigraphic analyses will be critical to refine the stratigraphic framework and depositional history of the area.

The paleomagnetic results from this region are equally complex. Many sections do not show any reversed polarities and appear to be significantly overprinted by the present-day field, making it difficult to extract a reliable primary signal. In several other sections, samples acquired a gyroremanent magnetization during demagnetization, further complicating the interpretation. To mitigate this issue, sister samples could be measured using permutated axes and a combination of alternating field and thermal demagnetization procedures, which may prevent the acquisition of gyroremanence and allow stable directions to be recovered. Among all the studied sections, only two subsections yielded more stable paleomagnetic data. Interestingly, one of these successful results came from a formation with relatively low magnetic mineral concentrations. To better characterize the magnetic carriers in these rocks, additional rock magnetic experiments, such as temperature curves on magnetic extracts, are recommended.

6.4 Broader implications and future directions

One of the key findings of this thesis is that dynamic topography, driven by density anomalies and convective flow in the mantle, can significantly reshape the Earth's surface. It can reactivate faults, reorganize drainage networks, and even influence regional climate. For instance, the drying of the North American continental interior in the early Miocene was likely caused by the formation of a rain shadow, precisely in the region where we expect dynamic uplift associated with the Yellowstone plume. This climatic shift promoted a transition from forested to open habitats, allowing grasses to flourish and contributing to the diversification of mammalian species. The evolutionary success of grasses, including major agricultural crops such as corn and wheat, underscores the far-reaching consequences of such landscape transformations. Understanding what triggered these environmental changes, offers valuable insight into

long-term species evolution, particularly in the context of ongoing climate change. These connections between deep Earth processes and surface evolution highlight the broad significance of dynamic topography within Earth system science.

Capturing such complex interactions between mantle processes and surface expression requires a multidisciplinary approach. This thesis demonstrates the value of integrating diverse datasets—including (magneto)stratigraphy, sedimentology, provenance analysis, and geochronology—to reconstruct regional geologic history. Rock magnetic measurements are fast and nondestructive, making them a useful screening tool when combined with more resource-intensive techniques such as radiometric dating. Together, these complementary techniques enable more detailed and robust interpretations of the sedimentary record.

Within the sedimentary record, unconformities are often regarded as inconvenient breaks in a continuous stratigraphy. However, this thesis highlights their diagnostic value: rather than being mere gaps, they often mark key transitions in the section. In all three study regions, we observed shifts in rock magnetic parameters at or near unconformities, suggesting that these surfaces preserve key evidence of paleoenvironmental adjustment. As such, unconformities can serve as important markers of dynamic, tectonic, or climatic change.

One of the major challenges of this work remains distinguishing between plate-driven and plume-driven processes. It is unclear to what extent these two modes operate independently or whether, for example, the onset of Basin and Range extension may have been triggered by the rising Yellowstone plume. Tectonic processes introduce shear components, which cause vertical-axis rotations that are observable in paleomagnetic data. However, the paleomagnetic record in this region is particularly difficult to interpret: the Eocene–Miocene geomagnetic field closely resembles the present-day field, making it hard to differentiate between them in the absence of reversed-polarity samples. Additional work is needed to fully resolve these ambiguities and accurately isolate the primary remanent magnetization.

Another poorly constrained component is the interaction between the subducting Farallon slab and the ascending Yellowstone plume. One hypothesis proposes that the plume initially erupted beneath the Pacific Ocean after which it was suppressed by the downgoing Farallon plate. Only after breaching this barrier did it emerge at the surface as the CRBG. Volcanic material from the initial eruptions may have accreted to the continental margin and now form part of the Siletzia terrane. Understanding the timing and mechanics of this sequence is essential to unravel how mantle plumes interact with subduction zones, and how those interactions influence dynamic topography at the surface.

The most compelling evidence for dynamic topography in this thesis comes from the deeper continental interior, in Montana, where we observe clear shifts in drainage patterns and sediment provenance just prior to the CRBG eruptions. Building on these findings, the John Day region in Oregon emerges as a promising target for future research. This area lies near the center of the plume but, unlike Washington, is neither part of an accreted terrane nor submerged during key intervals. These characteristics make it an ideal location to investigate early surface expressions of dynamic topography and further constrain its onset and timing.

Finally, this thesis presents geologic signals of dynamic topography on the continent, providing both temporal and spatial constraints on its development. These results offer valuable input to the geodynamic modeling community, as replicating such features in models requires tightly controlled parameters, such as mantle viscosity structure and plume buoyancy. In turn, this provides insight into the dynamics and composition of Earth's deep interior.

Appendix A:
Supplementary Information Chapter 2

Text S1. Laboratory Methods

We carried out alternating field (AF) demagnetization with 11 steps up to 90 mT, anhysteretic remanent magnetization (ARM) acquisition experiments, and magnetic moment measurements using an automated measurement system (SushiBar) based on a 2G Enterprises, three-axis superconducting magnetometer (Wack and Gilder, 2012). Stepwise AF demagnetization was performed on 235 specimens. Thermal demagnetization was conducted on 123 specimens using 14 heating steps up to 580°C. We measured the anisotropy of ARM (AARM) by applying a switching field window from 90 to 10 mT with a DC bias field of 0.1 mT in 12 independent directions (Wack and Gilder, 2012). Remanent magnetization directions were determined by principal component analysis (Kirschvink, 1980) using PaleoMac software (Cogné, 2003). Magnetic extracts were taken from four intervals, two in each formation. Thermomagnetic curves, backfield curves, and hysteresis loops of the extracts were measured using a MAG Instruments variable field translation balance (VFTB).

Rock magnetic parameters of all samples helped determine magnetic mineralogy and grain size variations throughout the section. Magnetic susceptibility (χ) was measured with a Bartington MS2 meter. We used a LakeShore MicroMag 3900 vibrating sample magnetometer (VSM) to measure backfield curves, defining the coercivity of remanence (Bcr), and hysteresis loops. The latter were interpreted using HystLab software (Paterson et al., 2018) to determine coercive force (Bc), saturation magnetization (Ms), saturation remanent magnetization (Mrs), the hysteresis shape parameter (σ_{hys}) (Fabian, 2003), and high-field susceptibility (χ_{HF}). S-ratios were determined by applying a 1 T saturation isothermal remanent magnetization (SIRM) followed by a reversed field IRM of −0.3 T: $[(-IRM_{-0.3T}/SIRM) + 1]/2$ (Bloemendal et al., 1992). Attenuated total reflection (ATR) analysis was performed using a Thermo Scientific NICOLET iS50 FT-IR. The 6.97 μm transmittance peak was recognized as a CO_3 stretching vibration peak (Huang and Kerr, 1960); the relative peak height is interpreted as a calcite proxy.

Text S2. Quality classification of demagnetization data

We divided the samples into four quality classes based on their demagnetization behavior. Class A directions (N=56: 55 AF and one thermally demagnetized sample) were assigned to samples whose directions decayed univectorally to the origin on orthogonal plots, with best-fit line components based on >5 steps with maximum angular deviations (MAD) <10° (Figure 3). Class B directions have <5 steps and/or MAD >10° (N=7) or yield great circle trajectories with an angular uncertainty <10° (N=32) (Figure S4A). Class C directions (N=34) had great circle trajectories based on <5 steps, and/or had angular

uncertainties >10°, and/or only used demagnetization levels <30 mT or <350°C (Figure S4B). Class D samples (N=19) were assigned polarities based on the demagnetization trajectories, but no direction was interpreted (Figure S4C). 13 horizons were discarded as their natural remanent magnetization intensities/χ were $>10^5$ A/m, compared to a median of $1.49 \times 10^4 \pm 1.82 \times 10^4$ A/m, indicative of lightning strikes.

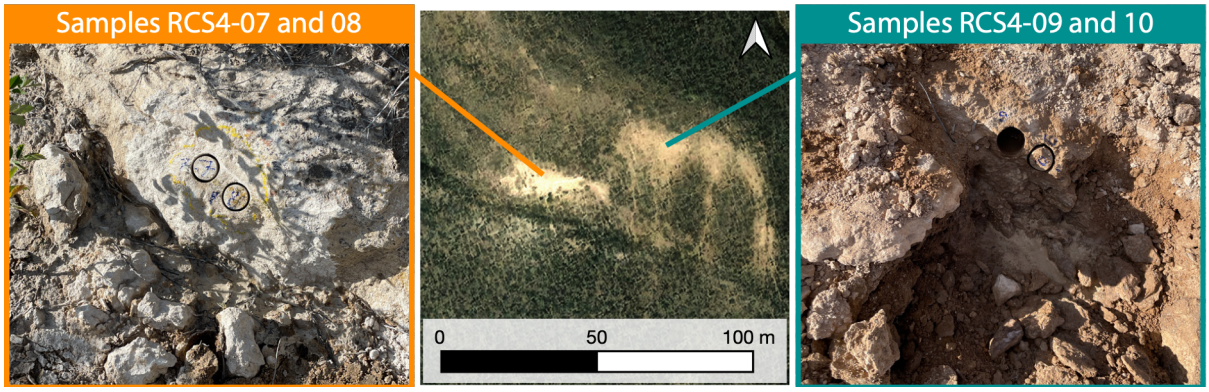

Figure S1. (middle) Satellite image (Environmental Systems Research Institute, 2009) showing the lithologic color change around the EMU at section RCS4. **(left and right)** Photos of outcrops drilled in the Renova and Sixmile Creek formations, respectively, highlighting the color differences.

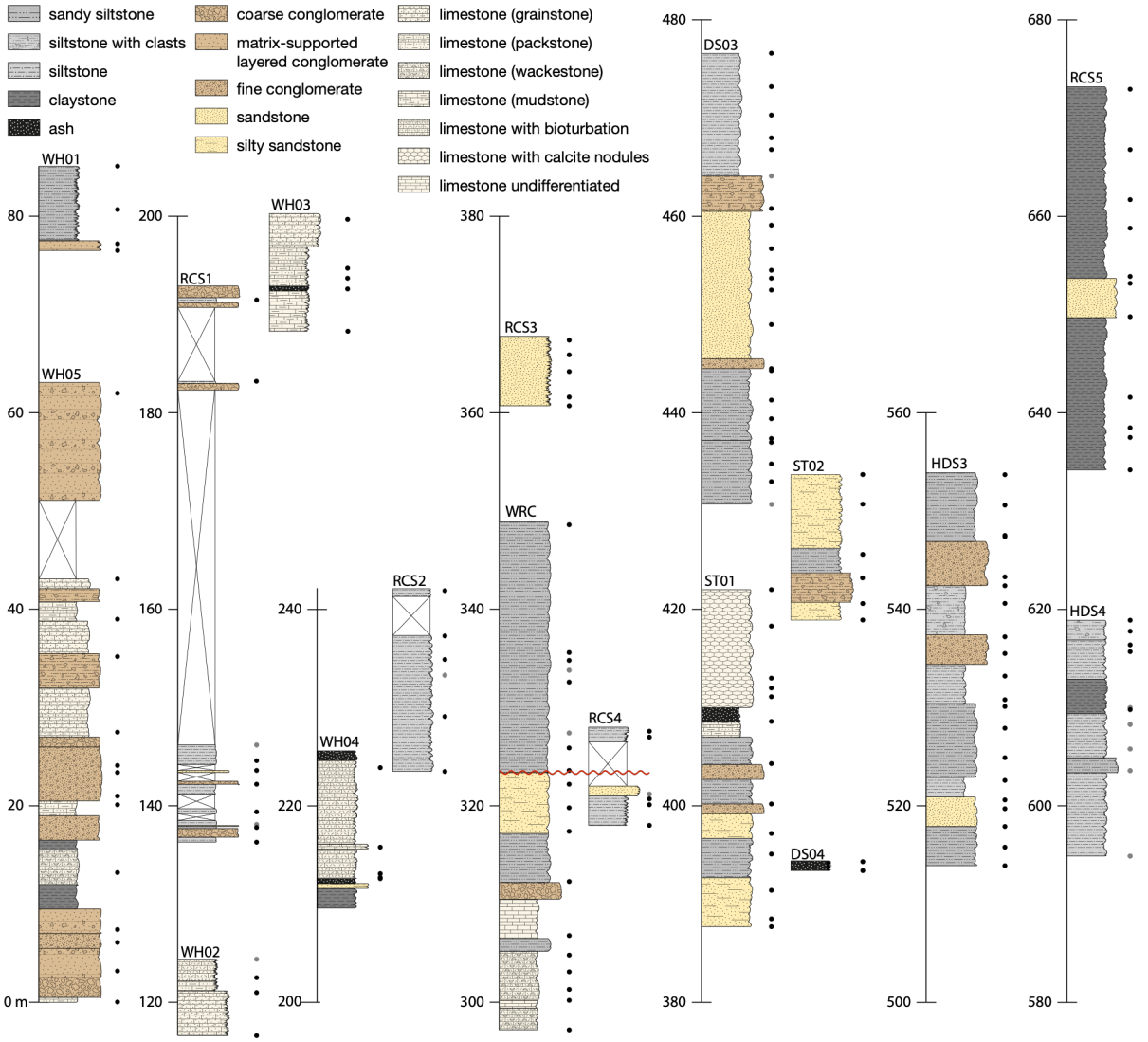

Figure S2. Detailed sedimentary columns of individual sections that together made the composite section in Figure 2. Dots indicate the sampling sites; grey dots indicate samples that were interpreted to be lightning struck. Curvy red line shows the stratigraphic position of the early Miocene unconformity (EMU).

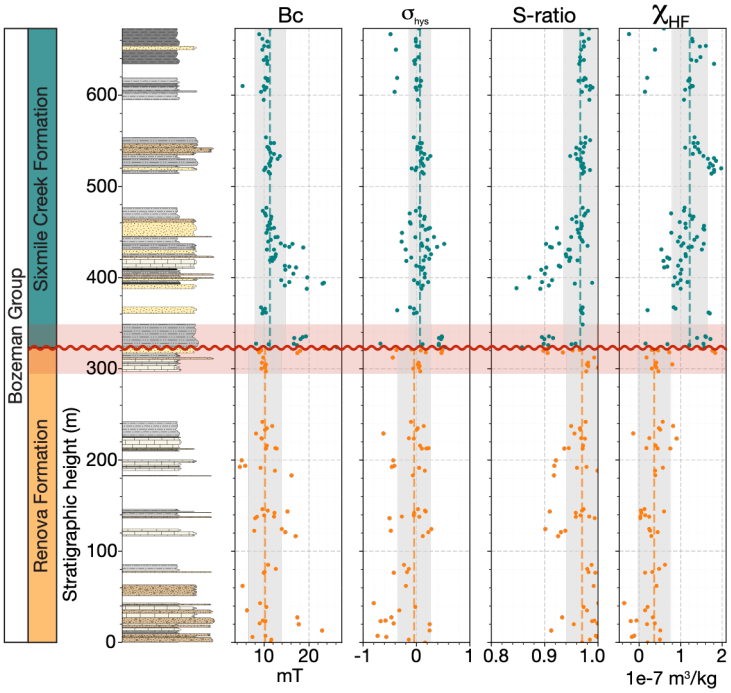

Figure S3. Simplified sedimentary log and rock magnetic properties of the section. From left to right: coercive force (Bc), hysteresis shape parameter (σ_{hys}), S-ratio (1=pure magnetite), and high-field susceptibility (χ_{HF}). Orange and teal points represent samples taken from the Renova and Sixmile Creek formations, respectively. Dashed lines indicate the median values (grey shaded regions 1σ uncertainty). Curvy red line and opaque red zone represent the early Miocene unconformity (EMU) and the zone of mixing around it, respectively.

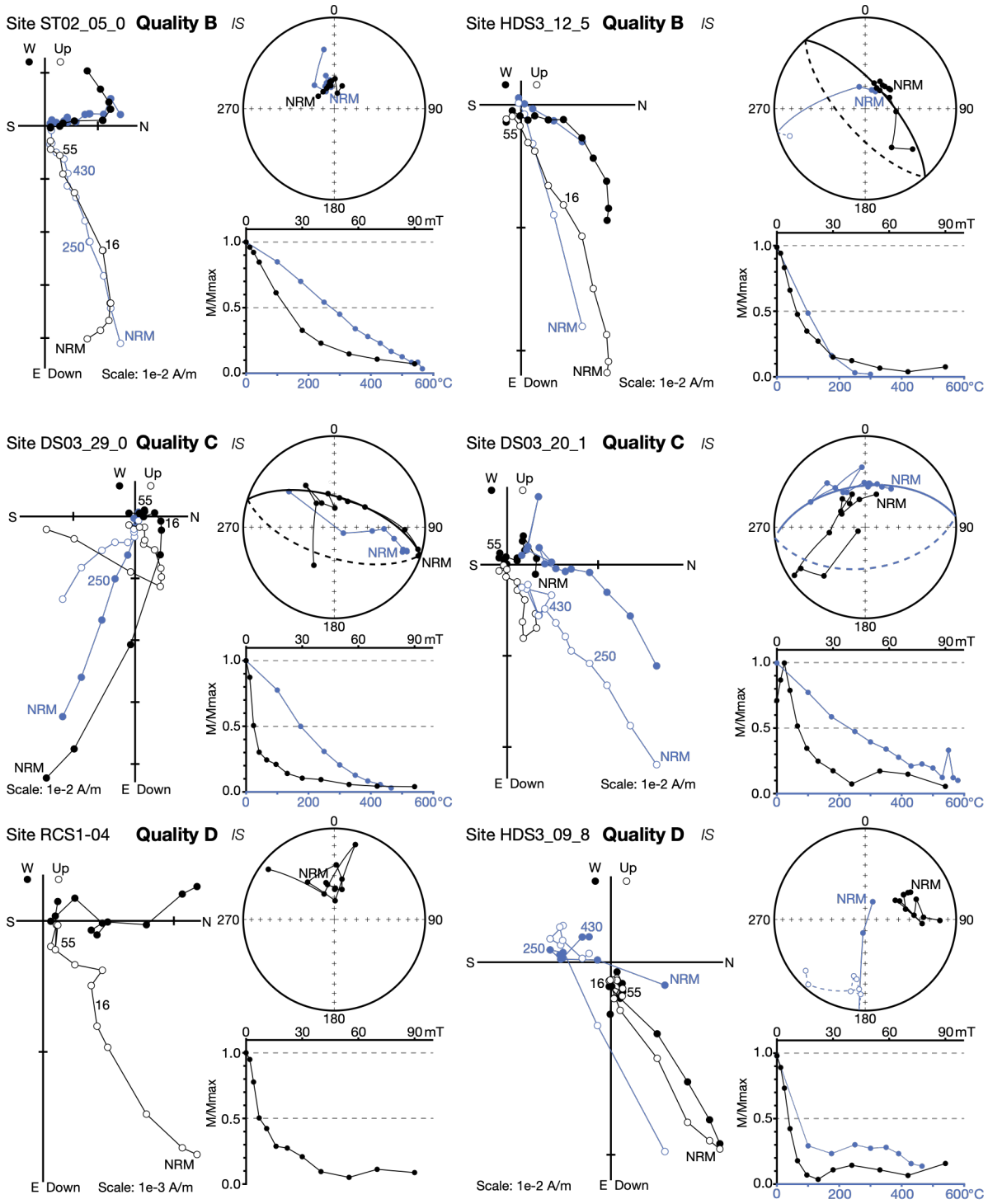

Figure S4. Stepwise AF (black) and thermal (blue) demagnetization trajectories for a normal **(left)** and reversed **(right)** polarity sample pair from the same horizon as a function of quality criteria B-D. Thermal demagnetization data were cut off at the minimum intensity.

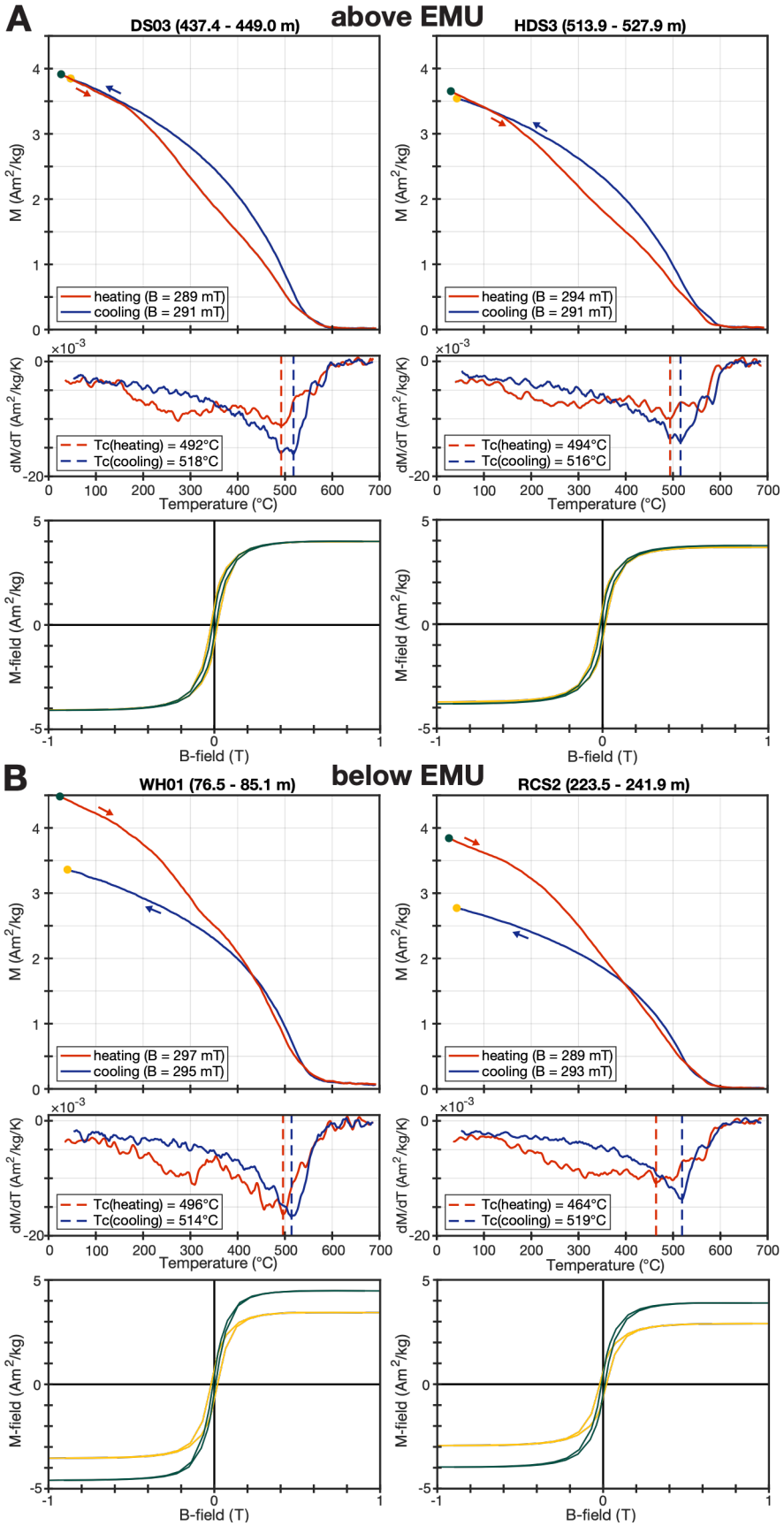

Figure S5. Thermomagnetic curves, their first derivatives, and hysteresis loops of magnetic extracts from above **(A)** and below **(B)** the early Miocene unconformity (EMU). Hysteresis loops before and after heating are shown in green and yellow, respectively.

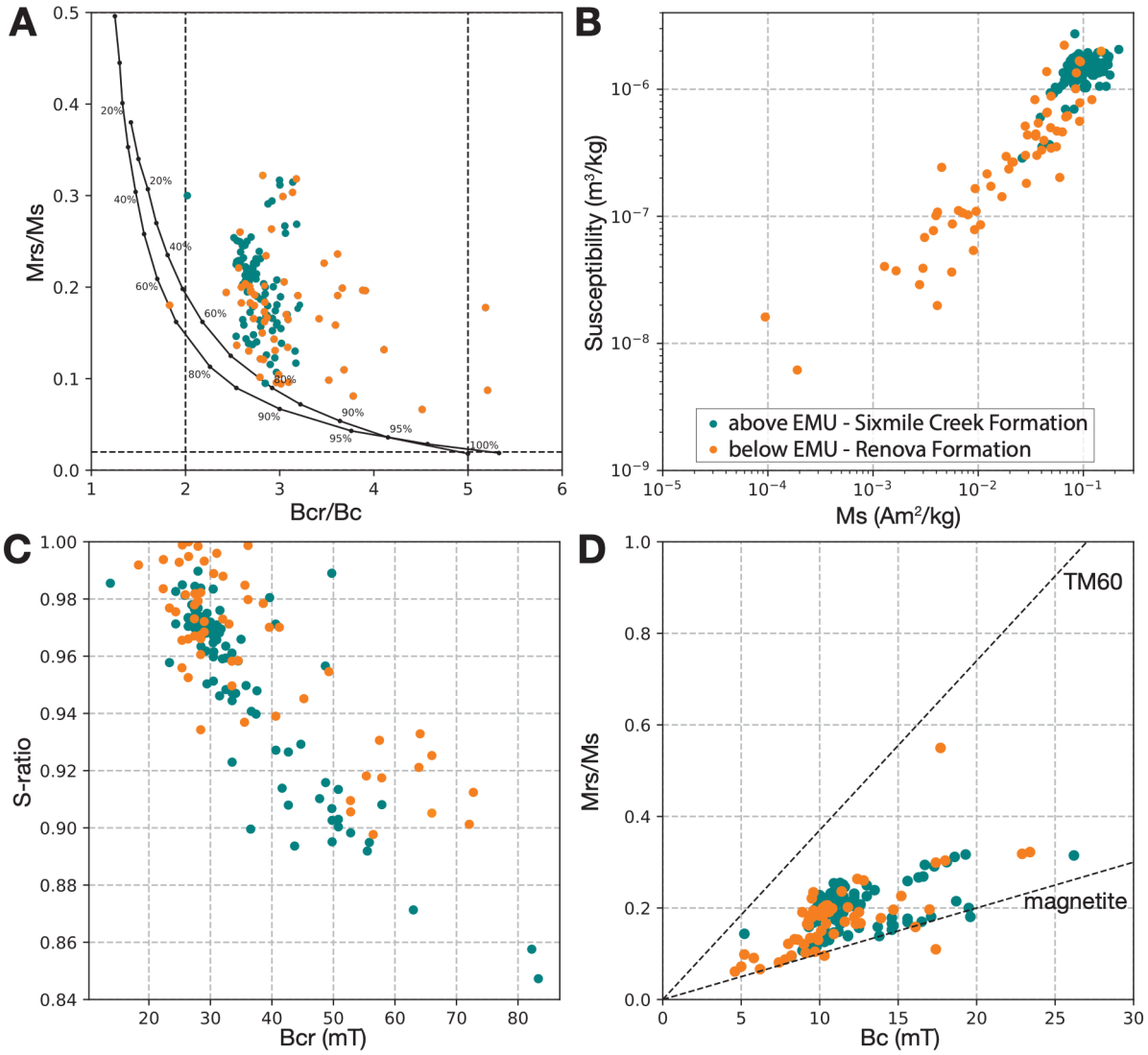

Figure S6. (A) Day diagram (Day et al., 1977) with the SD+MD mixing curves of Dunlop (2002). **(B)** Ms versus susceptibility. **(C)** Bcr versus S-ratio. **(D)** Néel diagram (Néel, 1955) with the trend lines for magnetite and titanomagnetite with x=0.6 (TM60) of Wang and van der Voo (2004). Orange and teal points represent samples taken from the Renova and Sixmile Creek formations, respectively.

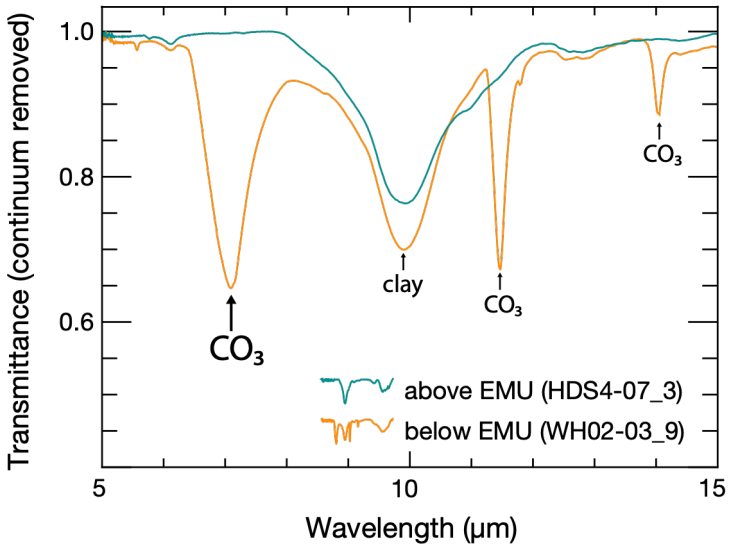

Figure S7. Examples of transmittance spectra from the attenuated total reflection (ATR) analysis for end member samples from above (HDS4-07 3) and below (WH02-03 9) the early Miocene unconformity (EMU). CO_3 and clay reference peaks from the ASTER spectral library are shown.

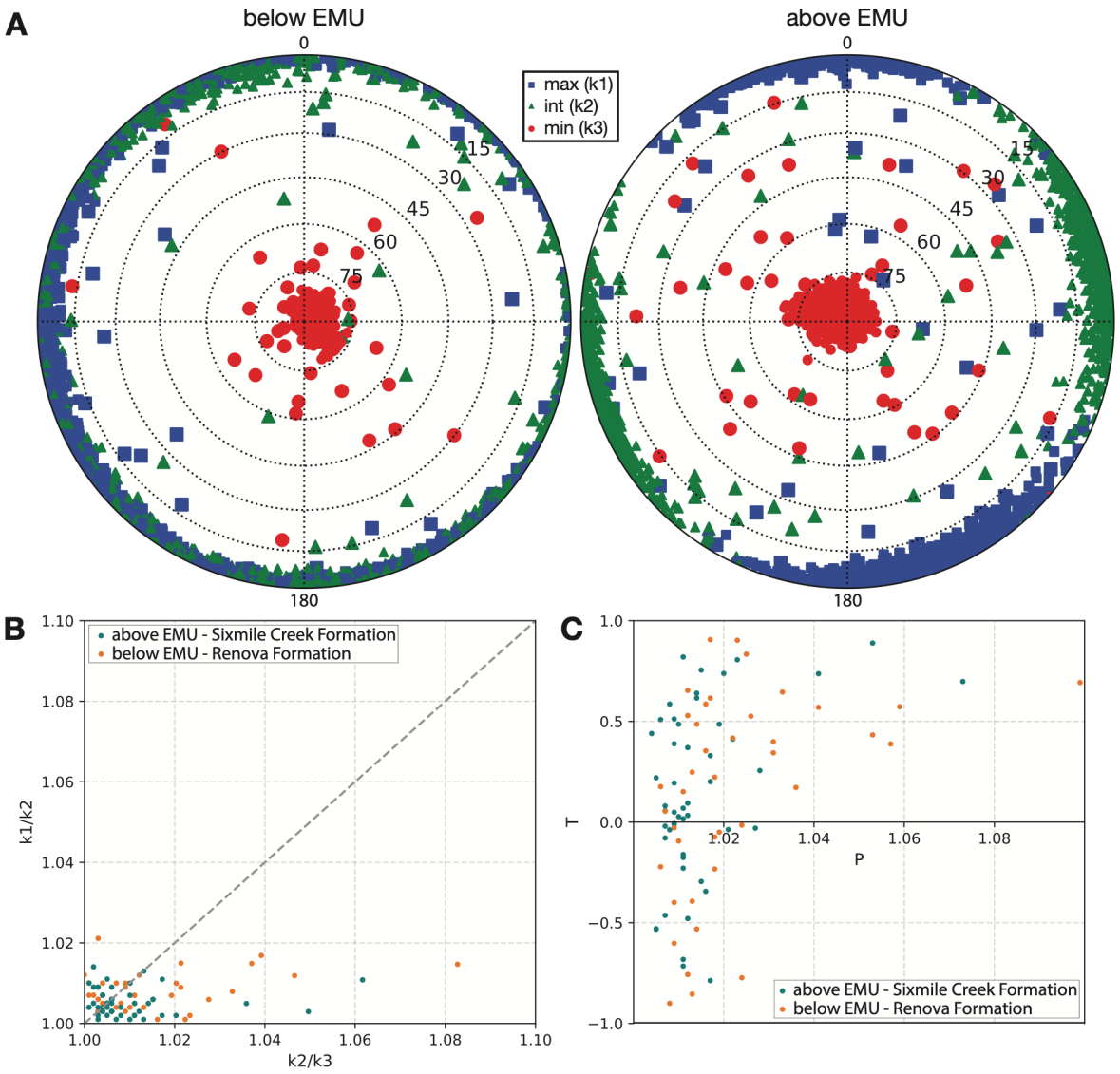

Figure S8. (A) Bootstrapped principal axis directions for anisotropy of anhysteretic remanent magnetization (AARM) tensors in tilt corrected coordinates plotted on the lower hemisphere. **(B)** Flinn (1962) diagram, where the vertical axis is lineation (k1/k2) and the horizontal axis is foliation (k2/k3). **(C)** Shape parameter (T) versus anisotropy degree (P).

Table S1. Sun compass-corrected bedding measurements.

Formation	Section	Dip direction (°)	Dip (°)	Included in average
Sixmile Creek	HDS4	18.5	4	yes
Sixmile Creek	DS03	53.5	4	yes
Sixmile Creek	ST02	28.5	8	yes
Sixmile Creek	ST01	33.5	8	yes
Sixmile Creek	DS04	33.5	4	yes
Sixmile Creek	WRC	313.5	5	no
Renova	WRC	8.5	12	no
Renova	RCS4	47.0	5	yes
Renova	WH02	48.5	10	yes
Renova	WH01	43.5	8	yes
Renova	WH05	53.5	10	yes
Renova	WH05	57.5	4	yes
Renova	WH05	57.5	4	yes
Renova	WH05	53.5	8	yes

Table S2. Mean directions in in-situ (Dg, Ig) and tilt-corrected (Ds, Is) coordinates and Fisher (1953) statistic parameters for the different quality classes; Fisher mean (Fisher, 1953) for Class A directions and mixed mean (McFadden and McElhinny, 1988) for combination of best-fit and great circle directions (Class B and C).

Class	n	D_g (°)	I_g (°)	k_g	α_{95} (°)	D_s (°)	I_s (°)	k_s	α_{95} (°)
A	56	359.7	65.6	45.2	2.9	4.8	60.0	48.6	2.8
A + B	95	357.9	64.9	44.0	2.2	4.0	59.6	46.0	2.2
A + B + C	129	357.9	64.9	43.2	1.9	4.2	59.7	44.2	1.9

Table S3. Date, latitude, longitude, and elevation from handheld GPS measurements, Jacob staff measurements within each subsection, and projected stratigraphic position of each sample. A comment was added in case we diverged from the standard method of projecting the GPS latitude, longitude, and elevation of each sample with the average bedding. Excel file available at: https://doi.org/10.1111/ter.12779

Table S4. Rock magnetic parameters, interpreted palaeomagnetic directions and principal AARM directions. Excel file available at: https://doi.org/10.1111/ter.12779

Data Set S1. All raw palaeomagnetic measurements are available in the online database MagIC: https://earthref.org/MagIC/20192

Appendix B:
Supplementary Information Chapter 3

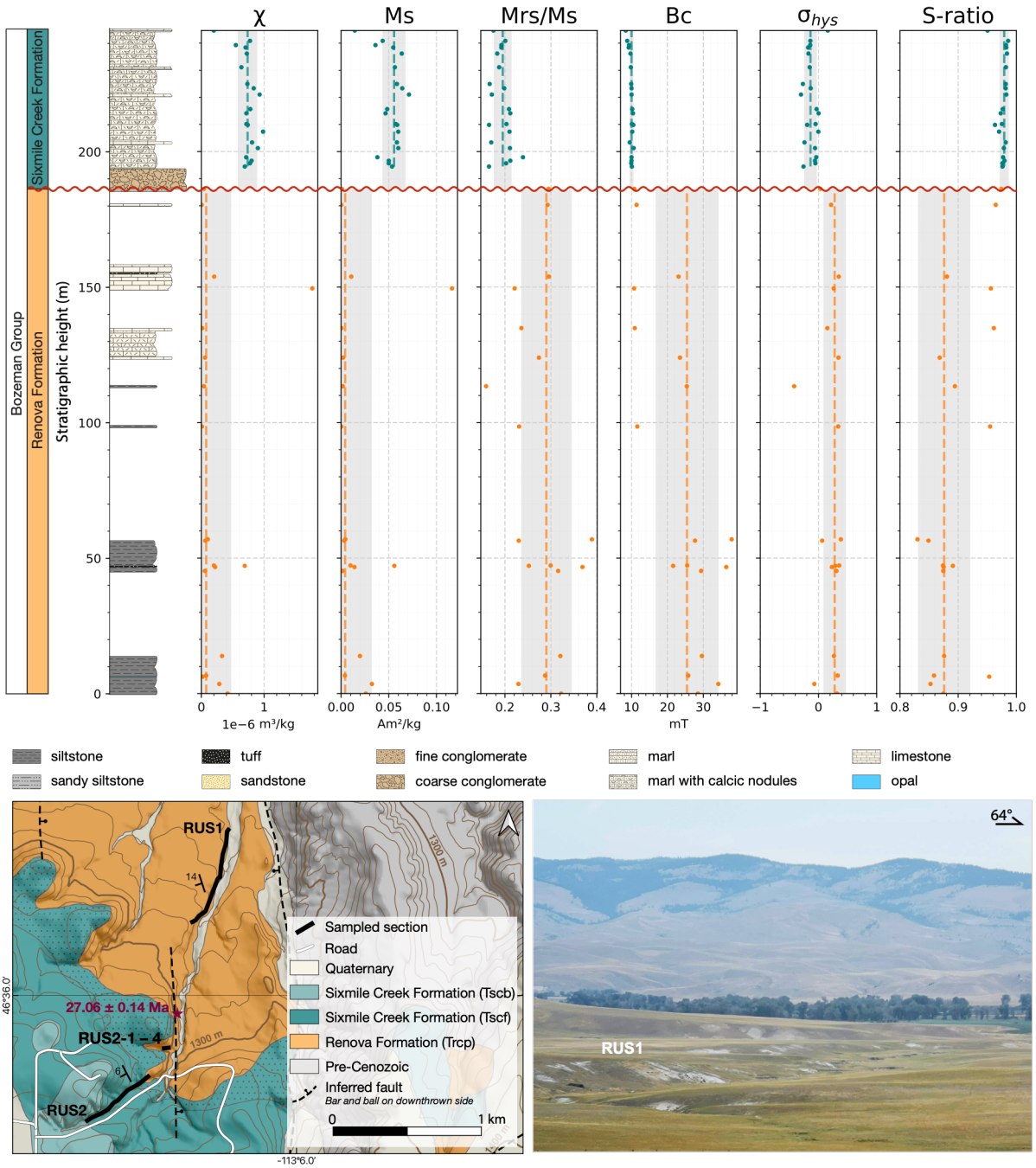

Figure S1. Overview of the RUS section. Top: Simplified sedimentary log and rock magnetic properties. From left to right: magnetic susceptibility (χ), saturation magnetization (Ms), saturation remanent magnetization (Mrs) divided by Ms, coercive force (Bc), hysteresis shape parameter (σ_{hys}), and hematite to magnetite concentration (S-ratio). Orange and teal points represent samples taken from the Renova Formation (N = 19) and Sixmile Creek Formation (N = 20), respectively. Dashed orange and teal lines indicate their median values (gray shaded regions 1σ uncertainty). Curvy red line represents the early Miocene unconformity (EMU). Bottom left: Geologic map (Portner and Hendrix, 2005). The dotted unit on the geologic map represents a conglomerate at the base of the Sixmile Creek Formation, immediately above the EMU (Fig. 1D). Red star indicates location of U-Pb age with 2σ uncertainty (Portner et al., 2011). Bottom right: Field photograph.

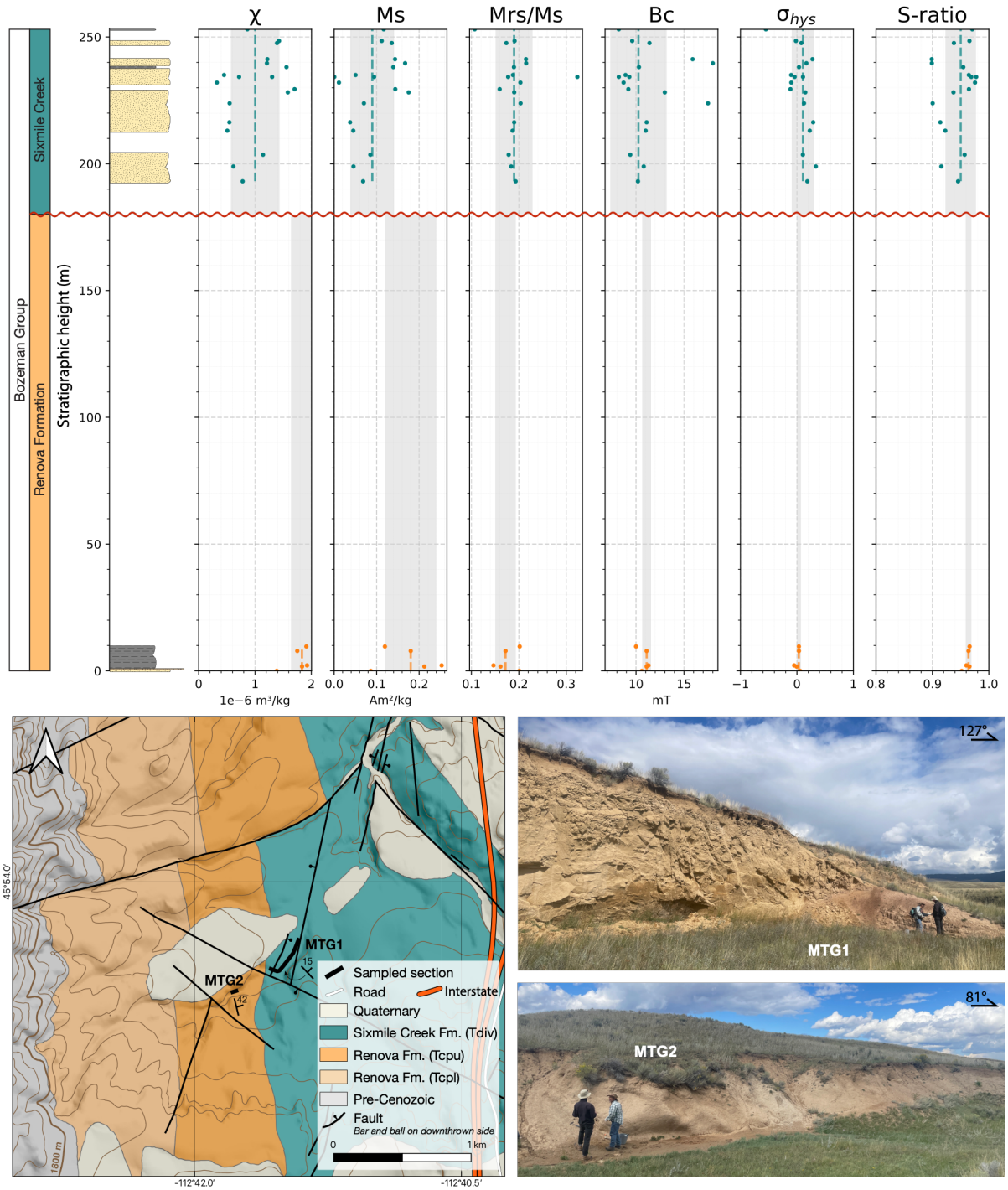

Figure S2. Overview of the MTG section. Top: Simplified sedimentary log (legend in fig. S1) and rock magnetic properties. From left to right: magnetic susceptibility (χ), saturation magnetization (Ms), saturation remanent magnetization (Mrs) divided by Ms, coercive force (Bc), hysteresis shape parameter (σ_{hys}), and hematite to magnetite concentration (S-ratio). Dashed orange and teal points represent samples taken from the Renova Formation (N = 5) and Sixmile Creek Formation (N = 18), respectively. Orange and teal lines indicate their median values (gray shaded regions 1σ uncertainty). Curvy red line represents the early Miocene unconformity (EMU). Bottom left: Geologic map (Elliott and McDonald, 2009). Bottom right: Field photographs.

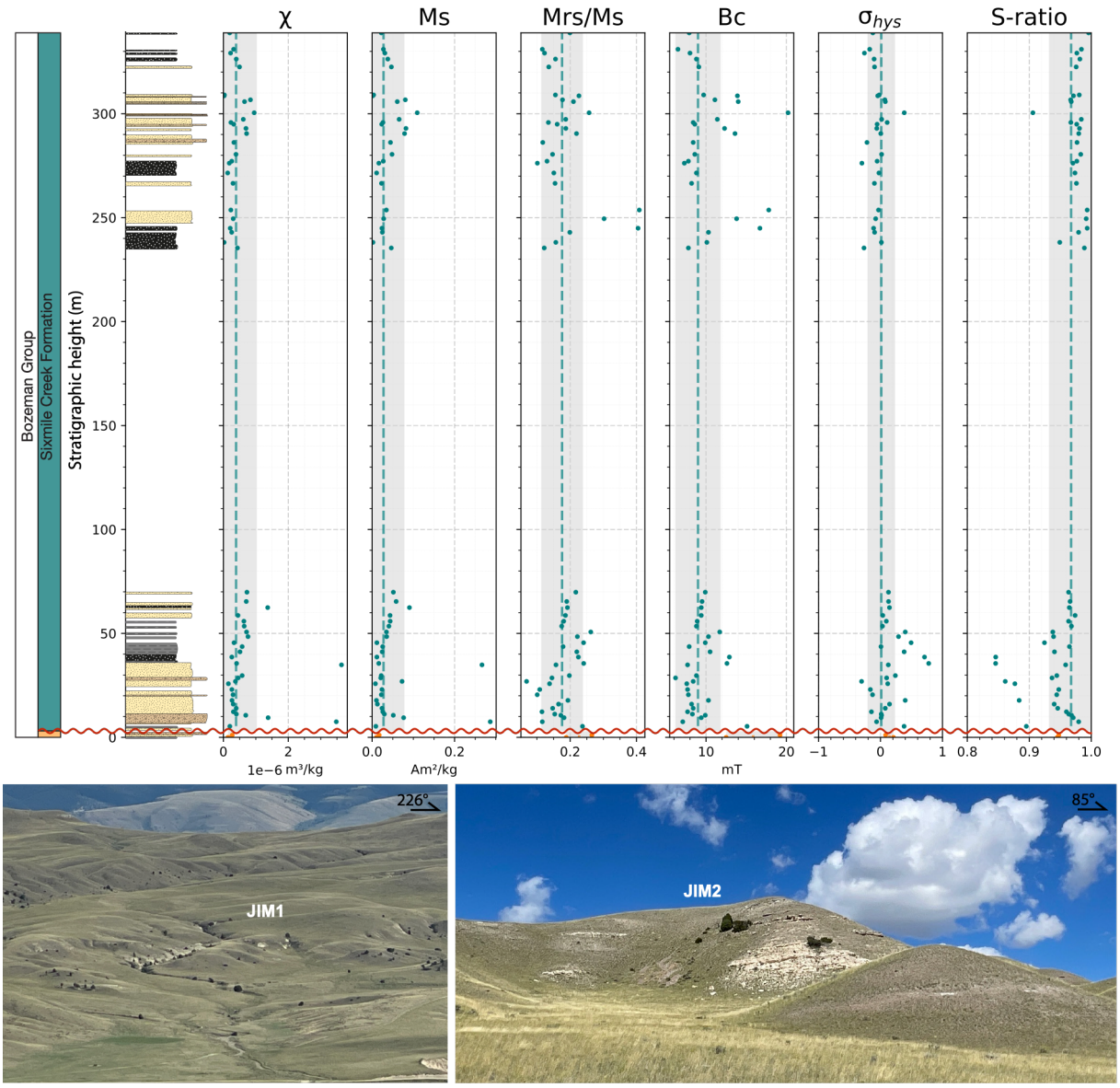

Figure S3. Overview of the JIM section. Top: Simplified sedimentary log (legend in fig. S1) and rock magnetic properties. From left to right: magnetic susceptibility (χ), saturation magnetization (Ms), saturation remanent magnetization (Mrs) divided by Ms, coercive force (Bc), hysteresis shape parameter (σ_{hys}), and hematite to magnetite concentration (S-ratio). Orange and teal points represent samples taken from the Renova Formation (N = 2) and Sixmile Creek Formation (N = 56), respectively. Dashed orange and teal lines indicate their median values (gray shaded regions 1σ uncertainty). Curvy red line represents the early Miocene unconformity (EMU). Bottom: Field photographs.

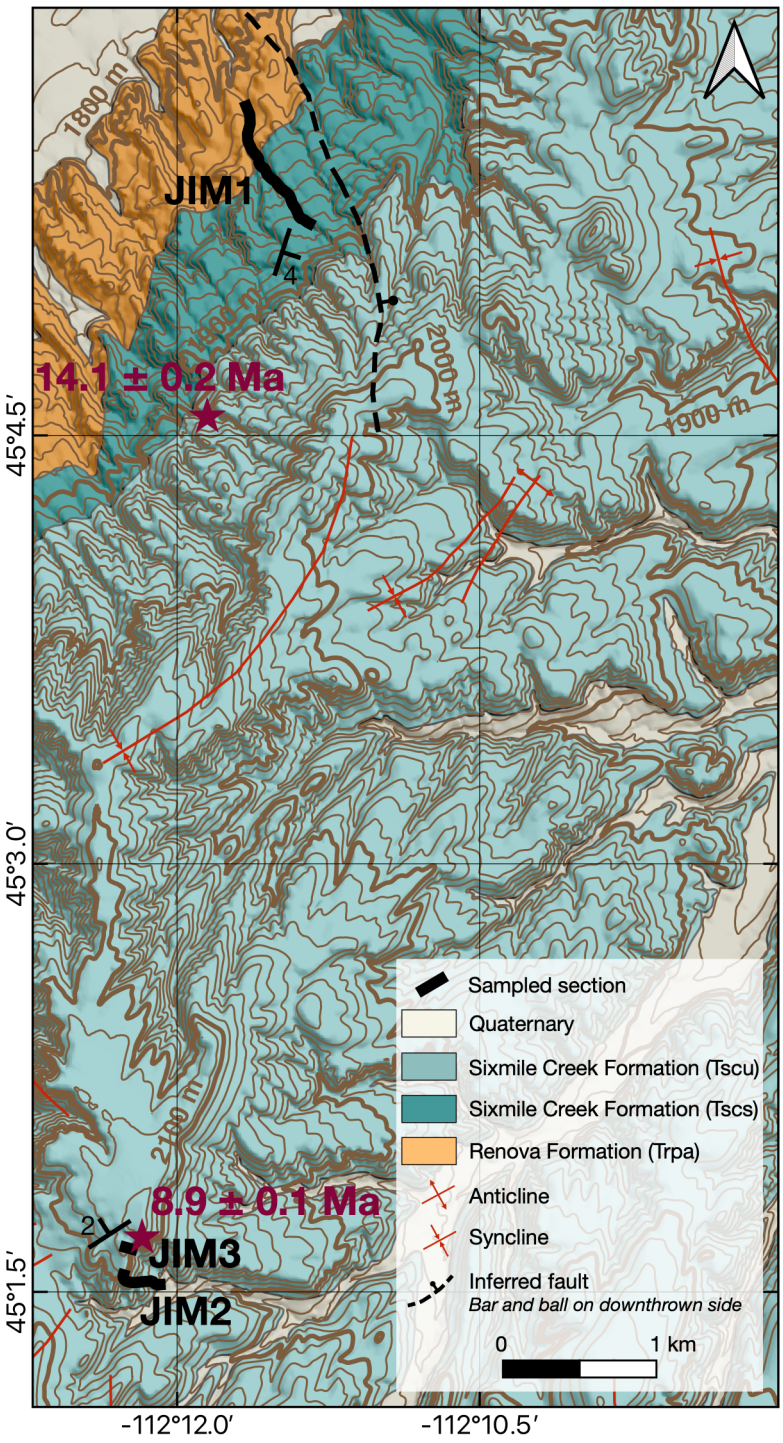

Figure S3 (cont.). Geologic map, with red stars indicating locations of U-Pb ages with 2σ uncertainties (Brennan et al., 2024).

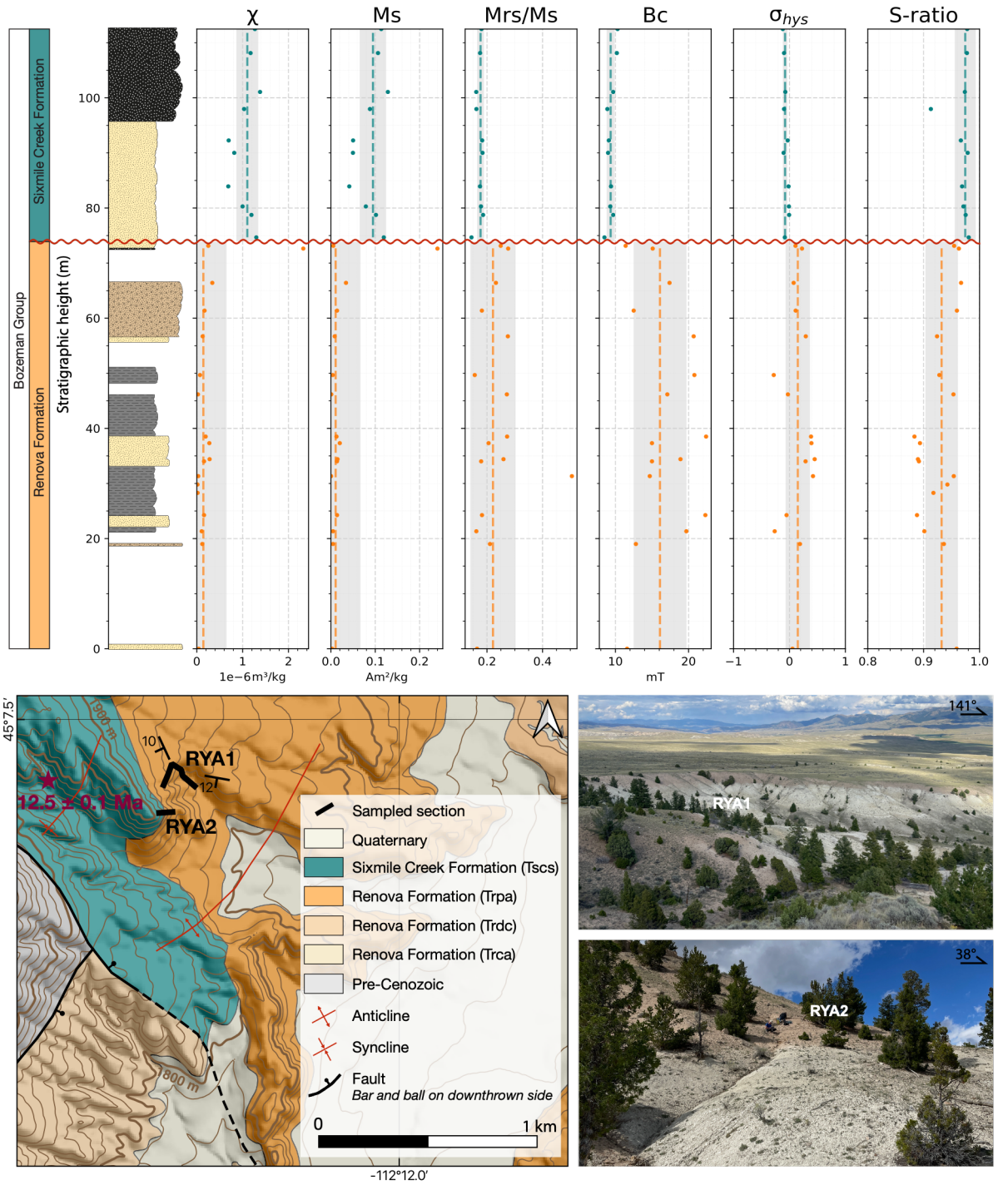

Figure S4. Overview of the RYA section. Top: Simplified sedimentary log (legend in fig. S1) and rock magnetic properties. From left to right: magnetic susceptibility (χ), saturation magnetization (Ms), saturation remanent magnetization (Mrs) divided by Ms, coercive force (Bc), hysteresis shape parameter (σ_{hys}), and hematite to magnetite concentration (S-ratio). Orange and teal points represent samples taken from the Renova Formation (N = 18) and Sixmile Creek Formation (N = 10), respectively. Dashed orange and teal lines indicate their median values (gray shaded regions 1σ uncertainty). Curvy red line represents the early Miocene unconformity (EMU). Bottom left: Geologic map, with red stars indicating locations of U-Pb ages with 2σ uncertainties (Brennan et al., 2024). Bottom right: Field photographs; notice the well-defined difference in lithologic color.

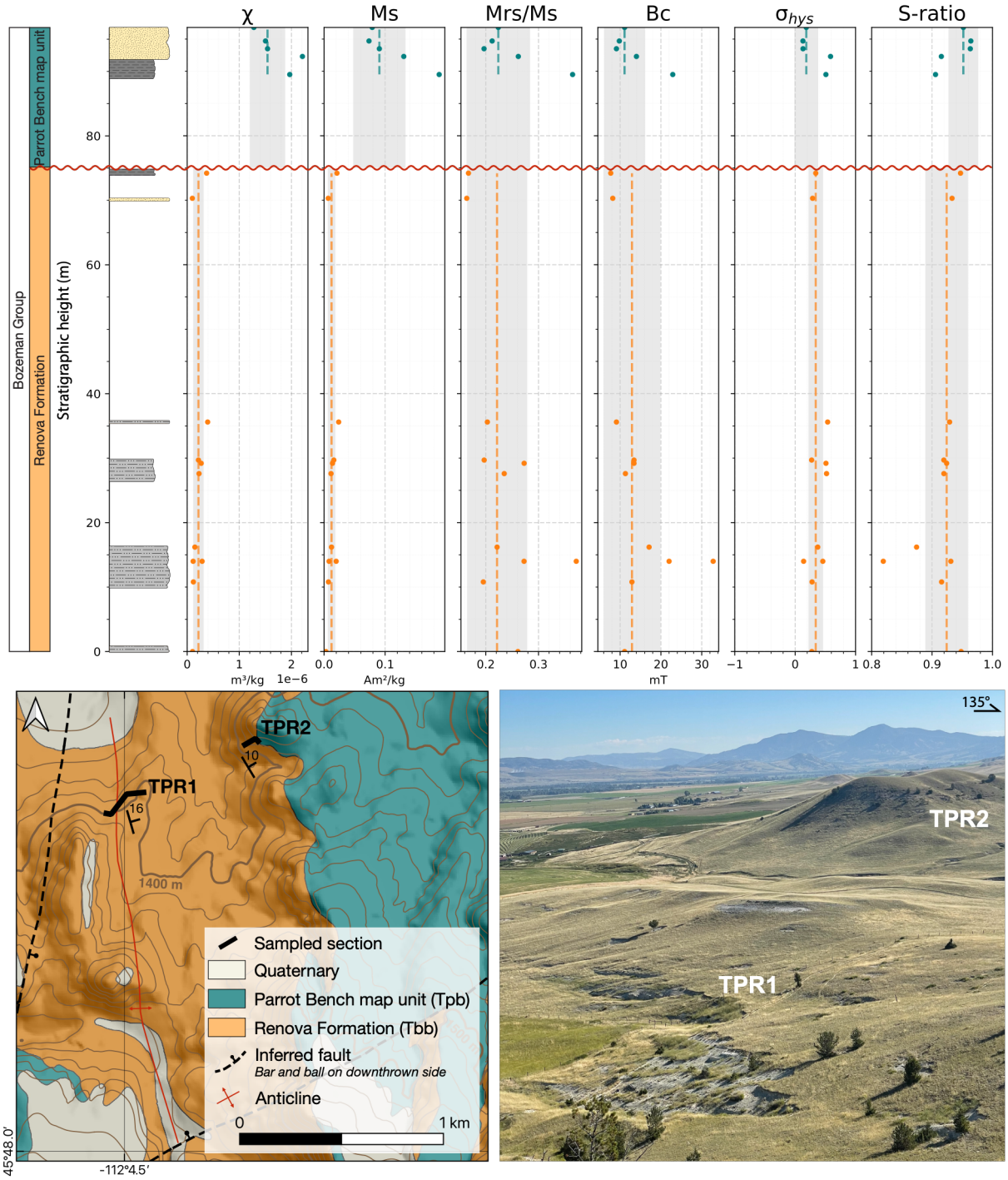

Figure S5. Overview of the TPR section. Top: Simplified sedimentary log (legend in fig. S1) and rock magnetic properties. From left to right: magnetic susceptibility (χ), saturation magnetization (Ms), saturation remanent magnetization (Mrs) divided by Ms, coercive force (Bc), hysteresis shape parameter (σ_{hys}), and hematite to magnetite concentration (S-ratio). Dashed orange and teal points represent samples taken from the Renova Formation (N = 11) and Sixmile Creek Formation (N = 5), respectively. Orange and teal lines indicate their median values (gray shaded regions 1σ uncertainty). Curvy red line represents the early Miocene unconformity (EMU). Bottom left: Geologic map (Vuke et al., 2004). Bottom right: Field photograph.

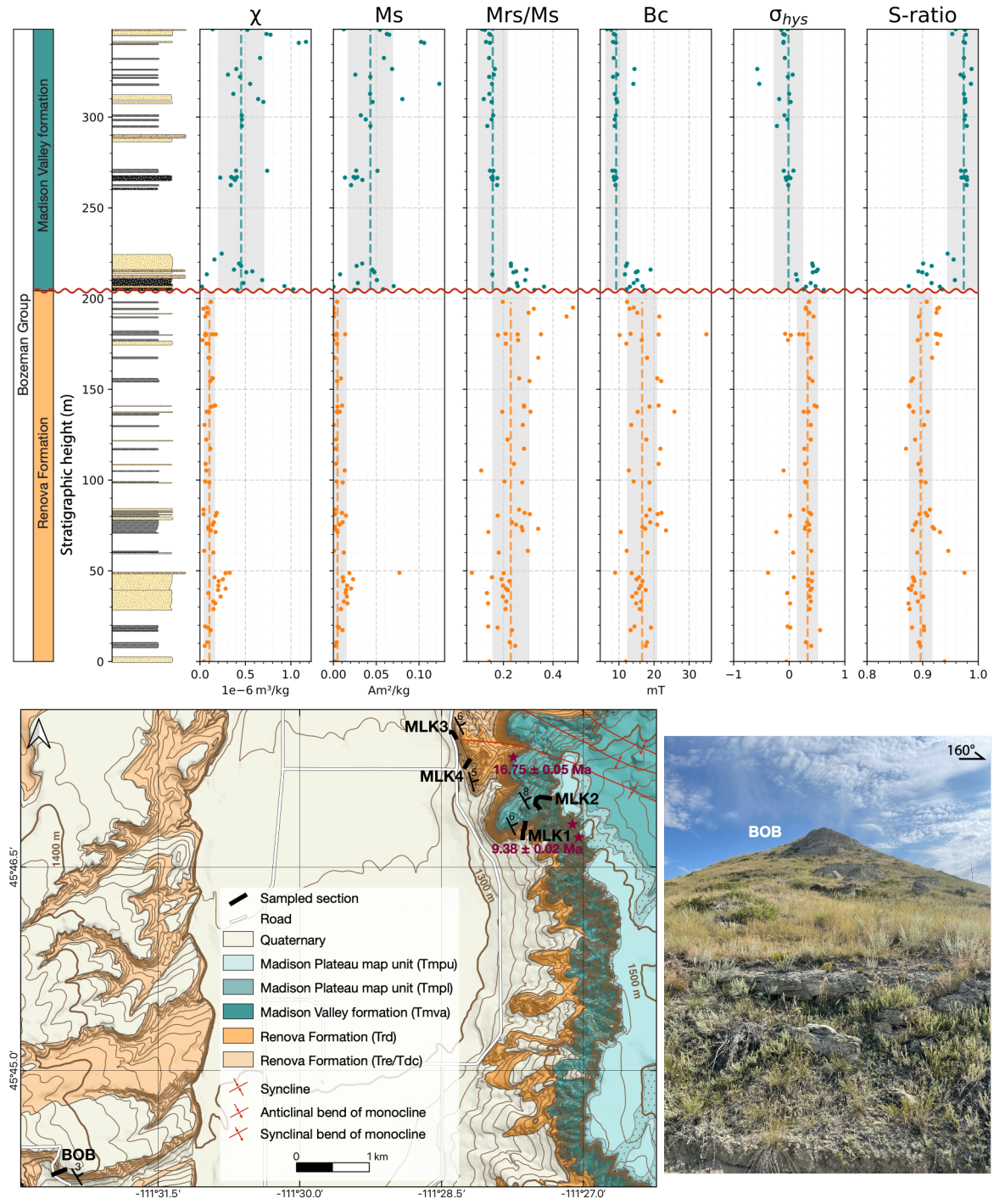

Figure S6. Overview of the MLK and BOB sections. Top: Simplified sedimentary log (legend in fig. S1) and rock magnetic properties. From left to right: magnetic susceptibility (χ), saturation magnetization (Ms), saturation remanent magnetization (Mrs) divided by Ms, coercive force (Bc), hysteresis shape parameter (σ_{hys}), and hematite to magnetite concentration (S-ratio). Orange and teal points represent samples taken from the Renova Formation (N = 65) and Sixmile Creek Formation (N = 39), respectively. Dashed orange and teal lines indicate their median values (gray shaded regions 1σ uncertainty). Curvy red line represents the early Miocene unconformity (EMU). Bottom left: Geologic map of the MLK (Vuke, 2003) and BOB (Vuke, 2006) sections. Red stars indicate locations of U-Pb ages with 2σ uncertainties (Montejo et al., 2023). Bottom right: Field photograph.

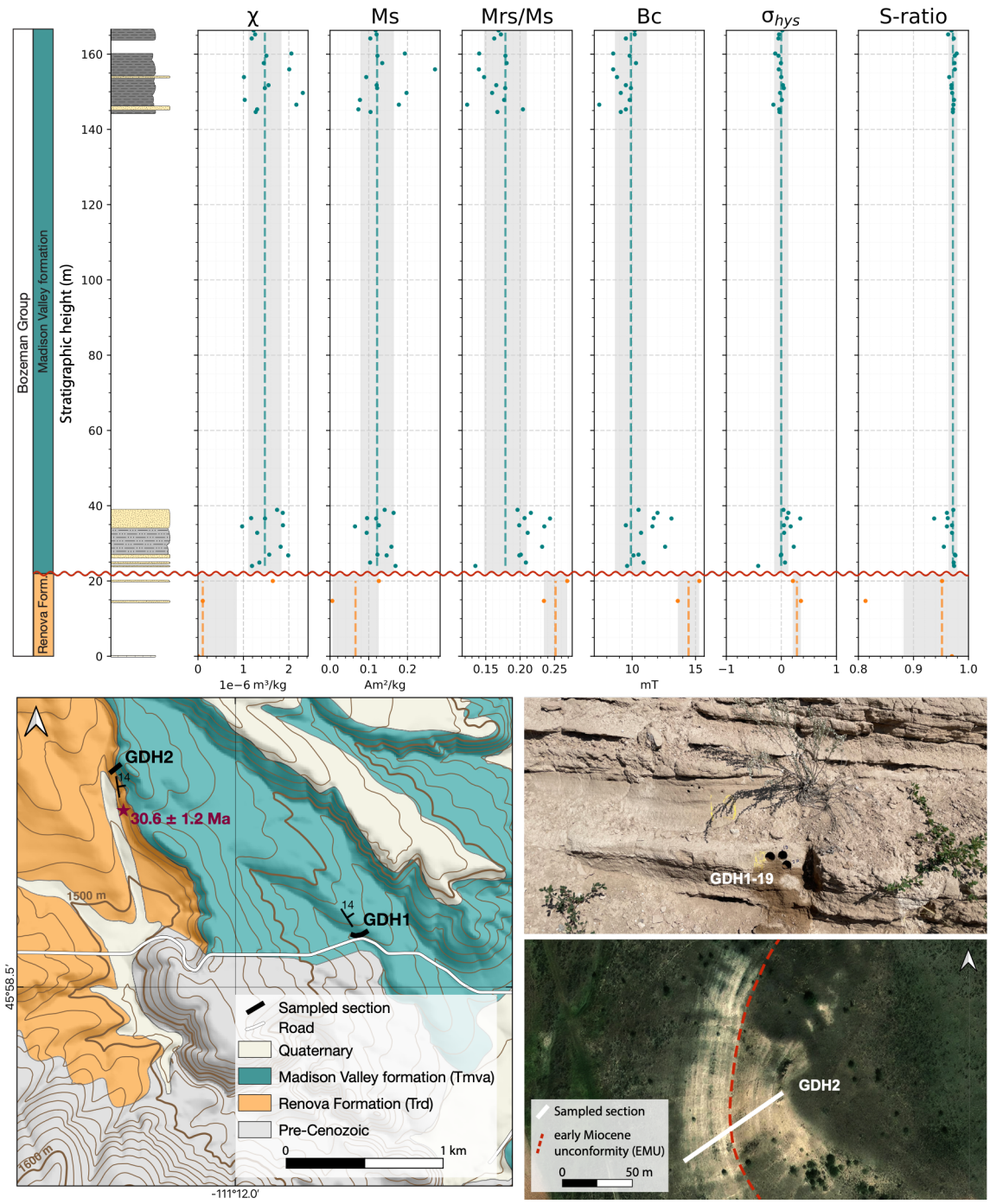

Figure S7. Overview of the GDH section. Top: Simplified sedimentary log (legend in fig. S1) and rock magnetic properties. From left to right: magnetic susceptibility (χ), saturation magnetization (Ms), saturation remanent magnetization (Mrs) divided by Ms, coercive force (Bc), hysteresis shape parameter (σ_{hys}), and hematite to magnetite concentration (S-ratio). Orange and teal points represent samples taken from the Renova Formation (N = 3) and Sixmile Creek Formation (N = 27), respectively. Dashed orange and teal lines indicate their median values (gray shaded regions 1σ uncertainty). Curvy red line represents the early Miocene unconformity (EMU). Bottom left: Geologic map; adjusted from Vuke (2003) by projecting the observed position of the EMU on the map, assuming a constant bedding attitude of dip direction = 62°N and dip = 14°. Approximate location of K–Ar age indicated by the red star (Hughes, 1980). Right: Field photograph. Bottom right: Satellite image (Environmental Systems Research Institute, 2009).

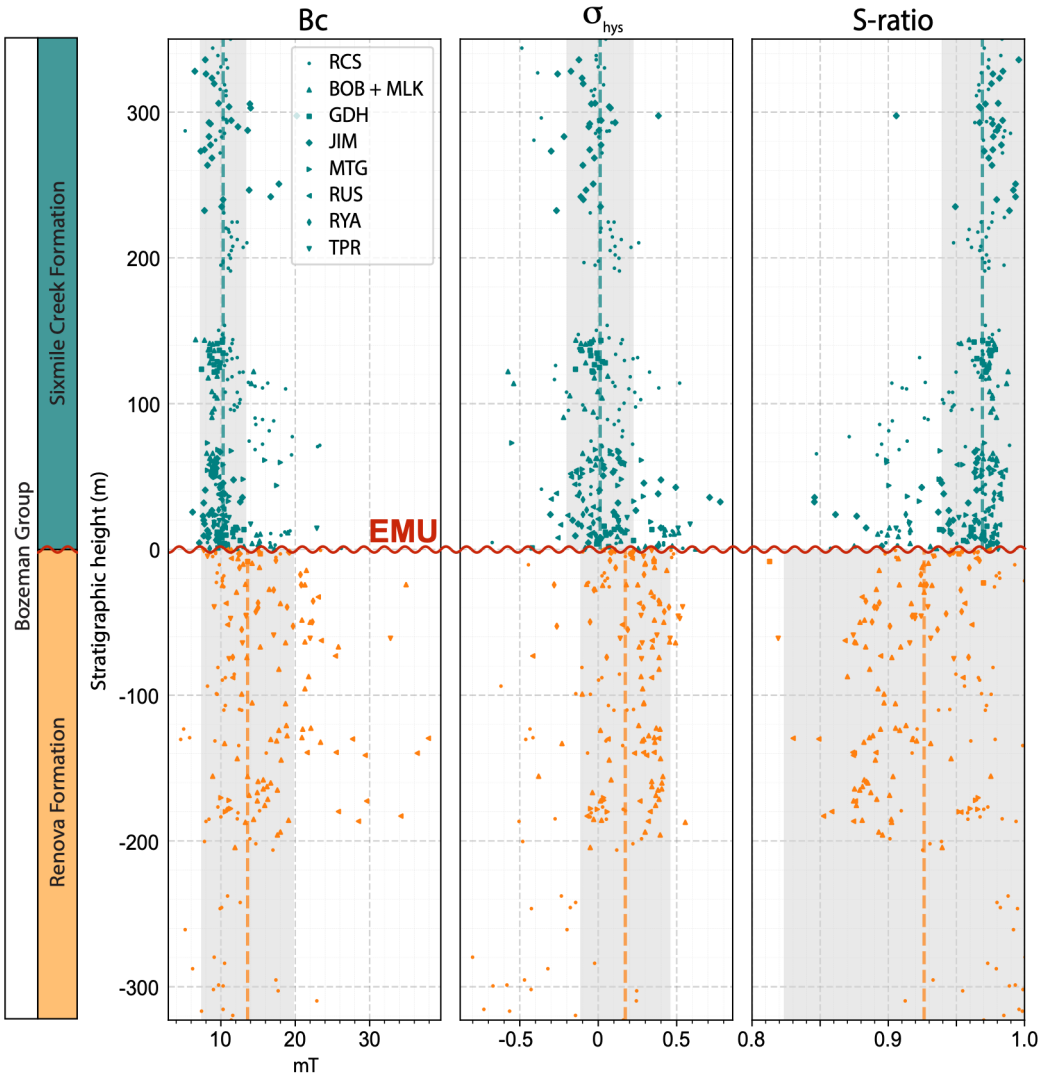

Figure S8. Additional rock magnetic properties of the eight sections. Sections aligned at the early Miocene unconformity (EMU; curvy red line) positioned at 0 m. From left to right: coercive force (Bc), hysteresis shape parameter (σ_{hys}), and S-ratio. Orange and teal points represent samples taken from the Renova Formation (N = 123) and Sixmile Creek Formation (N = 175), respectively. Dashed orange and teal lines indicate median values; shaded regions, 1σ uncertainty.

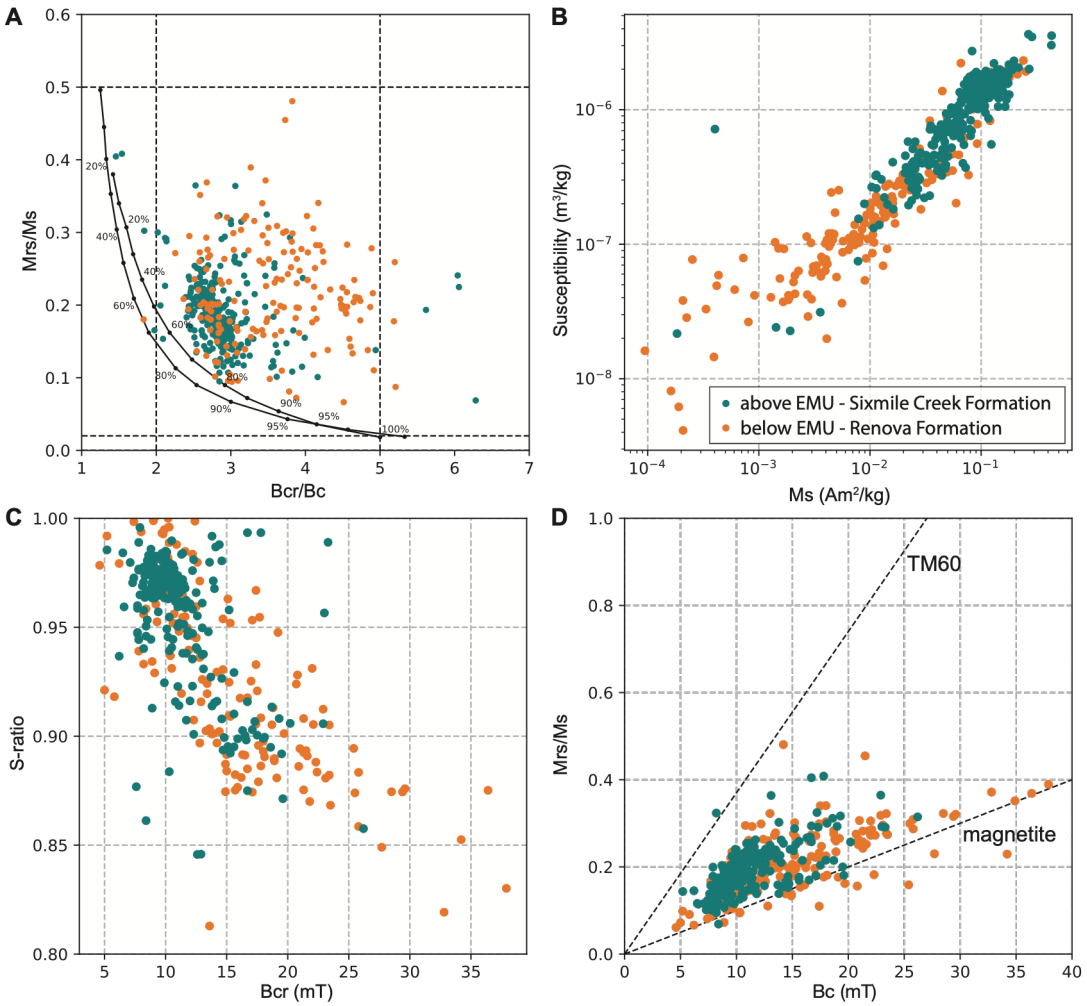

Figure S9. Rock magnetic diagrams. (A) Day diagram (Day et al., 1977) with the SD + MD mixing curves of Dunlop (2002). **(B)** Susceptibility versus the saturation magnetization (Ms). **(C)** Coercivity of remanence (Bcr) versus the S-ratio. **(D)** Néel diagram (Néel, 1955) with the trend lines for magnetite and titanomagnetite with x = 0.6 (TM60) of Wang and Van der Voo (2004). Orange and teal points represent samples taken from the Renova Formation (N = 123) and Sixmile Creek Formation (N = 175), respectively.

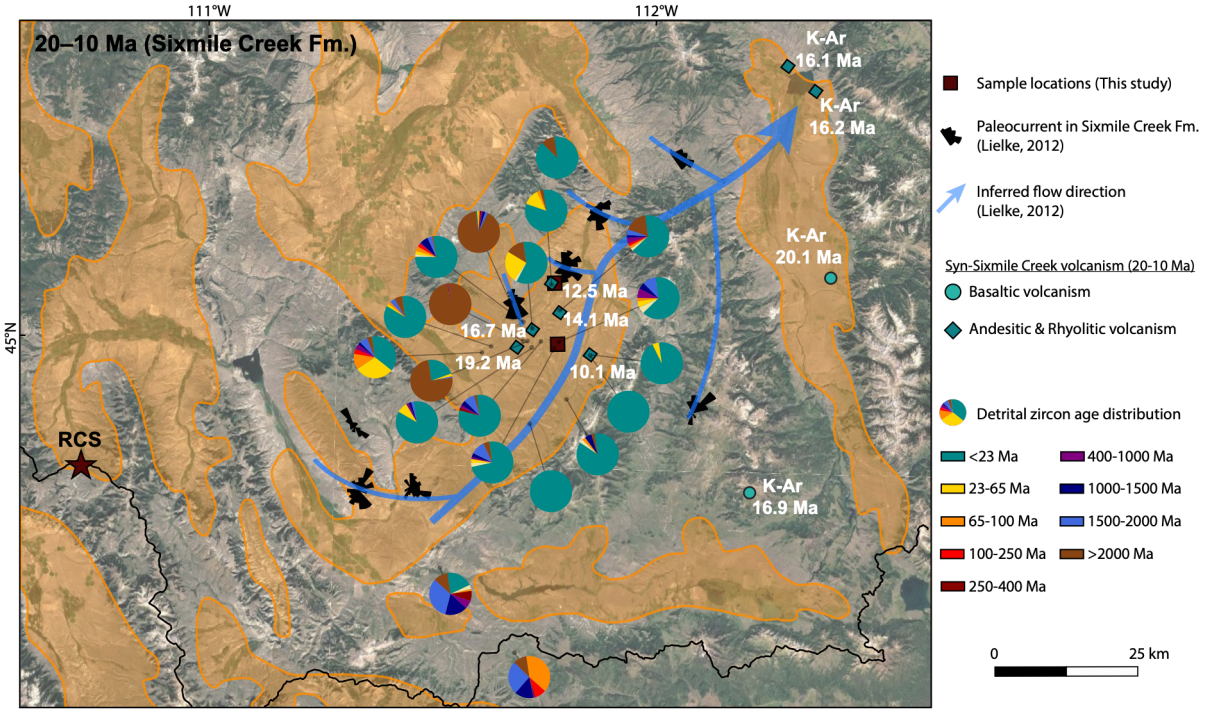

Figure S10. Zoom-in of Ruby Basin data. Ruby Basin detrital zircon pie charts (Brennan et al., 2024; Mosolf et al., 2023; Staisch et al., 2022) and paleocurrent rose diagrams (Lielke, 2012) from the Sixmile Creek Formation. Miocene volcanic K–Ar ages (Fritz et al., 2007) and U-Pb ages (Brennan et al., 2024; Mosolf, 2015,2021). Orange basin outlines from Vuke (2020). Satellite image from Environmental Systems Research Institute (2009).

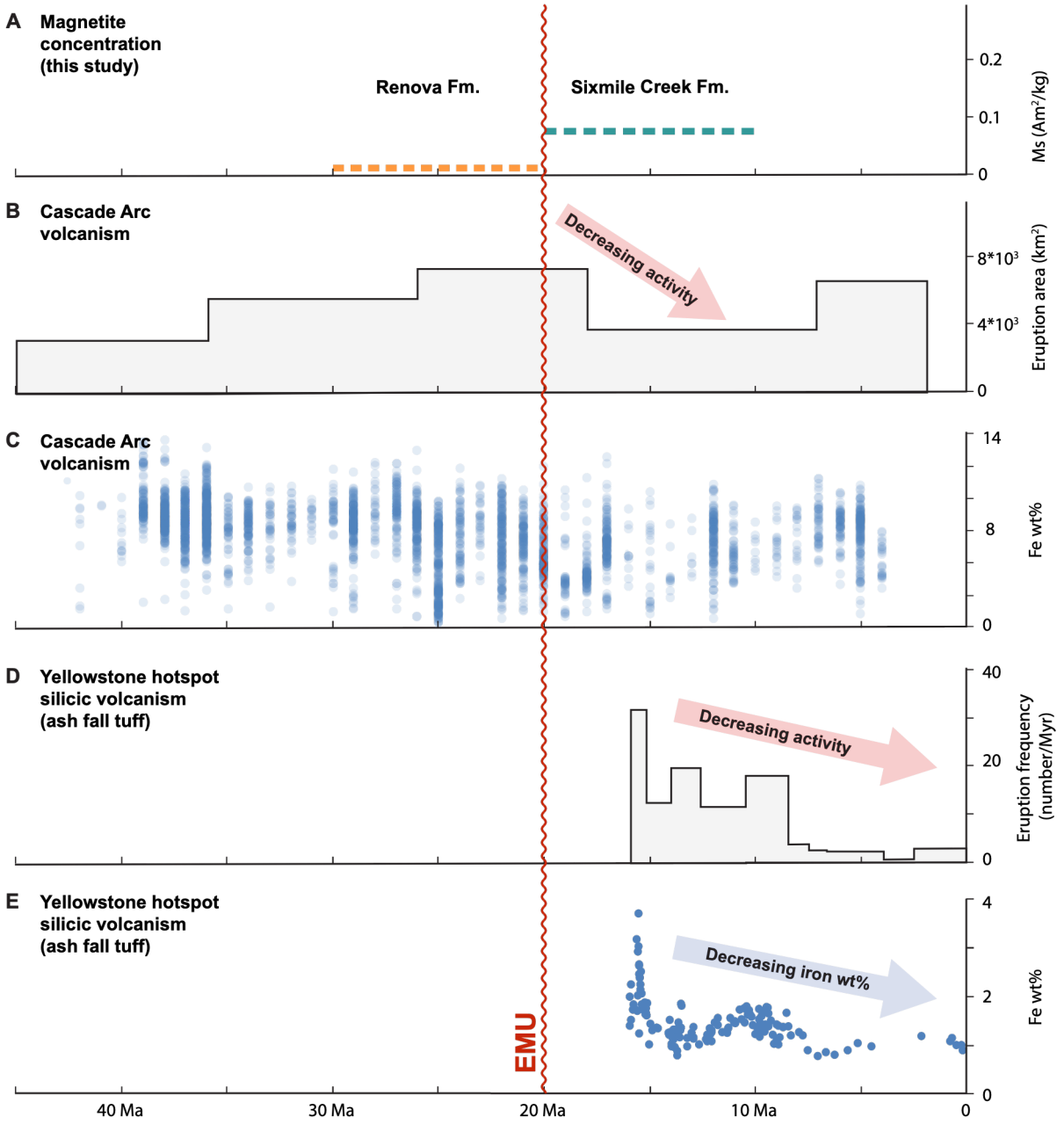

Figure S11. Overview of volcanic activity 45–0 Ma. (A) Median magnetite concentration (Ms = saturation magnetization) from southwestern Montana. **(B)** Eruption activity and **(C)** iron concentration related to Cascade Arc volcanism (du Bray and John, 2011). **(D)** Activity and **(E)** iron concentration of Yellowstone hotspot silicic volcanism (Perkins and Nash, 2002). EMU = early Miocene unconformity.

Data S1. GPS coordinates. Date, latitude, longitude, and elevation from handheld GPS measurements, visually estimated stratigraphy within each subsection, and projected stratigraphic position of each sample. A comment was added in case we diverged from the standard method of projecting the GPS latitude, longitude, and elevation of each sample with the average bedding. Excel file available at: https://doi.org/10.1126/sciadv.adz4275

Data S2. Bedding measurements and rock magnetic parameters. Excel file available at: https://doi.org/10.1126/sciadv.adz4275

Data S3. Detrital zircon samples and their references. Excel file available at: https://doi.org/10.1126/sciadv.adz427

Appendix C:
Supplementary Information Chapter 4

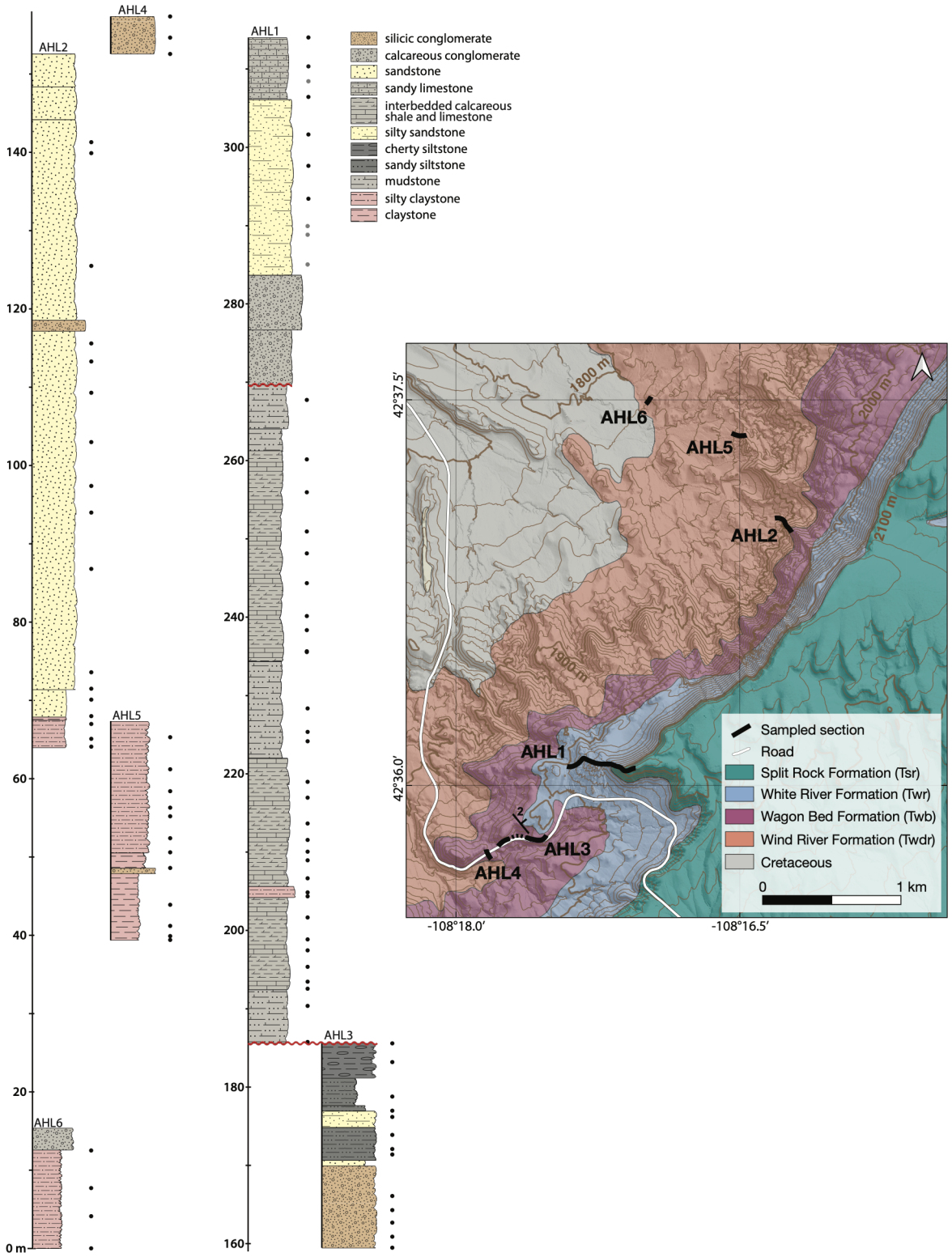

Figure S1. (left) Detailed sedimentary columns of individual sections (AHL1-AHL6) that together make the composite section in Figure 7. Dots indicate the sampling sites; grey dots indicate samples that were interpreted to be lightning-struck. The curvy red line shows the stratigraphic position of unconformities. **(right)** Geologic map of the Abandoned Highway Lander (AHL) section (Johnson and Sutherland, 2009). The displayed road is a now-abandoned alignment of U.S. Route 287, corresponding to the course depicted in the plates of Van Houten (1964). Shaded relief map from NOAA (2022).

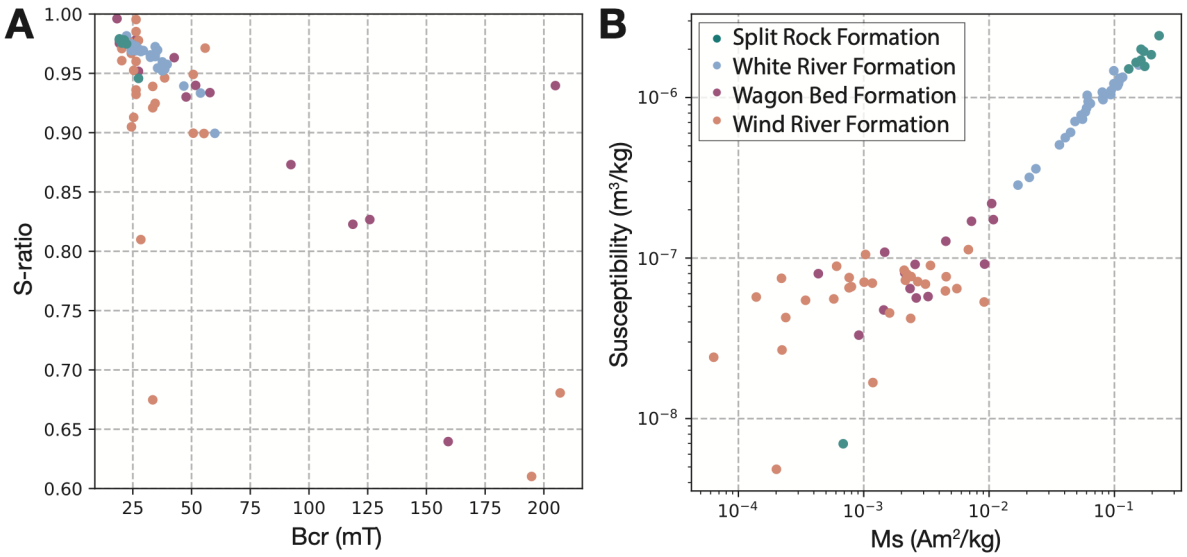

Figure S2. (A) Coercivity of remanence (Bcr) versus S-ratio. **(B)** Susceptibility versus saturation magnetization (Ms).

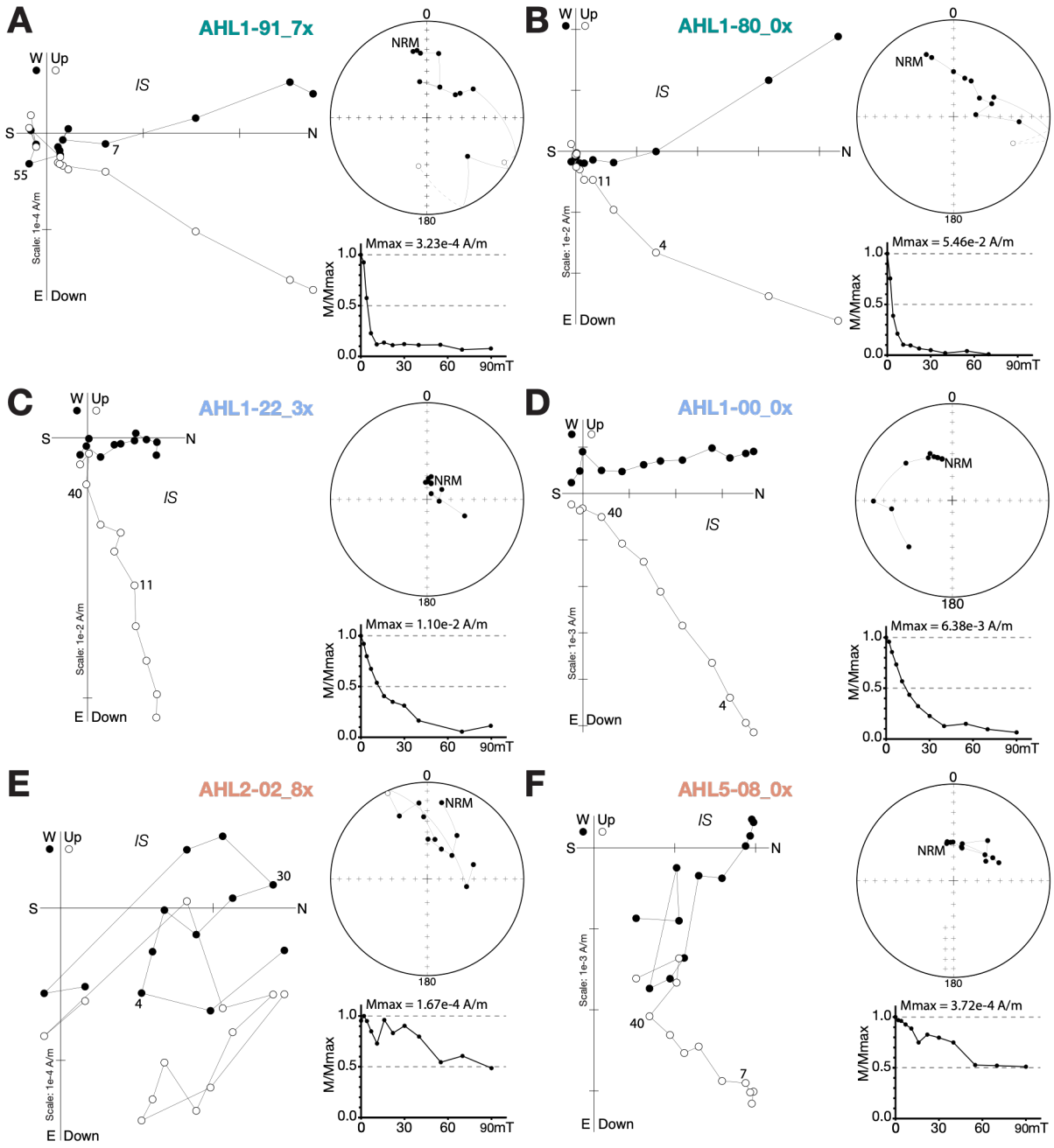

Figure S3. Examples of paleomagnetic and rock magnetic data of samples from the Split Rock Formation **(A–B)**, White River Formation **(C–D)**, and Wind River Formation **(E–F)**. Displayed are the Zijderveld diagram, stereographic projection, and moment decay plot of the AF directional data.

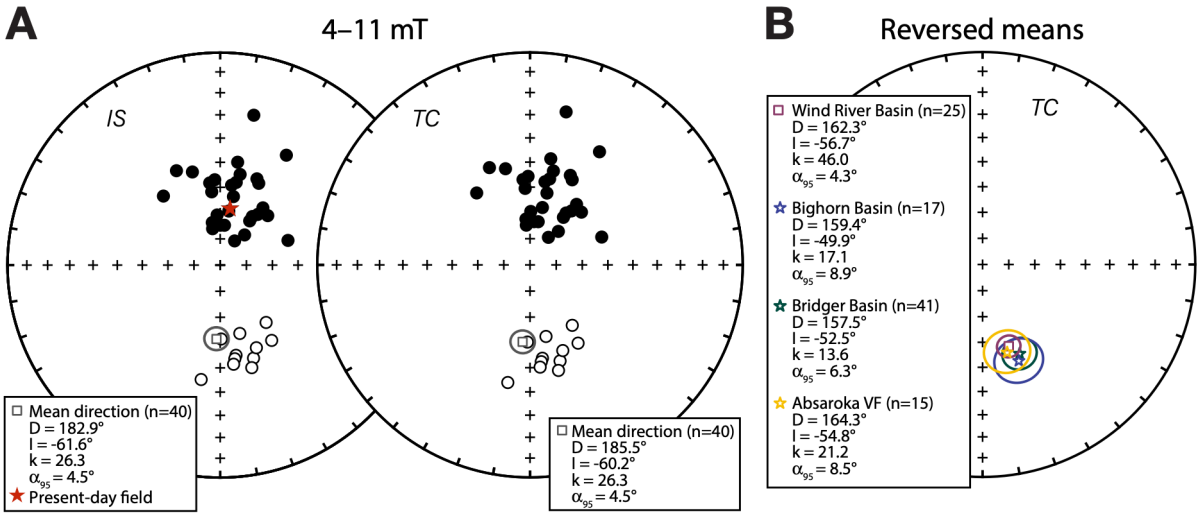

Figure S4. (A) Best-fit directions of low coercivity steps (4–11 mT) of the Wind River Basin data in in-situ (IS) and tilt-corrected (TC) coordinates. **(B)** Mean directions of reversed data from the Wind River Basin (this study), Bighorn Basin (Clyde et al., 2007), Bridger Basin (Tsukui et al., 2025), and Absaroka Volcanic Field (VF) (Harlan and Morgan, 2010).

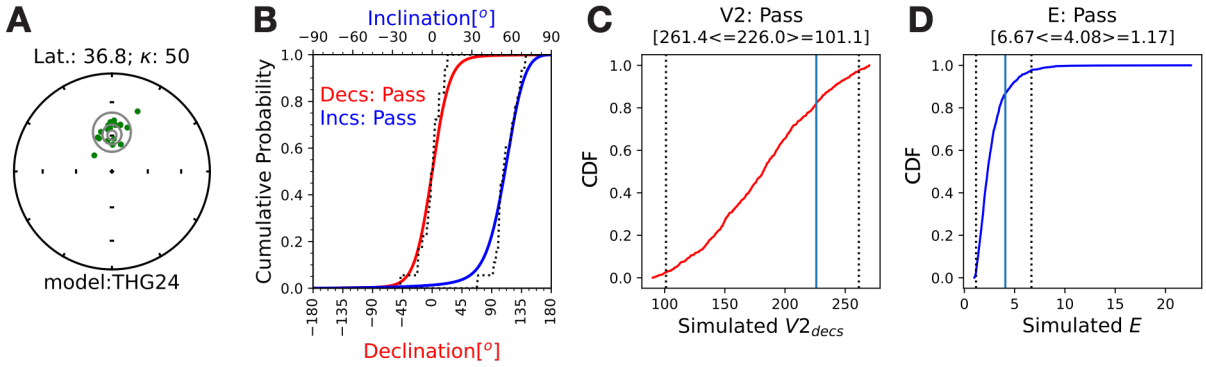

Figure S5. Results of the SVEI test of Wagon Bed Formation data (n=18) against the THG24 model (Tauxe et al., 2024). **(A)** Equal area projection of the best-fit data from the Wagon Bed Formation (n=18); gray contours are probability densities. The latitude (Lat.) listed above the equal area projection was calculated from the data based on the average inclination. **(B)** Two Anderson-Darling tests (A2D, A2I). Empirical cumulative distribution functions (dotted lines) of data drawn from the THG24 model plotted against the predicted cumulative density functions (CDF) of the data (solid lines). **(C)** Declination of the V2 direction ($V2_{dec}$) from the data (solid vertical line) compared to the CDF of 1000 datasets drawn from THG24 (red line); dotted vertical lines are bounds containing 95% of the datasets. **(D)** Elongation (E) of the data (solid vertical line) and the simulations (solid blue line).

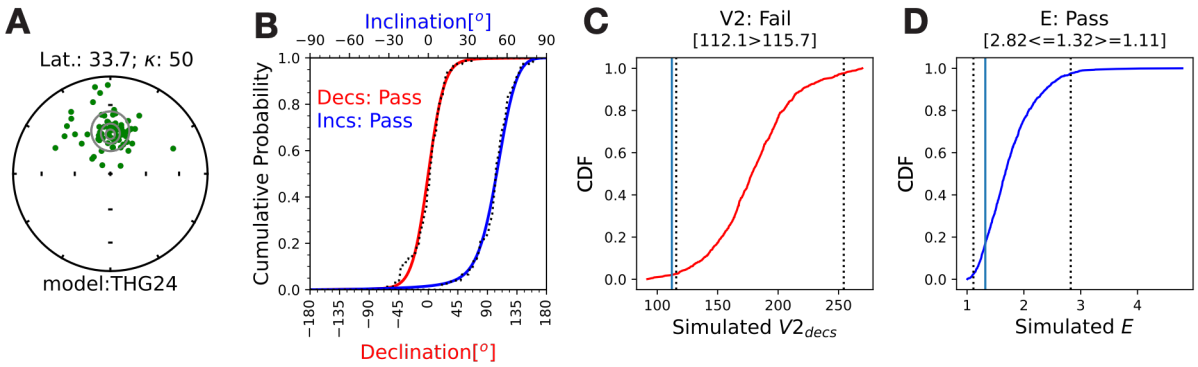

Figure S6. Results of the SVEI test of the Eocene sedimentary dataset against the THG24 model (Tauxe et al., 2024); dataset consists of data from the Wind River Basin (n = 18; this study), Bighorn Basin (n = 17; Clyde et al., 2007), and Bridger Basin (n = 41; Tsukui et al., 2025). **(A)** Equal area projection of the dataset; gray contours are probability densities. The latitude (Lat.) listed above the equal area projection was calculated from the data based on the average inclination. **(B)** Two Anderson-Darling tests (A2D, A2I). Empirical cumulative distribution functions (dotted lines) of data drawn from the THG24 model plotted against the predicted cumulative density functions (CDF) of the data (solid lines). **(C)** Declination of the V2 direction ($V2_{dec}$) from the data (solid vertical line) compared to the CDF of 1000 datasets drawn from THG24 (red line); dotted vertical lines are bounds containing 95% of the datasets. **(D)** Elongation (E) of the data (solid vertical line) and the simulations (solid blue line).

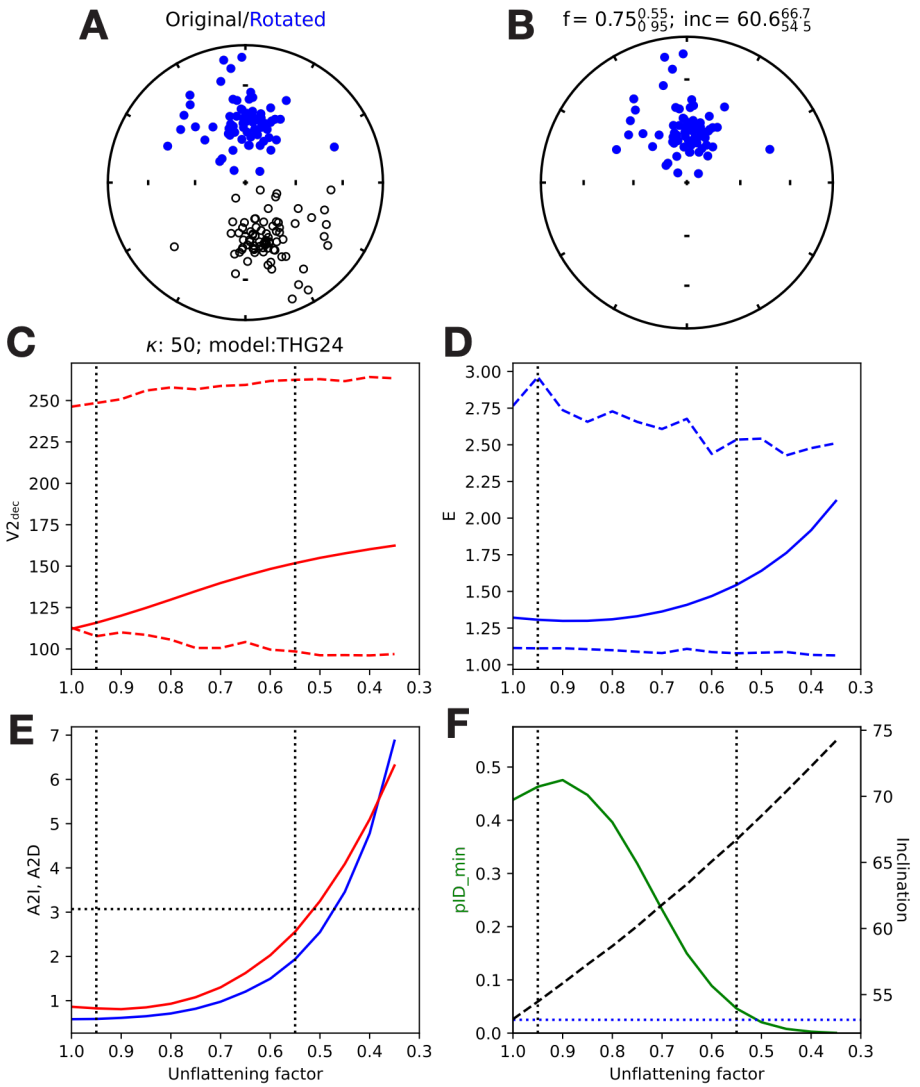

Figure S7. Results from progressive unflattening using the THG24 field model (Tauxe et al., 2024). Equal area projections of the Eocene sedimentary data **(A)** originally (black) and after reversing and rotating to North (blue), and **(B)** after unflattening. Distributions of the **(C)** V2 direction ($V2_{dec}$) and **(D)** elongation from Monte Carlo simulations (95% of results are between the dashed lines) compared with the data (solid line). **(E)** Anderson-Darling tests; red (blue) line is A2D (A2I). **(F)** The green line represents pID_{min}, the dotted blue line represents the 95% confidence level above which the distribution is consistent with the model, and the black dashed line represents the inclination. Vertical dotted lines in panels (C–F) are bounds within which all tests pass.

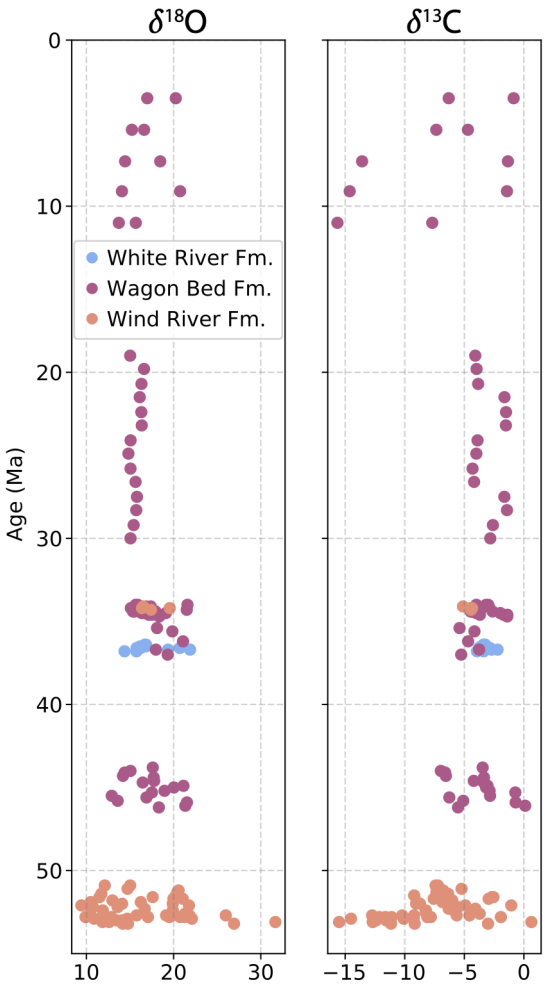

Figure S8. Isotope records from calcite cement in the Wind River Basin (Chamberlain et al., 2012). The vertical axis represents the age assigned by Chamberlain et al. (2012). Color represents the sampled formation based on the sample GPS location on the geologic map.

Table S1. Date, latitude, longitude, and elevation from handheld GPS measurements, visually estimated stratigraphy within each subsection, and projected stratigraphic position of each sample. A comment was added in case we diverged from the standard method of projecting the GPS latitude, longitude, and elevation of each sample with the average bedding. File available at: https://github.com/DiekeGerritsen/PhDThesis_Gerritsen_2025

Table S2. Rock magnetic parameters and paleomagnetic directions. File available at: https://github.com/DiekeGerritsen/PhDThesis_Gerritsen_2025

Table S3. Detrital zircon samples and their references. File available at: https://github.com/DiekeGerritsen/PhDThesis_Gerritsen_2025

Appendix D:
Supplementary Information Chapter 5

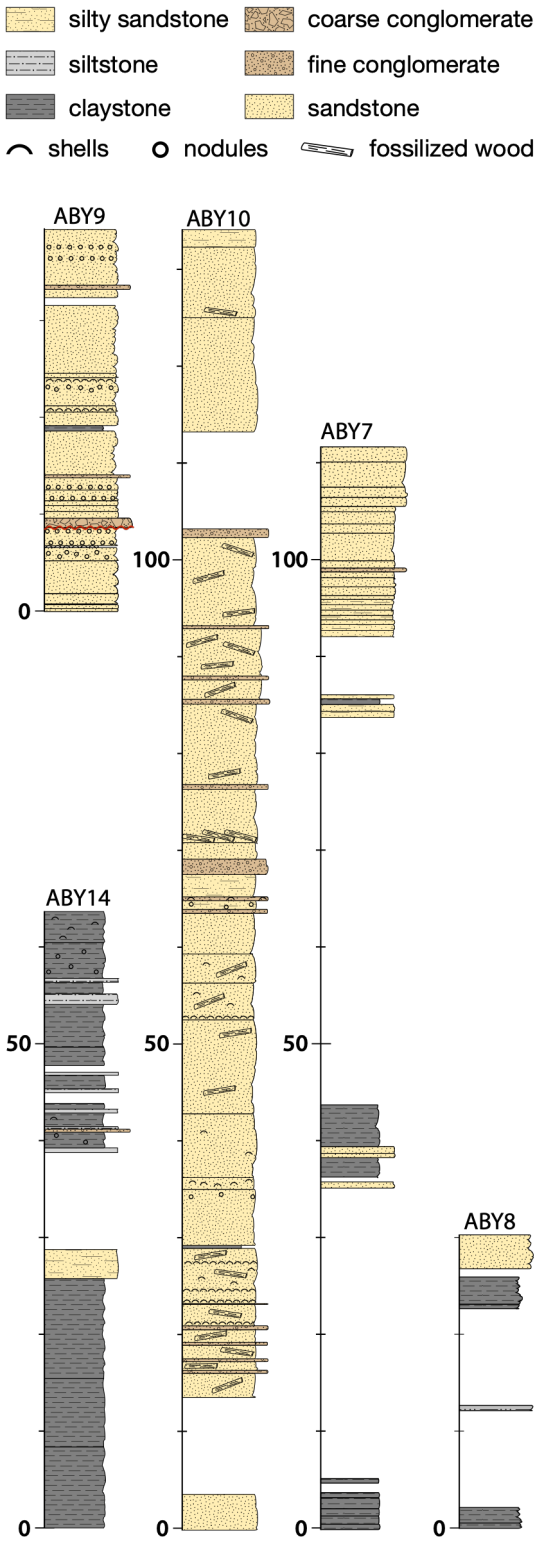

Figure S1. Detailed sedimentary columns of individual sections (ABY7–ABY10 and ABY14) that together made the composite section in Figure 4.

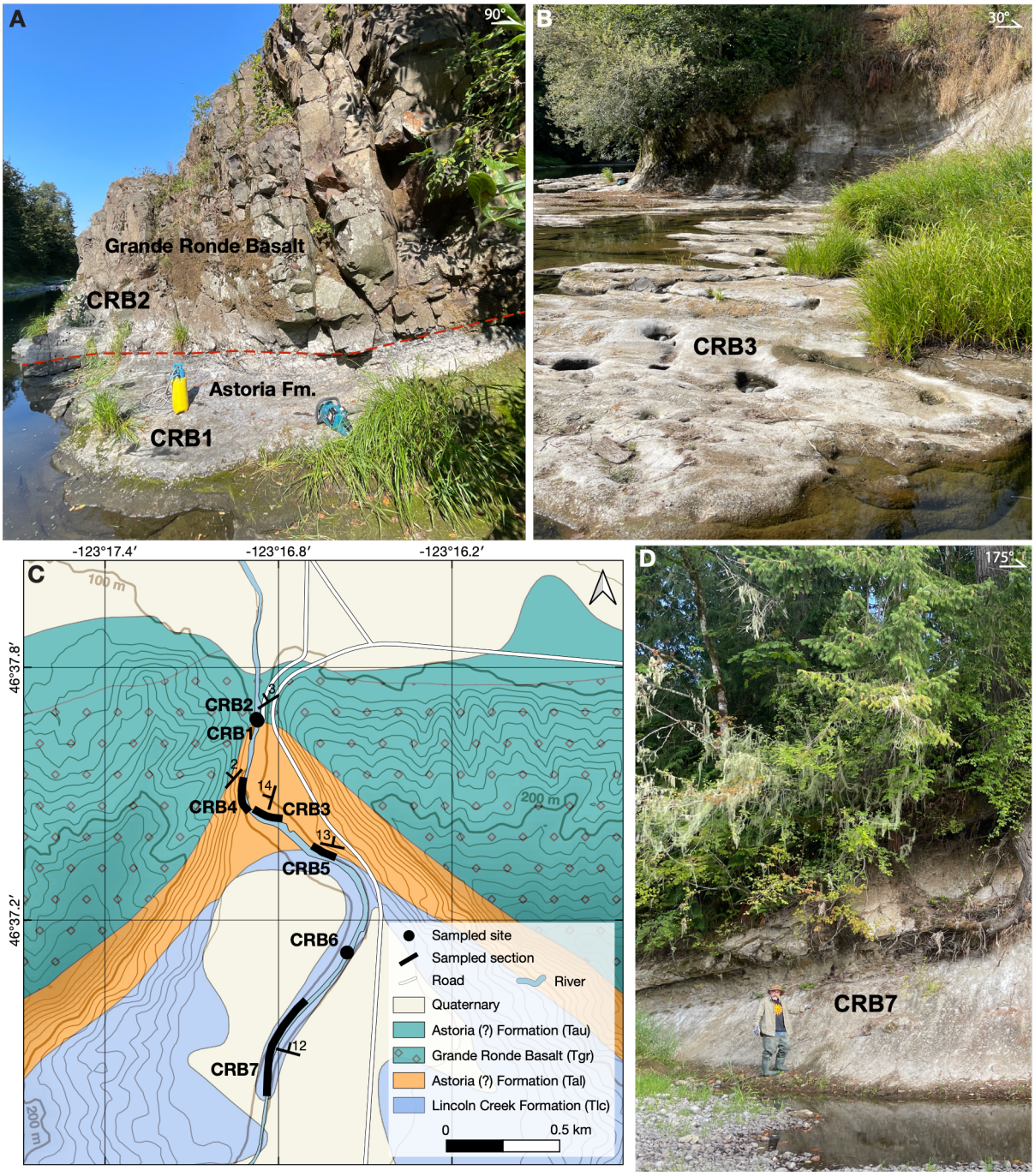

Figure S2. (A) Contact between the Astoria Formation (CRB1) and the Grande Ronde Basalt (CRB2). **(B)** Overview of the flat-lying beds of the CRB3 subsection. **(C)** Geologic map of the CRB sites and subsections along the Chehalis River (Pease and Hoover, 1957; Wells and Sawlan, 2014). Shaded relief map from NOAA (2022). **(D)** Overview of the CRB7 site.

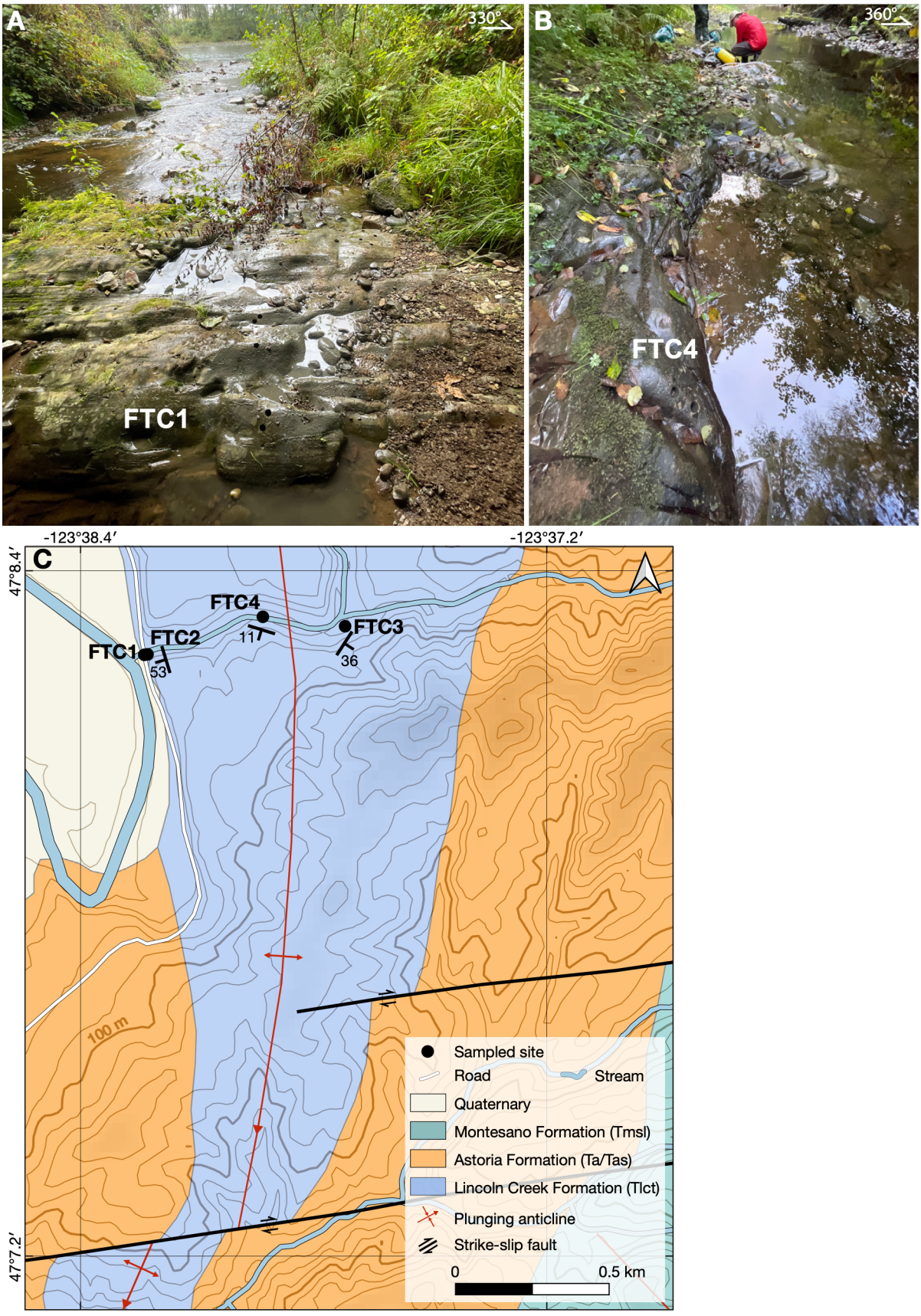

Figure S3. (A) Overview of the FTC1 site. **(B)** Overview of the FTC4 site. **(C)** Geologic map of the FTC sites in Carter Creek flowing into the Wynoochee River, which crosses the Wynoochee Valley Anticline (Rau, 1967; Tabor and Cady, 1978). Shaded relief map from NOAA (2022).

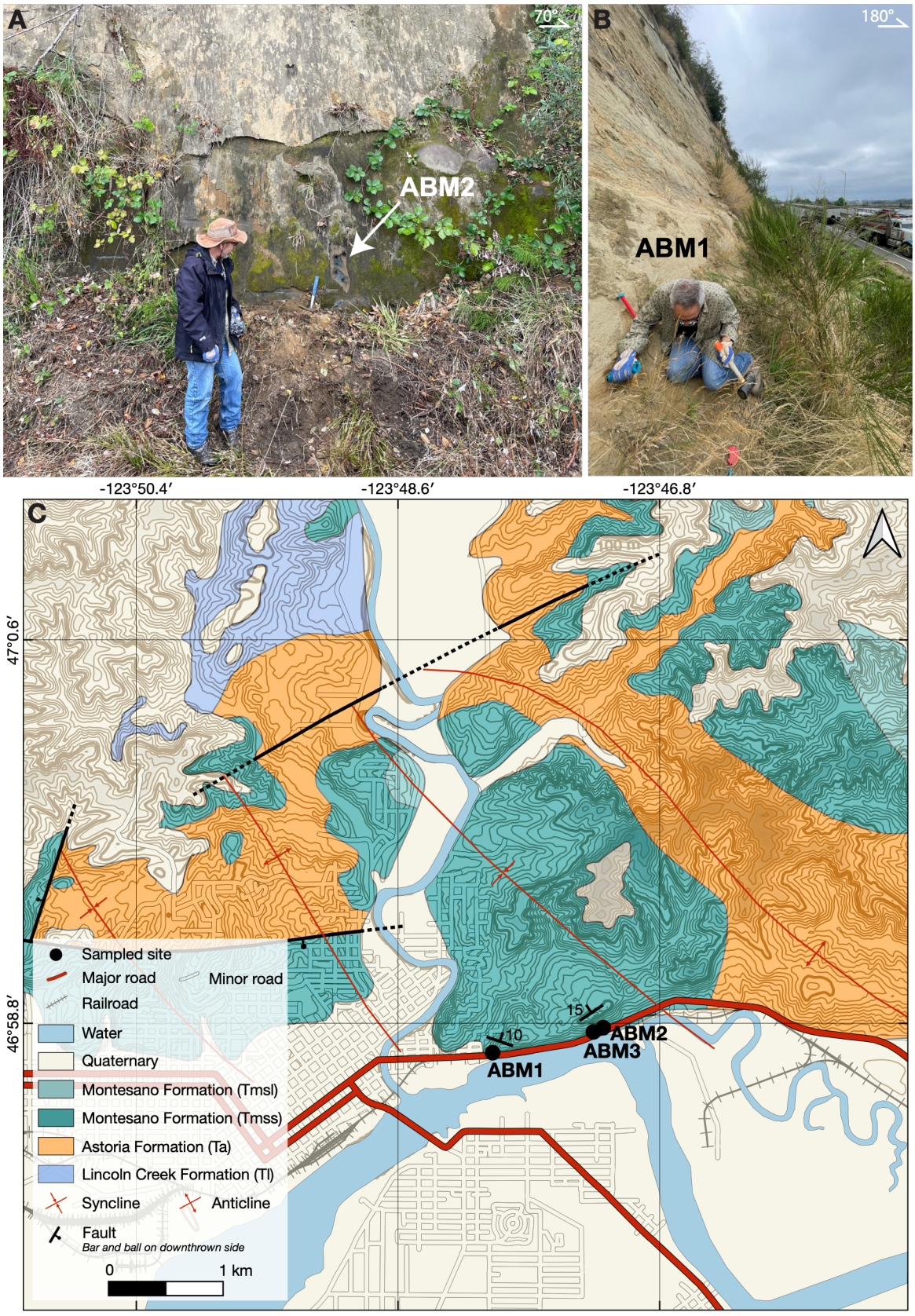

Figure S4. (A) Overview of the ABM2 site. **(B)** Overview of the ABM1 site; sampling with the soft sediment sampler. **(C)** Geologic map of the ABM sites in Aberdeen along the U.S. Highway 12, in between the Reservoir Anticline and the Cemetery Syncline (Gower and Pease, 1965; Rau, 1986). Shaded relief map from NOAA (2022).

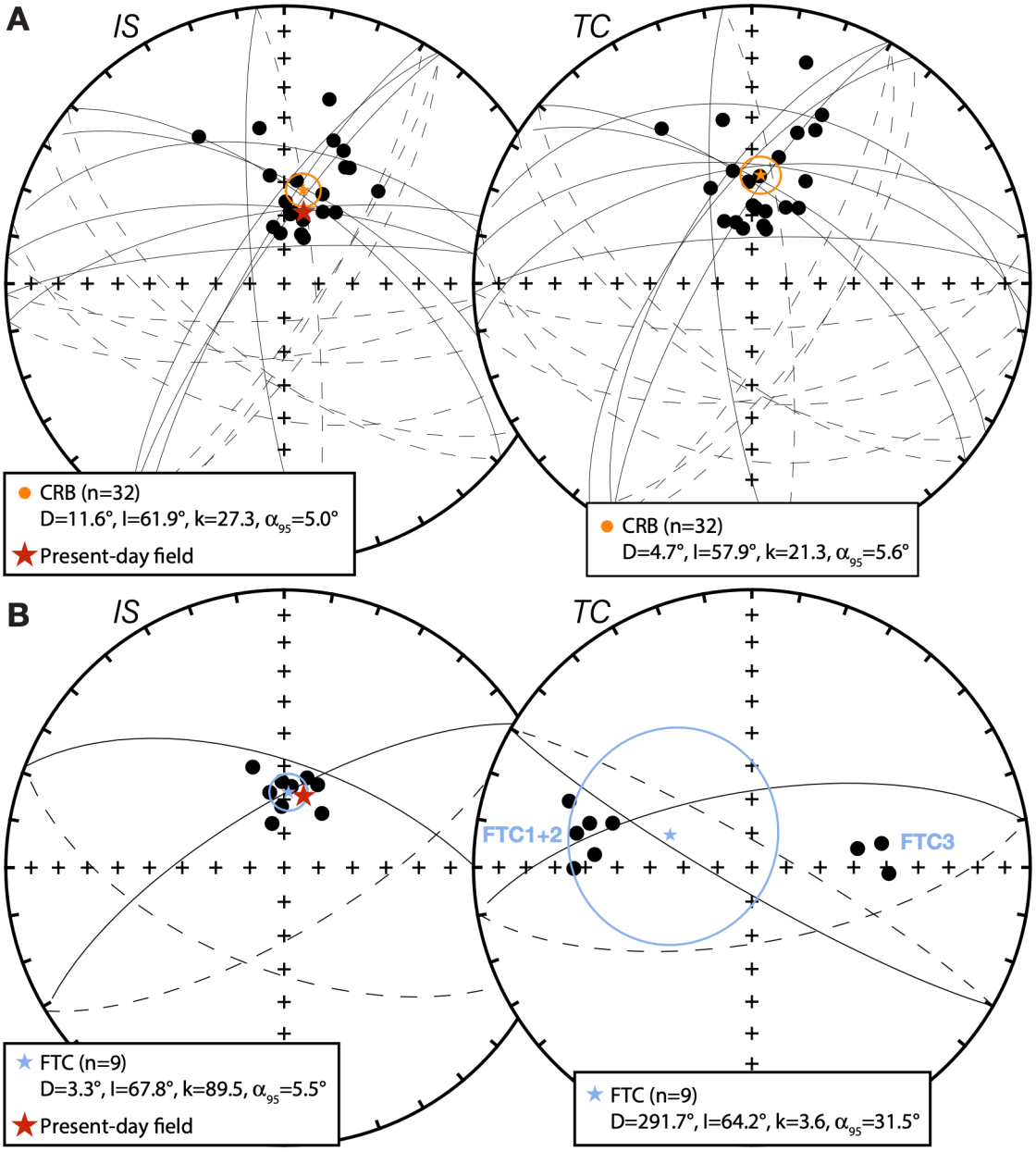

Figure S5. Stereographic projection of the best-fit (points) and great circle paleomagnetic directions of the **(A)** CRB section and **(B)** FTC location in in-situ (IS) and tilt-corrected (TC) coordinates. Closed (open) symbols indicate lower (upper) hemisphere. The mean direction of the CRB section (McFadden and McElhinny, 1988) and the Fisher (1953) mean of the FTC location and their Fisher (1953) statistic parameters are displayed.

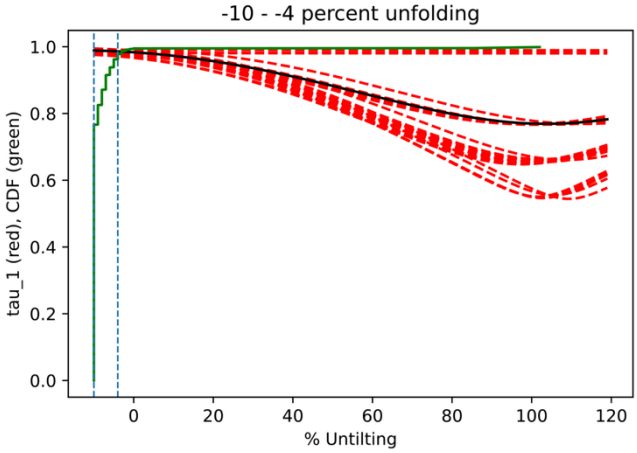

Figure S6. Results of the bootstrap fold test of Tauxe and Watson (1994) on the best-fit data of the FTC site (n=9). Tightest grouping of vectors obtained between -4% and -10% of unfolding (95% confidence bounds, indicated with dashed blue lines). CDF = cumulative distribution function, τ_1 = largest eigenvalue of the orientation matrix.

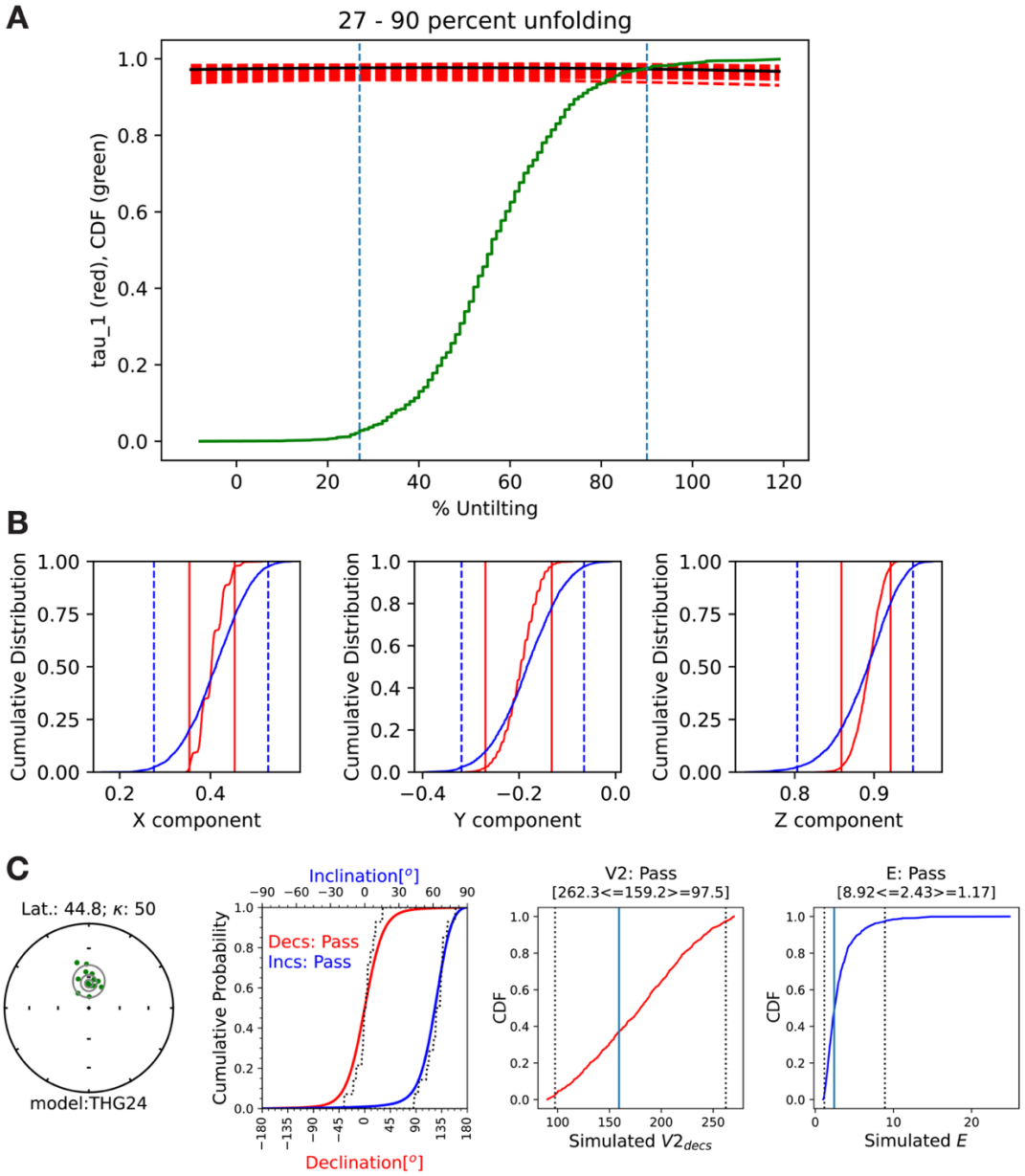

Figure S7. Statistical tests on ABY10 data (n=14). **(A)** Results of the bootstrap fold test (Tauxe and Watson, 1994), indicating the tightest grouping of vectors is obtained between 27% and 90% of unfolding (95% confidence bounds, indicated with dashed blue lines). CDF = cumulative distribution function, τ_1 = largest eigenvalue of the orientation matrix. **(B)** Results of the parametric bootstrap reversal test on normal (blue) and reversed (red) data (Tauxe, 2010). Vertical lines represent intervals containing 95% of each set. **(C)** Results of the SVEI test (Tauxe et al., 2024) against the THG24 model. (left) Equal area projection of the data; gray contours are probability densities. The latitude (Lat.) listed above the equal area projection was calculated from the data based on the average inclination. (middle left) Two Anderson-Darling tests (A2D, A2I). Empirical cumulative distribution functions (dotted lines) of data drawn from the THG24 model plotted against the predicted CDF of the data (solid lines). (middle right) $V2_{dec}$ from the data (solid vertical line) compared to the CDF of 1000 datasets drawn from THG24 (red line); dotted vertical lines are bounds containing 95% of the datasets. (right) Elongation (E) of the data (solid vertical line) and the simulations (solid blue line).

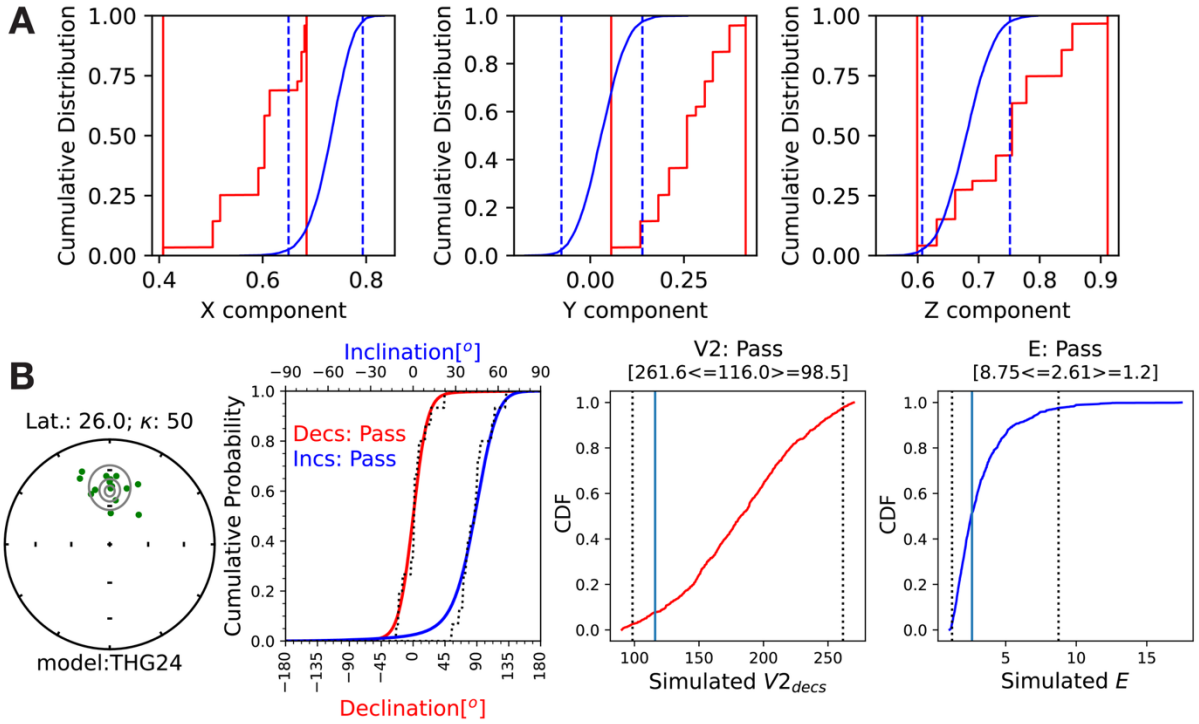

Figure S8. Statistical tests on ABY14 data (n=15). **(A)** Results of the parametric bootstrap reversal test on normal (blue) and reversed (red) data (Tauxe, 2010). Vertical lines represent intervals containing 95% of each set. **(B)** Results of the SVEI test (Tauxe et al., 2024) against the THG24 model. Caption in Figure S7.

Table S1. Latitude and longitude from handheld GPS measurements and bedding attitude measurements. Stratigraphic position of samples from the ABY section, determined from manual measurements within a subsection and GPS location in combination with bedding attitude between subsections. Excel file available at:
https://github.com/DiekeGerritsen/PhDThesis_Gerritsen_2025

Table S2. Excel spreadsheet of rock magnetic parameters and paleomagnetic directions. Excel file available at: https://github.com/DiekeGerritsen/PhDThesis_Gerritsen_2025

Bibliography

Addicott, W.O. (1976). Neogene molluscan stages of Oregon and Washington, *in* Fritsche, A.E., Ter Best, H., Jr., , Wornardt, W.W., eds., The Neogene symposium-Selected technical papers on paleontology, sedimentology, petrology, tectonics and geologic history of the Pacific Coast of North America. Society for Economic Paleontologists and Mineralogists Pacific Section, 51st Annual Meeting, p. 95-115.

Anderson, A.L. (1947). Drainage diversion in the northern Rocky Mountains of east-central Idaho. *The Journal of Geology*, 55(2):61-75. doi:10.1086/625402.

Armentrout, J.M., Hull, D.A., Beaulieu, J.D., and Rau, W.W. (1983). Correlation of Cenozoic stratigraphic units in western Oregon and Washington State of Oregon Department of Geology and Mineral Industries.

Armentrout, J.M. (1987). Cenozoic stratigraphy, unconformity-bounded sequences, and tectonic history of southwestern Washington, *in* Schuster, J.E., ed., Selected papers on the geology of Washington, vol.77. Washington Division of Geology and Earth Resources Bulletin, p. 291-320.

Axelrod, R.B. (1984). Tertiary sedimentary facies depositional environments and structure Jefferson Basin southwest Montana. [MSc Thesis: University of Montana].

Barnosky, A.D., and Labar, W.J. (1989). Mid-Miocene (Barstovian) environmental and tectonic setting near Yellowstone Park, Wyoming and Montana. *GSA Bulletin*, 101:1448-1456. doi:10.1130/0016--7606(1989)101<1448:MMBEAT>2.3.CO;2.

Barnosky, A.D. (2001). Distinguishing the effects of the Red Queen and Court Jester on Miocene mammal evolution in the northern Rocky Mountains. *Journal of Vertebrate Paleontology*, 21(1):172-185. doi:10.1671/0272-4634(2001)021[0172:DTEOTR]2.0.CO;2.

Barnosky, A.D., and Carrasco, M.A. (2002). Effects of Oligo-Miocene global climate changes on mammalian species richness in the northwestern quarter of the USA. *Evolutionary Ecology Research*, 4(6):811-841.

Barnosky, A.D., Bibi, F., Hopkins, S.S.B., and Nichols, R. (2007). Biostratigraphy and magnetostratigraphy of the mid-Miocene Railroad Canyon Sequence, Montana and Idaho, and age of the mid-Tertiary unconformity west of the continental divide. *Journal of Vertebrate Paleontology*, 27:204-224. doi:10.1671/0272-4634(2007)27[204:BAMOTM]2.0.CO;2.

Barnosky, A.D., Holmes, M., Kirchholtes, R., Lindsey, E., Maguire, K.C., Poust, A.W., Stegner, M.A., Sunseri, J., Swartz, B., and Swift, J. (2014). Prelude to the Anthropocene: Two new North American land mammal ages (NALMAs). *The Anthropocene Review*, 1(3):225-242. doi:10.1177/2053019614547433.

Barry, T.L., Self, S., Kelley, S.P., Reidel, S., Hooper, P., and Widdowson, M. (2010). New 40Ar/39Ar dating of the Grande Ronde lavas, Columbia River Basalts, USA: Implications for duration of flood basalt eruption episodes. *Lithos*, 118:213-222. doi:10.1016/j.lithos.2010.03.014.

Barton, K.E., Howell, D.G., and Vigil, J.F. (2003). The North America tapestry of time and terrain (No. 2781) U.S. Geological Survey, scale 1:8,000,000. doi:10.3133/i2781.

Barton, M.A., and Fricke, H.C. (2006). Mapping topographic relief and elevation of the central Rocky Mountain region during the latest Eocene using stable isotope data from mammalian tooth enamel, *in*, Geological Society of America Abstracts with Programs, vol 38. p. 202.

Batt, G.E., Brandon, M.T., Farley, K.A., and Roden-Tice, M.K. (2001). Tectonic synthesis of the Olympic Mountains segment of the Cascadia wedge, using two-dimensional thermal and kinematic modeling of therrnochronological age. *Journal of Geophysical Research: Solid Earth*, 106(B11):26,731-726,746. doi:10.1029/2001JB000288.

Beaudoin, N., Lacombe, O., Roberts, N.M.W., and Koehn, D. (2018). U-Pb dating of calcite veins reveals complex stress evolution and thrust sequence in the Bighorn Basin, Wyoming, USA. *Geology*, 46(11):1015-1018. doi:10.1130/G45379.1.

Besse, J., and Courtillot, V. (2002). Apparent and true polar wander and the geometry of the geomagnetic field over the last 200 Myr. *Journal of Geophysical Research: Solid Earth*, 107(B11):EPM 6-31. doi:10.1029/2000jb000050.

Bigelow, P.K. (1987). The petrology, stratigraphy and basin history of the Montesano Formation, southwestern Washington and southern Olympic Peninsula. [MSc Thesis: Western Washington University].

Bloemendal, J., King, J.W., Hall, F.R., and Doh, S.-J. (1992). Rock magnetism of late Neogene and Pleistocene deep-sea sediments: Relationship to sediment source, diagenetic processes, and sediment lithology. *Journal of Geophysical Research*, 97:4361-4375. doi:10.1029/91jb03068.

Brandon, M.T., Roden-Tice, M.K., and Garver, J.I. (1998). Late Cenozoic exhumation of the Cascadia accretionary wedge in the Olympic Mountains, northwest Washington State. *GSA Bulletin*, 110(8):985-1009. doi:10.1130/0016-7606(1998)110%3C0985:LCEOTC%3E2.3.CO;2.

Braun, J. (2010). The many surface expressions of mantle dynamics. *Nature Geoscience*, 3(12):825-833. doi:10.1038/ngeo1020.

Brennan, D.T., Sears, J.W., and Mosolf, J.G. (2024). Geologic map of the Belmont Park Ranch 7.5' quadrangle, Madison County, Montana: Montana Bureau of Mines and Geology Geologic Map 99, 1 sheet, scale 1:24,000. doi:10.59691/TJCH2055.

Burbank, D.W., and Barnosky, A.D. (1990). The magnetochronology of Barstovian mammals in southwestern Montana and implications for the initiation of Neogene crustal extension in the northern Rocky Mountains. *GSA Bulletin*, 102:1093-1104. doi:10.1130/0016-7606(1990)102%3C1093:TMOBMI%3E2.3.CO;2.

Burgess, P.M., Gurnis, M., and Moresi, L. (1997). Formation of sequences in the cratonic interior of North America by interaction between mantle, eustatic, and stratigraphic processes. *GSA Bulletin*, 109(12):1515–1535. doi:10.1130/0016-7606(1997)109<1515:FOSITC>2.3.CO;2.

Butler, R.F. (1992). Paleomagnetism: Magnetic domains to geologic terranes. Blackwell Scientific Publications, Boston.

Byerly, A., Tikoff, B., Kahn, M., Jicha, B., Gaschnig, R., and Fayon, A.K. (2016). Internal fabrics of the Idaho batholith, USA. *Lithosphere*, 9(2):283-298. doi:doi.org/10.1130/L551.1.

Cahoon, E.B., Streck, M.J., Koppers, A.A., and Miggins, D.P. (2020). Reshuffling the Columbia River Basalt chronology—Picture Gorge Basalt, the earliest- and longest-erupting formation. *Geology*, 48:348-352. doi:10.1130/G47122.1.

Calede, J.J., and Rasmussen, D.L. (2015). Field guide to the geology and paleontology of the Cabbage Patch beds in the Flint Creek Basin (Renova Formation, Arikareean). *Northwest Geology*, 44:157-188.

Calede, J.J.M. (2020). Pattern and processes of the mammalian turnover of the Arikareean in the northern Rocky Mountains. *Journal of Vertebrate Paleontology*, 40(1). doi:10.1080/02724634.2020.1767117.

Camp, V.E., and Wolff, J.A. (2025). Spatio-temporal evolution of the main-phase Columbia River Basalt Group and its genetic link to the Yellowstone hotspot. *GSA Bulletin*. doi:10.1130/B38098.1.

Campbell, I.H., and Griffiths, R.W. (1990). Implications of mantle plume structure for the evolution of flood basalts. *Earth and Planetary Science Letters*, 99(1-2):79-93. doi:10.1016/0012-821X(90)90072-6.

Carena, S., Bunge, H.P., and Friedrich, A.M. (2019). Analysis of geological hiatus surfaces across Africa in the Cenozoic and implications for the timescales of convectively-maintained topography. *Canadian Journal of Earth Sciences*, 56(12):1333-1346. doi:10.1139/cjes-2018-0329.

Carroll, A.R., Chetel, L.M., and Smith, M.E. (2006). Feast to famine: Sediment supply control on Laramide basin fill. *Geology*, 34(3):197-200. doi:10.1130/G22148.1.

Carroll, A.R., Doebbert, A.C., Booth, A.L., Chamberlain, C.P., Rhodes-Carson, M.K., Smith, M.E., Johnson, C.M., and Beard, B.L. (2008). Capture of high-altitude precipitation by a low-altitude Eocene lake, western U.S. *Geology*, 36(10):791-794. doi:10.1130/G24783A.1.

Cassiliano, M. (2008). A new genus and species of Stenomylinae (Camelidae, Artiodactyla) from the Moonstone Formation (late Barstovian–early Hemphillian) of central Wyoming. *Rocky Mountain Geology*, 43(1):41-110. doi:10.2113/gsrocky.43.1.41.

Cather, S.M., Chapin, C.E., and Kelley, S.A. (2012). Diachronous episodes of Cenozoic erosion in southwestern North America and their relationship to surface uplift, paleoclimate, paleodrainage, and paleoaltimetry. *Geosphere*, 8(6):1177-1206. doi:10.1130/GES00801.1.

Caylor, E., Carrapa, B., Jepson, G., Sherpa, T.Z.L., and DeCelles, P.G. (2023). The rise and fall of Laramide topography and the sediment evacuation from Wyoming. *Geophysical Research Letters*, 50(14). doi:10.1029/2023GL103218.

Cerveny, P.F., and Steidtmann, J.R. (1993). Fission track thermochronology of the Wind River Range, Wyoming: Evidence for timing and magnitude of Laramide exhumation. *Tectonics*, 12(1):77-91. doi:10.1029/92TC01567.

Chamberlain, C.P., Mix, H.T., Mulch, A., Hren, M.T., Kent-Corson, M.L., Davis, S.J., Horton, T.W., and Graham, S.A. (2012). The Cenozoic climatic and topographic evolution of the western North American Cordillera. *American Journal of Science*, 312:213-262. doi:10.2475/02.2012.05.

Charreau, J., Chen, Y., Gilder, S., Barrier, L., Dominguez, S., Augier, R., Sen, S., Avouac, J.P., Gallaud, A., Graveleau, F., and Wang, Q. (2009). Neogene uplift of the Tian Shan Mountains observed in the magnetic record of the Jingou River section (northwest China). *Tectonics*, 28. doi:10.1029/2007TC002137.

Chetel, L.M., Janecke, S.U., Carroll, A.R., Beard, B.L., Johnson, C.M., and Singer, B.S. (2011). Paleogeographic reconstruction of the Eocene Idaho River, North American Cordillera. *GSA Bulletin*, 123(1-2):71-88. doi:10.1130/B30213.1.

Christiansen, R.L. (2001). The Quaternary and Pliocene Yellowstone volcanic field of Wyoming, Idaho, and Montana. U.S. Geological Survey Professional Paper 729-G. doi:10.3133/pp729G.

Clyde, W.C., Sheldon, N.D., Koch, P.L., Gunnell, G.F., and Bartels, W.S. (2001). Linking the Wasatchian/Bridgerian boundary to the Cenozoic Global Climate Optimum: new magnetostratigraphic and isotopic results from South Pass, Wyoming. *Palaeogeopgraphy, Palaeoclimatology, Palaeoecology*, 167(1-2):175-199. doi:10.1016/S0031-0182(00)00238-8.

Clyde, W.C., Hamzi, W., Finarelli, J.A., Wing, S.L., Schankler, D., and Chew, A. (2007). Basin-wide magnetostratigraphic framework for the Bighorn Basin, Wyoming. *GSA Bulletin*, 119(7-8):848-859. doi:10.1130/B26104.1.

Coble, M.A., and Mahood, G.A. (2012). Initial impingement of the Yellowstone plume located by widespread silicic volcanism contemporaneous with Columbia River flood basalts. *Geology*, 40(7):655-658. doi:10.1130/G32692.1.

Cogné, J.P. (2003). PaleoMac: A Macintosh application for treating paleomagnetic data and making plate reconstructions. *Geochemistry, Geophysics, Geosystems*, 4. doi:10.1029/2001GC000227.

Constenius, K.N. (1996). Late Paleogene extensional collapse of the Cordilleran foreland fold and thrust belt. *GSA Bulletin*, 108(1):20-39. doi:10.1130/0016-7606(1996)108%3C0020:LPECOT%3E2.3.CO;2.

Constenius, K.N., Esser, R.P., and Layer, P.W. (2003). Extensional collapse of the Charleston-Nebo salient and its relationship to space-time variations in Cordilleran orogenic belt tectonism and continental stratigraphy, *in* Raynolds, R.G., Flores, R.M., eds., Cenozoic systems of the Rocky Mountain Region. Rocky Mountain SEPM, p. 303-353.

Courtillot, V., Davaille, A., Besse, J., and Stock, J. (2003). Three distinct types of hotspots in the Earth's mantle. *Earth and Planetary Science Letters*, 205:195-308.

Cox, K. (1989). The role of mantle plumes in the development of continental drainage patterns. *Nature*, 342(6252):873.

Day, R., Fuller, M., and Schmidt, V.A. (1977). Hysteresis properties of titanomagnetites: Grain-size and compositional dependence. *Physics of the Earth and Planetary Interiors*, 13:260-267. doi:10.1016/0031-9201(77)90108-X.

DeCelles, P.G. (2004). Late Jurassic to Eocene evolution of the Cordilleran thrust belt and foreland basin system, western U.S.A. *American Journal of Science*, 304(2):105-168. doi:10.2475/ajs.304.2.105.

Dickinson, W.R., and Snyder, W.S. (1978). Plate tectonics of the Laramide orogeny, *in* Matthews, V., ed., Laramide folding associated with basement block faulting in the western United States. Geological Society of America Memoir 151, p. 355-366. doi:10.1130/MEM151-p355.

Dickinson, W.R., Klute, M.A., Hayes, M.J., Janecke, S.U., Lundin, E.R., McKittrick, M.A., and Olivares, M.D. (1988). Paleogeographic and paleotectonic setting of Laramide sedimentary basins in the central Rocky Mountain region. *GSA Bulletin*, 100(7):1023-1039. doi:10.1130/0016-7606(1988)100%3C1023:PAPSOL%3E2.3.CO;2.

Dickinson, W.R. (2002). The Basin and Range province as a composite extensional domain. *International Geology Review*, 44:1-38. doi:10.2747/0020-6814.44.1.1.

Dobbs, S.C., Malkowski, M.A., Schwartz, T.M., Sickmann, Z.T., and Graham, S.A. (2022). Depositional controls on detrital zircon provenance: An example from Upper Cretaceous strata, southern Patagonia. *Frontiers in Earth Science*, 10:824930. doi:10.3389/feart.2022.824930.

du Bray, E.A., and John, D.A. (2011). Petrologic, tectonic, and metallogenic evolution of the Ancestral Cascades magmatic arc, Washington, Oregon, and northern California. *Geosphere*, 7(5):1102-1133. doi:10.1130/GES00669.1.

Duncan, R.A. (1982). A captured island chain in the Coast Range of Oregon and Washington. *Journal of Geophysical Research: Solid Earth*, 87(B13):10827–10837. doi:10.1029/JB087iB13p10827.

Dunlop, D.J. (2002). Theory and application of the Day plot (Mrs/Ms versus Hcr/Hc) 1. Theoretical curves and tests using titanomagnetite data. *Journal of Geophysical Research: Solid Earth*, 107(B3):EPM-4. doi:10.1029/2001JB000486.

Dunlop, D.J., and Özdemir, Ö.E. (2007). Magnetizations in rocks and minerals, *in* Schubert, G., ed., Treatise on geophysics, vol.5. Elsevier B.V., p. 277-336. doi:10.1016/B978-044452748-6.00093-6.

Elliott, C.G., and McDonald, C. (2009). Geologic map and geohazard assessment of Silver Bow County, Montana Montana Bureau of Mines and Geology Open-File Report 585, 88 p., 3 sheets, scale 1:50,000.

Emry, R.J. (1975). Revised Tertiary stratigraphy and paleontology of the western Beaver Divide, Fremont County, Wyoming. *Smithsonian contributions to paleobiology*, 25. doi:10.5479/si.00810266.25.1.

Environmental Systems Research Institute (2009). World Imagery. https://hub.arcgis.com/maps/esri::world-imagery. Accessed January 2024.

Epis, R.C., and Chapin, C.E. (1975). Geomorphic and tectonic implications of the post-Laramide, late Eocene erosion surface in the soutern Rocky Mountains, *in* Curtis, B.F., ed., Cenozoic history of the southern Rocky Mountains: Geological Society of America Memoir 144. p. 45-74. doi:10.1130/MEM144-p45.

Evanoff, E. (1990). Early Oligocene paleovalleys in southern and central Wyoming: Evidence of high local relief on the late Eocene unconformity. *Geology*, 18(5):443-446. doi:10.1130/0091-7613(1990)018%3C0443:EOPISA%3E2.3.CO;2.

Evans, M.E., and Heller, F. (2003). Environmental magnetism: Principles and applications of enviromagnetics. Academic Press, p. 299.

Evernden, J.F., Savage, D.E., Curtis, G.H., and James, G.T. (1964). Potassium-argon dates and the Cenozoic mammalian chronology of North America. *American Journal of Science*, 262(2):145-198. doi:10.2475/ajs.262.2.145.

Fabian, K. (2003). Some additional parameters to estimate domain state from isothermal magnetization measurements. *Earth and Planetary Science Letters*, 213:337-345. doi:10.1016/S0012-821X(03)00329-7.

Fan, M., and Dettman, D.L. (2009). Late Paleocene high Laramide ranges in northeast Wyoming: Oxygen isotope study of ancient river water. *Earth and Planetary Science Letters*, 286:110-121. doi:10.1016/j.epsl.2009.06.024.

Fan, M., DeCelles, P.G., Gehrels, G.E., Dettman, D.L., Quade, J., and Pyton, S.L. (2011). Sedimentology, detrital zircon geochronology, and stable isotope geochemistry of the lower Eocene strata in the Wind River Basin, central Wyoming. *GSA Bulletin*, 123(5-6):979-996. doi:10.1130/B30235.1.

Fan, M., Heller, P., Allen, S.D., and Hough, B.G. (2014a). Middle Cenozoic uplift and concomitant drying in the central Rocky Mountains and adjacent Great Plains. *Geology*, 42(6):547-550. doi:10.1130/G35444.1.

Fan, M., Hough, B.G., and Passey, B.H. (2014b). Middle to late Cenozoic cooling and high topography in the central Rocky Mountains: Constraints from clumped isotope geochemistry. *Earth and Planetary Science Letters*, 408:35-47. doi:10.1016/j.epsl.2014.09.050.

Fan, M., Mankin, A., and Chamberlain, K. (2015). Provenance and depositional ages of late Paleogene fluvial sedimentary rocks in the central Rocky Mountains, U.S.A. *Journal of Sedimentary Research*, 85:1416-1430. doi:10.2110/jsr.2015.87.

Fields, R.W., Tabrum, a.R., and Nichols, R. (1985). Cenozoic rocks of the intermontane basins of western Montana and eastern Idaho: a summary, *in* Flores, R.M., Kaplan, S.S., eds., Cenozoic paleogeography of west-central United States. Rocky Mountain Section, Society of Economic and Petroleum Geologists, p. 9-36.

Finarelli, J.A., and Badgley, C. (2010). Diversity dynamics of Miocene mammals in relation to the history of tectonism and climate. *Proceedings of the Royal Society B: Biological Sciences*, 277:2721-2726. doi:10.1098/rspb.2010.0348.

Fisher, R.A. (1953). Dispersion on a sphere. *Proceedings of the Royal Society of London Series A Mathematical and Physical Sciences*, 217(1130):295-305. doi:10.1098/rspa.1953.0064.

Flinn, D. (1962). On folding during three-dimensional progressive deformation. *Quarterly Journal of the Geological Society*, 118(1-4):385-428. doi:10.1144/gsjgs.118.1.0385.

Foster, D., Mueller, P.A., Heatherington, A., Gifford, J.N., and Kalakay, T.J. (2012). Lu–Hf systematics of magmatic zircons reveal a Proterozoic crustal boundary under the Cretaceous Pioneer batholith, Montana. *Lithos*, 142-143:216-225. doi:10.1016/j.lithos.2012.03.005.

Fowler, C.M.R. (2004). The solid Earth: An introduction to global geophysics. Cambridge University Press, United Kingdom. doi:10.1017/CBO9780511819643.

Fowler, G.A. (1965). The stratigraphy, foraminifera, and paleoecology of the Montesano Formation, Grays Harbor County, Washington. [Ph.D.: Univeristy of Southern California].

Friedrich, A.M. (2018). Palaeogeological hiatus surface mapping: A tool to visualize vertical motion of the continents. *Geological Magazine*, 156(2):308-319. doi:10.1017/S0016756818000560.

Friedrich, A.M., Bunge, H.P., Rieger, S.M., Colli, L., Ghelichkhan, S., and Nerlich, R. (2018). Stratigraphic framework for the plume mode of mantle convection and the analysis of interregional unconformities on geological maps. *Gondwana Research*, 53:159-188. doi:10.1016/j.gr.2017.06.003.

Fritz, W.J., and Sears, J.W. (1993). Tectonics of the Yellowstone hotspot wake in southwestern Montana. *Geology*, 21:427-430.

Fritz, W.J., Sears, J.W., and Wampler, J.M. (2007). Cenozoic volcanic rocks of southwestern Montana. *Northwest Geology*, 36:91-110.

Frost, B.R., Chamberlain, K.R., Swapp, S., Frost, C.D., and Hulsebosch, T.P. (2000). Late Archean structural and metamorphic history of the Wind River Range: Evidence for a long-lived active margin on the Archean Wyoming craton. *GSA Bulletin*, 112(4):564-578. doi:10.1130/0016-7606(2000)112%3C564:LASAMH%3E2.0.CO;2.

Frost, C.D., Frost, B.R., Chamberlain, K.R., and Hulsebosch, T.P. (1998). The Late Archean history of the Wyoming province as recorded by granitic magmatism in the Wind River Range, Wyoming. *Precambrian Research*, 89:145-173. doi:10.1016/S0301-9268(97)00082-X.

Gallo, L.C., Domeier, M., Sapienza, F., Swanson-Hysell, N.L., Vaes, B., Zhang, Y., Arnould, M., Eyster, A., Gürer, D., Király, Á., Robert, B., Rolf, T., Shephard, G., and van der Boon, A. (2023). Embracing Uncertainty to Resolve Polar Wander: A Case Study of Cenozoic North America. *Geophysical Research Letters*, 50. doi:10.1029/2023GL103436.

Galloway, W.E., Whiteaker, T.L., and Ganey-Curry, P. (2011). History of Cenozoic North American drainage basin evolution, sediment yield, and accumulation in the Gulf of Mexico basin. *Geosphere*, 7(4):938-973. doi:10.1130/GES00647.1.

Gerritsen, D., Gilder, S.A., Chen, Y.-W., and Wack, M.R. (2025). Yellowstone plume drives drainage reorganization in the early Miocene. *Science Advances*, 11(47):eadz4275. doi:10.1126/sciadv.adz4275.

Gerritsen, D., Gilder, S.A., Ludat, A.L., and Wack, M.R. (2026). Magnetostratigraphy and source characterization across the early Miocene unconformity, northern Rocky Mountains, USA. *Terra Nova*, 38(1):1-8. doi:10.1111/ter.12779.

Gilder, S., Chen, Y., and Sen, S. (2001). Oligo-Miocene magnetostratigraphy and rock magnetism of the Xishuigou section, Subei (Gansu Province, western China) and implications for shallow inclinations in central Asia. *Journal of Geophysical Research*, 106:30505-30521. doi:10.1029/2001JB000325.

Gower, H.D., and Pease, M.H. (1965). Geology of the Montesano Quadrangle, Washington USGS Numbered Series: Geologic Quadrangle 374, 1 sheet, scale 1:62,500. doi:10.3133/gq374.

Griffiths, R.W., and Campbell, I.H. (1991). Interaction of mantle plume heads with the Earth's surface and onset of small-scale convection. *Journal of Geophysical Research*, 96(B11):18,295-218,310. doi:10.1029/91JB01897.

Grimley, D.A., and Arruda, N.K. (2007). Observations of magnetite dissolution in poorly drained soils. *Soil Science*, 172(12):968-982. doi:10.1097/ss.0b013e3181586b77.

Hager, B.H., Clayton, R.W., Richards, M.A., Comer, R.P., and Dziewonski, A.M. (1985). Lower mantle heterogeneity, dynamic topography and the geoid. *Nature*, 313(14):541-545.

Hall, M.K., and Chase, C.G. (1989). Uplift, unbuckling, and collapse: Flexural history and isostacy of the Wind River Range and Granite Mountains, Wyoming. *Journal of Geophysical Research*, 94(B12):17.581-517.593. doi:10.1029/JB094iB12p17581.

Hanneman, D.L., and Wideman, C.J. (1991). Sequence stratigraphy of Cenozoic continental rocks, southwestern Montana. *GSA Bulletin*, 103:1335-1345. doi:10.1130/0016-7606(1991)103<1335:SSOCCR>2.3.CO;2.

Hanneman, D.L., and Wideman, C.J. (2006). Calcic pedocomplexes - Regional sequence boundary indicators in Tertiary deposits of the Great Plains and western United States, *in* Alonzo-Zarza, A.M., Tanner, L.H., eds., Paleoenvironmental record and applications of calcretes and palustrine carbonates. Geological Society of America Special Paper 416, p. 1-15. doi:10.1130/2006.2416(01).

Hanneman, D.L., and Wideman, C.J. (2010). Contintental sequence stratigraphy and continental carbonates, *in* Alonzo-Zarza, A.M., Tanner, L.H., eds., Carbonates in continental settings: Geochemistry, diagenesis, and applications, vol.62. Elsevier, The Netherlands, p. 215-273. doi:10.1016/S0070-4571(09)06205-0.

Harlan, S.S. (2006). 40Ar/39Ar dates from alkaline intrusions in the northern Crazy Mountains, Montana: Implications for the timing and duration of alkaline magmatism in the central Montana alkalic province. *Rocky Mountain Geology*, 41(1):45-55. doi:10.2113/gsrocky.41.1.45.

Harlan, S.S., and Morgan, L.A. (2010). Paleomagnetic results from Tertiary volcanic strata and intrusions, Absaroka Volcanic Supergroup, Yellowstone National Park and vicinity: Contributions to the North American apparent polar wander path. *Tectonophysics*, 485:245-259. doi:10.1016/j.tecto.2009.12.025.

Harms, T.A., and Baldwin, J.A. (2020). Paleoproterozoic geology of Montana, *in*, Geology of Montana Volume I—Geologic History, vol.122. Montana Bureau of Mines and Geology Special Publication.

Harris, E.B., Strömberg, C.A.E., Sheldon, N.D., Smith, S.Y., and Ibañez-Mejia, M. (2017). Revised chronostratigraphy and biostratigraphy of the early-middle Miocene Railroad Canyon section of central-eastern Idaho, USA. *GSA Bulletin*, 129(9/10):1241-1251. doi:10.1130/B31655.1.

Harris, E.B., Kohn, M.J., and Strömberg, C.A.E. (2020). Stable isotope compositions of herbivore teeth indicate climatic stability leading into the mid-Miocene Climatic Optimum, in Idaho, U.S.A. *Palaeogeography, Palaeoclimatology, Palaeoecology*, 546:109610. doi:10.1016/j.palaeo.2020.109610.

Hayek, J.N., Vilacís, B., Bunge, H.P., Friedrich, A.M., Carena, S., and Vibe, Y. (2020). Continent-scale Hiatus Maps for the Atlantic Realm and Australia since the Upper Jurassic and links to mantle flow induced dynamic topography: Hiatus Maps and links to mantle flow. *Proceedings of the Royal Society A: Mathematical, Physical and Engineering Sciences*, 476(2242). doi:10.1098/rspa.2020.0390.

Henry, C.D., and John, D.A. (2013). Magmatism, ash-flow tuffs, and calderas of the ignimbrite flareup in the western Nevada volcanic field, Great Basin, USA. *Geosphere*, 9(3):951-1008. doi:10.1130/GES00867.1.

Hoggard, M., White, N., and Al-Attar, D. (2016). Global dynamic topography observations reveal limited influence of large-scale mantle flow. *Nature Geoscience*, 9(6):456–463. doi:10.1038/ngeo2709.

Hoggard, M., Winterbourne, J., Czarnota, K., and White, N. (2017). Oceanic residual depth measurements, the plate cooling model, and global dynamic topography. *Journal of Geophysical Research: Solid Earth*, 122(3):2328-2372. doi:10.1002/2016JB013457.

Hoggard, M., Austermann, J., Randel, C., and Stephenson, S. (2021). Observational estimates of dynamic topography through space and time, *in* Marquardt, H., Konter, J., Ballmer, M., Cottaar, S., eds., Mantle convection and surface expressions. American Geophysical Union (AGU), Washington DC, USA, p. 371–411. doi:10.1002/9781119528609.ch15.

Holdt, M.C., White, N.J., Stephenson, S.N., and Conway-Jones, B.W. (2022). Densely sampled global dynamic topographic observations and their significance. *Journal of Geophysical Research: Solid Earth*, 127(7):e2022JB024391. doi:10.1029/2022JB024391.

Hu, S., Stephenson, A., and Appel, E. (2002). A study of gyroremanent magnetisation (GRM) and rotational remanent magnetisation (RRM) carried by greigite from lake sediments. *Geophysics Journal International*, 151(2):469-474. doi:10.1046/j.1365-246X.2002.01793.x.

Huang, C.K., and Kerr, P.F. (1960). Infrared study of the carbonate minerals. *The American Mineralogist*, 45:311-324.

Hughes, G.C. (1980). Cenozoic geology and geomorphology of the Dry Creek Valley, Gallatin County, Montana. [MSc Thesis: Montana State University].

Izett, G.A., and Obradovich, J.D. (2001). 40Ar/39Ar ages of Miocene tuffs in basin-fill deposits (Santa Fe Group, New Mexico, and Troublesome Formation, Colorado) of the Rio Grande Rift System. *The Mountain Geologist*, 38(2):77-86.

Janecke, S.U. (1994). Sedimentation and paleogeography of an Eocene to Oligocene rift zone, Idaho and Montana. *GSA Bulletin*, 106:1083-1095. doi:10.1130/0016-7606(1994)106<1083:SAPOAE>2.3.CO;2.

Janecke, S.U., VanDenburg, C.J., Blankenau, J.J., and M'Gonigle, J.W. (2000). Long-distance longitudinal transport of gravel across the Cordilleran thrust belt of Montana and Idaho. *Geology*, 28(5):439-442.

Janecke, S.U., Dorsey, R.J., Kickham, J., Matoush, J.P., and McIntosh, W. (2005). Geologic Map of the Bachelor Mountain 7.5' Quadrangle Beaverhead County, Montana: Montana Bureau of Mines Open File Report 525, 27 p., 1 sheet, scale 1:24,000.

Janecke, S.U. (2007). Cenozoic extensional processes and tectonics in the northern Rocky Mountains: Southwest Montana and eastern Idaho. *Northwest Geology*, 36:111-132. doi:10.1130/0091-7613(2000)28%3C439:LLTOGA%3E2.0.CO;2.

Johnson, J.F., and Sutherland, W.M. (2009). Geologic map of the Lander 30' x 60' quadrangle, Fremont County, Wyoming Wyoming State Geological Survey Map Series 87, version 1.0, 31 p., scale 1:100,000.

Keefer, W.R. (1970). Structural geology of the Wind River Basin, Wyoming: U.S. Geological Survey Professional Paper 495-D: 35 p., 3 plates. doi:10.3133/pp495D.

King, J.W. (1955). The remanent magnetism of artificially deposited sediments. *Geophysical Supplements to the Monthly Notices of the Royal Astronomical Society*, 7(3):115–134. doi:10.1111/j.1365-246X.1955.tb06558.x.

Kirschvink, J.L. (1980). The least-squares line and plane and the analysis of palaeomagnetic data. *Geophysical Journal International*, 62(3):699-718. doi:10.1111/j.1365-246X.1980.tb02601.x.

Kleinpell, R.M. (1938). Miocene stratigraphy of California. American Association of Petroleum Geologists Special Volume SP9, Tulsa, Okla.

Kohn, M.J., and Fremd, T.J. (2008). Miocene tectonics and climate forcing of biodiversity, western United States. *Geology*, 36(10):783-786. doi:10.1130/G24928A.1.

Krijgsman, W., and Turner, G. (2014). Sediments, Terrestrial (Paleomagnetism), *in* Rink, W.J., Thompson, J.W., eds., Encyclopedia of scientific dating methods. Springer, Dordrecht, p. 752–760. doi:10.1007/978-94-007-6326-5_110-1.

Kuenzi, W.D., and Fields, R.W. (1971). Tertiary stratigraphy, structure, and geologic history, Jefferson Basin, Montana. *GSA Bulletin*, 82:3373-3394. doi:10.1130/0016-7606(1971)82[3373:TSSAGH]2.0.CO;2.

Kukla, T., Rugenstein, J.K.C., Ibarra, D.E., Winninck, M.J., Strömberg, C.A.E., and Chamberlain, C.P. (2022). Drier winters drove Cenozoic open habitat expansion in North America. *AGU Advances*, 3:e2021AV000566. doi:10.1029/2021AV000566.

Lallier, F., Antoine, C., Charreau, J., Caumon, G., and Ruiu, J. (2013). Management of ambiguities in magnetostratigraphic correlation. *Earth and Planetary Science Letters*, 371-372:26-36. doi:10.1016/j.epsl.2013.04.019.

Lielke, K.J. (2012). The climatic, biotic and tectonic evolution of the Paleogene Renova formation of southwestern Montana. [Ph.D. Thesis: University of Montana].

Lillegraven, J.A., and Ostresh, L.M. (1988). Evolution of Wyoming's Early Cenozoic Topography and Drainage Patterns. *National Geographic Research*, 4(3):303-327.

Lillegraven, J.A. (1993). Correlation of Paleogene strata across Wyoming—A user's guide, *in* Snoke, A.W., Steidtmann, J.R., Roberts, S.M., eds., Geology of Wyoming. Geological Survey of Wyoming Memoir 5, p. 414-477.

Link, P.K., Fanning, C.M., and Beranek, L.P. (2005). Reliability and longitudinal change of detrital-zircon age spectra in the Snake River system, Idaho and Wyoming: An example of reproducing the bumpy barcode. *Sedimentary Geology*, 182(1-4):101-142. doi:10.1016/j.sedgeo.2005.07.012.

Link, P.K., Fanning, C.M., and Stroup, C.N. (2008). Detrital zircon U-Pb geochronologic data for selected Cretaceous, Paleogene, Neogene, and Holocene sandstones and river sands in southwest Montana and east-central Idaho: Montana Bureau of Mines and Geology Open-File Report 569.

Liter, M.R., Prothero, D.R., and Hopkins, S.S.B. (2008). Magnetic stratigraphy of the late Hemingfordian-?Barstovian (lower to middle Miocene) Split Rock Formation, central Wyoming, *in* Lucas, S.G., Morgan, G.S., Spielmann, J.A., Prothero, D.R., eds., Neogene Mammals: Bulletin 44. New Mexico Museum of Natural History and Science.

Liu, L., and Stegman, D.R. (2012). Origin of Columbia River flood basalt controlled by propagating rupture of the Farallon slab. *Nature*, 482(7385):386-389. doi:10.1038/nature10749.

Lonn, J.D., Elliott, C.G., Stewart, D.E., Mosolf, J.G., Burmester, R.F., Lewis, R.S., and Pearson, D.M. (2019). Geologic map of the Bannock Pass 7.5' quadrangle, Beaverhead County, Montana, and Lemhi County, Idaho Montana Bureau of Mines and Geology Geologic Map 76, scale 1:24,000.

Lonn, J.D., Burmester, R.F., Lewis, R.S., and McFaddan, M.D. (2020). The Mesoproterozoic Belt Supergroup, *in*, Geology of Montana Volume I—Geologic History, vol.122. Montana Bureau of Mines and Geology Special Publication.

Love, J.D. (1961). Split Rock Formation (Miocene) and Moonstone Formation (Pliocene) in Central Wyoming. *Geological Survey Bulletin* 1121-1. doi:10.3133/b1121I.

Love, J.D. (1978). Cenozoic thrust and normal faulting, and tectonic history of the Badwater area, northeastern margin of Wind River Basin, Wyoming, *in* Boyd, R.G., Olson, G.M., Boberg, W.W., eds.,

Resources of the Wind River Basin, 30th Annual Field Conference Guidebook. Wyoming Geological Association, Casper, p. 234-238.

Lund, K. (2018). Geologic map of the central Beaverhead Mountains, Lemhi County, Idaho, and Beaverhead County, Montana U.S. Geological Survey, scale 1:24,000. doi:10.3133/sim3413.

M'Gonigle, J.W. (1994). Geologic Map of the Deadman Pass Quadrangle, Beaverhead County Montana, and Lemhi County, Idaho: U.S. Geological Survey, scale 1:24,000. doi:10.3133/gq1753.

Malone, D.H., Craddock, J.P., Link, P.K., Foreman, B.Z., Scroggins, M.A., and Rappe, J. (2017). Detrital zircon geochronology of quartzite clasts, northwest Wyoming: Implications for Cordilleran Neoproterozoic stratigraphy and depositional patterns. *Precambrian Research*, 289:116-128.

Mankinen, E.A., Prévot, M., Grommé, C.S., and Coe, R.S. (1985). The Steens Mountain (Oregon) geomagnetic polarity transition: 1. Directional history, duration of episodes, and rock magnetism. *Journal of Geophysical Research: Solid Earth*, 90(B12):10393-10416. doi:10.1029/JB090iB12p10393.

McCafferty, A.E., San, C.A., Lawley, C., Graham, G.E., Gadd, M.G., Huston, D.L., Kelley, K.D., Paradis, S., Peter, J.M., and Czarnota, K. (2023). Magnetic and related derivative GeoTIFF grids and data for the United States and Canada: U.S. Geological Survey data release Publisher. doi:10.5066/P970GDD5.

McFadden, P.L., and Lowes, F.J. (1981). The discrimination of mean directions drawn from Fisher distributions. *Geophysics Journal International*, 67(1):19-33. doi:10.1111/j.1365-246X.1981.tb02729.x.

McFadden, P.L., and McElhinny, M.W. (1988). The combined analysis of remagnetization circles and direct observations in palaeomagnetism. *Earth and Planetary Science Letters*, 87:161-172. doi:10.1016/0012-821X(88)90072-6.

McKenna, M.C., and Love, J.D. (1972). High-level strata containing early Miocene mammals on the Bighorn Mountains, Wyoming. *American Museum novitates*, 2490.

McMillan, M.E., Heller, P.L., and Wing, S.L. (2006). History and causes of post-Laramide relief in the Rocky Mountain orogenic plateau. *GSA Bulletin*, 118(3/4):393-405. doi:10.1130/B25712.1.

Methner, K., Mulch, A., Fiebig, J., Krsnik, E., Löffler, N., Bajnai, D., and Chamberlain, C.P. (2021). Warm high-elevation mid-latitudes during the Miocene climatic optimum: Paleosol clumped isotope temperatures from the northern Rocky Mountains, USA. *Paleoceanography and Paleoclimatology*, 36(6). doi:10.1029/2020PA003991.

Mitrovica, J.X., Beaumont, C., and Jarvis, G.T. (1989). Tilting of continental interiors by the dynamical effects of subduction. *Tectonics*, 8(5):1079–1094. doi:10.1029/TC008i005p01079.

Montejo, C., Stanley, J.R., and Miller, D.E. (2023). Stratigraphy of the Neogene Sixmile Creek Formation from the Gallatin Basin – Implications for Middle Miocene to Pliocene landscape evolution in the Yellowstone region, *in*, 73rd Annual Meeting Rocky Mountain Section of The Geological Society of America, vol 55. Fort Collins, Colorado, USA. doi:10.1130/abs/2023RM-387984.

Mosolf, J.G. (2015). Geologic Field guide to the Tertiary volcanic rocks in the Elliston 30’ × 60’ quadrangle, west-central Montana. *Northwest Geology*, 44:213-232.

Mosolf, J.G., and Vuke, S.M. (2017). Geologic map of the Gravely Mountain 7.5' quadrangle, Powell County, Montana: Montana Bureau of Mines and Geology Open-File Report 693, 1 sheet, scale 1:24,000.

Mosolf, J.G. (2021). Geologic map of the Virginia City 7.5' quadrangle, Madison County, Montana: Montana Bureau of Mines and Geology Geologic Map 80, 1 sheet, scale 1:24,000.

Mosolf, J.G., Brennan, D.T., and Kylander-Clark, A. (2023). U-Pb geochronology data from rock samples collected in the Dillon, Ennis, Gardiner, Hamilton, Hebgen Lake, Lima, and Wisdom 30' x 60' quadrangles, western Montana, 2022-2023: Montana Bureau of Mines and Geology Analytical Dataset 5 Publisher. doi:10.59691/ZQRI9918.

Müller, R.D., Seton, M., Zahirovic, S., Williams, S.E., Matthews, K.J., Wright, N.M., Shephard, G.E., Maloney, K.T., Barnett-Moore, N., Hosseinpour, M., Bower, D.J., and Cannon, J. (2016). Ocean basin evolution and global-scale plate reorganization events since Pangea breakup. *Annual Review of Earth and Planetary Sciences*, 44(1):107-138. doi:10.1146/annurev-earth-060115-012211.

Murphy, J.B., Hynes, A.J., Johnston, S.T., and Keppie, J.D. (2003). Reconstructing the ancestral Yellowstone plume from accreted seamounts and its relationship to flat-slab subduction. *Tectonophysics*, 365(1-4):185-194. doi:10.1016/S0040-1951(03)00022-2.

Nash, B.P., Perkins, M.E., Christensen, J.N., Lee, D.-C., and Halliday, A.N. (2006). The Yellowstone hotspot in space and time: Nd and Hf isotopes in silicic magmas. *Earth and Planetary Science Letters*, 247:143-156. doi:10.1016/j.epsl.2006.04.030.

Néel, L. (1949). Influence des fluctuations thermiques sur l'aimantation de grains ferro-magnétiques très fins. *Comptes Rendus Hebdomadaires Des Seances De L Academie Des Sciences*, 228(8):664–666.

Néel, L. (1955). Some theoretical aspects of rock-magnetism. *Advances in Physics*, 4(14):191-243. doi:10.1080/00018735500101204.

Nielsen, K., and Thomas, R.C. (2004). Paleoenvironmental reconstruction of the mid-Miocene Beaverhead Graben in southwest Montana. *Geological Society of America Abstracts with Programs*, 36(5):546.

Niem, A.R., and Niem, W.A. (1985). Oil and gas investigation of the Astoria basin, Clatsop and northernmost Tillamook Counties, northwest Oregon, scale 1:100,000.

NOAA (2022). ETOPO 2022 15 Arc-Second Global Relief Model: NOAA National Centers for Environmental Information Publisher. doi:10.25921/fd45-gt74.

O'Neill, C., Müller, D., and Steinberger, B. (2005). On the uncertainties in hot spot reconstructions and the significance of moving hot spot reference frames. *Geochemistry, Geophysics, Geosystems*, 6(4):Q04003. doi:10.1029/2004GC000784.

Ogg, J.G. (2020). Chapter 5 - Geomagnetic Polarity Time Scale, *in* Gradstein, F.M., Ogg, J.G., Schmitz, M.D., Ogg, G.M., eds., Geologic Time Scale 2020, vol.1. Elsevier, p. 159-192. doi:10.1016/B978-0-12-824360-2.00005-X.

Opdyke, M.D., and Channell, J.E. (1996). Magnetic stratigraphy. International Geophysics Series 64 Oxford University Press.

Paterson, G.A., Zhao, X., Jackson, M., and Heslop, D. (2018). Measuring, processing, and analyzing hysteresis data. *Geochemistry, Geophysics, Geosystems*, 19(7):1925-1945. doi:10.1029/2018GC007620.

Pease, M.H., and Hoover, L. (1957). Geology of the Doty-Minot Peak area, Washington U.S. Geological Survey Oil and Gas Investigation Map 188, 1 sheet, scale 1:62,500. doi:10.3133/om188.

Perkins, M.E., and Nash, B.P. (2002). Explosive silicic volcanism of the Yellowstone hotspot: The ash-fall tuff record. *GSA Bulletin*, 114(3):367–381. doi:10.1130/0016-7606(2002)114%3C0367:ESVOTY%3E2.0.CO;2.

Peyton, S.L., Reiners, P.W., Carrapa, B., and DeCelles, P.G. (2012). Low-temperature thermochronology of the northern Rocky Mountains, western U.S.A. *American Journal of Science*, 312:145-212. doi:10.2475/02.2012.04.

Portner, R., and Hendrix, M. (2005). Preliminary geologic map of the eastern Flint Creek Basin west-central Montana: Montana Bureau of Mines and Geology Open-File Report 521, 17 p., 1 sheet, scale 1:24,000.

Portner, R.A., Hendrix, M.S., Stalker, J.C., Miggins, D.P., and Sheriff, S.D. (2011). Sedimentary response to orogenic exhumation in the northern rocky mountain basin and range province, flint creek basin, west-central Montana. *Canadian Journal of Earth Sciences*, 48(7):1131-1153. doi:10.1139/e10-107.

Priest, G.R. (1990). Volcanic and tectonic evolution of the Cascade Volcanic Arc, central Oregon. *Journal of Geophysical Research*, 95(B12):19583-19599. doi:10.1029/JB095iB12p19583.

Prothero, D.R., and Armentrout, J.M. (1985). Magnetostratigraphic correlation of the Lincoln Creek Formation, Washington: Implications for the age of the Eocene/Oligocene boundary. *Geology*, 13(3):208-211. doi:10.1130/0091-7613(1985)13%3C208:MCOTLC%3E2.0.CO;2.

Prothero, D.R., Jaquette, C.D., and Armentrout, J.M. (2001). Magnetic stratigraphy of the upper Eocene-upper Oligocene Lincoln Creek Formation, Porter Bluffs, Washington, *in* Prothero, D.R., ed., Magnetic Stratigraphy of the Pacific Coast Cenozoic, vol.91. Pacific Section SEPM (Society for Sedimentary Geology).

Prothero, D.R., and Lau, J.N. (2001). Magnetic stratigraphy of the upper Miocene (type Wishkahan-Graysian) Montesano Formation, Grays Harbor County, Washington, *in* Prothero, D.R., ed., Magnetic stratigraphy of the Pacific Coast Cenozoic, vol.Book 91. Pacific Section SEPM (Society for Sedimentary Geology).

Prothero, D.R., and Sanchez, F. (2004). Magnetic stratigraphy of the middle to upper Eocene section at Beaver Divide, Fremont County, Central Wyoming. *New Mexico Museum of Natural History and Science Bulletin*, No. 26:151-154.

Prothero, D.R., Hoffman, J.M., and Goedert, J.L. (2008). Paleomagnetism of the Oligocene and Miocene Lincoln Creek and Astoria formations, Knappton, Washington, *in* Wang, X., Barnes, L.G., eds., Geology and Vertebrate Paleontology of Western and Southern North America, vol.Science Series 41. Natural History Museum of Los Angeles County.

Pyle, D., Duncan, R., Wells, R.E., Graham, D.W., Harrison, B., and Hanan, B. (2009). Siletzia: An oceanic large igneous province in the Pacific Northwest. *Geological Society of America Abstracts with Programs*, 41(7):369.

Rainbird, R.H., and Ernst, R.E. (2001). The sedimentary record of mantle-plume uplift, *in* Ernst, R.E., Buchan, K.L., eds., Mantle plumes: their identification through time, vol.352. Geological Society of America, p. 227-245. doi:10.1130/0-8137-2352-3.227.

Rasmussen, D.L. (2003). Tertiary history of western Montana and east-central Idaho: A synopsis, *in* Raynolds, R.G., Flores, R.M., eds., Cenozoic systems of the Rocky Mountain region. Rocky Mountain Section SEPM, Denver, p. 459–477.

Rau, W.W. (1966). Stratigraphy and Foraminifera of the Stasop River Area, Southern Olympic Peninsula, Washington.

Rau, W.W. (1967). Geology of the Wynoochee Valley Quadrangle, Grays Harbor County, Washington. *AAPG Bulletin*, 52(3).

Rau, W.W. (1986). Geologic map of the Humptulips Quadrangle and adjacent areas, Grays Harbor County, Washington, scale 1:62,500.

Reidel, S.P. (2005). A lava flow without a source: The Cohassett Flow and its compositional components, Sentinel Bluffs Member, Columbia River Basalt Group. *The Journal of Geology*, 113:1-21. doi:10.1086/425966.

Reidel, S.P., and Tolan, T.L. (2013). The Grande Ronde Basalt, Columbia River Basalt Group, *in* Reidel, S.P., Camp, V.E., Ross, M.E., Wolff, J.A., Martin, B.S., Tolan, T.L., and Wells, R.E., ed., The Columbia River Flood Basalt Province: Geological Society of America Special Paper 497. p. 117–153. doi:10.1130/2013.2497(05).

Retallack, G.J. (2009). Refining a pedogenic-carbonate CO2 paleobarometer to quantify a middle Miocene greenhouse spike. *Palaeogeography, Palaeoclimatology, Palaeoecology*, 281:57-65. doi:10.1016/j.palaeo.2009.07.011.

Reynolds, M.W. (1979). Character and extent of basin-range faulting, western Montana and east-central Idaho, *in* Newman, G.W., Goodge, H.D., eds., Basin and Range symposium and field conference proceedings. Rocky Mountain Association of Geologists and Utah Geological Association, Denver, Colorado, p. 185–193.

Roberts, A.P., Hu, P., Harrison, R.J., Heslop, D., Muxworthy, A.R., Oda, H., Sato, T., Tauxe, L., and Zhao, X. (2019). Domain State Diagnosis in Rock Magnetism: Evaluation of Potential Alternatives to the Day Diagram. *Journal of Geophysical Research: Solid Earth*, 124(6):5286-5314. doi:10.1029/2018JB017049.

Roe, W.P. (2010). Tertiary sediments of the Big Hole valley and Pioneer Mountains, southwestern Montana: Age, provenance, and tectonic implications. [MSc Thesis: The University of Montana].

Rohde, R.A. (2005). GeoWhen Database Publisher.

Rothfuss, J.L., Lielke, K., and Weislogel, A.L. (2012). Application of detrital zircon provenance in paleogeographic reconstruction of an intermontane basin system, Paleogene Renova Formation, southwest Montana, *in* Rasbury, E.T., Hemming, S.R., Riggs, N.R., eds., Mineralogical and

Geochemical Approaches to Provenance: Geological Society of America Special Paper 487. p. 63–95. doi:10.1130/2012.2487(04).

Rowley, J., and Fan, M. (2016). Middle Cenozoic diachronous shift to eolian deposition in the central Rocky Mountains: Timing, provenance, and significance for paleoclimate, tectonics, and paleogeography. *Geosphere*, 12(6):1-18. doi:10.1130/GES01218.1.

Ruppel, E.T. (1982). Cenozoic block uplifts in east-central Idaho and southwest Montana: Geological Survey Professional Paper 1224.24 p. doi:10.3133/pp1224.

Sahagian, D. (1987). Epeirogeny and eustatic sea level changes as inferred from Cretaceous shoreline deposits: Applications to the central and western United States. *Journal of Geophysical Research: Solid Earth*, 92(B6):4895-4904. doi:10.1029/JB092iB06p04895.

Samuels, J.X., and Hopkins, S.S.B. (2017). The impacts of Cenozoic climate and habitat changes on small mammal diversity of North America. *Global and Planetary Change*, 149:36-52. doi:10.1016/j.gloplacha.2016.12.014.

Saunders, A.D., Jones, S.M., Morgan, L.A., Pierce, K.L., Widdowson, M., and Xu, Y.G. (2007). Regional uplift associated with continental large igneous provinces: The roles of mantle plumes and the lithosphere. *Chemical Geology*, 241(3-4):282-318. doi:10.1016/j.chemgeo.2007.01.017.

Scarberry, K.C., Yakovlev, P.V., and Schwartz, T.M. (2020). Mesozoic magmatism in Montana, *in*, Geology of Montana Volume I—Geologic History, vol.122. Montana Bureau of Mines and Geology Special Publication.

Schenck, H.G., and Kleinpell, R.M. (1936). Refugian Stage of Pacific Coast Tertiary. *American Association of Petroleum Geologists Bulletin*, 20(2):215-225. doi:10.1306/3D932DAE-16B1-11D7-8645000102C1865D.

Schmeelk, D., Bendick, R., Stickney, M., and Bomberger, C. (2017). Kinematic evidence for the effect of changing plate boundary conditions on the tectonics of the northern U.S. Rockies. *Tectonics*, 36(6):1090-1102. doi:10.1002/2016TC004427.

Schwartz, T.M., and Schwartz, R.K. (2013). Paleogene postcompressional intermontane basin evolution along the frontal Cordilleran fold-and-thrust belt of southwestern Montana. *GSA Bulletin*, 125(5-6):961-984. doi:10.1130/B30766.1.

Schwartz, T.M., Methner, K., Mulch, A., Graham, S.A., and Chamberlain, C.P. (2019a). Paleogene topographic and climatic evolution of the Northern Rocky Mountains from integrated sedimentary and isotopic data. *GSA Bulletin*, 131(7-8):1203-1223. doi:10.1130/B32068.1.

Schwartz, T.M., Schwartz, R.K., and Weislogel, A.L. (2019b). Orogenic recycling of detrital zircons characterizes age distributions of North American Cordilleran strata. *Tectonics*, 38:4320-4334. doi:10.1029/2019TC005810.

Sears, J.W., and Ryan, P.C. (2003). Cenozoic evolution of the Montana Cordillera: Evidence from paleovalleys, *in* Raynolds, R.G., Flores, R.M., eds., Cenozoic Systems of the Rocky Mountain Region. Rocky Mountain Section (SEPM), Denver, Colorado.

Sears, J.W., Hendrix, M.S., Thomas, R.C., and Fritz, W.J. (2009). Stratigraphic record of the Yellowstone hotspot track, Neogene Sixmile Creek Formation grabens, southwest Montana. *Journal of Volcanology and Geothermal Research*, 188:250-259. doi:10.1016/j.jvolgeores.2009.08.017.

Sherrod, D.R., and Smith, J.G. (2000). Geologic map of upper Eocene to Holocene volcanic and related rocks of the Cascade Range, Oregon: U.S. Geological Survey Miscellaneous Investigations Map I-2569, 17 p., 2 sheets, scale 1:500,000.

Smedes, H.W., and Prostka, H.J. (1972). Stratigraphic framework of the Absaroka Volcanic Supergroup in the Yellowstone National Park region: U.S. Geological Survey Professional Paper 729-C. doi:10.3133/pp729C.

Smith, J.G. (1993). Geologic map of upper Eocene to Holocene volcanic and related rocks in the Cascade Range, Washington: U.S. Geological Survey Miscellaneous Investigations Map I-2005, 20 p., 2 sheets, scale 1:500,000.

Staisch, L.M., O'Connor, J.E., Cannon, C.M., Holm-Denoma, C., Link, P.K., Lasher, J., and Alexander, J.A. (2022). Major reorganization of the Snake River modulated by passage of the Yellowstone Hotspot. *GSA Bulletin*, 134(7-8):1834-1844. doi:10.1130/B36174.1.

Steidtmann, J.R., and Middleton, L.T. (1986). Eocene-Pliocene stratigraphy along the southern margin of the Wind River Range, Wyoming: Revisions and implications from field and fission-track studies. *Mountain Geologist*, 23:19-25.

Steidtmann, J.R., Middleton, L.T., and Shuster, M.W. (1989). Post-Laramide (Oligocene) uplift in the Wind River Range, Wyoming. *Geology*, 17:38-41. doi:10.1130/0091-7613(1989)017%3C0038:PLOUIT%3E2.3.CO;2.

Steidtmann, J.R., and Middleton, L.T. (1991). Fault chronology and uplift history of the southern Wind River Range, Wyoming: Implications for Laramide and post-Laramide deformation in the Rocky Mountain foreland. *GSA Bulletin*, 103(4):472-485. doi:10.1130/0016-7606(1991)103<0472:FCAUHO>2.3.CO;2.

Steiger, R.H., and Jäger, E. (1977). Subcommission on geochronology: Convention on the use of decay constants in geo- and cosmochronology. *Earth and Planetary Science Letters*, 36:359-362. doi:10.1016/0012-821X(77)90060-7.

Steinberger, B., Nelson, P.L., Grand, S.P., and Wang, W. (2019). Yellowstone plume conduit tilt caused by large-scale mantle flow. *Geochemistry, Geophysics, Geosystems*, 20:5896-5912. doi:10.1029/2019GC008490.

Stephenson, S.N., Hoggard, M.J., Holdt, M.C., and White, N. (2024). Continental residual topography extracted from global analysis of crustal structure. *Journal of Geophysical Research: Solid Earth*, 129(4):e2023JB026735. doi:10.1029/2023JB026735.

Stevens, A.L., Balgord, E.A., and Carrapa, B. (2016). Revised exhumation history of the Wind River Range, WY, and implications for Laramide tectonics. *Tectonics*, 35:1121-1136.

Stickney, M.C., and Bartholomew, M.J. (1987). Seismicity and late Quarternary faulting of the northern Basin and Range Province, Montana and Idaho. *SSA Bulletin*, 77(5):1602-1625. doi:10.1785/BSSA0770051602.

Strömberg, C.A.E. (2005). Decoupled taxonomic radiation and ecological expansion of open-habitat grasses in the Cenozoic of North America. *Proceedings of the National Academy of Sciences*, 102(34):11980-11984. doi:10.1073/pnas.0505700102.

Strömberg, C.A.E. (2011). Evolution of Grasses and Grassland Ecosystems. *Annual Review of Earth and Planetary Sciences*, 39:517-544. doi:10.1146/annurev-earth-040809-152402.

Stroup, C.N., Link, P.K., and Fanning, C.M. (2008). Provenance of late Miocene fluvial strata of the Sixmile Creek Formation, southwest Montana: Evidence from detrital zircon. *Northwest Geology*, 37:69-84.

Sutherland, W.M., and Hausel, W.D. (2006). Geologic map of the South Pass 30' x 60' quadrangle, Fremont and Sweetwater counties, Wyoming Wyoming State Geological Survey Map Series 70, scale 1:100,000.

Swisher, C.C., and Prothero, D.R. (1990). Single-crystal 40Ar/39Ar dating of the Eocene-Oligocene transition in North America. *Science*, 249(4970):760-762.

Tabor, R.W., and Cady, W.M. (1978). Geologic map of the Olympic Peninsula, Washington USGS Numbered Series IMAP 994: 2 plates, scale 1:125,000. doi:10.3133/i994.

Tabor, R.W. (1987). Geology of Olympic National Park Pacific Northwest National Parks & Forest Association.

Tauxe, L., and Watson, G.S. (1994). The fold test: an eigen analysis approach. *Earth and Planetary Science Letters*, 122(3-4):331-341. doi:10.1016/0012-821X(94)90006-X.

Tauxe, L. (2003). Paleomagnetic principles and practice. Springer, Dordrecht, p. 301. doi:10.1007/0-306-48128-6.

Tauxe, L. (2010). Essentials of paleomagnetism. University of California Press, Berkeley, p. 368.

Tauxe, L., Heslop, D., and Gilder, S.A. (2024). Assessing paleosecular variation averaging and correcting paleomagnetic inclination shallowing. *Journal of Geophysical Research: Solid Earth*, 129:e2024JB029502. doi:10.1029/2024JB029502.

Tedford, R.H., Albright, L.B., Barnosky, A.D., Ferrusquia-Villafranca, I., Hunt, R.M., Storer, J.E., Swisher, C.C., Voorhies, M.R., Webb, S.D., and Whistler, D.P. (2004). Mammalian biochronology of the Arikareean through Hemphillian interval (late Oligocene through early Pliocene epochs), *in* Woodburne, M.O., ed., Late Cretaceous and Cenozoic mammals of North America: biostratigraphy and geochronology. Columbia University Press.

Thomas, R.C., and Sears, J.W. (2020). Middle Miocene through Pliocene sedimentation and tectonics in Montana: A record of the outbreak and passage of the Yellowstone hotspot, *in*, Geology of Montana Volume I—Geologic History, vol.122. Montana Bureau of Mines and Geology Special Publication.

Thompson, G.A., Fields, R.W., and Alt, D. (1982). Land-based evidence for Tertiary climatic variations: Northern Rockies. *Geology*, 10:413-417. doi:10.1130/0091-7613(1982)10<413:LEFTCV>2.0.CO;2.

Torsvik, T.H., Müller, R.D., Van Der Voo, R., Steinberger, B., and Gaina, C. (2008). Global plate motion frames: Toward a unified model. *Reviews of Geophysics*, 46(3):1-44. doi:10.1029/2007RG000227.

Tsukui, K., Flynn, J.J., Hemming, S.R., Ramezani, J., Machlus, M.L., Nuñez, C., McCarroll, S.J., and Bowring, S.A. (2025). Magnetostratigraphy and U-Pb geochronology of the middle Eocene Bridger Formation (Wyoming, USA): Implications for the age and correlation of the Bridgerian/Uintan NALMA boundary and calibration of the Geomagnetic Polarity Time Scale. *GSA Bulletin*. doi:10.1130/B37223.1.

Van Houten, F.B. (1964). Tertiary geology of the Beaver Rim area Fremont and Natrona Counties, Wyoming. *GSA Bulletin*, 1164. doi:10.3133/b1164.

Vandenburg, C.J., Janecke, S.U., and McIntosh, W.C. (1998). Three-dimensional strain produced by >50 My of episodic extension, Horse Prairie basin area, SW Montana, U.S.A. *Journal of Structural Geology*, 20:1747-1767. doi:10.1016/S0191-8141(98)00084-4.

Vibe, Y., Friedrich, A.M., Bunge, H.P., and Clark, S.R. (2018). Correlations of oceanic spreading rates and hiatus surface area in the North Atlantic realm. *Lithosphere*, 10:677-684. doi:10.1130/L736.1.

Vilacís, B., Hayek, J.N., Stotz, I.L., Bunge, H.P., Friedrich, A.M., Carena, S., and Clark, S. (2022). Evidence for active upper mantle flow in the Atlantic and Indo-Australian realms since the Upper Jurassic from hiatus maps and spreading rate changes. *Proceedings of the Royal Society A: Mathematical, Physical and Engineering Sciences*, 478(2262). doi:10.1098/rspa.2021.0764.

Vilacís, B., Brown, H., Bunge, H.-P., Carena, S., Hayek, J.N., Stotz, I.L., Wang, Z.R., and Friedrich, A.M. (2024). Dynamic topography and the planform of mantle convection since the Jurassic inferred from global continental hiatus maps. *Proceedings of the Royal Society A*, 480(2302):20240311. doi:10.1098/rspa.2024.0311.

Vilacís, B. (2025). Inferring mantle flow histories from global continental hiatus surfaces. [Ph.D. Thesis: Ludwig-Maximilians-Universität München], 161 p.

Vuke, S.M. (2003). Geology of western and northern Gallatin Valley, southwestern Montana Montana Bureau of Mines and Geology Open-File Report 481, 40 p., 1 sheet, scale 1:50,000.

Vuke, S.M. (2004). Geologic map of the Divide area, southwest Montana: Montana Bureau of Mines and Geology Open-File Report 502, 36 p., 1 sheet, scale 1:50,000.

Vuke, S.M., Coppinger, W.W., and Cox, B.E. (2004). Geologic map of Cenozoic deposits in the Upper Jefferson Valley, southwestern Montana: Montana Bureau of Mines and Geology Open-File Report 505, 35 p., 1 sheet, scale 1:50,000.

Vuke, S.M. (2006). Geologic map of the Cenozoic deposits of the lower Jefferson Valley, southwestern Montana: Montana Bureau of Mines and Geology Open-File Report 537, 41 p., 1 sheet, scale 1:50,000.

Vuke, S.M., Porter, K.W., Lonn, J.D., and Lopez, D.A. (2007). Geologic map of Montana: Montana Bureau of Mines and Geology Geologic Map 62, 73 p., 2 sheets, scale 1:500,000.

Vuke, S.M. (2020). The Eocene through early Miocene sedimentary record in western Montana, *in*, Geology of Montana Volume I—Geologic History, vol.122. Montana Bureau of Mines and Geology Special Publication.

Wack, M.R., and Gilder, S.A. (2012). The SushiBar: An automated system for paleomagnetic investigations. *Geochemistry, Geophysics, Geosystems*, 13(12). doi:10.1029/2011GC003985.

Walker, J.D., Bowers, T.D., Black, R.A., Glazner, A.F., Farmer, G.L., and Carlson, R.W. (2006). A geochemical database for western North American volcanic and intrusive rocks (NAVDAT). *in* Sinha, A.K., ed., Geoinformatics: Data to Knowledge. Geological Society of America. doi:10.1130/2006.2397(05).

Wang, D., and van der Voo, R. (2004). The hysteresis properties of multidomain magnetite and titanomagnetite/titanomaghemite in mid-ocean ridge basalts. *Earth and Planetary Science Letters*, 220:175-184. doi:10.1016/S0012-821X(04)00052-4.

Wang, X., Wideman, B.C., Nichols, R., and Hanneman, D.L. (2004). A new species of Aelurodon (Carnivora, Canidae) from the Barstovian of Montana. *Journal of Vertebrate Paleontology*, 24(2):445-452. doi:10.1671/2493.

Warnock, A.C. (1992). Paleomagnetism and tectonics of the Crescent Formation northern Olympic Mountains, Washington. MSc Thesis: Western Washington University.

Weaver, C.E. (1944). Correlation of the marine Cenozoic formations of western North America. *GSA Bulletin*, 55(5):569–598. doi:10.1130/GSAB-55-569.

Wells, R., Bukry, D., Friedman, R., Pyle, D., Duncan, R., Haeussler, P., and Wooden, J. (2014). Geologic history of Siletzia, a large igneous province in the Oregon and Washington Coast Range: Correlation to the geomagnetic polarity time scale and implications for a long-lived Yellowstone hotspot. *Geosphere*, 10(4):692-719. doi:10.1130/GES01018.1.

Wells, R.E., and Coe, R.S. (1985). Paleomagnetism and geology of Eocene volcanic rocks of southwest Washington, implications for mechanism of tectonic rotation. *Journal of Geophysical Research: Solid Earth*, 90(B2):1925-1947. doi:10.1029/JB090iB02p01925.

Wells, R.E., and Sawlan, M.G. (2014). Preliminary geologic map of the eastern Willapa Hills, Cowlitz, Lewis, and Wahkiakum Counties, Washington U.S. Geological Survey Open-File Report 2104-1063, 2 sheets, scale 1:50,000. doi:10.3133/ofr20141063.

Zachos, J., Pagani, M., Sloan, L., Thomas, E., and Billups, K. (2001). Trends, rhythms, and aberations in global climate 65 Ma to present. *Science*, 292(5517):686-693. doi:10.1126/science.1059412.

Zheng, J. (1996). Magnetostratigraphy of a Miocene sedimentary sequence in Railroad Canyon, Idaho. [Ph.D. Thesis: University of Pittsburgh], 248 p.

Zijderveld, J. (1967). A.C. demagnetization of rocks: Analysis of results, *in* Runcorn, S., Creer, K., Collinson, D., eds., Methods in palaeomagnetism. Elsevier, Amsterdam, p. 254–286. doi:10.1016/B978-1-4832-2894-5.50049-5.

Acknowledgements

There are many people I'd like to thank for being there for me during this PhD journey.

First and foremost, I want to thank Stu. I'm really grateful to have had you as my supervisor and mentor. Whenever I had a question, your office was just a few steps away. Although you've gotten busier and busier over the years, you would always make time. You taught me to stay optimistic and focus on the data that work, rather than getting hung up on those that don't. I'm still dazzled by how much you know about everything related to geology. Thinking back of singing "These Boots Are Made for Walkin'" in the field together will always bring a smile to my face!

Bedankt Wout dat je me destijds op deze positie gewezen hebt en voor je bereidheid af te reizen naar München om mijn tweede beoordelaar te zijn.

I'd like to thank Berta, Sabrina, and Iuliia, with whom I had the pleasure of living together. Thanks for listening to me complaining as well as distracting me from work during movie nights, drinking cocktails on the balcony, or just chatting in the kitchen. Berta, thanks for making me feel at home in Munich. I very much enjoyed the Zumba Mondays with you, which were always a great mood booster. Sabrina, thanks for introducing me to trashy German shows and joining me on many great hikes. Iuliia, I loved our endless conversations about language, culture, and life—thank you for your openness.

Thanks to all my fellow PhD students and postdocs from the fourth floor with whom I enjoyed lunch or beer Friday: Egi, Rachel, Gabriel, Isi, Suganth, Nasi, Yuchen, Felix, Yara, Kathi, Andi, Ricardo, Leon, Artem, Hamish, Roman, Anna, Tanya, Anang, Sandra, and Ingo. With many of you I also went bouldering, hiking, or even biking. Thanks for your company and welcome distraction from work.

I would also like to thank all the others in the UPLIFT project. It was great to be part of a group and go through this journey together. I've learned a great deal from our discussions and communicating my research to such an interdisciplinary crowd. Yi-Wei, thanks for collaborating with me on the US topic; I enjoyed our discussions and your thoughtful comments. Alina, although our expectations for the PhD together didn't quite work out as planned, you were always willing to collaborate and we enjoyed some great trips together —thank you!

A huge thanks to my students, Timon, Sophia, Simon, and Marti, who deserve lots of credit for the endless VSM hours and late SushiBar shifts; without you, I would still be working in the lab by now.

Thanks to Michi, whom I got to know whilst road tripping through the western US with our enormous RV, which was so loud we'd often just turn up the music as loud as possible. Thanks for always being there to answer my ignorant questions. I enjoyed all the field trips we've been on together in the US, China, and the Alps and will cherish those moments. Danke dir, Stefan, und allen anderen aus der Werkstatt, dass ihr die SushiBar am Laufen gehalten habt und zum zigsten Mal die Arme repariert habt.

Als laatste wil ik natuurlijk ook mijn vrienden en familie in Nederland bedanken. Ondanks de afstand kon ik altijd van jullie op aan. Flore, Kim, Irene, Frenk, Nathalie, Stan, Bente, Margo, Arjan en Joren, we kennen elkaar inmiddels tien jaar en ik hoop dat er nog vele volgen. Tijdens mijn tijd hier in München heb ik veel contact met jullie gehad en erg genoten van onze gezamenlijke weekendjes weg en het "writing retreat" naar Italië. Froukje en Doortje, bedankt voor de bezoekjes aan München en het altijd maken van tijd als ik weer eens even kort in Utrecht was. Ar, Cootje en Beer, jullie zijn natuurlijk als ervaringsdeskundigen altijd mijn vraagbaak geweest. Bedankt voor alle gezellige nachtjes logeren tijdens mijn bezoekjes aan Nederland, de telefoontjes en de vele online bordspelletjes. Pap en mam, bedankt voor jullie luisterend oor en onvoorwaardelijke steun door de jaren heen.